Impact of Converter Interfaced Generation and Load on Grid Performance

by

Deepak Ramasubramanian

A Dissertation Presented in Partial Fulfillment
of the Requirements for the Degree
Doctor of Philosophy

Approved January 2017 by the
Graduate Supervisory Committee:

Vijay Vittal, Chair
John Undrill
Raja Ayyanar
Jiangchao Qin

ARIZONA STATE UNIVERSITY

May 2017

ABSTRACT

Alternate sources of energy such as wind, solar photovoltaic and fuel cells are coupled to the power grid with the help of solid state converters. Continued deregulation of the power sector coupled with favorable government incentives has resulted in the rapid growth of renewable energy sources connected to the distribution system at a voltage level of 34.5kV or below. Of late, many utilities are also investing in these alternate sources of energy with the point of interconnection with the power grid being at the transmission level. These converter interfaced generation along with their associated control have the ability to provide the advantage of fast control of frequency, voltage, active, and reactive power. However, their ability to provide stability in a large system is yet to be investigated in detail. This is the primary objective of this research.

In the future, along with an increase in the percentage of converter interfaced renewable energy sources connected to the transmission network, there exists a possibility of even connecting synchronous machines to the grid through converters. Thus, all sources of energy can be expected to be coupled to the grid through converters. The control and operation of such a grid will be unlike anything that has been encountered till now. In this dissertation, the operation and behavior of such a grid will be investigated. The first step in such an analysis will be to build an accurate and simple mathematical model to represent the corresponding components in commercial software. Once this bridge has been crossed, conventional machines will be replaced with their solid state interfaced counterparts in a phased manner. At each stage, attention will be devoted to the control of these sources and also on the stability performance of the large power system.

This dissertation addresses various concerns regarding the control and operation of a futuristic power grid. In addition, this dissertation also aims to address the issue

of whether a requirement may arise to redefine operational reliability criteria based on the results obtained.

ACKNOWLEDGMENTS

I would like to thank and express my deepest gratitude to Dr. Vijay Vittal for providing me with the opportunity to work on this project. It has been a great learning experience for me. Dr. Vittal has been an infinite source of support, encouragement and guidance. His positive critique and insightful comments have played a significant role in the completion of this dissertation.

I would also like to thank Dr. John Undrill for being a guiding light during the duration of my stay at ASU. He has been a constant source of encouragement and knowledge. The numerous hours I have spent discussing my dissertation with him have always been fruitful and insightful. I would also like to thank him for taking time out to review this work and for being on my graduate supervisory committee.

I would like to thank Dr. Raja Ayyanar and Dr. Jiangchao Qin, for taking time out to review this work and for being on my graduate supervisory committee. Their comments and suggestions helped in bridging the gap between power electronics and power systems.

I would like to thank Ziwei Yu from ASU for contributing to the validation process in the initial stages of this dissertation. Also, special thanks to Thibault Prévost from Réseau de transport d'électricité - RTE France for his valuable comments and suggestions during my research work.

I am thankful to the Power Systems Engineering Research Center (PSerc) for providing financial support during the course of this work.

Being hundreds of leagues away from home is never easy, and I would like to express my heartfelt gratitude to my parents Dr. S. Ramasubramanian and Mrs. Chandra Ramasubramanian for their unwavering love, support and encouragement. I am also grateful to my elder brother Bhaskar Ramasubramanian for his continuous support and encouragement. I am thankful to all my friends for their support and to

anyone else who contributed directly or indirectly in aiding the successful completion of this dissertation.

TABLE OF CONTENTS

CHAPTER Page

CHAPTER Page

CHAPTER Page

LIST OF TABLES

LIST OF FIGURES

Figure Page

Figure Page

Figure Page

Figure Page

Figure Page

Figure Page

Figure Page

Figure Page

Figure Page

LIST OF SYMBOLS

Symbol	Description
$a_{ind}, b_{ind}, c_{ind}$	Quadratic equation coefficients in induction motor powerflow inclusion
A_{sat}, B_{sat}	Saturation function constants
ACE	Area control error
AZ	Arizona
ac	Alternating current
C_{dc}	dc capacitor of inverter
CIG	Converter interfaced generation
CIL	Converter interfaced load
CSC	Current source converter
d/dt	Time derivative
D	Speed damping coefficient in synchronous machine
D_{ind}	Speed damping coefficient in induction machine
DFIG	Doubly-fed induction generator
DSA	Dynamic security assessment
dc	Direct current
e	Denotes the error signal in an exciter
e''	Complex value of voltage behind subtransient reactance in the dq frame
e''_d, e''_q	d and q axis components of the voltage behind subtransient reactance
$E_{a,b,c}$	Internal converter voltage in abc frame
E'_d, E'_q	d and q axis components of the transient voltage
E_d, E_q	d and q axis components of internal converter voltage

E_{ln}	Line to neutral voltage magnitude on ac side of rectifier
E'	Voltage behind transient reactance in a synchronous machine in *abc* frame
E''	Voltage behind subtransient reactance in a synchronous machine in *abc* frame
E^*	Magnitude of internal converter voltage
E	Magnitude of reference internal converter voltage
E_{FD}	Synchronous machine stator voltage corresponding to field voltage
E_{thev}	Magnitude of voltage of Thévenin source
EMF	Electro motive force
EWTGFC	PSLF wind turbine controller model
EXAC4,EXST1	AC and static exciter models in PSLF
f	Denotes the feedback signal in exciter
$f()$	Function denoting a differential equation
$\mathfrak{f}_{thev}$	Frequency of Thévenin source
fmetr	Frequency meter model in PSLF
FACTS	Flexible AC transmission system
$g()$	Function denoting an algebraic equation
GE	General electric
GENCLS	Classical machine model in PSLF
GENROU	Detailed synchronous machine model in PSLF
GENTPF	Synchronous machine model in PSLF
GEWTG	PSLF GE wind generator model
H	Inertia constant of synchronous machine
H_{ind}	Inertia constant of induction motor

i	Synchronous machine behind rectifier-inverter set current magnitude
i_d, i_q	Converter current along the d and q axis
i_{d1}, i_{q1}	Converter current loop output currents along the d and q axis
I_{dc}^{dr}	dc current of induction motor speed drive
$i_{inv_d}^{dr}, i_{inv_q}^{dr}$	d and q axis stator current components of an induction motor
I	Current injected by the machine into the network in the abc frame
$\overline{I}$	Vector of network currents
I_{grid}	Current injected into the power network by converter
I_i, I_o	Inverter dc capacitor input and output current
I_{inv}^{dr}	Inverter current of induction motor speed drive
I_{max}	Maximum converter current
I_{Pcmd}, I_{Qcmd}	Active and reactive current commands in converter controller
I_r	Induction motor complex rotor current
I_{rect}^{dr}	Rectifier current of induction motor speed drive
I_s	Induction motor complex stator current
IEEE	Institute of Electrical and Electronics Engineers
kV	Unit of voltage (kilo volts)
K	Constant to denote constant air gap flux in induction motor
K_a	Exciter gain
K_f	Feedback gain in exciter
K_{fv}	Gain in converter frequency control path
K_{gi}, K_{gp}	Integral and proportional gains in governor of synchronous machine behind rectifier-inverter set
K_i, K_p	Integral and proportional gains in converter controller

K_{idc}, K_{pdc}	Integral and proportional gains in rectifier firing angle control of synchronous machine behind rectifier-inverter set
K_{idrive}	Integral gain in induction motor speed control drive
K_{ip}, K_{iq}	Integral gains in converter controller
K_{limit}	Anti-windup proportional gain in converter controller
K_n	Constants in induction motor steady state powerflow equations; n=1,2,3,4
K_{pdrive}	Proportional gain in induction motor speed control drive
K_{pp}, K_{pq}	Proportional gains in inner current loop of converter controller
L_{dc}	Rectifier dc side filter inductor
L'_d, L'_q	Synchronous machine transient inductances along the d and q axis
L''_d, L''_q	Synchronous machine subtransient inductances along the d and q axis
L_f	Converter coupling inductance
LADWP	Los Angeles Department of Water and Power
LVPL	Low voltage power logic
m	Amplitude modulation ratio in converter
m_{ind}	Amplitude modulation ratio in inverter speed control drive
M	Transformed reduced admittance matrix
MVA	Unit of complex power (mega volt amp)
MVA_{base}	Power base
MVAR,MW	Units of reactive and active power (mega vars and mega watts)
MPPT	Maximum power point tracking
pf	Power factor
P	Power

P_{actual}	Converter active power
P_{cmd}	Active power command generated by converter controller
P_{conv}	Inverter active power of rectifier-inverter set of generator
P_{dc}^{dr}	dc power of rectifier-inverter set of induction motor speed drive
P_e	Output electrical power of machine
$P_{e_{ind}}$	Electrical active load of induction motor
P_g	Scheduled generator output power at rated speed
P_{gen}	Synchronous machine active power behind rectifier-inverter set
P_g'	Final achieved steady state power at frequency ω_p
P_{inv}^{dr}	Inverter active power of induction motor speed drive
P_m	Input mechanical power of a synchronous machine
P_{max}	Maximum active power of a power source
P_{mech}	Mechanical power signal of synchronous machine behind rectifier-inverter set
P_{m0}	Steady state load power of an induction motor
P_{ord}	Reference active power signal for converter controller in PSLF
P_{rect}	Rectifier active power of rectifier-inverter set of generator
P_{rect}^{dr}	Rectifier active power of rectifier-inverter set of induction motor
P_{ref}	Reference active power set point
P_{set}	Reference active power set point in governor of synchronous machine behind rectifier-inverter set
PI	Proportional Integral
PSLF	Positive sequence load flow
PSS	Power system stabilizer
PSS/E	Power system simulator for engineering
PV	Photo voltaic

PV1G,PV1E	PSLF converter models
PWM	Pulse width modulation
q_{max_1}, q_{max_2}	Reactive power values at 1.0pu and 0.75pu terminal voltage for converter
Q_{cmd}	Reactive power command generated by converter controller
Q_{conv}	Inverter reactive power of rectifier-inverter set
$Q_{e_{ind}}$	Electrical reactive load of induction motor
Q_g	Generated reactive power
Q_{gen}	Synchronous machine reactive power behind rectifier-inverter set
Q_{inv}^{dr}	Reactive power of inverter of induction motor speed drive
Q_{max}, Q_{min}	Maximum and minimum reactive power of a power source
Q_{rect}^{dr}	Reactive power consumed by rectifier of induction motor speed drive
r	Synchronous machine stator resistance
R	Droop coefficient for thermal governor
$R - L$	Resistance and inductance series circuit
R_a	Synchronous machine stator resistance
R_f	Resistance of converter coupling inductor
R_p	Active power droop coefficient in converter controller
R_q	Reactive power droop coefficient in converter controller
R_r	Rotor resistance of an induction motor
R_s	Stator resistance of an induction motor
RPS	Renewable portfolio standards
s	Represents complex frequency $j\omega$ in Laplace domain
s_i	Indicates the i^{th} state in a block diagram

s_{ind}	Slip of an induction motor
SCC_{MVA}	Short Circuit Capacity in MVA
SCR	Short Circuit Ratio
SOCAL	Southern California
t	Time
T	Transformation matrix
T_1, T_2	Time constants of the lead lag block in a turbine governor
T_a	Exciter time constant
T_b, T_c	Time constants of the lead lag block in a exciter
T_e	Electrical torque of an induction machine
T_{ed}, T_{eq}	Converter voltage time constants
T_f	Feedback time constant in exciter
T_{frq}	Angular frequency measurement time constant internal to PSLF
T_{frqv}	Time constant in converter frequency control path
T_r	Transducer time constant
T_D, T_Q	Converter current time constants
T_G	Time constant of the first order time delay block in a turbine governor
T_{Gpv}	Time constant of the first order time delay block in converter controller
T_{Gsync}	Time constant of the first order time delay block in governor of synchronous machine behind rectifier-inverter set
T_m	Mechanical/load torque of a synchronous/induction machine
T'_o	Time constant of stator circuit in an induction motor
TGOV1	Governor model in PSLF

u	Vector of input/control variables
$varflg$	Flag setting in PSLF converter controller model
v'_d, v'_q	Induction motor induced voltage along the d and q axis
v_d, v_q	Synchronous machine/converter terminal voltage along the d and q axis
v_{ds}, v_{qs}	Induction machine terminal voltage along the d and q axis
v_D, v_Q	Synchronous machine stator voltage along the D and Q axis
$\overline{V}$	Vector of network voltages
V'	Internal complex induced voltage in induction motor
V_{abc}	Converter voltage in abc frame
$V_{a,b,c}^{stator}$	Induction motor stator phase voltages
V_{ac}	Rectifier ac voltage of induction motor speed drive
V_{dc}	Converter dc voltage
V_{dc}^{dr}	dc voltage of induction motor speed drive
V_{dc}^{rect}	Rectifier dc side voltage
$\hat{V}_{dc_{new}}^{dr}$	Estimated new value of dc voltage of induction motor speed drive
V_{dcbase}	Converter dc voltage base
V_{dcref}	Converter dc voltage reference
V_{err}	Converter terminal voltage error signal fed into PI controller
V_{ref}	Reference terminal voltage level
V_{sch}	Scheduled voltage
V_s	Terminal voltage of induction motor
V_s^{ref}	Reference stator voltage for an induction motor
V_t	Terminal voltage of generator/converter
$V_{t_{d0}}, V_{t_{q0}}$	Terminal voltage of converter along the d and q axis

V_{tgen}	Terminal voltage of synchronous machine behind rectifier-inverter set
V_{tref}	Reference terminal voltage of synchronous machine behind rectifier-inverter set
V_T	Converter carrier voltage for PWM switching
V/ƒ	Constant voltage-frequency control element
V_ℓ	Voltage behind leakage reactance
VSC	Voltage source converter
WECC	Western electricity coordinating council
x	Vector of state variables in a system
$\dot{x}$	Vector of time derivatives of the state variables
x_d, x_q	d and q axis synchronous reactance of a synchronous machine
x'_d, x'_q	d and q axis transient reactance of a synchronous machine
x''_d, x''_q	d and q axis subtransient reactance of a synchronous machine
x_{tran}	Reactance of transformer behind rectifier-inverter set of generator
x^{dr}_{tran}	Reactance of transformer in front of rectifier-inverter set of induction motor
x''	Subtransient reactance of a synchronous machine
x_ℓ	Synchronous machine leakage reactance
X_e	Reactance of external network inductor
X_f	Reactance of converter coupling inductor
X_m/L_m	Induction motor synchronous frequency mutual reactance/inductance
X_r/L_r	Induction motor synchronous frequency rotor reactance/inductance

$X_{r\ell}$	Induction motor synchronous frequency rotor leakage reactance
$X_{s\ell}$	Induction motor synchronous frequency stator leakage reactance
X'_s	Induction motor synchronous frequency stator transient reactance
y	Vector of network variables
$\overline{Y}$	Reduced network admittance matrix
α	Internal voltage angle of synchronous machine behind rectifier-inverter set
α_{rect}	Firing angle of rectifier for synchronous machine behind rectifier-inverter set
δ	Torque angle of synchronous machine/Angle of converter internal voltage
λ_d, λ_q	d and q axis flux linkage along the air gap of a synchronous machine
λ_D, λ_Q	d and q axis flux linkage of the synchronous machine damper windings
ϕ	Angle of reference internal voltage of converter
ϕ_{sync}	Air gap flux of synchronous machine
ϕ_{airgap}	Air gap flux of induction machine
ϕ_{rect}	Power factor angle of rectifier of rectifier-inverter set
ψ	Angle of synchronous machine current behind rectifier-inverter set
$\psi_{ind}^{dr}, \psi_{ind}^{qr}$	Induction motor rotor flux linkages along d and q axis
τ	Inverter dc capacitor time constant

τ'_{d0}, τ'_{q0}	d and q axis components of the open circuit transient time constant
τ''_{d0}, τ''_{q0}	d and q axis components of the open circuit subtransient time constant
θ	Angle output from phased locked loop in converter
ω	Rotor speed of a synchronous generator/Angular frequency in power system
ω_p	Steady state frequency achieved by the droop controller after a disturbance
ω_{ref}	Value of angular frequency for which zero electrical power produced in droop controller
$\omega_{r_{ind}}$	Speed of the rotor of an induction motor
$\omega_{r_{ind}}^{ref}$	Reference speed of the rotor of an induction motor
ω_R	Rated rotor speed of a synchronous machine
ω_s	Synchronous rotor speed/Reference angular frequency in power system
ω_s^{ref}	Angular frequency reference for stator field in an induction motor
$\omega_{sl_{ind}}^{ref}$	Reference slip speed of the rotor of an induction motor
Δ	Indicates a small change in a quantity

Chapter 1

INTRODUCTION

1.1 Background

Fossil fuel fired steam power plants form the backbone of the electric power infrastructure. In 2013, in the United States alone, fossil fuel power plants have contributed close to 67% of the total 4 trillion kilowatt-hours of electricity generation, Figure 1.1 [1]. However, the contribution of coal to power generation has been

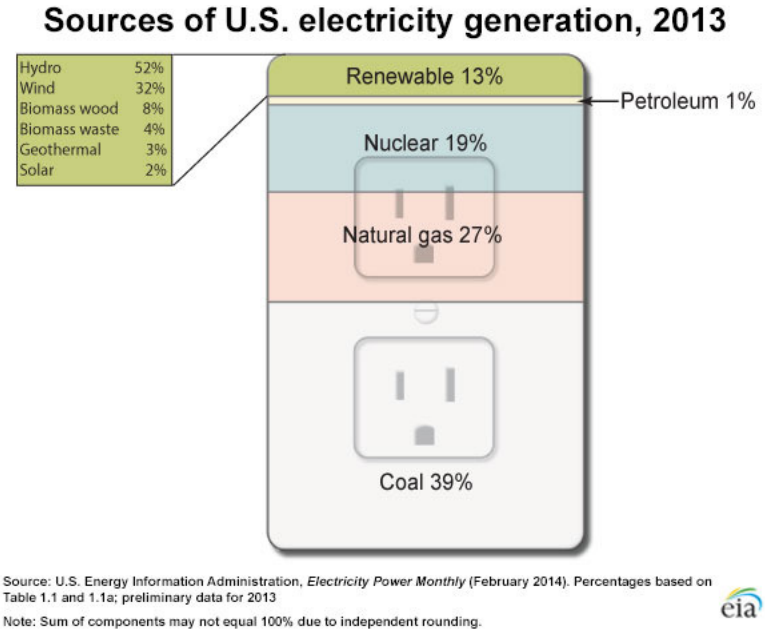

Figure 1.1: Sources of electricity generation in U.S. in 2013

steadily shrinking due to the increased production of electricity from natural gas, nuclear and wind resources. As it can be seen from Figure 1.1, presently natural gas and coal fired power plants provide the maximum contribution for the generation of electricity. This generation resource portfolio however will soon have to have a different profile as the predicted reserves of coal, natural gas and petroleum are set

to last only for another 100 years or so [2, 3]. These figures bring about the need to explore different viable options of power generation. Further, with more stringent environmental considerations and emission controls, there is a need and requirement for cleaner energy generation sources. These sources, at present, represent the remaining 32% of the electrical energy generated. While nuclear power is considered to be a clean and efficient energy source, there are many concerns with regard to the safe operation of a nuclear power plant. The incident in Japan in 2011 has resulted in many countries, such as Germany, Australia, Portugal and Switzerland, restructuring their nuclear policy [4–6]. With the stacking of such odds, the electrical energy extracted from renewable energy sources will have to rise from the present 13% to a significant proportion of the total electricity energy generated.

Power systems are at present dominated by synchronous machines which generate electricity at an almost constant frequency of 60Hz (50Hz in certain parts of the world). These large machines are the work horses of the power grid and are interconnected with each other through transmission lines, thereby enabling the transfer of power to load centers located far away from the generation sources. The machines operate in synchronism with each other and thus give rise to an inherent 'in-built' torque known as the *synchronizing torque*. Within a certain range of operation, upon the occurrence of a disturbance, this torque is able to keep the generators in synchronism with each other. Further, due to the internal electromagnetic field in these machines, there is an inherent *damping torque* too which serves to damp out certain oscillations that may arise [7].

The development of a nation brings about an increase in the standard of living of a majority of its population. This results in an increase in electricity consumption resulting in a situation wherein the large generators are now forced to operate at a point close to their maximum capacity [8] as new sources of generation cannot be

added quickly. A higher operating point reduces the synchronizing torque and can cause the machines to lose synchronism with each other even upon the occurrence of small disturbances. Thus, with generators operating close to their maximum capacity, the system stability margin reduces. Two effective solutions leading to the increase in the stability margins are the expansion of the transmission network and the commissioning of new generating plants. These solutions are however time consuming, expensive and require long term planning. In the short term, the reduction in the stability margin can be tackled to a large extent with the addition of precise control equipment such as power system stabilizer (PSS) and FACTS devices. In addition to increasing the speed of response to a disturbance, these control equipment also serve to increase the operating range of the synchronous machine.

In recent years, there has been an increase in generation from converter interfaced sources. These converter interfaced sources do not operate in a synchronous manner and thus, an almost constant frequency output is provided by the converter through stringent control. While some of these sources such as wind farms and tidal energy sources contain rotating parts, there are sources which are static in nature too, such as solar farms and fuel cells. For the scope of this dissertation, all these sources will be referred to as converter interfaced generation (CIG). The power system already has a small penetration of CIG sources which can be easily accommodated and tolerated due to the large presence of synchronous machines. However, due to technology improvements and requirements to meet renewable portfolio standards (RPS), the penetration level of CIG in some areas of the power system can and will rise within a short period of time. Presently, this boom of CIG has taken place predominantly at the distribution level. However, with the recent announcement of the Clean Power Plan by the Environmental Protection Agency [9], an increase in the penetration of converter interfaced generation in the transmission system is a distinct possibility.

The future electric network will consist of various sources of energy such as wind, solar, hydro and natural gas. In addition, a combination of ac and dc networks along with a wide spread use of energy storage would warrant the use of converters to interface an energy source/storage element to the network [10, 11].

Many utilities are now investing in alternate sources of energy resulting in the connection of CIG at the transmission level. This connection to the bulk power system presents a significant challenge with respect to the operation of the power system. Supplementary storage devices or control mechanisms have to be usually included to reduce the effect of the uncertainty in the power source (wind, solar and tidal). The converters, either current source converters (CSC) or voltage source converters (VSC), decouple the source of power from the network. Thus the mass and inertia of a rotating machine like a wind turbine will now be electrically decoupled from the network. In order to utilize the kinetic energy of the rotating wind turbine, control algorithms have to be built into the converter operation. Further, to promote maximum utilization of these renewable energy sources, many of them operate using a maximum power point tracking (MPPT) algorithm. This reduces the number of sources that can be scheduled by the system operator.

The use of Type 4 wind turbines has increased and will continue to increase [12]. Taking converter interfaced technology one step further, there is a prospect of even interfacing synchronous machines through converters with candidates including variable speed, pressure controlled industrial expander turbines and hydro turbines. A large number of the future synchronous machines would be powered by gas turbines. From a thermodynamic point of view, a large gas turbine is more efficient when compared to a combination of smaller turbines. However due to compressor-turbine material stress constraints, a larger turbine would be required to operate at a lower speed [13]. Thus, interfacing the synchronous machine to the grid through a converter

releases it from operating at a fixed speed and can bring about an increase in the efficiency of the overall power system. Further, in order to smooth renewable energy fluctuations, hydro turbines are now moving towards a variable speed operation to provide larger regulation capability, thereby requiring a power electronic interface with the network [14].

The presence of converters is felt not only on the generation side but also on the load end. Induction motors, due to their ruggedness and ease of manufacturing have become the workhorse of many industries [15]. Precise control of motor speed is however required in many process control operations. In addition to this, use of speed control drives can bring about a reduction in the electrical energy consumed by the motor [16, 17] in terms of reactive power drawn from the network. It is estimated that in the United States, motors are responsible for greater than 60% consumption of the total electrical power generated [18]. The impact of these motor drives is to be analyzed on the performance of the system.

1.2 Motivation and Objectives

The increase in CIG penetration brings about significant challenges to the operation of a power system. Various paradigms that have been set in stone for conventional synchronous machine operation may now have to be revisited and revised. Equipment and control requirements may have to be specified considering the fact that these new CIG may last for more than 30-40 years. It is akin to rebuilding the power system as it would have been done when the first synchronous machine was connected to the ac power grid.

The objectives of the research work are as given below:

1. *Examination of the efficacy of CIG to provide frequency control.* In large systems, with the increased penetration of CIG, their ability to provide frequency

control under the occurrence of load/generation changes will be investigated. Further, with their fast response and lack of inertia, the existing concepts of primary frequency response need to be examined.

2. *Full control of variable resources on a large scale.* The variability of wind and solar power has to be overcome by using multiple storage devices with a combination of precise control spanning the entire length and breadth of a large power system.

3. *Dynamic behavior of the power grid.* Even with full control of CIG, the dynamic behavior of the power grid with only power converters feeding power into the grid will be examined.

4. *Behavior of various load profiles.* Nowadays, the impact of power converters is felt at the load end too with the advent of power drives and solid state electronic devices. The impact of these loads on the network will be examined.

5. *Transient and steady state stability.* The stability of the power grid, which until now relied largely on the natural operation of the synchronous machine, will be re-evaluated under the presence of CIG.

6. *Reactive power support.* The present grid code does not allow for converters at the distribution level to control voltage. However, the converters at the transmission level will have to regulate the voltage at their buses. This would result in converters with increased ratings. The ability of converters to regulate the voltage and provide reactive power support is to be examined.

7. *Development of accurate dynamic models to represent CIG.* Commercial software have dynamic models representing the converters and their associated control blocks. However these control blocks are complex while the converter

models do not seem to be robust with respect to system configuration. As part of this work, simple and accurate converter models will be developed that represent the characteristics of a practical converter. Further, integration of the developed models in commercial software will be explored. In addition, importance of modeling the source behind the converter will also be discussed.

By the end of this dissertation, a better handle on the operational aspect of the power grid with a large penetration of CIG would be obtained. Further, the behavior of the large scale power system with these distributed generation sources will be examined and validated under the existence of the proposed control schemes and stability profiles.

1.3 Organization of the Dissertation

Following this introductory chapter, Chapter 2 will discuss an overview of the work present in literature. Subsequently, the modeling of conventional power system components will be presented in Chapter 3 while Chapter 4 covers the modeling of converters and their associated control mechanisms. The testing of the converter models along with proposed control strategies on systems of varying degrees of complexity will be shown in Chapter 5. The words converter and inverter have been used interchangeably throughout this dissertation. Chapter 6 concludes this dissertation.

Chapter 2

LITERATURE REVIEW

2.1 Past and Present

Solid state converters will form the backbone of new age power systems. The presence of solid state switches in the power generation system can be traced back to 1951 with the appearance of the first static exciter [19]. These excitation systems had a fast transient response and made the alternator self-regulating. However, until 1961, these exciters were applied only to small generators with applications predominantly in aircraft and ship power systems. In 1961, the first static excitation system was developed for application to large land based steam turbine generators [20]. The success of these static excitation systems brought about a change in the definitions for excitation systems [21].

With the help of many design refinements through the passage of time and with improvements in technology, nowadays, the basic framework of the static exciter for large generators is different from the one proposed in 1961. Although these excitation systems give the desired transient response, they are known to cause problems with regard to steady state stability [22]. The development of PSS and FACTS devices has however alleviated this scenario to a certain extent.

The transformation of the power grid and the advent of CIG sources will bring the solid state switch to the foreground in power systems. This calls for a detailed study of the control of converter sources. Though this topic is a relatively new one, significant research activity has already been devoted to it starting from the micro second level control of the switching signals, driving through the millisecond control

of the production of the reference signals and ending at an analysis of the effects of these sources on the power system.

The study of the behavior of the bulk power system is usually undertaken at a millisecond level. It can thus be safely assumed that the micro second level switching actions of the converter switches occur as expected. The onus is now to obtain the appropriate reference signals at the millisecond level. The rapid growth of microgrids has ensured that there is adequate literature on this aspect of control. As microgrids are designed to be self-sufficient and can be expected to island from the main grid, voltage and frequency control within the microgrid is of importance. The presence of diesel generators in microgrids is quite common and [23] discusses the frequency and voltage control in a small system when an unintentional islanding of the microgrid occurs. The point raised by the authors of this paper is that under certain conditions, renewable energy sources will have to operate in a derated manner. This can bring about more control and also provide a reserve margin as shown in the paper.

With an increased penetration of CIG in the transmission system, it would be worthwhile to have these sources contribute to the frequency recovery. Reference [24] presents few of the key issues surrounding this issue. One of the issues mentioned is that since renewable energy sources are variable, they cannot be considered as reserves. Due to this variability, many utilities are still hesitant to include these sources into the dispatchable set of sources. Further, unlike synchronous alternators which have a large mass, wind turbines are comparatively small and their inertia contribution is thus relatively small. Their contribution can only help during the intervening time it takes for the slower acting conventional units to react. The authors mention the necessity of designing primary and secondary frequency response control loops which would act with the presence of minimal storage devices. Also, concerns have been raised about the lack of accurate dynamic models to represent

these sources. The most significant aspect shown by this paper is that with the addition of wind generators to the system, the total inertia of the system is shown to increase as the kinetic energy in the rotating blades of the large wind turbines are also considered. The typical value of inertia constant for wind turbines is 2s to 6s. Few other papers, [25–28], have tackled the issue of wind turbine machines participating in system frequency regulation. These papers discuss a variety of control mechanisms and strategies specific to wind turbines. Though the concept of these mechanisms are sound, their testing and validation has been performed only on small systems.

One of the aims of this research work is to explore the possibility of operating a CIG grid in the same manner as the present grid. This would prevent a requirement for a large scale change in terminology and metrics. Similar to primary frequency response in the conventional power grid, the concept of applying droop control to renewable sources has been widely discussed in [29–35]. However, as with previous literature, these papers discuss the control strategies within a specified microgrid. The concept of derating renewable sources is further explored in [30] wherein the possibility of a frequency reserve margin from wind generators is proposed. Also, the authors propose to continuously vary the droop coefficient with variation in wind velocity. In order to improve the accuracy of existing droop control, [31] proposes an addition of a supplementary control loop while [34] introduces cascaded control loops of angle, frequency and power in order to improve the power sharing accuracy in microgrids. The conventional frequency droop control loop is augmented with an angle quantity to improve its accuracy.

Most of the above literature is based on wind turbine generator machines. Since these are rotating machines with some amount of kinetic energy, it is easier to control them for frequency response. However with photovoltaic sources few other issues arise. These are succinctly described in [36]. The authors state that if PV sources are

to contribute to frequency response, then, three options are available: (1) Continue operation of PV at MPPT with energy storage devices; (2) Utilize a load bank to dump the surplus power; and (3) Make the PV sources dispatchable. The authors of [37] analyze that the best return on investment is obtained by operating the sources as dispatchable sources. In order to tackle the input power fluctuation, [38] proposes a fuzzy logic based frequency control for PV systems while [39] proposes the use of an electric double layer capacitor to maintain a spinning reserve.

Presently, utility scale solar plants have the capability to curtail their power output on the directive of the system operator. In addition, if curtailed, they also have the ability to increase their output if required [40]. The Midcontinent Independent System Operator (MISO) has introduced a scheme which allows for wind generators to fully participate in the energy market and be dispatched in a manner similar to a conventional energy source. These wind sources are termed as dispatchable intermittent resources (DIRs) [41]. It is thus not unrealistic to assume that in the future, with increased penetration of renewable resources, solar plants (and wind farms) can be scheduled to operate at an operating point below their maximum power output thereby providing a reserve margin to the system. Further, with the increase in renewable energy, energy storage elements will have a significant presence and thus also contribute to the reserve margin.

It has thus been established that there exists sufficient literature addressing frequency recovery in the presence of CIG. However, as mentioned before, these techniques have only been tested on small systems. As these sources start appearing in the transmission system, the long distances and the requirement to transfer reactive power may play a role in deciding the stability of the system. With renewable resources, the question of variability and adequacy of reserves comes into the picture. The aim of approaching close to 100% CIG in the power system includes the possi-

bility of having conventional synchronous machines also interfaced to the network via converters. Hydro power plants and gas turbine units can be interfaced to the grid in this manner. For these sources, variability and adequacy of reserve is no longer a major issue. However the issue of reactive power support over long transmission lines still exists. This can be a deciding factor in maintaining the stability of the system. According to the authors of [42], CIG providing reactive power support can increase the probability of islanding especially when the penetration of CIG is high. However if the power grid has to function in a stable manner, CIG will have to be called on to provide reactive power support as has been analyzed in [43] with the possibility of wind turbines providing reactive power support to improve rotor angle stability.

Analysis of the behavior of these sources in a large power system has turned up very few articles in the literature. Further, with most converter based units appearing in the distribution system, it is assumed that these units will have negligible impact on the behavior of the bulk power system. The authors of [44] have analyzed the effect of these units and have arrived at the conclusion that the effects are strongly dominated by the type of distributed generator technology. The authors have used the small New England Test System in their work with the maximum penetration of additional CIG being around 33%. According to the authors, raising the penetration level above this value was considered unrealistic as it would require a reconsideration of the classical power system concepts. A maximum penetration level of 30% was considered even in [8].

The first inkling of an analysis of a large power system with CIG is provided by [45] wherein the impact of wind generators on the primary frequency control of the British transmission grid has been analyzed. Though these generators are assumed to not have any frequency control capability, an analysis of the amount of reserve required has been carried out. Subsequent to this, [7] and [46] have analyzed the effect on the

transient and small signal stability of the power system due to increased penetration of DFIG based wind turbines. Further, a control strategy has been proposed by the authors in [46] to alleviate the impact of wind turbines in large power systems. However, though the system considered is large, the total penetration of CIG is quite low.

With the consideration of a large system for analysis, namely the Western Electricity Coordinating Council (WECC) system, [47] examined the impact of PV sources on the small signal and transient stability. A portion of the conventional generation was replaced to include the PV sources. However, the PV sources were added only to those parts of the system that contained relatively large amounts of conventional generation. It has also been assumed that the reactive power support decreases with increase in CIG as most of the sources are rooftop PV which are not allowed to regulate voltage as per the existing grid code. The utility scale PV sources however provide reactive power support. The analysis has been carried out with a maximum penetration of 20% by the authors. Further, the PV sources were assumed to operate in a constant power mode. It was shown that these sources can be both beneficial and detrimental to the behavior of the grid. The exact effect depends on the location of the disturbance and the location of the PV sources.

The analysis in [48] is with regard to the impact that CIG will cause on the modes of oscillation of the power system. The authors tackle the task of analyzing the behavior of a future WECC system, year 2020 and 2022, with an increased penetration of CIG. The impact of these devices on the existing electromechanical modes has been analyzed. Following this, it was further analyzed that certain modes in the inter area frequency range arise that are entirely due to CIG. This aspect of operation is vital for future high penetration schemes.

In [49], a renewable penetration of 53% has been assumed and it has been shown that for most contingencies, the system is stable and the behavior abides by the grid code. The effect of converter based sources contributing to frequency response has also been explored. However, the renewable sources were again spread across the system and not concentrated in a particular area.

There is a definite possibility that the future power network would have a significant percentage of synchronous machines interfaced through power electronic converters. Additionally, due to the presence of the capacitor on the dc bus, the modeling of the source behind the inverter is important while considering the transient performance of CIG on the dynamic behavior of systems. While generic mathematical models representing the positive sequence behavior of synchronous machines are well established, development of generic mathematical models representing the positive sequence behavior of converter interfaced generation (CIG) is still an active research topic [50]. Present generic converter models in positive sequence time domain simulation software have been constructed with two primary assumptions

1. The dc bus capacitor is large enough to provide an invariant dc voltage.

2. The time scale of dc voltage control does not play a significant role in analyzing the interaction between CIG and the bulk power system.

Reference [10] looks at the performance of power electronics interfaced distributed generation in small systems. The authors mention that with the connection of a rotating machine to the network through a power electronics interface, there is no increase in the net inertia of the system as the inverter decouples the machine from the network. As a result, upon the occurrence of a disturbance, the energy stored in the rotating mass of the rotor is not transferred to the grid. Thus, the response of the rotating machine behind the inverter is not addressed.

However, the analysis of a synchronous machine connected to a rectifier supplying a dc load, common in subsystems used to power aircrafts and ships [51], has been well discussed in literature. Reference [52] develops a mathematical model describing the behavior of a 3 phase synchronous machine connected to a dc load. The output of the synchronous machine is fed to a three phase bridge rectifier connected to a dc load. The effect of a load increase on the field of the machine was investigated.

Reference [51] examines the development of an average value model for the rectifier portion of a synchronous machine fed rectifier circuit with a dc load. The value of the voltage on the dc capacitor is used as an input to the excitation system of the synchronous machine. The analysis is performed for a single machine-rectifier-load setup. While the model is developed in [51], reference [53] extends the development of the model to obtain a generalized procedure for extracting the parameters of the average model for a variety of operating points.

Examining the dc distribution system used in marine and aerospace applications, [54] describes an admittance/impedance based stability analysis. The improvement in power electronics technology has resulted in the wide spread use of synchronous machines behind rectifiers in stand alone power supplies [55]. Reference [55] examines the modeling and control of a synchronous generator when connected to an inverter through a non controlled rectifier. The focus is on the synchronous generator and rectifier with the inverter only modeled as a load. The authors however neglect the dynamics of the dc bus with the assumption that the capacitor on the dc bus is large and prevents any ripples in the dc voltage.

With the increase in penetration of CIG (both in number and megawatt capacity), the assumptions of a stiff dc bus would not be valid under all situations. In recent years, various articles in literature have delved into aspects of the dc bus voltage dynamics. In [56,57], reduced order models have been developed to analyze the small

signal and large signal stability of the dc link voltage control for a Type 3 wind turbine. Although, the rotor side converter has been modeled as a controlled current source; additionally, the transients of the stator have been neglected. Also, the performance of both these models have been analyzed on a single machine infinite bus system.

With the price of magnetic materials reducing [58], permanent magnet synchronous generators could be an integral part of the future grid. The use of permanent magnets for excitation allows for a smaller pole pitch resulting in a wide range of possible synchronous operating speeds [59]. The point on wave simulation analysis of a permanent magnet synchronous generator wind energy system connected to the grid through a rectifier-inverter setup has been conducted in [60].

Traditionally, three phase synchronous machines have been used to directly connect to the electrical network. However, with the possibility of a converter interface between the machine and the grid, higher phase machines could be used. A higher phase machine results in reduced current rating per phase, torque pulsations, current ripple and dc-link voltage ripple [61]. In many dc power systems, the power source is the rectified output from a 6-phase synchronous machine. In addition, with a 6 phase machine, the output can be easily rectified using two parallel 6 pulse rectifiers thereby eliminating the need for a phase shifting transformer which results in lower cost [62]. The possibility of converter interfaced synchronous generators could allow for the use of a 6-phase machine for use in ac power systems.

The energy derived from natural gas fired electric power plants in the United States is slated to increase by an average 1.3% annually to around 1600 million megawatthours by 2040 [63]. It is also projected that by 2040, natural gas power plants would account for 31% of the total electrical energy production as compared to 34% produced from coal fired power plants [64]. Presently, single shaft gas turbines are used to drive synchronous machines, due to the constant speed limitation imposed

by the machine. In a single shaft gas turbine, the compressor and the turbine are located on the same shaft. Thus, a reduction in the speed of the synchronous machine due to a sudden load increase affects the speed of the compressor and the turbine too. The alternative to a single shaft turbine is a two shaft turbine which is used when the load on the turbine can be operated at varying speeds. In a two shaft turbine, the compressor and the power turbine are located on different shafts. In addition, the part load efficiency of a multi-shaft turbine is higher than the part load efficiency of a single shaft turbine [13]. Thus, synchronous machines powered by multi-shaft turbines operating at loading point specific optimal speeds can be interfaced to the future power network through a rectifier-inverter setup.

The variable speed of a modern wind turbine requires a power electronic interface to exist between the turbine and network. Reference [65] looks at the point on wave simulation of a permanent magnet synchronous machine wind generator connected to the network through a diode rectifier which is less expensive in comparison to an IGBT based rectifier. Reference [66] provides a brief analysis of a wind turbine connected to a direct drive synchronous generator and interfaced to the network through a back to back voltage source converter. The dynamics of the inverter and the dc bus are however neglected. An experimental setup of a wind turbine with a synchronous generator, dc boost chopper and inverter is discussed in [67]. Again, it is assumed that the capacitor on the dc bus is large.

The stability assessment of a direct drive synchronous generator connected to the network through a rectifier-inverter combination is discussed in [68]. In order to reduce the computation time of transient simulation for large systems, a simplified model was derived with the assumption that the dc bus voltage is constant due to the presence of a large capacitance in the dc circuit and fast acting dc voltage controllers.

With this assumption, only the grid side inverter was modeled in simulations with a dc voltage source as the input to the inverter.

However, there has been limited work done in developing a model for use in large scale positive sequence time domain simulations to describe the behavior of a synchronous machine interfaced through a power electronics device. Initial work on this subject has been carried out in [14]. However, a classical model of the synchronous generator has been used and as a result, the electrical characteristics of the machine and its excitation systems have not been addressed. In addition, an ideal unity power factor operation of the generator side rectifier has been assumed. Reference [69] explored the changes to be made to the existing generic Type 4 wind turbine model and proposed an inclusion of a controller to simulate the drive train oscillations.

Discussing various fault ride through control schemes, [70] recognizes the impractical aspect of requiring a large capacitor on the dc bus (of the back-to-back converter of the Type 4 turbine) to store excess energy from the wind turbine during a network voltage dip, thereby reducing the voltage rise. Various other aspects of low voltage ride through control schemes have been discussed in [71–73]. However, a positive sequence analysis has not been carried out.

In positive sequence analysis, the general assumption made until now is that the capacitance on the dc bus is large and hence the source behind the inverter can be represented as an ideal dc voltage source. For large MVA rating synchronous machines, this assumption will be impractical due the sheer size of capacitance required. In addition, in a future grid, with widespread converter interfaced generation, the transfer of energy from the synchronous machine to the network through the rectifier-inverter has to be analyzed. Use of a large capacitor on the dc bus to prevent voltage rise during network faults was considered to be impractical in [70]. The same thought process can be applied while evaluating the size of the capacitor for reduction in volt-

age. Thus, the capacitor on the dc bus cannot serve as a near infinite source/sink of energy.

Moving away from generation and towards load, the development of speed control drives for induction motors is not a new topic and considerable research has already been reported. References [74, 75], among others, give a concise description of the various control schemes available for speed control drives. With vast improvement in power electronic devices and technology, the use of speed control drives has greatly increased.

Positive sequence time domain simulation techniques are used in analyzing the behavior of the bulk power system. The positive sequence modeling of a squirrel cage induction motor is well established [22]. There has however been little development/implementation of a positive sequence model for motor speed control drives that are suitable for use in large scale positive sequence time domain simulation software such as PSS/E or PSLF [76, 77]. Present drive models are developed for use in electromagnetic point on wave type of simulations. However, with the present wide spread use of power electronic drives, it is important that a positive sequence drive model be implemented for the analysis of the performance of large power systems. Further, with the increase in penetration of renewable energy sources, it is possible that a futuristic grid would have both load and generation interfaced through power electronic converters. Preliminary work on this topic is reported in [78] which discusses the stability of a CIG based microgrid along with a converter interfaced load (CIL).

2.2 Gaps in Literature

In this dissertation, a positive sequence converter model developed for the purpose of coupling CIG into the standard production version of a large scale grid

simulation will be discussed. While the modeling of converters at the point on wave level and the 'average voltage' level is well established [79], difficulties arise in coupling many established converter models into the network modeling of large scale grid simulation programs.

The positive sequence converter model developed for a CIG makes use of and demonstrates the effect of the fast maneuvering capability of a CIG on the power system. When connected to the network through converters, sources like solar, wind and batteries can very quickly provide frequency and voltage support upon the occurrence of a disturbance. The convergence properties of the network solution in conjunction with the boundary conditions imposed by loads and converter coupled devices is strongly influenced by the form in which the boundary condition is expressed [80–82]. The models described in [76, 83–86] (henceforth referred to as boundary current representation) form the converter boundary conditions as a nonlinear algebraic relationship between complex power and the current and voltage phasors at the point of connection. In contrast, the model described in this work is interfaced with the network by a Thévenin voltage source. This approach has given good convergence of the network solutions in the simulations conducted. Additionally, it will be shown that the boundary current representation is unable to capture the near instantaneous response possible from controlled converters. Many research efforts are tackling the task of improving the representation of these converters in positive sequence time domain simulations [87]. Converters, in practice, are voltage sources which generate an ac side voltage by manipulating the switching of the solid state switches. In the proposed Thévenin representation, the current injected into the network is now due to the generated voltage and the terminal voltage on the network side of the coupling inductor. It will be shown that this explicit representation of the coupling inductor directly impacts the behavior of the converter at the instant of disturbance.

It can also be seen that there has been little work done with regard to examining the behavior of large systems with increased penetration of CIG. This research work aims to study this aspect of large system with close to 100% penetration of CIG. The conventional sources in all 21 areas of the WECC system were represented as converter interfaced generation. Existing wind and solar farms that are already operational in the WECC system were represented by converter models presently used in positive sequence time domain simulation software although these models differ from the converter model proposed in this research work.

For a CIG to participate in frequency regulation, a reserve margin has to be present. As per the associated material for the WECC system operating case [88], all areas of the system have a defined amount of headroom available for frequency regulation. This reserve is however not distributed uniformly among all generators in the area, with some generators operating with the governors blocked. In this dissertation, the maximum active power deliverable by a CIG unit has been assumed to be equal to the MW rating of the turbine of the generator which the CIG replaces while the MVA rating of the CIG has been assumed to be the same as the MVA rating of the replaced generator. If the CIG replaces a generator with its associated governor blocked, then it has been assumed that the CIG too cannot take part in frequency regulation. Thus, with available headroom on a significant fraction of the converter interfaced sources, a droop controller has been incorporated in the converter control architecture. The value of the droop coefficient for a CIG unit was taken to be the same as that of the droop coefficient in the governor mechanism of the generating unit the CIG replaced.

Further, in this research work, a positive sequence model for a synchronous machine interfaced to the network through a diode rectifier-voltage source inverter has also been developed. Such a model does not presently exist in any of the commercial

positive sequence transient simulation software packages [76, 77, 86]. Recognizing this limitation in modeling capability, and given that the power network is continuously moving towards an all CIG system, this model of the source behind the inverter has been developed. A non ideal operation of the rectifier has been considered and as a result, a static excitation system for the generator has been modeled. Each synchronous generator is also equipped with a governor.

While the individual operation of these elements have been well documented, the coordinated interaction between these elements and the bulk power network in positive sequence has not been addressed in literature. The detailed dynamics of a machine interfaced through a converter is well discussed in literature. However, in these studies, a strong ac system has been considered with minimal presence of converter interfaced machines. Thus, it was admissible to ignore the dynamics of the dc bus.

The focus in this section of the dissertation is thus not the detailed modeling of these converter interfaced machines. It is however on the practical implications & assessments of simulating a system with large number of converters. A mathematical tool will be required to control and manage the large amount of capacitance that may arise in the dc bus with these sources. Hence, with the possibility of having a significant portion of the generation fleet as converter interfaced synchronous machines, it is desirable to incorporate this level of modeling detail for the analysis of the bulk power system.

The well known sixth order representation of the synchronous machine [89] was used. To represent the inverter, the proposed controlled voltage source representation was used. The satisfactory performance of this model in commercial simulation software and its behavior on a test three machine nine bus equivalent system and the 18000 bus WECC system will be shown. In addition, the sensitivity of the dynamic

performance of the proposed model to variation in the value of the dc capacitance will be examined. It will also be shown that there is only a minor increase in simulation computation effort. Further, with these sources providing primary frequency response, the limitation of an ideal dc voltage converter representation will be shown.

There has been little work done with regard to consideration of detailed representation of loads. In this research work, the implementation of a positive sequence model for a squirrel cage induction motor speed control drive has been described. The behavior of the model is first analyzed using a three machine nine bus WSCC equivalent system under multiple scenarios with generation being conventional synchronous machines. Additionally, the performance of the model in a test distribution system has also been observed. The positive sequence time domain simulation has been carried out in an independently developed phasor based simulation program (referred to as C code) which represents the network in quasi steady-state using an algebraic model.

Chapter 3

MATHEMATICAL MODEL OF THE POWER SYSTEM

The power system is considered by some to be the largest man-made machine in the world. With a vast network of transmission lines spanning across large geographical areas, interspersed with generators and load centers all operating at almost the same frequency and in unison most of the time, it is indeed a large machine. Due to its size and complexity, detailed mathematical models of its components are required to study its behavior using computer simulations. The general equations of the nonlinear power system can be described by a set of differential and algebraic equations as in (3.1) [89]:

$$\begin{aligned} \dot{x} &= f(x, y, u) \\ 0 &= g(x, y) \end{aligned} \tag{3.1}$$

where, x is the vector of states, y is the vector of network variables and u is the vector of inputs/control signals. The functions f and g represent the right hand sides of the differential and algebraic equations respectively.

The differential equations represent the dynamics of each member device of the power system. These equations usually represent the section of the power system which is behind the network bus and not represented in the power flow. As an example, these equations can represent the dynamic behavior of the internal operation of a synchronous generator. The network variables of the vector y, bus voltage for example, depict the boundary between the device and the network. The algebraic equations of the function g link each device to one another through the network admittance matrix.

Simulation of large power systems involves a significant computational burden. To this end, commercial software such as PSLF, PSS/E and DSA Tools are employed. The results in this dissertation are from simulations run in PSLF. In the following sections of this chapter, the mathematical models of few important devices, as used by PSLF, will be discussed.

3.1 Synchronous Generator Model

In a large power system, depending on the system size, complexity, study criteria and area of disturbance, models with different levels of simplification are utilized. Three commonly used models are discussed below in decreasing order of complexity.

3.1.1 The E'' Model

This model is also known as the *'voltage behind subtransient reactance model'*. It is derived from the full model with the following assumptions:

1. The transformer voltage terms, $\dot{\lambda_d}$ and $\dot{\lambda_q}$, are considered negligible in the stator voltage equations when compared with the speed voltage terms $\omega\lambda_d$ and $\omega\lambda_q$.

2. Additionally, in the stator voltage equations, the variation of ω is considered negligible *i.e.* $\omega \cong \omega_R$.

   The stator voltage equations get modified as shown in (3.2) upon incorporation of the above assumptions.

$$\begin{aligned} v_d &= -ri_d - \omega\lambda_q - \dot{\lambda_d} \\ v_q &= -ri_q + \omega\lambda_d - \dot{\lambda_q} \end{aligned} \quad \Longrightarrow \quad \begin{cases} v_d &= -ri_d - \omega_R\lambda_q \\ v_q &= -ri_q + \omega_R\lambda_d \end{cases} \tag{3.2}$$

3. The subtransient reactances along the d and q axis are assumed to be equal *i.e.*$L''_d = L''_q$.

It should be noted that both the field circuit effects and the damper winding effects are represented in this generator model.

Representing all flux linkages as corresponding generated EMFs, the final stator voltage equations are,

$$\begin{aligned} v_d &= -ri_d - i_q x'' + e''_d \\ v_q &= -ri_q + i_d x'' + e''_q \end{aligned} \tag{3.3}$$

The EMF $e'' = e''_q + je''_d$ is known as the voltage behind the subtransient reactance and the equivalent circuit of the generator in the *abc* frame is as shown in Figure 3.1. With the stator voltage equations defined, the remaining dynamic equations

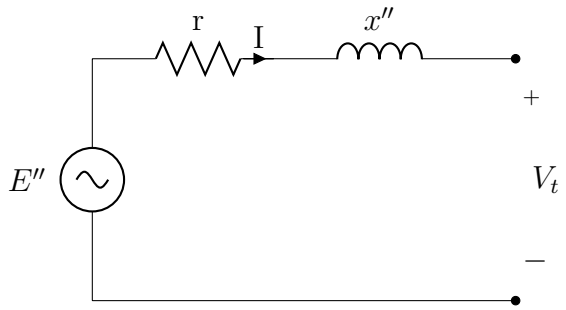

Figure 3.1: E'' model equivalent circuit

describing the machine can be derived as in Chapter 4 of [89]. In addition to the damper winding, a fictitious short circuited winding is assumed to be present on the q axis to mimic the field circuit winding in the d axis.

The final equations obtained as are given below:

$$\dot{\lambda_D} = \frac{1}{\tau''_{d0}}\sqrt{3}E'_q - \frac{1}{\tau''_{d0}}\lambda_D + \frac{1}{\tau''_{d0}}\left(x'_d - x_\ell\right) i_d \tag{3.4}$$

$$\begin{aligned} \sqrt{3}\dot{E}'_q = \frac{\sqrt{3}}{\tau'_{d0}}E_{FD} + \frac{\left(x_d - x'_d\right)\left(x''_d - x_\ell\right)}{\tau'_{d0}\left(x'_d - x_\ell\right)} i_d - \frac{\sqrt{3}}{\tau'_{d0}}\left[1 + \frac{\left(x_d - x'_d\right)\left(x'_d - x''_d\right)}{\left(x'_d - x_\ell\right)^2}\right] E'_q \\ + \frac{\left(x_d - x'_d\right)\left(x'_d - x''_d\right)}{\tau'_{d0}\left(x'_d - x_\ell\right)^2}\lambda_D \end{aligned} \tag{3.5}$$

$$\dot{\lambda_Q} = \frac{-1}{\tau''_{q0}}\sqrt{3}E'_d - \frac{1}{\tau''_{q0}}\lambda_Q + \frac{1}{\tau''_{q0}}\left(x'_q - x_\ell\right) i_q \tag{3.6}$$

$$\sqrt{3}\dot{E}'_d = \frac{-\left(x_q - x'_q\right)\left(x''_q - x_\ell\right)}{\tau'_{q0}\left(x'_q - x_\ell\right)} i_q - \frac{\sqrt{3}}{\tau'_{q0}}\left[1 + \frac{\left(x_q - x'_q\right)\left(x'_q - x''_q\right)}{\left(x'_q - x_\ell\right)^2}\right] E'_d - \frac{\left(x_q - x'_q\right)\left(x'_q - x''_q\right)}{\tau'_{q0}\left(x'_q - x_\ell\right)^2}\lambda_Q \tag{3.7}$$

$$2H\dot{\omega} = T_m - e''_q i_q/3 - e''_d i_d/3 - D\omega \tag{3.8}$$

$$\dot{\delta} = \omega - 1 \tag{3.9}$$

These differential equations are supported by the following algebraic equations

$$e''_q = \frac{x''_d - x_\ell}{x'_d - x_\ell}\sqrt{3}E'_q + \frac{x'_d - x''_d}{x'_d - x_\ell}\lambda_D \tag{3.10}$$

$$e''_d = \frac{x''_q - x_\ell}{x'_q - x_\ell}\sqrt{3}E'_d - \frac{x'_q - x''_q}{x'_q - x_\ell}\lambda_Q \tag{3.11}$$

This simplified model is the most detailed model used in power system transient stability simulations and its model name in PSLF is GENROU.

3.1.2 The E' Model

While the previous model accounted for the subtransient circuit effects, this model considers those effects as negligible. The remaining two assumptions with regard to the transformer voltages and the variation of ω still hold for the two axis model.

With the absence of the subtransient circuit, this model is also known as the *'voltage behind transient reactance model'*. The equivalent circuit for the model is as shown in Figure 3.2. As a further approximation, the model can be represented as a voltage behind the d axis transient reactance. The detailed reasoning behind this approximation along with the complete derivation of the dynamic equations can be obtained from Chapter 4 of [89].

The final dynamic equations are as given below:

$$\dot{E}'_q = \frac{1}{\tau'_{d0}}\left(E_{FD} - E'_q + \left(x_d - x'_d\right) I_d\right) \tag{3.12}$$

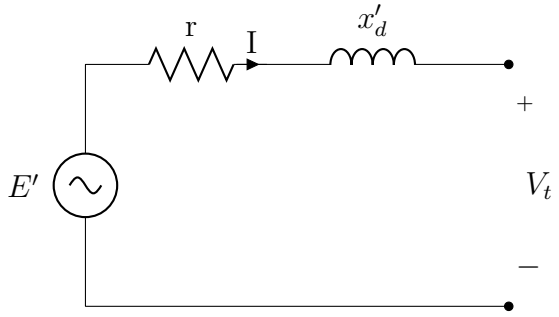

Figure 3.2: E' model equivalent circuit

$$\dot{E}'_d = \frac{1}{\tau'_{q0}} \left(-E'_d - \left(x_q - x'_q \right) I_q \right) \tag{3.13}$$

$$2H\dot{\omega} = T_m - \left(E'_d I_d + E'_q I_q \right) + \left(L'_q - L'_d \right) I_d I_q - D\omega \tag{3.14}$$

$$\dot{\delta} = \omega - 1 \tag{3.15}$$

3.1.3 Effect of saturation

To obtain an accurate representation of the field current drawn by the machine (and hence an estimate of the excitation system rating), the effect of magnetic saturation has to be taken into account. The saturation factor can be obtained by evaluating the value of voltage behind leakage reactance at a given operating point. The voltage behind leakage reactance (V_ℓ) gives a good picture of the saturation curve as it is assumed that the leakage reactance would not saturate.

Since air gap flux (ϕ_{sync}) is proportional to voltage, V_ℓ can be used in the saturation function to obtain the saturation factor. The saturation function is described as follows:

$$S(\phi_{sync}) = A_{sat} e^{B_{sat} V_\Delta} \tag{3.16}$$

where $V_\Delta = (V_\ell - 0.8)$. A voltage of 0.8pu is assumed as the threshold for saturation in the machine. Using values of the saturation factor at rated flux ($S_{1.0}$) and 1.2pu

flux ($S_{1.2}$), the values of A_{sat} and B_{sat} are calculated as

$$B_{sat} = 5ln\left(\frac{S_{1.2}}{S_{1.0}}\right); A_{sat} = \frac{S_{1.2}}{e^{(B_{sat}*(1.2-0.8))}} \tag{3.17}$$

Alternatively, the saturation function can also be modeled as a quadratic function given as:

$$S(\phi_{sync}) = A_{sat}\left(V_\ell - B_{sat}\right)^2 \tag{3.18}$$

where,

$$\begin{aligned} B_{sat} =& \frac{1.2 - \sqrt{\frac{S_{1.2}}{S_{1.0}}}}{1.0 - \sqrt{\frac{S_{1.2}}{S_{1.0}}}} \\ A_{sat} =& \frac{S_{1.2}}{(1.2 - B_{sat})^2} \end{aligned} \tag{3.19}$$

The value of the saturation factor at any voltage can thus be calculated using either (3.16) or (3.18).

As the machine saturates, its effect is incorporated as a change in the values of the synchronous, transient and subtransient reactances.

$$x_{d_{sat}} = x_\ell + \frac{x_d - x_\ell}{1 + S(\phi_{sync})}; x_{q_s} = x_\ell + \frac{x_q - x_\ell}{1 + S(\phi_{sync})\frac{x_q}{x_d}} \tag{3.20}$$

An example comparison of the magnetization characteristic obtained due to both exponential and quadratic saturation is shown in Figure 3.3 with $S_{1.2}$=0.42 and $S_{1.0}$=0.08. In the narrow region of interest up to a flux of around 1.3pu, there is little variation between the two functions. Hence, either saturation function can be used. In software, all non-classical machine models incorporate the effect of saturation to some degree.

3.1.4 Classical Model

This is the most simple model for the synchronous machine. The significant assumptions made for the development of this model are as given below:

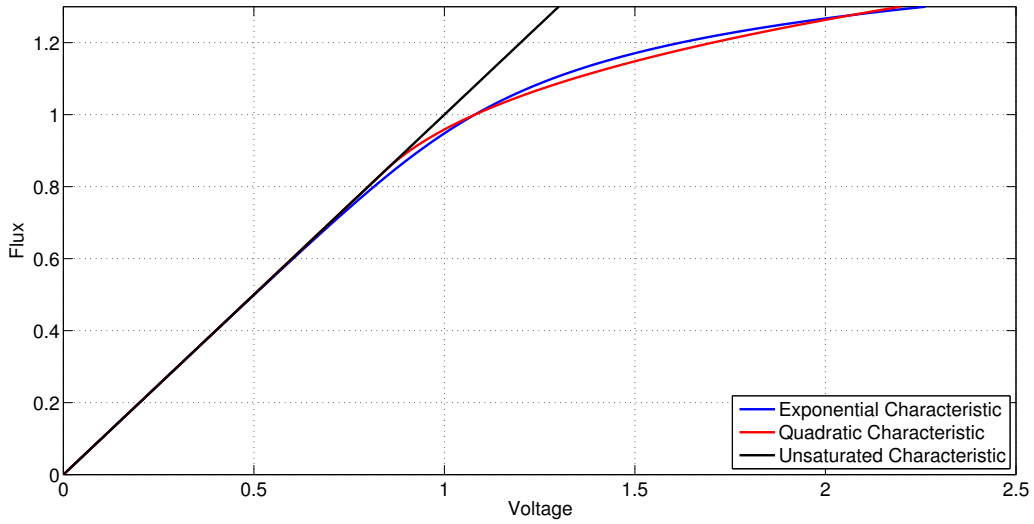

Figure 3.3: Magnetization characteristic comparison between exponential and quadratic saturation functions with $S_{1.2}$=0.42 and $S_{1.0}$=0.08

1. The air gap flux is constant. Thus the effects of armature reaction are neglected.

2. The voltage behind the transient reactance is constant.

3. The motion of the rotor of the machine coincides with the angle of the voltage behind the transient reactance.

4. No damper windings exist.

5. Input mechanical power P_m is constant.

Since constant flux constant voltage is assumed, no excitation system can be used for a generator represented by this model. Further, since the motion of the mechanical rotor angle is assumed to coincide with the internal voltage angle, no governor model can be used with this machine representation.

The equations representing this model are given below:

$$2H\dot{\omega} = P_m - P_e \tag{3.21}$$

$$\dot{\delta} = \omega - 1 \tag{3.22}$$

where, P_e is the electrical power injected into the network at the terminals of the machine. The value of this quantity can be obtained by using the network admittance matrix. In PSLF, this model goes by the name of GENCLS.

In simulations it is common to take one synchronous machine as the reference machine. This is done because we are primarily interested in the relative movement of machines with respect to one another. The relative movement also allows us to capture the oscillatory behavior of the machines and the system.

3.2 Governor Model

The main function of a governor is to vary the input power to the generator in accordance to the variation in frequency. While governors may have additional tasks depending on the type of fuel used, the main operational loop of all governors remains similar. To bring about primary frequency response, a droop controller is made use of in governors. The operational characteristic of droop controllers is as shown in Figure 3.4. At the rated frequency of $\omega_s = 1.0pu$ the output of the generator is the

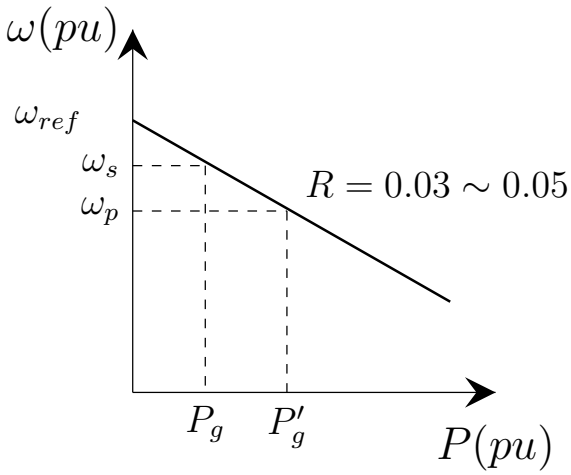

Figure 3.4: Droop characteristic

scheduled power P_g. With a drop in frequency, the characteristic makes the governor

increase the active power thereby arresting the fall in frequency. Eventually a steady state frequency ω_p is attained with an increased power output of P'_g.

Based on this characteristic, a simple governor model can be derived as shown in Figure 3.5. The differential equations describing the dynamic behavior of this governor are as given by (3.23)-(3.25).

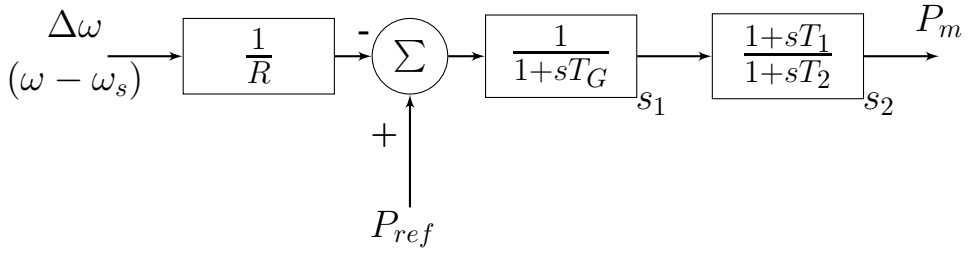

Figure 3.5: Governor based on droop characteristics

$$\frac{ds_1}{dt} = \frac{1}{T_G}\left[P_{ref} - \frac{\Delta\omega}{R} - s_1\right] \tag{3.23}$$

$$\frac{ds_2}{dt} = \frac{1}{T_2}\left[s_1 - s_2 - s_1\frac{T_1}{T_2}\right] \tag{3.24}$$

$$P_m = s_2 + s_1\frac{T_1}{T_2} \tag{3.25}$$

In PSLF, a governor model very similar to this model is present under the model name of TGOV1.

3.3 Static Exciter Model

Any realistic generator model, E'' or two axis model, has to have an associated excitation system model to represent the exciter. While a handful of generators across the system continue to have a dc exciter, the static exciter and the brushless ac exciter are the most common exciters nowadays.

The basic framework of a static exciter model is shown in Figure 3.6 with the dynamic equations given by (3.26)-(3.31).

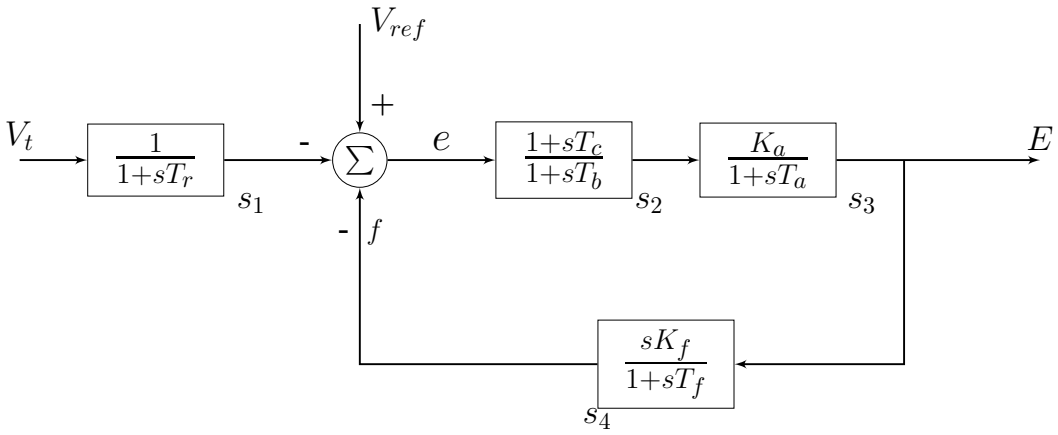

Figure 3.6: Static exciter basic framework

$$\frac{ds_1}{dt} = \frac{1}{T_r}(V_t - s_1) \tag{3.26}$$

$$e = V_{ref} - s_1 - f \tag{3.27}$$

$$\frac{ds_2}{dt} = \frac{1}{T_b}\left[e - s_2 - e\frac{T_c}{T_b}\right] \tag{3.28}$$

$$\frac{ds_3}{dt} = \frac{dE}{dt} = \frac{1}{T_a}\left[K_a\left[s_2 + e\frac{T_c}{T_b}\right] - E\right] \tag{3.29}$$

$$\frac{ds_4}{dt} = \frac{1}{T_f}\left[\frac{-K_f}{T_f}E - s_4\right] \tag{3.30}$$

$$f = s_4 + E\frac{K_f}{T_f} \tag{3.31}$$

In ac and dc exciters, the signal E is the input excitation to the exciter and the armature voltage of the exciter becomes the input excitation to the synchronous machine. In static exciters, the signal E can be directly applied as the input excitation to the synchronous machine field winding and under these circumstances, this signal can be denoted as E_{FD}. In PSLF, the ac and static exciters models EXAC4 and EXST1 are used.

3.4 Load Model

While nonlinear loads are represented by differential equations depicting their dynamic behavior, static loads have been traditionally represented by either an *ex-*

ponential model or a *polynomial* model. Both models can represent a load as either constant power, constant current or constant impedance. Usually a complex mix of all three types of load are present in the system at any given point in time. However, if for some reason no detailed load information exists, then active power loads are represented as constant current loads while reactive power loads are represented as constant impedance loads [22].

A common simulation technique is to represent all static loads as admittance loads. Constant power and constant current loads are then represented as varying current injections at each time step. The current injection is the difference between the current required to maintain its constant power/current characteristic and the current drawn by the load's steady state admittance representation. The current injection into the network now comes from only those components that have been represented by dynamic equations and the constant power and constant current load buses. The remaining zero current injection buses can now be eliminated from the network equations using matrix reduction techniques [89].

Since all generator models are representative of a voltage behind reactance model, the generator reactance too can be absorbed into the admittance matrix and thereby represent the generator internal bus as being directly hooked onto the network.

3.5 Network Model

While running a power flow algorithm, the slack bus angle is usually set to zero and taken as the reference for all other bus angles. In dynamic simulations the slack bus voltage phasor is considered to coincide with the Q axis of the synchronously rotating network frame of reference with the D axis leading the Q axis by 90°.

The network equations of (3.1) *i.e.* $g(x, y) = 0$ describe the transmission network in relation to the bus quantities and injections as given by (3.32) & (3.33).

$$\overline{I} = \overline{YV} \tag{3.32}$$

where,

$$\overline{I} \triangleq \begin{bmatrix} \overline{I}_1 \\ \overline{I}_2 \\ ... \\ \overline{I}_n \end{bmatrix} \text{ and } \overline{V} \triangleq \begin{bmatrix} \overline{V}_1 \\ \overline{V}_2 \\ ... \\ \overline{V}_n \end{bmatrix} \tag{3.33}$$

To complete Ohm's law, $\overline{Y}$ is the reduced admittance matrix of the network.

Since a network reduction has already been performed, $\overline{I}$ and $\overline{V}$ are vectors of length *nx1* wherein it is assumed that there are n buses in the system at which a non zero current injection occurs. Correspondingly, the matrix $\overline{Y}$ is of size *nxn*. When each phasor of $\overline{I}$, $\overline{V}$ and $\overline{Y}$ is projected into its components onto the DQ frame, then the length of the vectors become *2nx1* while the size of the reduced admittance matrix becomes *2nx2n*.

Each synchronous machine is said to have a dq axis which rotates in synchronism with the rotor of that machine [90]. Due to the different loading levels of each machine, the dq axis of any particular machine will be displaced from the network DQ axis by an angle equal to the torque angle δ of that particular machine. Figure 3.7 shows the displacement between the two reference frames for any individual machine i. The relationship between the network and machine frame quantities, as given by (3.34), can be easily obtained by inspection of Figure 3.7.

$$\begin{aligned} V_{Qi} + jV_{Di} &= (V_{qi}\cos\delta_i - V_{di}\sin\delta_i) + j\,(V_{qi}\sin\delta_i + V_{di}\cos\delta_i) \\ \Rightarrow \qquad V_{D,Q} &= V_{d,q}e^{j\delta_i} \end{aligned} \tag{3.34}$$

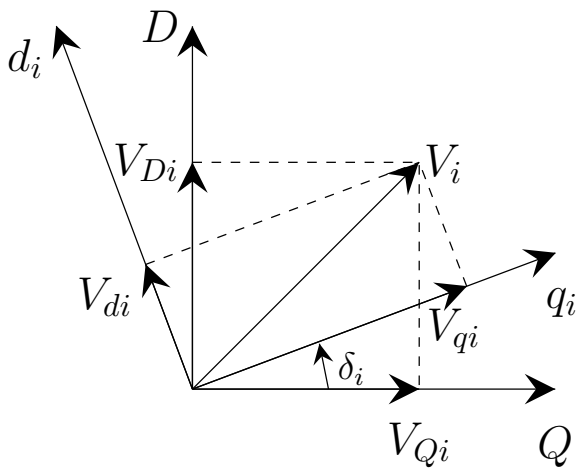

Figure 3.7: Machine and network reference frames for machine i

Therefore, (3.32) can now we re-written as,

$$I_{D,Q} = YV_{D,Q} \Leftrightarrow V_{D,Q} = Y^{-1}I_{D,Q} \tag{3.35}$$

Since the aim of a dynamic simulation is to observe the behavior of the devices connected to the network, it is preferred that the machine reference frame is maintained throughout the simulation. Thus (3.35) has to be converted from the network frame to the machine frame. The procedure as given in [89] is discussed below.

Using the transformation factor defined in (3.34), a transformation matrix T can be formed for the entire network. Since the transformation factor for each bus is independent of the other buses, the matrix T will be a diagonal matrix of size *nxn* as given,

$$T = \begin{bmatrix} e^{j\delta_1} & 0 & ... & 0 \\ 0 & e^{j\delta_2} & ... & 0 \\ ... & ... & ... & ... \\ 0 & 0 & ... & e^{j\delta_n} \end{bmatrix} \qquad T^{-1} = \begin{bmatrix} e^{-j\delta_1} & 0 & ... & 0 \\ 0 & e^{-j\delta_2} & ... & 0 \\ ... & ... & ... & ... \\ 0 & 0 & ... & e^{-j\delta_n} \end{bmatrix} \tag{3.36}$$

At a load bus k, with non zero current injection, $\delta_k = 0$. The vector of voltages in the network and machine frame of reference is given by,

$$V_{D,Q} = \begin{bmatrix} V_{Q1} + jV_{D1} \\ V_{Q2} + jV_{D2} \\ \dots \\ V_{Qn} + jV_{Dn} \end{bmatrix} \qquad V_{d,q} = \begin{bmatrix} V_{q1} + jV_{d1} \\ V_{q2} + jV_{d2} \\ \dots \\ V_{qn} + jV_{dn} \end{bmatrix} \tag{3.37}$$

Using the transformation matrix T, the two voltage vectors can be related as

$$\begin{aligned} V_{D,Q} &= TV_{d,q} \\ V_{d,q} &= T^{-1}V_{D,Q} = T^{*}V_{D,Q} \end{aligned} \tag{3.38}$$

Similar equations can be written to relate the current vectors of both frames of reference.

To transform (3.35), the relations in (3.38) are used.

$$I_{D,Q} = YV_{D,Q} \Longrightarrow TI_{d,q} = YTV_{d,q} \tag{3.39}$$

Upon premultiplying by T^{-1},

$$I_{d,q} = \left(T^{-1}YT\right) V_{d,q} \triangleq MV_{d,q} \Leftrightarrow V_{d,q} = M^{-1}I_{d,q} \tag{3.40}$$

where,

$$M \triangleq \left(T^{-1}YT\right) \tag{3.41}$$

Thus (3.40) gives the desired relation between the currents and voltages of each device connected by the network, in the machine frame of reference.

If each device is represented as a Thévenin source, then the solution of the differential equations will give the values of the voltage vector of (3.40). In order to proceed to the next time step, (3.40) is now solved to obtain the values of the current vector. These new values of the current vector are then used in the next time step

to obtain the solution of the differential equations. If the devices are represented as Norton sources, then the solution of the differential equations would return the values of the current vector and (3.40) would have to be solved to obtain the values of the voltage vector. Since some of the elements of the transformation matrix T depend on the torque angle of the machine, the transformation plays an important role in the dynamic simulation.

In the following chapter, the modeling of the converters and their corresponding control strategies will be discussed.

Chapter 4

MODELING OF CONVERTERS

The previous chapter discussed the mathematical modeling aspects of *'conventional'* power systems. Recently, due to the increasing addition of renewable sources of energy, converter models are being included into all commercial software. These models however differ in complexity from one software vendor to another. In addition, the development of generic models had been stalled for quite some time due to non negotiable proprietary information held by the manufacturers. In PSLF, the converter models and their associated control models are mainly representative of GE's converter models for wind and solar applications [83–85], though, some manufacturer independent wind models also exist. The basic framework of connecting a converter based source to the grid in PSLF is as shown in Figure 4.1 [84] for a solar photovoltaic source and in Figure 4.2 [85] for a wind turbine-generator.

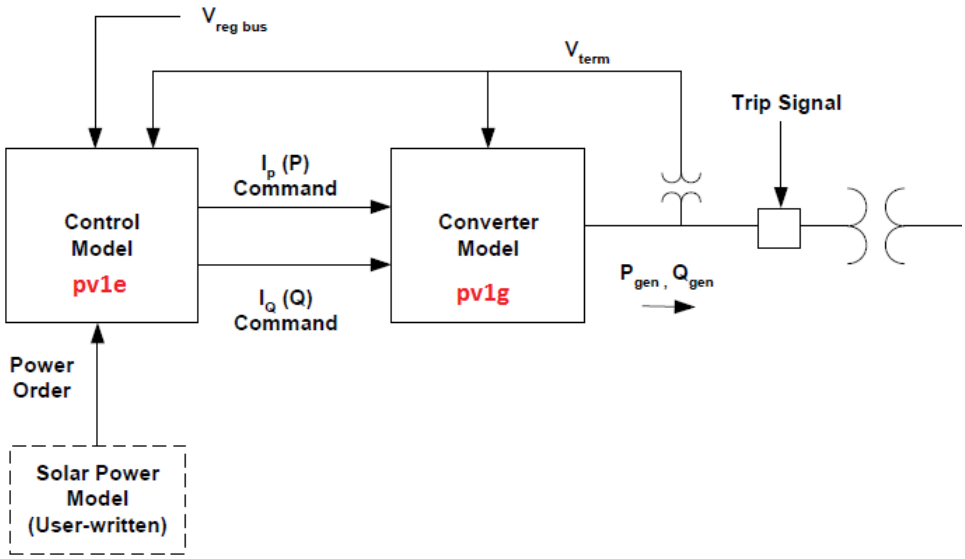

Figure 4.1: Modeling solar photovoltaic plants in PSLF

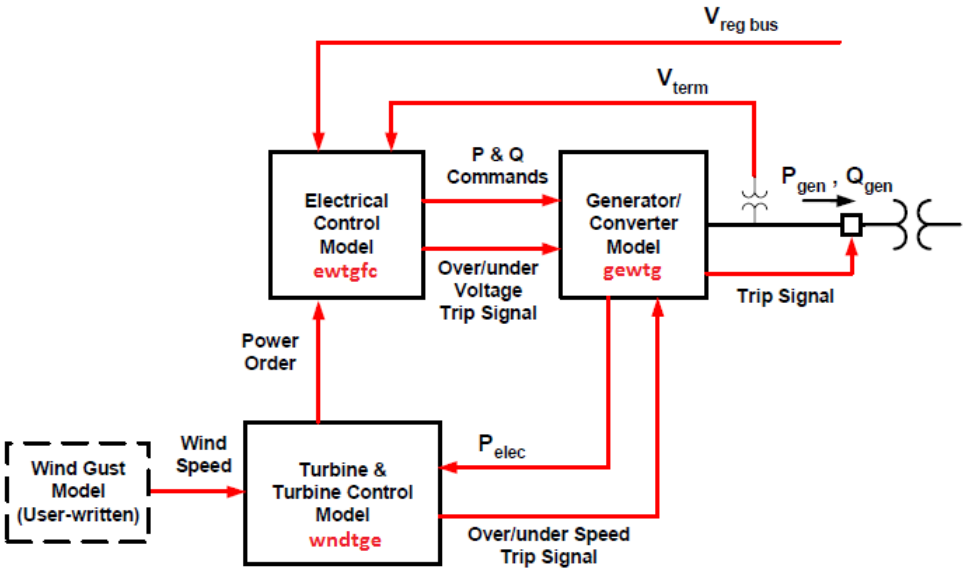

Figure 4.2: Modeling wind turbine-generators in PSLF

4.1 The Converter Model in Commercial Software (pv1g,gewtg)

The converter is the interface between the source of power and the network. In PSLF, the models *pv1g* and *gewtg* represent the converter model for solar photovoltaic and wind applications respectively. There is minimal difference between the two models. Figure 4.3 shows the block diagram of this converter model [91]. The converter is represented as a current injection device which injects the required current into the network. The active and reactive current commands are issued from the control block. The model receives the individual current commands and injects a complex current into the network. The 20ms time constant in the control block of states s_0 and s_1 represents the switching of the solid state switches within the converter.

Additionally, built into this block is the behavior of few limiting devices. The low voltage power logic (LVPL) uses the terminal voltage magnitude to control the upper limit on the active power injected. If the bus voltage magnitude of the converter falls below a certain threshold, due to the occurrence of a disturbance, the LVPL block will

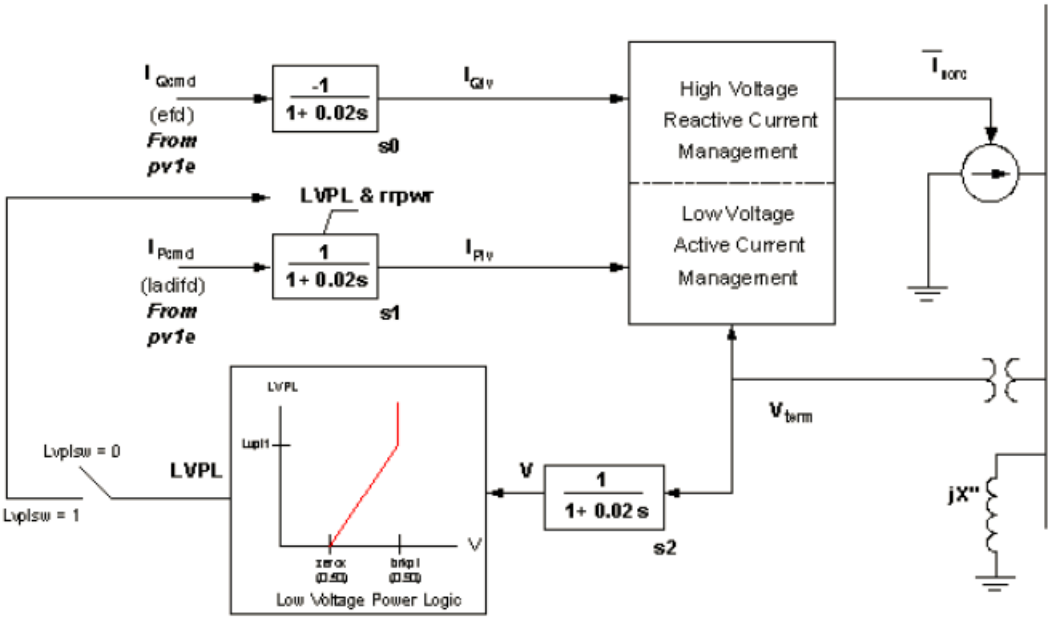

Figure 4.3: Converter model in PSLF

reduce the upper limit as per the characteristic shown. Within a range of low voltage magnitude values, the active current upper limit is varied in a linear fashion. If the voltage magnitude falls below the lower boundary of the range, the active current upper limit is made zero. In the normal operating voltage range, the LVPL block does not affect the active current upper limit. All settings in the LVPL block can be set by the user.

Two algebraic current limiters are also present in this block. The *high voltage reactive current management* section is instrumental in reducing the reactive power injected if the terminal voltage magnitude rises above a certain user defined limit. The user also has the freedom to set the rate at which the reactive power is ramped down. The *low voltage active current management* section takes care of reducing the active power injected while the voltage magnitdue falls below a certain value. Its function is similar to the LVPL block.

4.2 The Converter Control Model in Commercial Software (pv1e,ewtgfc)

The control model is responsible for generating the active and reactive current commands for the converter model. The block diagram of this model is depicted in Figure 4.4 [91]. The bottom section of the model shows the calculation of the active

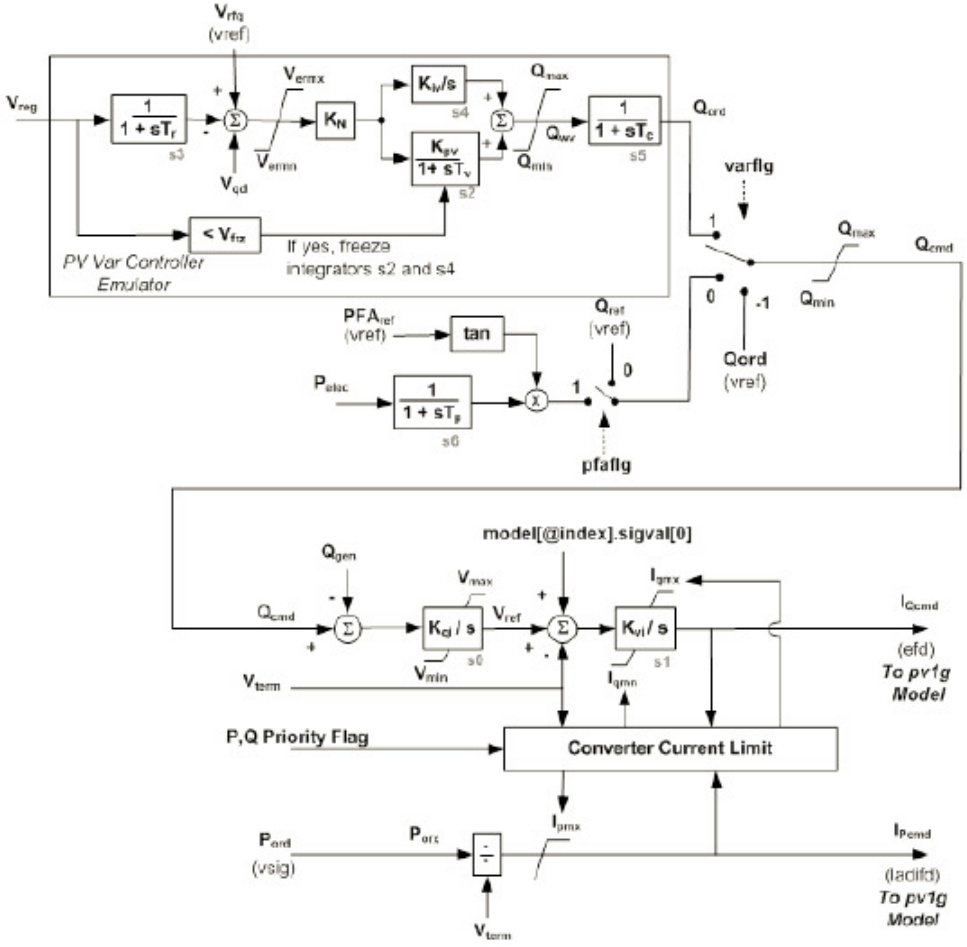

Figure 4.4: Converter control model in PSLF

current command. The reference active power, P_{ord}, can be either set by the user using an external user-written dynamic model or the value scheduled in the power flow. This feature thus allows for the inclusion of a governor type model to set the active power.

The model allows for three different ways of setting the reactive current command. These various modes can be toggled using the *varflg* parameter as shown in the block diagram. These different ways are:

1. PV VAr controller emulator: This emulator is essentially a voltage regulator. The terminal voltage magnitude is compared to its reference value and the desired amount of reactive power is calculated using a PI controller.

2. Power factor regulator: The converter can be operated at a desired power factor and the reactive power is calculated based on the required power factor and the active power.

3. User defined reactive power: The user has an option to provide a value of required reactive power.

The converter current limit block ensures that all current commands are within certain limits. The details of the operation of this limiter are provided in [84].

4.3 User Defined Converter Control Model

4.3.1 Generic Control Structure

While the control model described in the previous section was found to work as per design and specifications, it was deemed to be complex. With the aim of achieving close to 100% CIG penetration, a requirement arises for simpler control structures bearing in mind that the stability of the system hinges upon the interaction of these controls with one another. In addition, as different manufacturers would have their own variation of control architecture, a simple control was used to focus on the model of the converter. With this objective, a controller as shown in Figure 4.5 was designed for the converter.

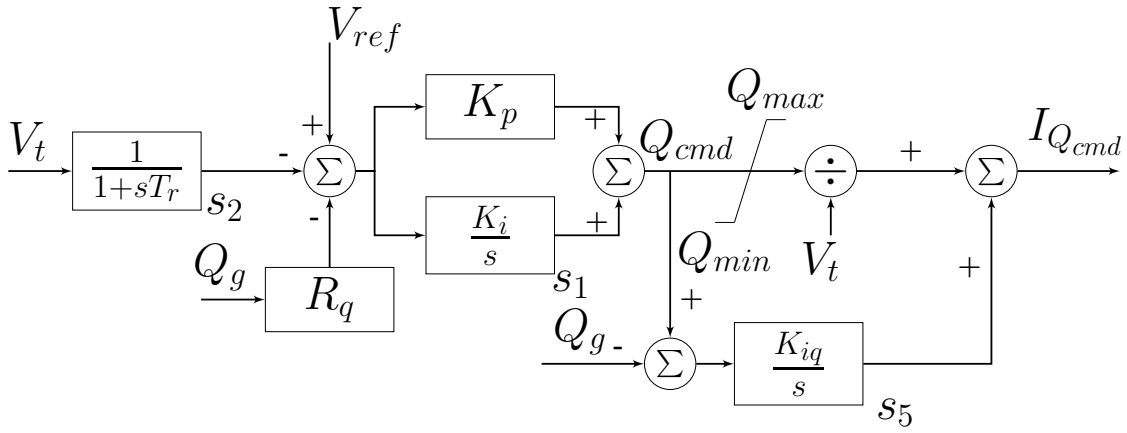

(a) Reactive power controller

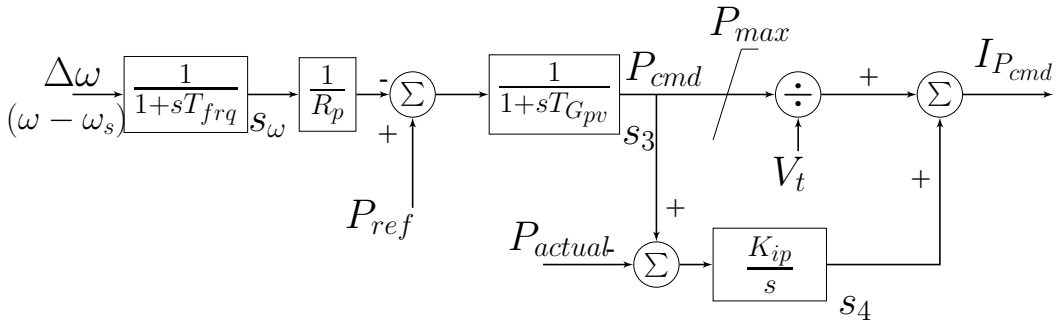

(b) Real power controller

Figure 4.5: User defined converter control model

The effective real power order (Figure 4.5(b)) is a combination of the power set-point and the active power droop coefficient while the reactive power order (Figure 4.5(a)) is obtained from the voltage error along with a reactive power droop. The QV droop is instrumental in obtaining a stable operation between converters when multiple converters are connected to the same bus. The active power droop coefficient is denoted as R_p and the reactive power droop coefficient is denoted as R_q. The equations describing the behavior of the controller are given by (4.1) to (4.9).

$$\frac{ds_1}{dt} = K_i \left[V_{ref} - s_2 - R_q Q_g\right] \tag{4.1}$$

$$\frac{ds_2}{dt} = (1/T_r) * [V_t - s_2] \tag{4.2}$$

$$\frac{ds_3}{dt} = (1/T_{Gpv}) * [P_{ref} - (\Delta\omega/R_p) - s_3] \tag{4.3}$$

$$P_{cmd} = s_3 \tag{4.4}$$

$$\frac{ds_4}{dt} = K_{ip}\,[P_{cmd} - P_{actual}] \tag{4.5}$$

$$\frac{ds_5}{dt} = K_{iq}\,[Q_{cmd} - Q_g] \tag{4.6}$$

$$Q_{cmd} = s_1 + K_p\,[V_{ref} - s_2 - R_q Q_g] \tag{4.7}$$

$$I_{Qcmd} = Q_{cmd}/V_t + s_5 \tag{4.8}$$

$$I_{Pcmd} = P_{cmd}/V_t + s_4 \tag{4.9}$$

Limits have been imposed on the maximum active and reactive power and minimum reactive power deliverable. In choosing the limits for the reactive and active power, it has been assumed that the converter can withstand an instantaneous MVA of 1.7 times its rating [84]. Further, it has been arbitrarily assumed that at a terminal voltage level of 0.75pu, the minimum operable power factor is 0.4. As the voltage dips, the limits of the converter control will change to allow for more reactive power to be delivered while curtailing the active power delivered to meet the MVA rating. Though a terminal voltage of 0.75pu has been chosen as the minimum voltage, the maximum deliverable reactive power is maintained constant for voltages below 0.8pu as shown in Figure 4.6. The value of q_{max_1} is taken from the power flow but is assumed to be the value of maximum reactive power at a voltage level of 1.0pu. The value of q_{max_2} is obtained as given by (4.10).

$$q_{max_2} = \sqrt{\frac{(1.7 * MVA)^2}{1 + \left(\frac{1}{\tan\cos^{-1} 0.4}\right)^2}} \tag{4.10}$$

Therefore, at any voltage level V_t above 0.8pu, the value of q_{max} is obtained as given by (4.11).

$$q_{max} = q_{max_1} + \frac{q_{max_2} - q_{max_1}}{0.8 - 1.0}\,(V_t - 1.0) \tag{4.11}$$

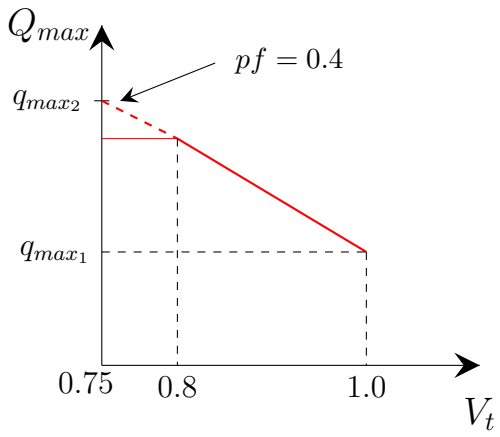

Figure 4.6: Variation of Q_{limit} with V_t

The value of q_{min} is maintained constant as specified in the power flow while the maximum active power is obtained as in (4.12) to maintain the MVA rating.

$$p_{max} = \sqrt{(1.7 * MVA)^2 - q_{max}^2} \tag{4.12}$$

For the integrator present in the reactive power loop, the windup limit has been converted to an anti-windup limit as per the scheme mentioned in [92]. The block diagram of this conversion is as shown in Figure 4.7 where the value of K_{limit} is appropriately chosen.

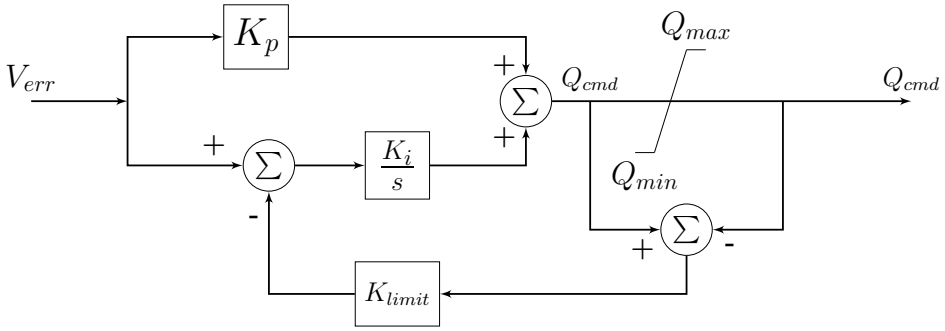

Figure 4.7: Conversion from windup to anti-windup limit

4.3.2 Presently used Converter Model

Presently, in positive sequence time domain simulation software, converters are represented as a boundary current injection in the network as shown in Figure 4.8 [87] and discussed in detail in Section 4.1. It will be shown in the next section

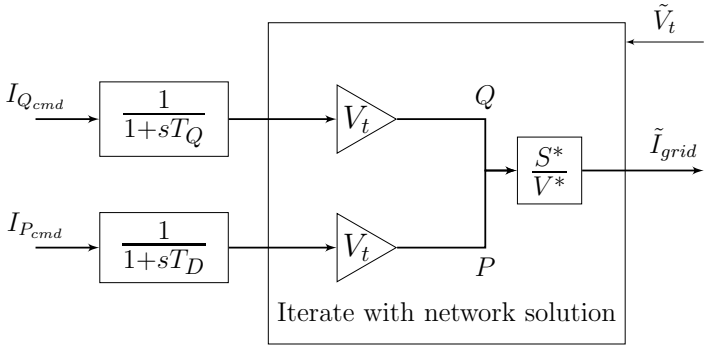

Figure 4.8: Boundary current converter representation for positive sequence simulation

that this positive sequence representation of the converter is unable to depict the near instantaneous response that can be achieved from a converter interfaced source. With a projected increase in CIG penetration in large systems, the ability of the CIG to provide a near instantaneous response to a disturbance can prove beneficial to the system and the positive sequence simulation model should be able to capture this feature.

4.3.3 Proposed Converter Model

To model the converter, this research work proposes a controlled voltage source representation of the converter to incorporate the effect of the converter coupling inductance. This representation allows for the depiction of the near instantaneous response that can be achieved from converter interfaced sources.

As the converter is practically a controlled ac voltage source with a voltage source on the dc side, the converter is modeled as a Thévenin voltage source described by

Figure 4.9 and (4.13).

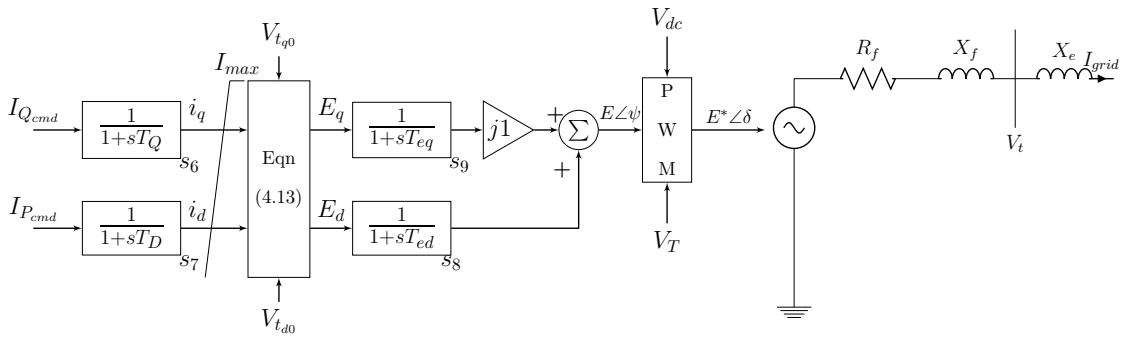

Figure 4.9: Controlled voltage source converter representation for positive sequence simulation

$$\begin{aligned} E_d &= V_{t_{d0}} + i_d R_f - i_q X_f \\ E_q &= V_{t_{q0}} + i_q R_f + i_d X_f \end{aligned} \tag{4.13}$$

The impedance $R_f + jX_f$ represents the coupling impedance which can be either a filter inductor or a transformer while E and δ represent the magnitude and angle of the developed converter voltage. $V_{t_{d0}}$ and $V_{t_{q0}}$ represent the dq axis components of the terminal voltage V_t. The current commands, $I_{Q_{cmd}}$ and $I_{P_{cmd}}$, represent the real and reactive current commands provided by the outer loop control. The time constants T_Q and T_D represent the effect of the inner current control loop of the converter control structure.

The converter representation includes the effect of the dc voltage and the amplitude modulation ratio m of the pulse-width modulation control depicted by the PWM block in Figure 4.9. To achieve a steady state modulation ratio of 0.6, the carrier voltage (V_T) and dc voltage (V_{dc}) are initialized to be:

$$V_T = \frac{\sqrt{E_d^2 + E_q^2}}{0.6}; V_{dc} = \frac{\sqrt{E_d^2 + E_q^2}}{0.5 * 0.6} \tag{4.14}$$

At every time step, the values of E_d and E_q from (4.13) are used in the following manner:

- magnitude and angle of the required internal voltage is obtained as $|E| = \sqrt{E_d^2 + E_q^2}$ and $\phi = \tan^{-1}(E_q/E_d)$
- The modulation index is calculated as $m = |E|/V_T$. The value of m is limited to be between 0.4 and 1.0. Figure 4.10 shows the generation of switching pulses for the inverter and the relation between the carrier voltage and the modulating/reference voltage. While the proposed positive sequence converter model does not represent the actual switching model of the inverter, the effect of the modulation index on the ac output voltage has been represented.
- The phase voltage values are then obtained as $E_{a,b,c} = 0.5mV_{dc}\cos(\omega_s t + \phi - 120i)$ where ω_s is 377 rad/s and $i = 0, 1, 2$ [93].
- values of E_d^* and E_q^* ($E^* \angle \delta$) are obtained by applying Park's transformation on $E_{a,b,c}$.

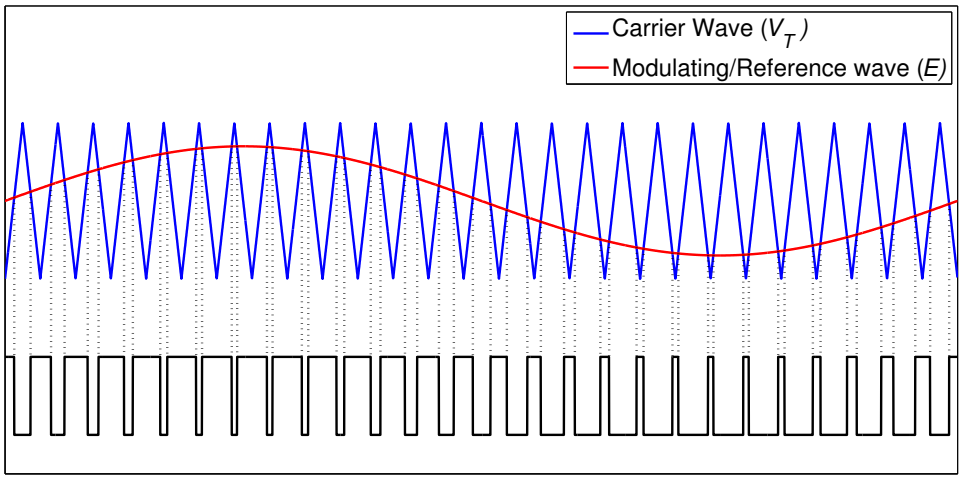

Figure 4.10: Generation of switching pulses for an inverter

A lower steady state modulation ratio will require a higher dc voltage magnitude to maintain the same ac voltage and would restrict the lower band gap of the modulation

ratio. A steady state modulation ratio of 0.6 has been chosen to allow for a sufficient range of values for the transient modulation ratio.

The converter model proposed in this work is interfaced with the network solution by a Thévenin voltage source which is a simple function of the state variables of the model and has a constant value from one iteration of the network solution to the next. This form of interface avoids the numerical convergence issues that can arise [80–82] when the model establishes a boundary condition based on the network solution.

In addition, two protection schemes have been incorporated:

- As the converters have a hard current limit, an instantaneous overcurrent protection has been implemented with a cut-off current of 1.7 pu [84].
- A time dependent overvoltage protection has also been implemented. If the voltage at the terminal V_t rises 0.15 pu more than the steady state voltage for more than 0.1s, the converter is tripped.

4.3.4 PLECS Model for Calibration

A point on wave simulation was used for calibration of this proposed positive sequence voltage source converter model. For the point on wave simulation, using the PLECS software package, an average model of the converter was used [79]. The inner current control loop uses the generated current commands as shown in Figure 4.11 to synthesize the reference voltage wave to be developed by the converter. While the fast inner current control loops are required in the electromagnetic transient simulation, these details of modeling the voltage source converter and its control are however not suitable for the transient stability simulation of large networks as it would require a smaller simulation time step to accurately capture the inner loop behavior and this would considerably increase the computational burden.

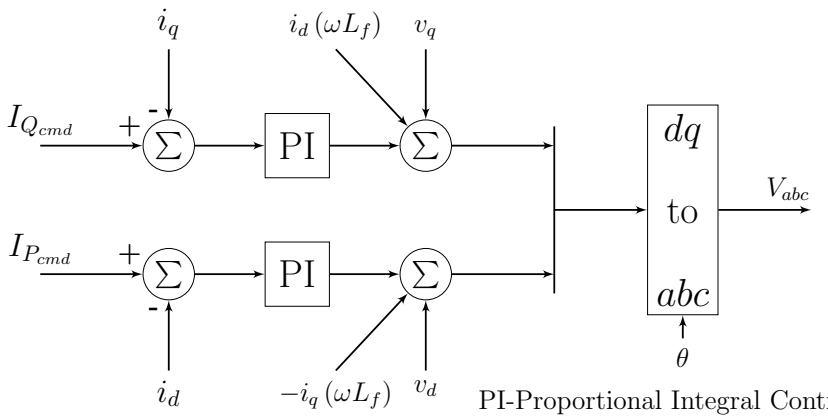

Figure 4.11: Inner current control loop in PLECS to synthesize reference voltage wave

Due to the effect of grid impedance on the operation of the inner current control loop [94], a wide variety of inner current control loops are used in practical inverters with the common characteristic of response times that are very fast in relation to the bandwidth proposed for grid level controls. Accordingly, for the positive sequence grid level model used in this research work, simple time constants represented as T_D and T_Q with a value of 10ms each represent the behavior of the inner control loops. This is a conservative estimate as practically, these inner control loops may have a quicker response time. The time constants T_{ed} and T_{eq} also have a conservative value of 10ms each and represent the delay in the PWM/switching process. Again, in reality, this value could be lower than 10ms.

4.3.5 Alternate Control Structure and Converter Model

While accurate power control is ensured with the generic control structure described in Section 4.3.1, current control is not guaranteed at all operating points and network topologies. With power and terminal voltage being controlled, variable power limiters and over current trip settings ensured that the current output of the converter with the generic control does not exceed the maximum current limit.

However, for certain applications and scenarios, accurate current control could also be a priority. Thus, an alternative generic control structure with an inner current loop control is also proposed for use with the developed controlled voltage source converter model. With current and voltage controlled, power control does not require an explicit control loop. The developed control model is as shown in Figure 4.12. The reactive power output of the converter (Q_g), terminal voltage (V_t), and the d-q axis components of the converter output current (i_d, i_q) are values at the point of interconnection of the converter. With the explicit representation of the inner loop

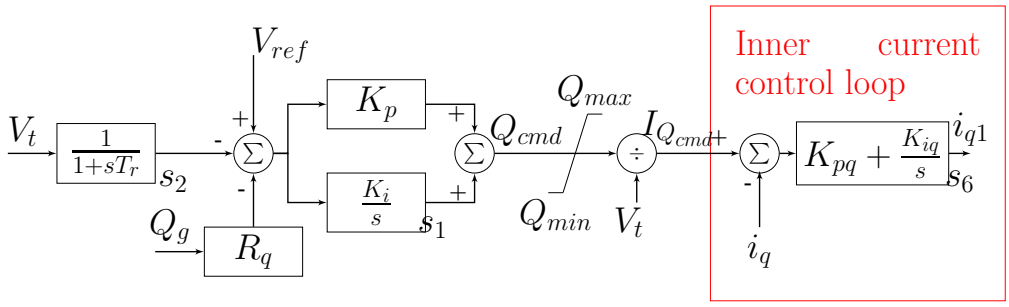

(a) Reactive power controller with inner current loop

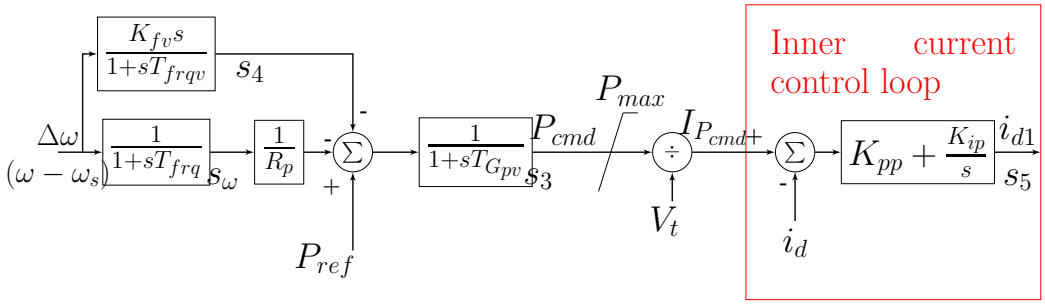

(b) Real power controller with inner current loop

Figure 4.12: User defined converter control model with inner current control loop

current controller, the ac side voltage of the converter is calculated as in (4.15) and the converter model is as shown in Figure 4.13.

$$\begin{aligned} E_d &= V_{t_{d0}} + i_d R_f - i_{q1} X_f \\ E_q &= V_{t_{q0}} + i_q R_f + i_{d1} X_f \end{aligned} \tag{4.15}$$

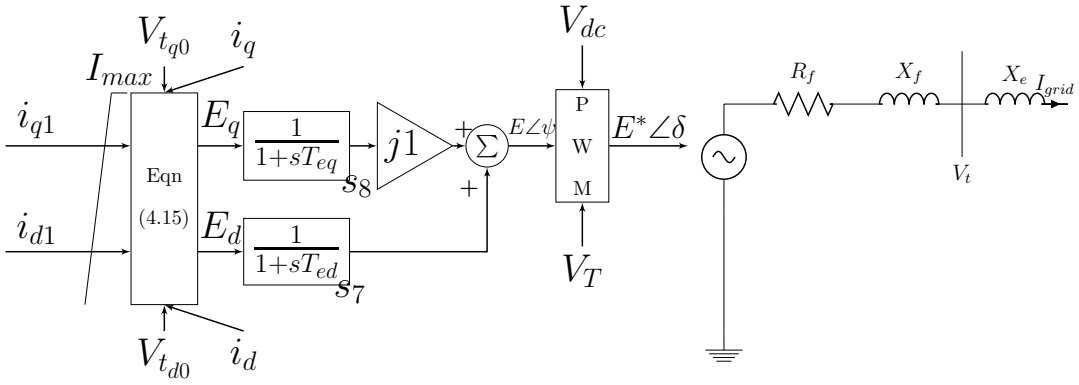

Figure 4.13: Controlled voltage source converter representation for positive sequence simulation with inner current loop control

In addition to an active power droop component proportional to $\Delta\omega$, a droop component proportional to the rate of change of frequency has also been included in this control structure.

The implementation of the proposed converter model and the associated control structures for positive sequence time domain simulation was carried out in PSLF [77] by writing an EPCL code as given in the appendix. EPCL is PSLF's in-built programming language.

4.4 Source behind Inverter Model

The one line diagram of the synchronous machine behind a rectifier-inverter set is as shown in Figure 4.14. To model the synchronous generator, the well known sixth order voltage behind subtransient reactance model (without saturation) as described in Section 3.1.1 has been used. The inverter is modeled using the proposed controlled voltage source model described in Section 4.3.3. The following subsections describe the mathematical modeling of the dc capacitance, the rectifier and the synchronous machine controls. An overview of the various control loops used in the entire synchronous machine behind rectifier-inverter model is shown in Figure 4.15.

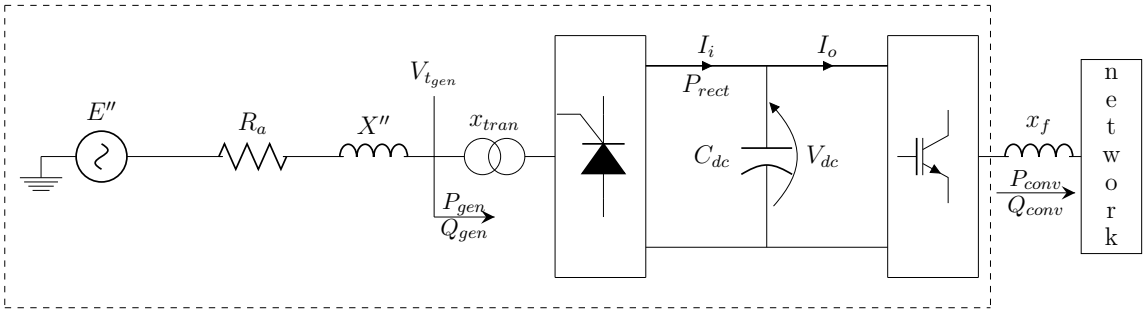

Figure 4.14: One line diagram of synchronous machine behind a rectifier-inverter set

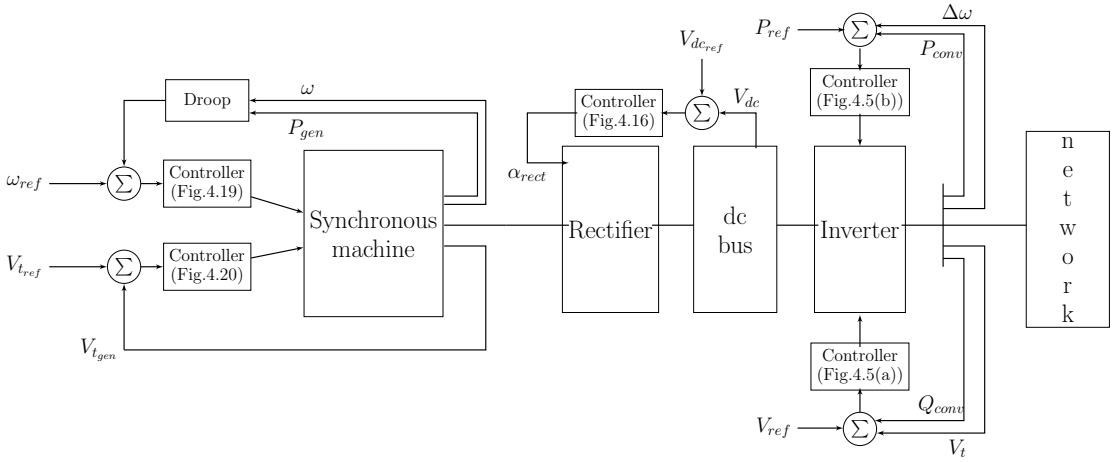

Figure 4.15: Control diagram of synchronous machine behind a rectifier-inverter set

4.4.1 dc Capacitance

From Figure 4.14, the variation of V_{dc} is governed by (4.16).

$$C_{dc}\frac{dV_{dc}}{dt} = I_i - I_o \tag{4.16}$$

Multiplying both sides of the equation by V_{dc} and ignoring the active power losses in the inverter,

$$C_{dc}V_{dc}\frac{dV_{dc}}{dt} = P_{rect} - P_{conv} \tag{4.17}$$

The rectifier behaves as a load on the synchronous generator. Thus, ignoring the small active power losses in the rectifier and transformer, $P_{rect} \approx P_{gen}$. Hence, (4.17) can be written as,

$$C_{dc}V_{dc}\frac{dV_{dc}}{dt} = P_{gen} - P_{conv} \tag{4.18}$$

In (4.18), all quantities are in standard units. Converting the equation to per unit, using the MVA base of the synchronous generator as the power base and the line to line voltage of the inverter as the dc voltage base,

$$\frac{C_{dc_{(Farad)}} V^2_{dcbase_{(kV)}}}{MVA_{base_{(VA)}}} V_{dc_{(pu)}} \frac{dV_{dc_{(pu)}}}{dt_{(seconds)}} = P_{gen_{(pu)}} - P_{conv_{(pu)}} \tag{4.19}$$

The sensitivity to C_{dc} is discussed in the next chapter.

4.4.2 Rectifier Model

The set of equations describing the relation between the terminal of the synchronous machine and the three phase bridge rectifier are given by (4.20)-(4.23) [22, 95].

$$V_{tgen} cos\alpha_{rect} = V_{dc} + \frac{3}{\pi} x_{tran} I_i \tag{4.20}$$

In the above equation, the quantities are in per unit with the ac voltage and dc voltage base chosen appropriately. α_{rect} is the firing angle of the rectifier switches. Upon the occurrence of a disturbance, the inverter control will act fast causing P_{conv} to change. The change in power will cause the dc voltage V_{dc} to change. Hence, to restore balance, the synchronous machine output P_{gen} would have to change and match P_{conv}. Thus, the required current I_i in (4.20) can be defined as

$$I_i = P_{conv}/V_{dc} \tag{4.21}$$

Converting the value of x_{tran} from an ac base to dc base,

$$V_{tgen} cos\alpha_{rect} = V_{dc} + \frac{3}{\pi} \frac{x_{tran}}{1.3505^2} \frac{P_{conv}}{V_{dc}} \tag{4.22}$$

Due to the presence of the source reactance (x_{tran}) and a non zero firing angle, the rectifier will consume reactive power. The approximate power factor of operation is given as [22],

$$\cos \phi_{rect} = V_{dc}/V_{tgen} \tag{4.23}$$

The required reactive power is obtained from the synchronous machine. Further, to help maintain the dc voltage level, the firing angle of the rectifier is varied as shown in Figure 4.16. The active power output of the rectifier is given as

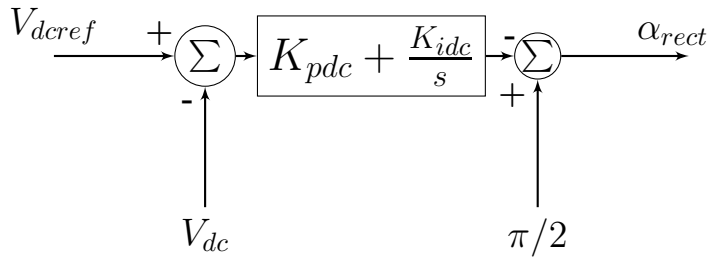

Figure 4.16: Rectifier firing angle control

$$P_{rect} = I_i V_{tgen} cos\alpha_{rect} - I_i^2 \frac{3}{\pi} \frac{x_{tran}}{1.3505^2} \tag{4.24}$$

4.4.3 Synchronous Machine Current

In steady state, the real and reactive power to be generated by the synchronous machine is defined by

$$\begin{aligned} P_{gen}(t) =& P_{conv}(t) = P_{rect}(t), t \to \infty \\ Q_{gen}(t) =& P_{gen}(t) \tan\phi, t \to \infty \end{aligned} \tag{4.25}$$

Upon the occurrence of a disturbance, energy is extracted from the dc capacitor. However, due to the time constant (τ) of the dc L-C circuit, the synchronous machine behind the dc bus, does not sense the disturbance immediately. This delay can be represented either by explicitly modeling the dc inductor or by using an approximate lag function. The explicit modeling of the dc inductor will be discussed first followed by the discussion of the approximate lag function.

4.4.3.1 Explicit Representation of dc Inductor

In Figure 4.14 only a capacitance is used to represent the dc circuit. However, a more detailed representation of the dc circuit is as shown in Figure 4.17. With (4.16)

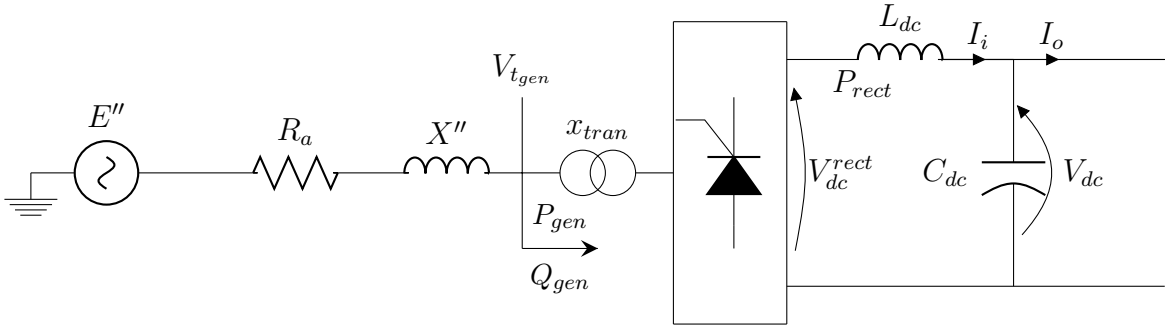

Figure 4.17: One line diagram of detailed dc circuit for the synchronous machine behind a rectifier-inverter set

governing the variation of V_{dc}, the variation of current I_i can be written as,

$$L_{dc}\frac{dI_i}{dt} = V_{tgen}cos\alpha_{rect} - I_i\frac{3}{\pi}\frac{x_{tran}}{1.3505^2} - V_{dc} \tag{4.26}$$

Thus, the approximate power factor of the rectifier can be written as,

$$\cos\phi_{rect} = V_{dc}^{rect}/V_{tgen} \tag{4.27}$$

where,

$$V_{dc}^{rect} = V_{dc} + L_{dc}\frac{dI_i}{dt} \tag{4.28}$$

The real and reactive power to be generated by the synchronous machine can now be evaluated as

$$\begin{aligned} P_{gen}(t) =& P_{rect}(t) \\ Q_{gen}(t) =& P_{gen}(t)\tan\phi_{rect} \end{aligned} \tag{4.29}$$

As the current I_i is a state variable, it cannot change value instantaneously thereby accounting for the delay/time constant of the dc L-C circuit.

4.4.3.2 Approximate Representation of Delay by Lag Function

Instead of using the detailed representation of the dc circuit, the approximate representation as in Figure 4.14 can be used with the delay of the dc circuit represented

in the control structure as,

$$\begin{aligned} P_{gen}(t) =& \frac{P_{rect}(t)}{1+s\tau} \\ Q_{gen}(t) =& \frac{P_{gen}(t)\tan\phi_{rect}}{1+s\tau} \end{aligned} \tag{4.30}$$

It will be shown in the next chapter that the performance of the model with this approximate representation of the time constant is similar to the performance with the detailed representation of the dc circuit. Thus, for simulation of large systems, the approximate representation leads to a saving in computation effort.

Irrespective of the method used to represent the dc circuit time constant, the generator terminal current is determined by control of the inverter and the voltage on the dc bus. The active power to be delivered by the generator is determined by the inverter and the charge on the dc capacitor. The reactive power to be delivered by the generator is determined by the operation of the rectifier. Hence the load on the generator, P_{gen} and Q_{gen}, is known and the one line diagram of the machine is as shown in Figure 4.18.

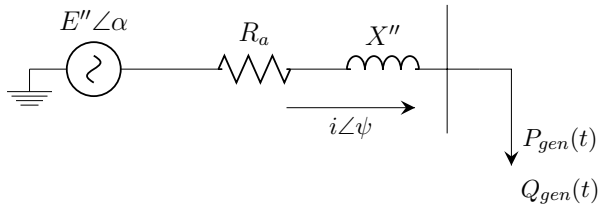

Figure 4.18: Loading of synchronous machine

As the generator is located behind the rectifier and is electrically decoupled from the ac network, the terminal voltage (V_{tgen}) is assumed to always be at an angle 0 with the real-imaginary (r-i) axis while the magnitude of the internal subtransient voltage (E'') is at an angle α with respect to the axis.

According to Faraday's law, a change in the induced voltage ($E''\angle\alpha$) can only occur with a change in the magnetic coupling in the machine. For a change in

load, the change in the magnetic coupling is brought about by the change in current flowing through the stator of the machine. However, from the law of constant flux linkages [96], an instantaneous change in the current is brought about solely due to the change in load impedance at the machine terminals. Hence, to calculate the current at a time instant t_n, the subtransient voltage at time instant t_{n-1} can be used. With the subtransient voltage ($E''\angle\alpha$) being a function of the generator state variables, the lower positive root of the quartic equation (4.31) gives the value of the magnitude of the current while (4.32) and (4.33) are used to obtain the value of the real ($\mathbb{R}$) and imaginary ($\mathbb{I}$) components of the current along the network axis.

$$\begin{aligned}\left(R_a^2 + X''^2\right) i^4 + \left(2P_{gen}(t) + 2Q_{gen}(t) - \left(\mathbb{R}\left(E''\angle\alpha\right)\right)^2 - \left(\mathbb{I}\left(E''\angle\alpha\right)\right)^2\right) i^2 \\ + \left(P_{gen}^2(t) + Q_{gen}^2(t)\right) = 0\end{aligned} \tag{4.31}$$

$$\mathbb{R}\left(i\angle\psi\right) = \frac{(P_{gen}(t) + i^2 R_a)\mathbb{R}\left(E''\angle\alpha\right) + (Q_{gen}(t) + i^2 X'')\mathbb{I}\left(E''\angle\alpha\right)}{E''^2} \tag{4.32}$$

$$\mathbb{I}\left(i\angle\psi\right) = \frac{(P_{gen}(t) + i^2 R_a)\mathbb{I}\left(E''\angle\alpha\right) - (Q_{gen}(t) + i^2 X'')\mathbb{R}\left(E''\angle\alpha\right)}{E''^2} \tag{4.33}$$

These components of current are then used in the differential equations of the synchronous machine.

4.4.4 Machine Governor and Exciter Models

With an increase in converter interfaced generation, the future grid operators would need the freedom to dispatch every source of energy. Maintaining a headroom on each source allows for the successful deployment of primary frequency control actions thereby increasing the stability margin of the system. Additionally, upon the occurrence of a disturbance, due to the fast action of the inverter active power control, energy is extracted from the dc capacitor causing the dc voltage to deviate from its pre-disturbance value. Due to the finite size of the capacitor, recovery of the

dc voltage depends on the recovery of this energy. Thus, the presence of an active governor on the synchronous machine is imperative.

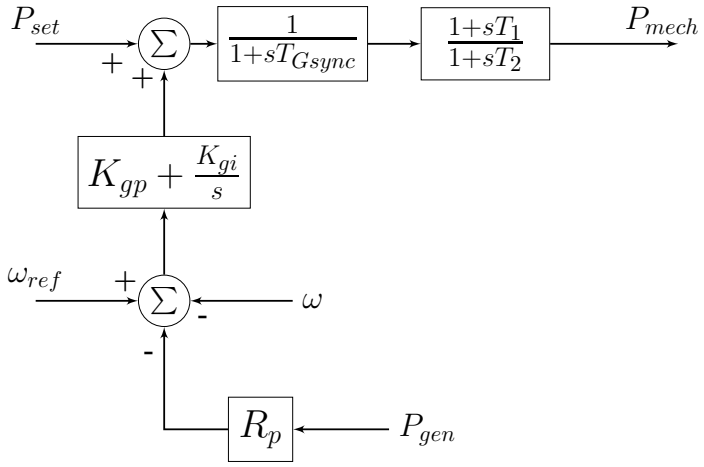

Figure 4.19: Governor of synchronous machine

The governor of the synchronous machine as shown in Figure 4.19 has speed error as its input. In addition, the governor is also enabled with an active power droop control with the same value of droop coefficient (R_p) as used in the active power loop of the inverter. The change in dc voltage changes the load on the synchronous machine. The change in speed of the machine due to this change in load, will cause the input mechanical power to change.

In this work, a non ideal operation of the rectifier has been used. Due to the presence of the transformer reactance x_{tran} the rectifier also consumes reactive power and operates at a non unity power factor. Further, it can be seen from (4.20) that the dc voltage magnitude is dependent on the terminal voltage of the synchronous machine. Hence, in order to support the voltage, an excitation system is required on the generator to maintain the generator terminal voltage. A static exciter as shown in Figure 4.20 has been modeled to maintain the generator terminal voltage (V_{tgen}).

The implementation of this model was also carried out in PSLF by writing an EPCL code.

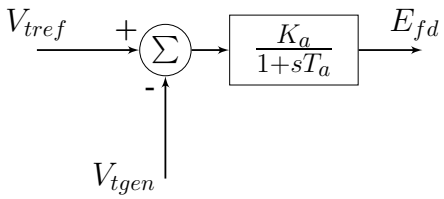

Figure 4.20: Static exciter of synchronous machine

4.5 Induction Motor Drive Model

The need for precise speed control of induction motors has resulted in the development of speed control power electronic drives. In a future grid, both the generation source and the loads could be interfaced through converters. It is thus important to simultaneously develop positive sequence models for converter interfaced loads. The one line diagram of the induction motor drive is as shown in Figure 4.21. In the following sub-sections, the mathematical model of each element of the one line diagram will be discussed.

4.5.1 Induction Motor Model

The equations representing the induction motor are as developed in [22] given here by (4.34)-(4.36) with the transient equivalent circuit as shown in Figure 4.21. As a squirrel cage induction motor is assumed to be used, the rotor side circuit is shorted and the rotor windings are represented as an equivalent three phase winding.

$$\frac{d\omega_{r_{ind}}}{dt} = \frac{1}{2H_{ind}}\left(T_e - T_m\right) \tag{4.34}$$

$$T'_o\frac{dv'_d}{dt} = -v'_d - \frac{X_m^2}{X_r}i_{inv_q}^{dr} + \frac{s_{ind}X_r v'_q}{R_r} \tag{4.35}$$

$$T'_o\frac{dv'_q}{dt} = -v'_q + \frac{X_m^2}{X_r}i_{inv_d}^{dr} - \frac{s_{ind}X_r v'_d}{R_r} \tag{4.36}$$

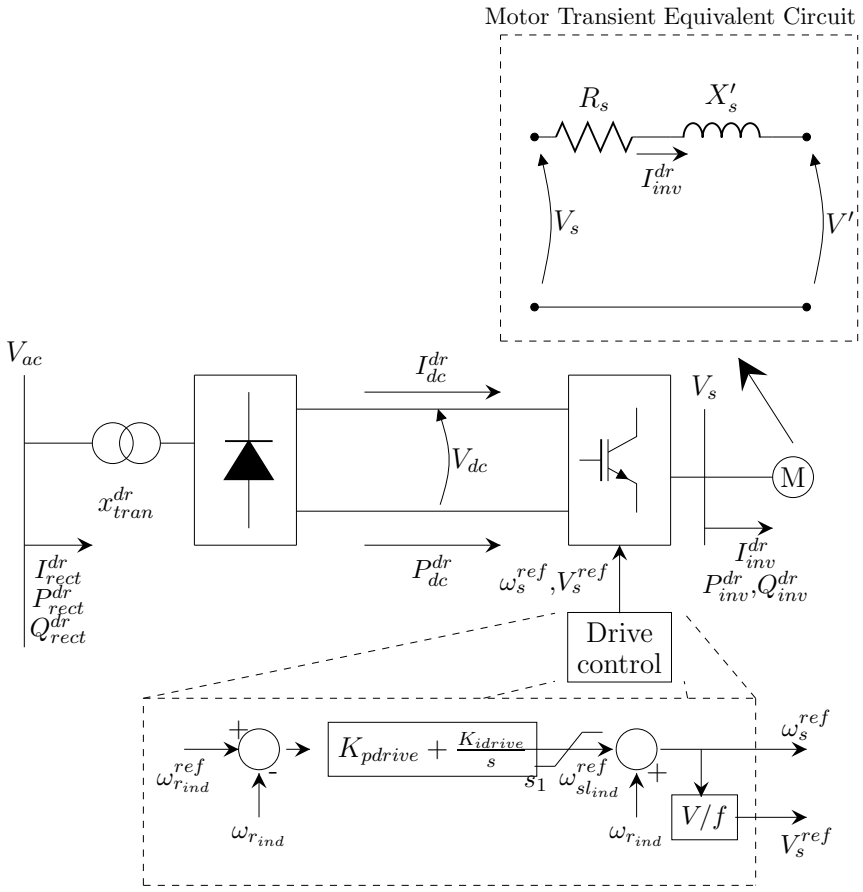

Figure 4.21: Induction motor drive model

V' is a voltage behind transient impedance which represents the effect of the rotor flux on the rotor voltages and is given by (4.37).

$$v'_d = -\frac{\omega_s L_m}{L_r}\psi^{qr}_{ind}; v'_q = \frac{\omega_s L_m}{L_r}\psi^{dr}_{ind} \tag{4.37}$$

The load torque T_m is represented as a function of speed as given by (4.38).

$$T_m = P_{m0}\omega^{D_{ind}-1}_{r_{ind}} \tag{4.38}$$

The value of P_{m0} is obtained during initialization as,

$$P_{m0} = \frac{v'_{d0} i_{ds_0} + v'_{q0} i_{qs_0}}{\omega^{D_{ind}-1}_{r_{ind_0}}} \tag{4.39}$$

where the subscript 0 indicates the value of the variable during initialization of the model.

4.5.2 Drive Model

The network one line diagram of the drive model is as shown in Figure 4.21 along with the control block diagram of the drive [93].

The rectifier for the drive was considered to be an uncontrolled full bridge diode rectifier. The sinusoidal pulse-width modulation reference signal, denoted by V_s^{ref} and ω_s^{ref}, was generated to maintain constant flux inside the motor while maintaining a constant rotor speed of $\omega_{r_{ind}}^{ref}$. The dynamics of the capacitor on the dc bus have been assumed to be negligible.

4.5.3 Inclusion of Model in Powerflow

At a conventional load bus, both the active and reactive power demand is specified. However for an induction motor or rectifier load, the reactive power drawn varies with variation in the terminal voltage magnitude. Hence, for inclusion in the power flow, two approaches have been used depending on whether the motor is directly connected or connected through a drive.

4.5.3.1 Directly Connected Motor

For a directly connected induction motor, the method of including the motor equations in the Newton Raphson powerflow setup as detailed in [97] has been used. From the steady state equivalent circuit of the motor as shown in Figure 4.22,

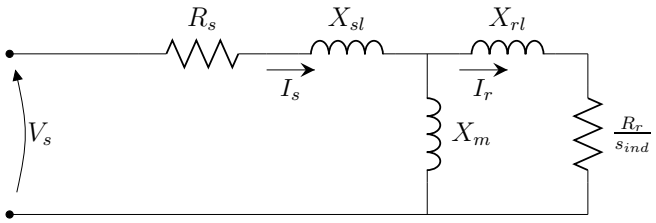

Figure 4.22: Steady state equivalent circuit of induction motor

$$P_{e_{ind}} = \frac{|V_s|^2 \left\{ \left(\frac{R_r}{s_{ind}}\right) \left[\left(\frac{R_r}{s_{ind}}\right) R_s - X_{s\ell}K_1 - X_{r\ell}X_m \right] + K_1 \left[\left(\frac{R_r}{s_{ind}}\right) (X_m + X_{s\ell}) + R_s K_1 \right] \right\}}{\left[\left(\frac{R_r}{s_{ind}}\right) R_s - X_{s\ell}K_1 - X_{r\ell}X_m \right]^2 + \left[\left(\frac{R_r}{s_{ind}}\right) (X_m + X_{s\ell}) + R_s K_1 \right]^2}$$

$$Q_{e_{ind}} = \frac{-|V_s|^2 \left\{ K_1 \left[\left(\frac{R_r}{s_{ind}}\right) R_s - X_{s\ell}K_1 - X_{r\ell}X_m \right] - \left(\frac{R_r}{s_{ind}}\right) \left[\left(\frac{R_r}{s_{ind}}\right) (X_m + X_{s\ell}) + R_s K_1 \right] \right\}}{\left[\left(\frac{R_r}{s_{ind}}\right) R_s - X_{s\ell}K_1 - X_{r\ell}X_m \right]^2 + \left[\left(\frac{R_r}{s_{ind}}\right) (X_m + X_{s\ell}) + R_s K_1 \right]^2} \tag{4.40}$$

In (4.40), the values of $|V_s|, s_{ind}$ and $Q_{e_{ind}}$ change with each iteration of the Newton Raphson solution. Assuming that the value of $P_{e_{ind}}$ is invariant to voltage, the active power equation of (4.40) can be rearranged as:

$$\left(\frac{R_r}{s_{ind}}\right)^2 a_{ind} + \left(\frac{R_r}{s_{ind}}\right) b_{ind} + c_{ind} = 0 \tag{4.41}$$

where,

$$\begin{aligned} a_{ind} &= P_{e_{ind}} \left(R_s^2 + K_3^2\right) - |V_s|^2 R_s \\ b_{ind} &= 2P_{e_{ind}} \left(R_s K_2 + K_3 K_4\right) - |V_s|^2 \left(K_2 + K_1 K_3\right) \\ c_{ind} &= P_{e_{ind}} \left(K_2^2 + K_4^2\right) - |V_s|^2 K_1 K_4 \end{aligned} \tag{4.42}$$

and,

$$\begin{aligned} K_1 &= X_{r\ell} + X_m;\ K_2 = -X_{s\ell}K_1 - X_{r\ell}X_m \\ K_3 &= X_{s\ell} + X_m;\ K_4 = R_s K_1 \end{aligned} \tag{4.43}$$

At the start of the Newton Raphson solution process, the constants K_1-K_4 are calculated. Subsequently, during each iteration of the process, the values of a_{ind}, b_{ind} and c_{ind} are calculated and used in (4.41) to solve for the value of R_r/s_{ind}. The larger value of R_r/s_{ind} is used in the reactive power equation of (4.40) to obtain the value of $Q_{e_{ind}}$. This value of $Q_{e_{ind}}$ is now used along with $P_{e_{ind}}$ as the value of load in the mismatch equations. To account for the voltage dependency, the partial derivative of $Q_{e_{ind}}$ given by (4.44), is added to the diagonal term of the Jacobian matrix

corresponding to the motor bus.

$$\frac{\partial Q}{\partial V} = \frac{2}{|V_s|} Q_{e_{ind}} \tag{4.44}$$

With this method, the converged power flow solution includes the values of s_{ind} and $Q_{e_{ind}}$ along with the value of V_s at every induction motor bus.

4.5.3.2 Drive Interfaced Motor

When the motor is connected to the network through a drive, the inverter supplies the reactive power required by the motor. The rectifier however draws reactive power from the network as commutation overlap occurs in the full bridge rectifier due to the presence of the interconnection transformer (x^{dr}_{tran} in Figure 4.21). Thus, to solve the powerflow, the values of P^{dr}_{rect} and Q^{dr}_{rect} are required.

Neglecting losses in both the rectifier and inverter, the active power terms can be equated as,

$$P^{dr}_{rect} \approx P^{dr}_{dc} \approx P^{dr}_{inv} = P_{e_{ind}} \tag{4.45}$$

In order to obtain the reactive power consumption of the rectifier, first, the dc voltage (V^{dr}_{dc}) has to be calculated. From [22], (4.46) relates the dc side voltage to the ac side voltage as

$$V^{dr}_{dc} = \frac{3\sqrt{2}}{\pi}|V_{ac}| - \frac{3}{\pi} x^{dr}_{tran} I^{dr}_{dc} \tag{4.46}$$

Converting the quantities of the above equation from standard units to per unit and recognizing that $I^{dr}_{dc} = P_{e_{ind}}/V^{dr}_{dc}$,

$$\left(V^{dr}_{dc}\right)^2 - |V_{ac}|\left(V^{dr}_{dc}\right) + \frac{\pi}{6} x^{dr}_{tran} P_{e_{ind}} = 0 \tag{4.47}$$

Using the value of $|V_{ac}|$ from the previous Newton Raphson iteration, the larger root of (4.47) is an estimated value for V^{dr}_{dc}. For this value of V^{dr}_{dc}, the reactive power

consumption of the rectifier can now be calculated as,

$$Q_{rect}^{dr} = P_{e_{ind}} \tan\cos^{-1}\left(\frac{V_{dc}^{dr}}{|V_{ac}|}\right) \tag{4.48}$$

Thus, at every iteration of the Newton Raphson solution process, (4.47) and (4.48) are used to obtain a new value of Q_{rect}^{dr}. This new evaluated value of Q_{rect}^{dr} and the known value of P_{rect}^{dr} are subsequently used in the next Newton Raphson iteration as values of load in the mismatch equations.

As the inverter supplies reactive power to the motor, the obtained value of V_{dc}^{dr} is now used instead of $|V_s|$ in (4.40)-(4.43) to calculate the values of the slip and reactive power consumption of the motor. The voltage bases are chosen to ensure that pre-disturbance, the per unit values of $V_{dc}^{dr} = |V_s|$. Due to the decoupling of the motor from the network by the drive, the reactive power consumption and slip of a drive connected motor do not affect the power mismatch at the network boundary bus.

The converged power flow solution includes the values of Q_{rect}^{dr}, V_{dc}^{dr}, s_{ind} and $Q_{e_{ind}}$ along with the value of V_{ac} at every drive connected induction motor bus.

4.5.4 Inclusion of Model in Transient Simulations

For a directly connected motor, (4.34)-(4.38) are used to represent the motor in transient simulations. However, for a drive connected motor with an uncontrolled rectifier, the value of V_{dc}^{dr} depends on the dc link current (I_{dc}^{dr}) and the network ac bus voltage magnitude ($|V_{ac}|$). But, the value of $|V_{ac}|$ is itself dependent on I_{dc}^{dr}, V_{dc}^{dr} and the rest of the network. Thus iterations within the network solution are required at every time step of the transient simulation. The algorithm is described below while the flowchart of the entire process is shown in Figure 4.23. The steps of the

algorithm are referenced to the corresponding blocks in the flowchart by encircled block numbers.

1. Estimate $\hat{V}_{dc_{new}}^{dr} = \cos\phi_{rect} * |V_{ac}|_{new}$, where $\cos\phi_{rect}$ is the rectifier power factor from the previous time step and $|V_{ac}|_{new}$ is the value obtained from the initial network solution (block (1)).

   (a) With the new inverter ac side voltage $|V_s| = m_{ind}\hat{V}_{dc_{new}}^{dr}$, the value of I_{inv}^{dr} is calculated as (block (2))

   $$I_{inv}^{dr} = \frac{|V_s|\angle 0 - V'}{R_s + jX_s'} \tag{4.49}$$

   (b) Using this value of I_{inv}^{dr}, the value of $I_{dc}^{dr} = m_{ind}\mathbb{R}\left(I_{inv}^{dr}\right)$. $\mathbb{R}$ indicates the real component of the quantity. (block (3))

   (c) Thus, the new value of the dc voltage is calculated as (block (3))

   $$V_{dc_{new}}^{dr} = |V_{ac}|_{new} - \frac{\pi}{6}x_{tran}^{dr}I_{dc}^{dr} \tag{4.50}$$

   (d) If $|\hat{V}_{dc_{new}}^{dr} - V_{dc_{new}}^{dr}| \leq \epsilon$, go to step 2. ϵ is a very small tolerance, e.g. 0.00001. (block (4))

   (e) Else set $\hat{V}_{dc_{new}}^{dr} = \beta * V_{dc_{new}}^{dr} + (1-\beta) * \hat{V}_{dc_{new}}^{dr}$ and go to step 1a. $\beta \leq 0.5$ (block (5))

2. Now, $I_{rect}^{dr} = I_{dc}^{dr}\angle\left(\angle V_{ac} - \cos^{-1}\left(V_{dc_{new}}^{dr}/|V_{ac}|_{new}\right)\right)$ (block (6))

3. Solve for the new estimate of the bus voltages ($|\hat{V}_{ac}|_{new}$) by solving the network equation $\tilde{I} = \tilde{Y}\tilde{V}$ (block (7))

4. If the difference between the estimated ac voltages from step 3 and the ac voltages from step 1 is lower than ϵ, exit and integrate the differential equations using the converged value of V_{ac} and V_{dc}^{dr} (block (8))

5. Else set $V_{ac_{new}} = \hat{V}_{ac_{new}}$ and go to step 1. (block (9))

Having obtained the value of $V^{dr}_{dc_{new}}$, the implementation of the drive model begins with the equations describing the controller of the drive as in (4.51)-(4.53).

$$\frac{ds_1}{dt} = K_{idrive}\left(\omega^{ref}_{r_{ind}} - \omega_{r_{ind}}\right) \tag{4.51}$$

$$\omega^{ref}_{sl_{ind}} = s_1 + K_{pdrive}\left(\omega^{ref}_{r_{ind}} - \omega_{r_{ind}}\right) \tag{4.52}$$

The slip speed is restricted to be between 0.15pu and 0.001pu.

$$\begin{aligned} \omega^{ref}_s &= \omega_{r_{ind}} + \omega^{ref}_{sl_{ind}} \\ V^{ref}_s &= \frac{V}{\mathfrak{f}}\omega^{ref}_s = \phi_{airgap}\omega^{ref}_s \end{aligned} \tag{4.53}$$

Using these quantities, the phase voltages to be applied by the inverter to the stator of the motor are obtained as,

$$\begin{aligned} V^{stator}_a &= m_{ind}V^{dr}_{dc_{new}}\cos(\omega^{ref}_s t) \\ V^{stator}_b &= m_{ind}V^{dr}_{dc_{new}}\cos(\omega^{ref}_s t - 120^\circ) \\ V^{stator}_c &= m_{ind}V^{dr}_{dc_{new}}\cos(\omega^{ref}_s t + 120^\circ) \end{aligned} \tag{4.54}$$

If V_T is designated as the triangular reference voltage to generate the pulsed width modulation signals for the inverter, then the amplitude modulation index is

$$m_{ind} = \frac{V^{ref}_s}{V_T} \tag{4.55}$$

Further, to maintain constant air gap flux

$$\phi_{airgap} = \frac{V^{ref}_s}{\omega^{ref}_s} \tag{4.56}$$

Combining (4.55) and (4.56) we get:

$$m_{ind} = \omega^{ref}_s \frac{\phi_{airgap}}{V_T} = K\omega^{ref}_s \tag{4.57}$$

With K being a constant determined during initialization of the model, the value of the amplitude modulation ratio can be obtained from the value of ω_s^{ref}. With the resultant values of the phase voltages from (4.54), the dq axis stator voltages are obtained by applying the Park's transformation on the phase voltages as in (4.58).

$$\begin{aligned} v_{qs} &= \frac{2}{3}\left[V_a^{stator}\cos(\omega_s^{ref}t) + V_b^{stator}\cos(\omega_s^{ref}t - 120^\circ) + V_c^{stator}\cos(\omega_s^{ref}t + 120^\circ)\right] \\ v_{ds} &= \frac{-2}{3}\left[V_a^{stator}\sin(\omega_s^{ref}t) + V_b^{stator}\sin(\omega_s^{ref}t - 120^\circ) + V_c^{stator}\sin(\omega_s^{ref}t + 120^\circ)\right] \end{aligned} \tag{4.58}$$

Subsequently, the values of currents $i_{inv_q}^{dr}$ and $i_{inv_d}^{dr}$ required in equations (4.35) and (4.36) are obtained using the obtained values of v_{qs} and v_{ds}.

In the following chapter, a discussion of the results verifying the performance of these converter models for various system configurations is recorded.

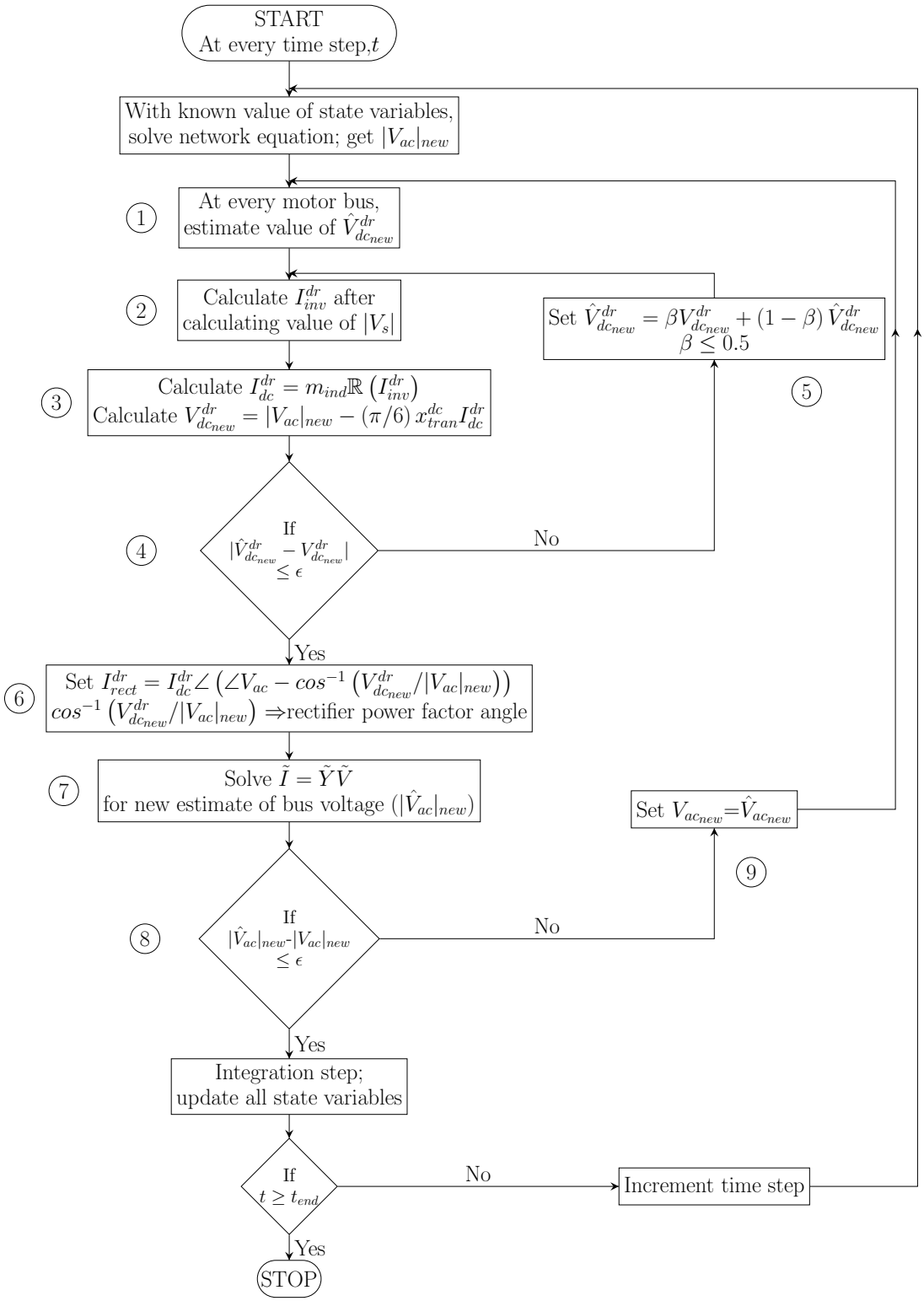

Figure 4.23: Flowchart of the procedure of inclusion of drive model in transient simulations

Chapter 5

SIMULATION AND RESULTS

The description of the simulation results in this chapter is divided into four sections. The behavior of the proposed controlled voltage source converter model is first discussed followed by the behavior of the synchronous machine behind the rectifier-inverter set. Subsequently, the behavior of the induction motor drive model is described. The final section discusses a couple of preliminary results for a system with all CIG and CIL.

5.1 Controlled Voltage Source Converter Model

The performance of the proposed controlled voltage source converter model along with its associated control was first validated with the performance of the converter in PLECS[1], a point on wave simulation software. Following this, the performance of the converter was analyzed in a 3 generator system and the 2012 WECC system with varying percentages of penetration.

5.1.1 Justification of Value of Inner Current Loop Time Constants

To justify the use of a 10ms time constant to represent the inner control loop (T_D and T_Q in Figure 4.9), a simple test network of a 247 MVA converter connected to an infinite bus as shown in Figure 5.1 was set up in PLECS. A local load of 90MW and 30MVAR was also present at the high voltage side of the transformer. At t=5s, the local load was increased by 30MW. The output current magnitude of the converter for different values of proportional gain of the PI controller of Figure 4.11 is

[1]PLECS Version 3.7.4

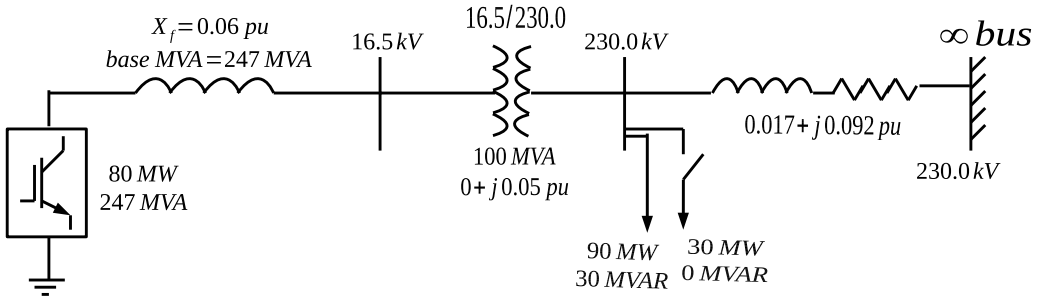

Figure 5.1: Converter connected to an infinite bus to justify the values of inner current loop time constants

as shown in Figure 5.2. The subscript indicates the factor by which the original gain was multiplied. The pre-disturbance active power set point of the converter was at 80MW. From Figure 5.2 it can be seen that the magnitude of the near instantaneous

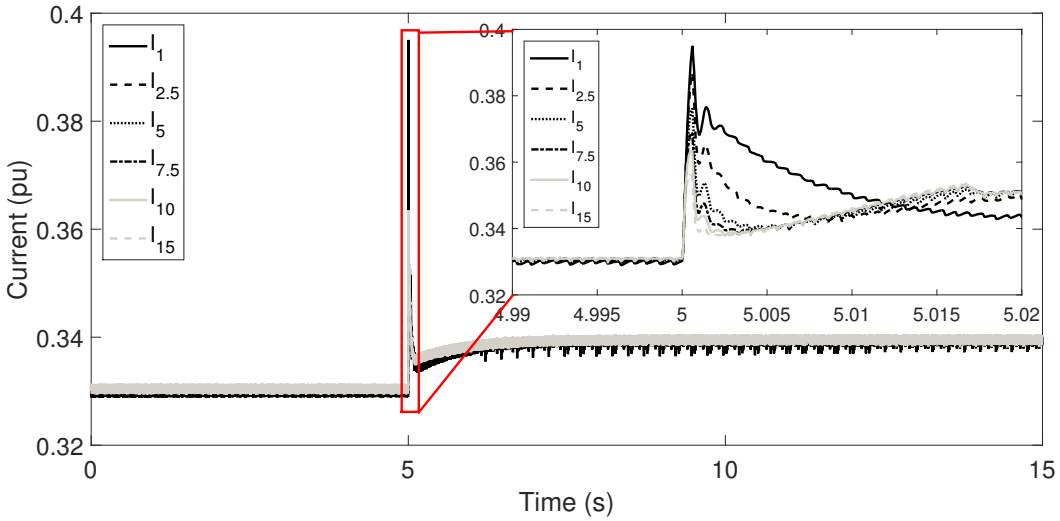

Figure 5.2: Converter current output for 30MW load increase with different inner current loop PI controller gains

response of the converter is controllable by adjusting the proportional gain of the PI controller of the inner current loop. It can also be seen that irrespective of the value of the proportional gain, the response trend is similar 10ms after the occurrence of the disturbance. The near instantaneous rise and subsequent settling of the converter current can also be observed from the plots of the three phase currents as seen in Figure 5.3. These figures showcase the fast maneuvering capability of a CIG.

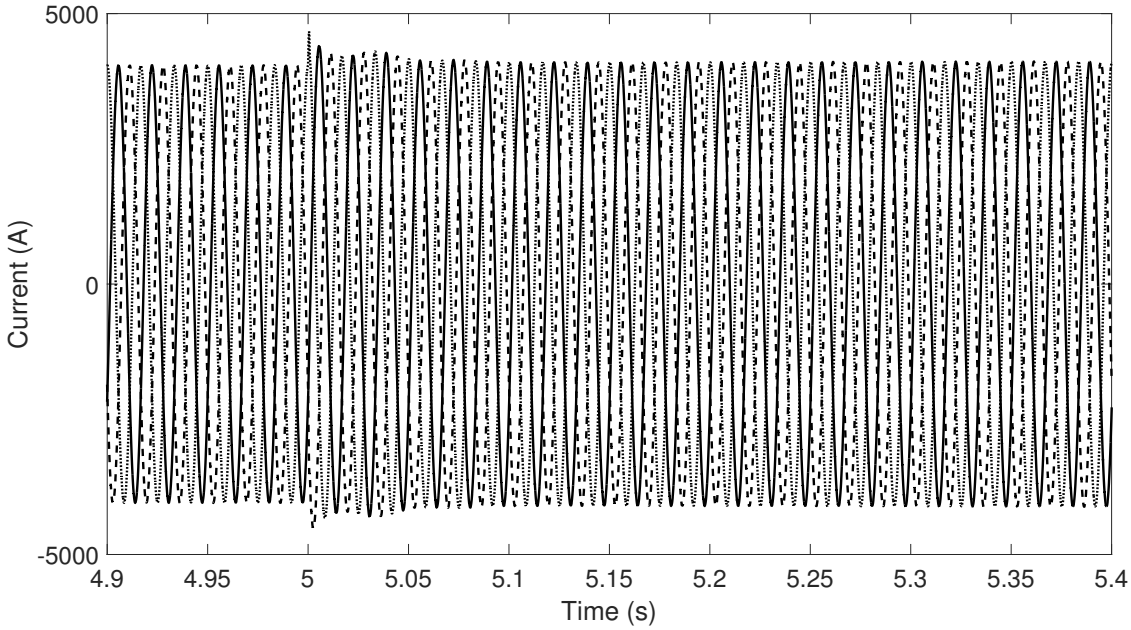

Figure 5.3: Three phase converter current output for 30MW load increase with inner current loop proportional gain I_1

While conducting positive sequence simulations, the standard time step of integration is taken as a quarter cycle of a 60 Hz sine wave. With this time step, it is impossible to accurately depict the same response as obtained in Figure 5.2. However, for the purpose of studying the behavior of the converter in a large system, it is sufficient for the response from the positive sequence software to have the same form as that obtained from the PLECS response within the bandwidth of the grid simulation. This validates the use of the 10ms time constant to represent the inner control loop. Further, for calibration and comparison, the proportional gain in PLECS was suitably chosen as will be shown in the following section.

The next section will discuss the implementation of the model in commercial positive sequence time domain simulation software. The proposed positive sequence converter model (Section 4.3.3) and the 'presently used' converter model (Section 4.3.2) were implemented with the 'user written model' feature of the large scale grid

simulation program PSLF[2] [77] for further comparison of performance. A user written model in PSLF is known as an 'epcgen' model wherein the mathematical model of the generation source is developed using PSLF's EPCL programming language.

5.1.2 Small Scale System-Validation of Results

A three machine nine bus equivalent system [89] shown in Figure 5.4 was used to validate the performance of the developed converter model along with its associated control in PSLF. This system consists of 9 buses, 3 generators and 3 static

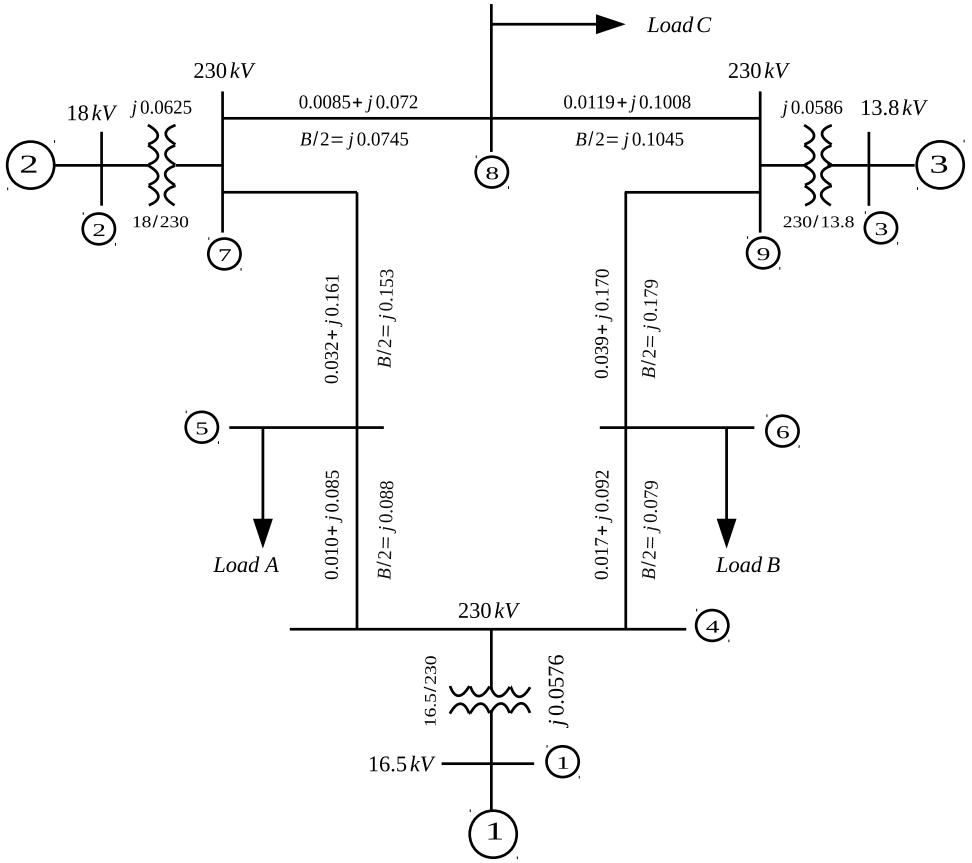

Figure 5.4: Three machine nine bus equivalent system

loads. Though the size of the system is small, it is sufficient to showcase a variety of

[2]PSLF Version 18.1_01

stability concepts. The powerflow solution of this network, power consumed by the load at buses 5, 6 and 8 and the dynamic data is given in the appendix.

From the structure of the system it can be seen that any type of fault will significantly affect all three sources. However the purpose of this system is to analyze the effect of small disturbances that occur frequently in the power system. The load in a system is continuously changing and the generation sources have to appropriately adjust their load setpoints to meet the demand. Thus, the behavior of the converter model to an increase in load was compared with its behavior in PLECS for the same disturbance. Simultaneously, the behavior of the proposed controlled voltage source converter model was also compared with the existing boundary current representation converter model.

With the loads treated as constant admittance, the load at bus 6 was increased by 10MW at t=5s. The proportional and integral gains of the PI controller in the reactive power loop were set at as 4.0 and 20.0 respectively while the integral gain K_{ip} and K_{iq} were each 10.0. The value of R_f was set to be 0.0025pu while X_f was set to be 0.06pu on the converter MVA base. In this work, the value of X_f was so chosen as to restrict the current ripple to a maximum of 5% and limit the THD in voltage to 3%. The remaining controller parameter values used for this simulation were as tabulated in Table 5.1.

In the first scenario, only the machine at bus 1 was replaced with a converter while the machines at buses 2 and 3 were retained as synchronous machines with associated governors and static exciter models. Figure 5.5 shows the active power output of the converter at bus 1.

The PLECS response has been compared with both the voltage and boundary current representation of the converter in positive sequence. The inset figure shows the response of the models at the instant of disturbance. It can be seen that both

Table 5.1: Converter-controller parameter values for three generator equivalent system

Parameter	**Value**
T_r	0.02s
R_q	0.0
R_p	0.05pu on 100 MVA
T_Q	0.01s
T_D	0.01s
T_{Gpv}	0.01s
T_{ed}	0.01s
T_{eq}	0.01s

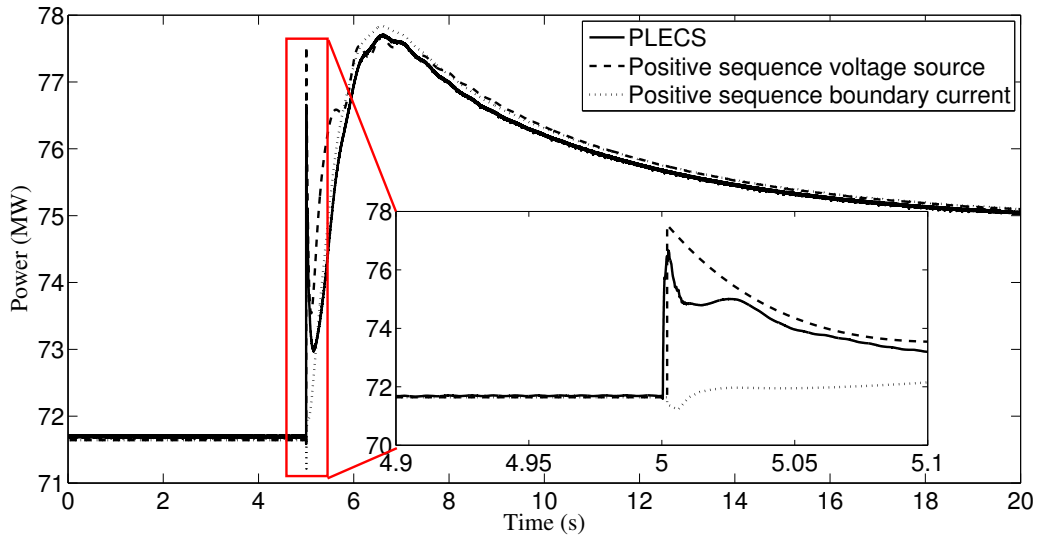

Figure 5.5: Comparison of the active power output of converter at bus 1 between PLECS and the 'epcgen' model in PSLF with synchronous machines at buses 2 and 3

the proposed controlled voltage source representation of the converter model and the PLECS response capture the near instantaneous response achievable by the converter while the boundary current representation is unable to do so. The difference in the peak value between the voltage source representation response and the PLECS

response can be attributed to the fact that the time step of simulation is much smaller in PLECS which allows for the change in the internally generated converter voltage upon recognition of the disturbance. In the positive sequence simulation however, at the instant of disturbance, the internally generated converter voltage is constant while the terminal voltage changes.

Further, the dissimilarity can be attributed to the difference between the point on wave modeling in PLECS wherein a differential R+sL model is used in PLECS for the filter inductor whereas in the positive sequence phasor model the filter is represented by its algebraic fundamental frequency resistance and reactance in the Thévenin impedance.

The instantaneous 3 phase voltage and current waves at the converter terminals are as shown in Figures 5.6 and 5.7 respectively. These figures show that there

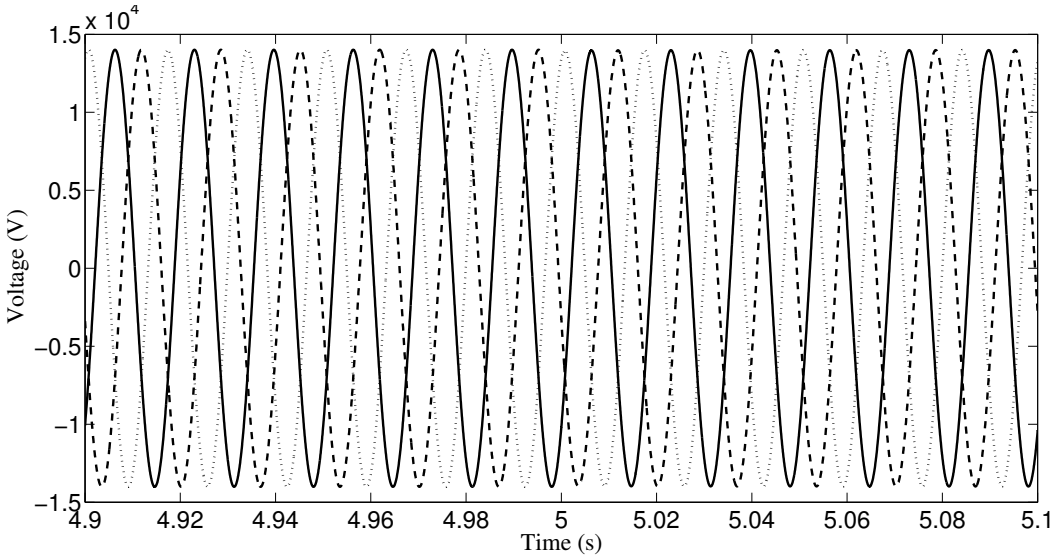

Figure 5.6: Phase voltage waveforms at the converter terminal from PLECS

is a negligible change in the terminal voltage while the converter current rises near instantaneously to meet the demand. The magnitude of the converter current output from PLECS is compared with the positive sequence simulations as shown in Figure 5.8. It can be seen that the near instantaneous response achievable by the converter

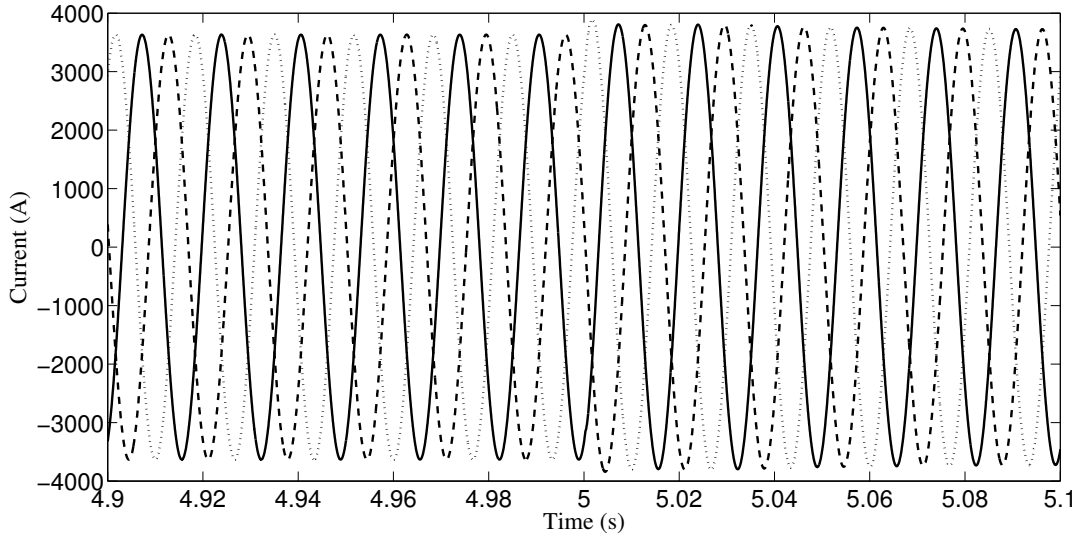

Figure 5.7: Line current waveforms at the converter terminal from PLECS

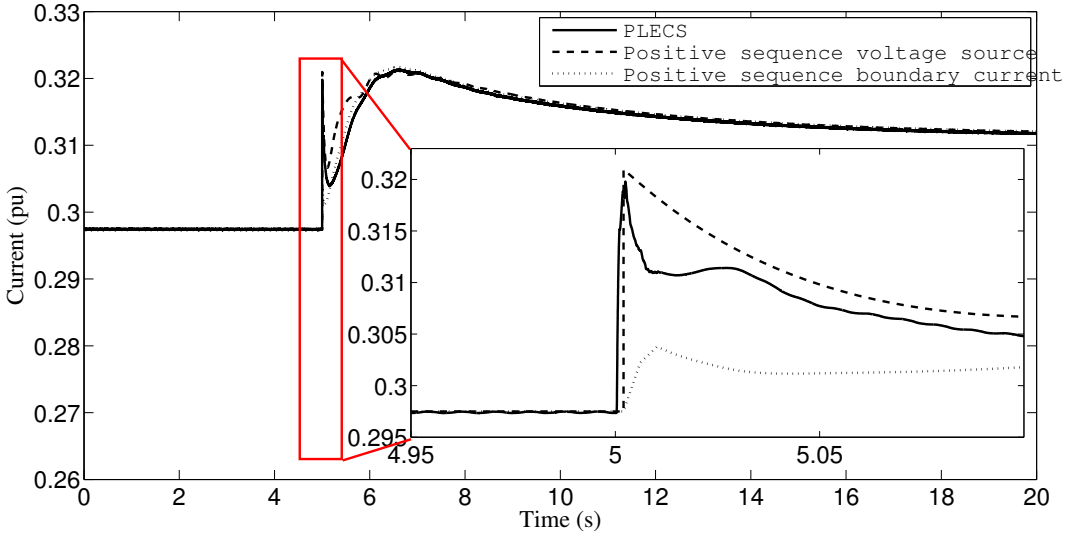

Figure 5.8: Comparison of current output of converter at bus 1 between PLECS and the 'epcgen' model in PSLF with synchronous machines at buses 2 and 3

is captured by voltage source representation of the converter.

The reactive power response is shown in Figure 5.9. It can be immediately observed from this figure that the voltage source representation response is the more acceptable positive sequence phasor approximation to the point on wave simulation. From the inset of the figure it can be seen that the reactive power trajectory of

the boundary current simulation is evidently inconsistent with the result from the PLECS simulation. The trajectory produced by the voltage source positive sequence model, while not reproducing the slight oscillatory component of the electromagnetic response, is consistent with the PLECS simulation in the direction of its initial change. This difference in the response at the instant of disturbance justifies the use of the voltage source representation as the model of choice for the simulation of large systems. Due to the absence of any connection to ground at the terminal bus of

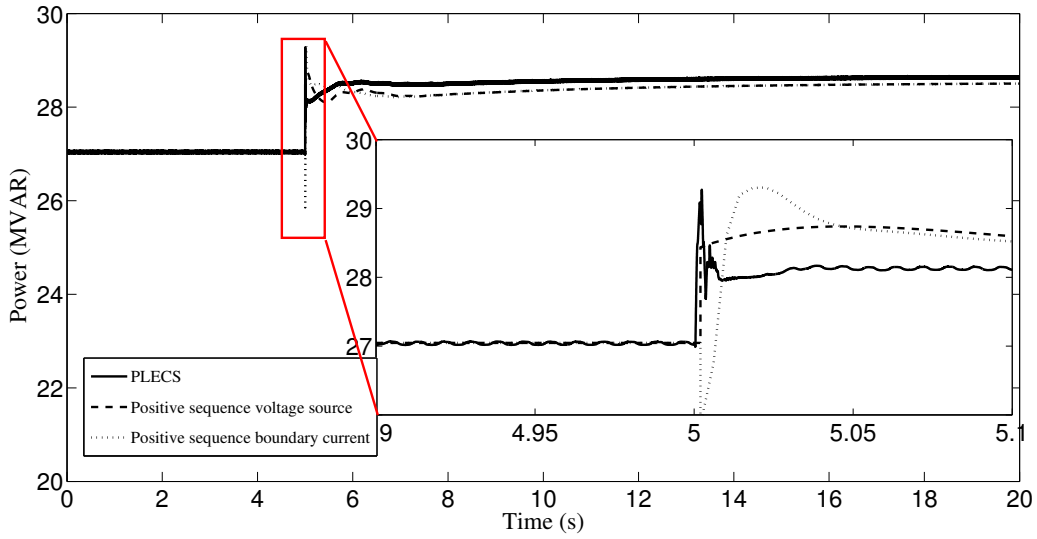

Figure 5.9: Comparison of reactive power output of converter at bus 1 between PLECS and the 'epcgen' model in PSLF with synchronous machines at buses 2 and 3

the converter in the positive sequence boundary current representation, the network solution results in an instantaneous large voltage dip at the instant of disturbance. This results in the initial change of reactive power in the direction opposite to the PLECS simulation.

The sensitivity of the terminal voltage to the value of the coupling inductor is as shown in Figure 5.10. It can be seen that as the per unit value of the coupling inductor increases, the nadir of the terminal voltage decreases. The boundary current representation of the converter is akin to a voltage source representation with a very

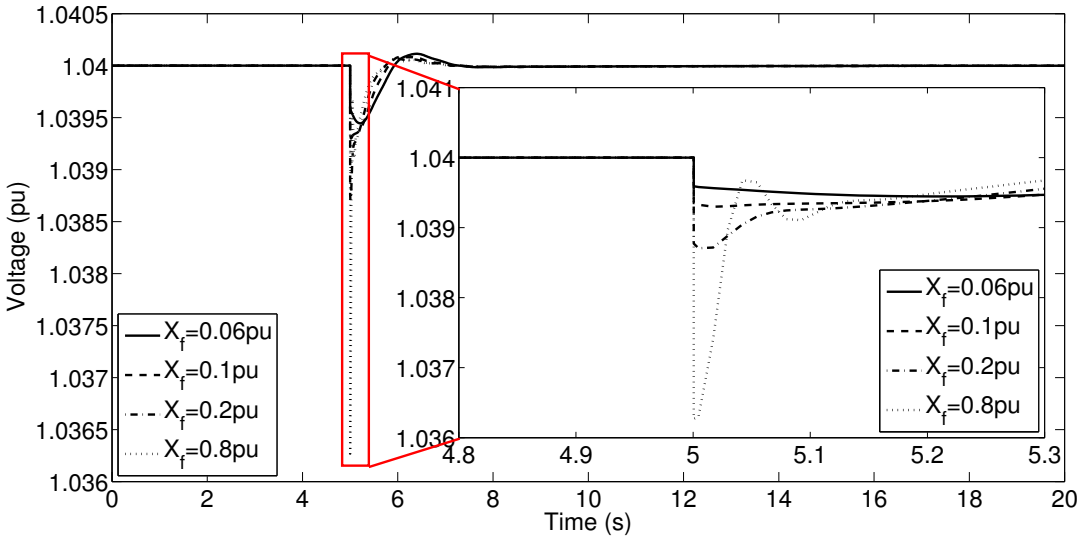

Figure 5.10: Sensitivity of the terminal voltage of converter at bus 1 for positive sequence controlled voltage source representation to different values of coupling inductor X_f

high value of coupling inductance as voltage sources are represented by their Norton equivalent in positive sequence time domain simulation software. Thus, as the value of the coupling inductor increases, the impedance to ground increases thereby causing a higher voltage drop at the terminal bus.

It could be argued that the nadir of the terminal voltage can be affected by the control mechanism used for the boundary current source representation. However to achieve the same nadir as the electromagnetic transient simulation response, an exceptionally high value of control gains would be required. This would however still not represent the near instantaneous response obtained and it could make the control structure unstable. Practically, a wide range of control techniques for converter interfaced generation exists. The intricacies of the control structure vary with the type of energy source and the manufacturer of the equipment used to harness said energy source. These control techniques can however become quite complicated and

since the focus of this research was to be on the representation of the converter, a simplified control structure was used.

The sensitivity of the magnitude of the converter terminal current to the value of the coupling inductor is as shown in Figure 5.11.

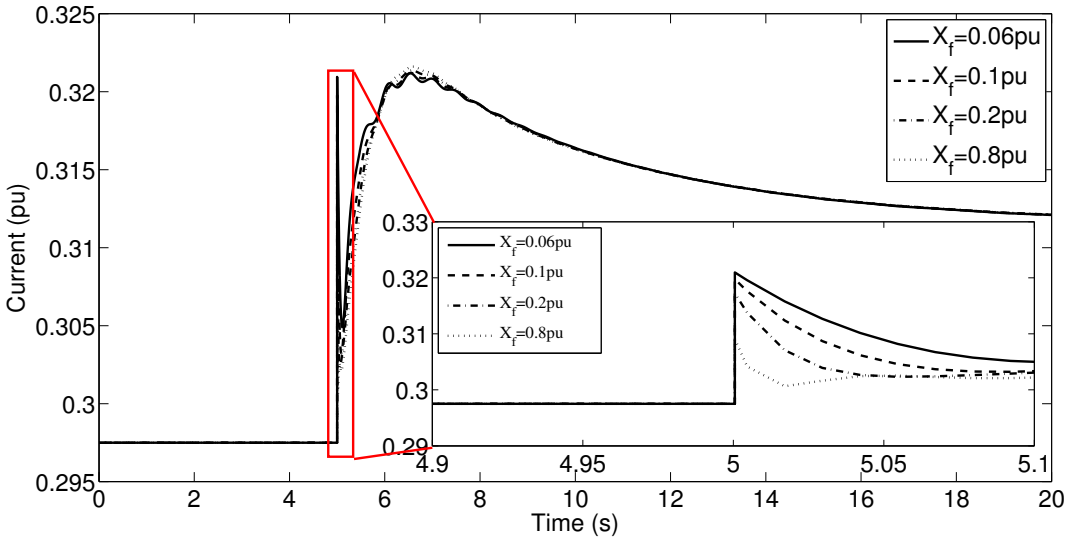

Figure 5.11: Sensitivity of the terminal current magnitude of converter at bus 1 for positive sequence controlled voltage source representation to different values of coupling inductor X_f

In order to look at an all CIG system, the machines at buses 2 and 3 were also replaced with both forms of the positive sequence converter model. The instantaneous rise in the active power of the voltage source representation can be calculated on the same lines as the distribution of impact calculation for synchronous machines.

Based on the electrical distance between the internal voltage source of the converter and the disturbance point, the instantaneous response of a converter at bus i for an impact at bus k can be obtained as:

$$P_{i\Delta}(0^+) = \left(P_{sik} / \sum_{j=1}^{n} P_{sjk} \right) P_{L\Delta}(0^+) \quad i = 1, 2, .., n \tag{5.1}$$

where

$$P_{sik} = V_i V_k \left(B_{ik} \cos \delta_{ik0} - G_{ik} \sin \delta_{ik0} \right) \tag{5.2}$$

and $P_{L\Delta}(0^+)$ is the load impact at bus k. The entire derivation of (5.1) is available in [89]. Thus, for a given converter rating, (5.1) could give an approximate idea of the maximum load change that the converter can handle and could be used as a tool by the system operator. Alternatively, it could also be used in a planning problem to decide the maximum rating of the converter to be placed at a particular bus.

For the same load increase of 10 MW at bus 6, the active power output from the converters is as shown in Figure 5.12 while Figure 5.13 shows the reactive power output. With the final steady state values being almost the same, the behavior of the models at the instant of disturbance becomes the deciding factor. It can be seen that in an all CIG system too, the boundary current representation response instantaneously moves in a direction opposite to what would be expected while the response from the voltage source representation is as expected and it conforms to (5.1).

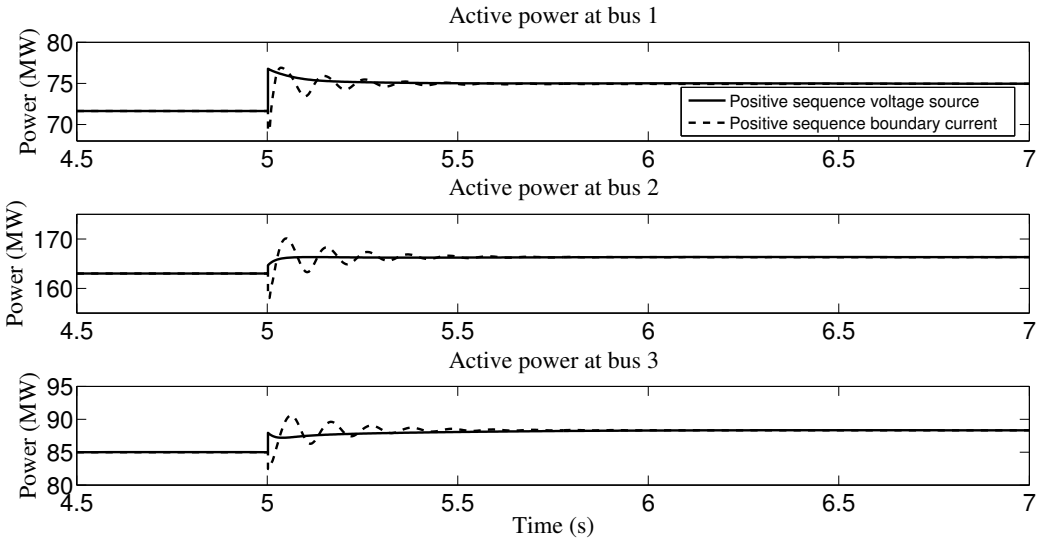

Figure 5.12: Active power output of the converters for an all CIG system with increase in active power load

To further compare the two positive sequence converter representations, the reactive power load at bus 6 was increased by 10MVAR at t=1s while the active part

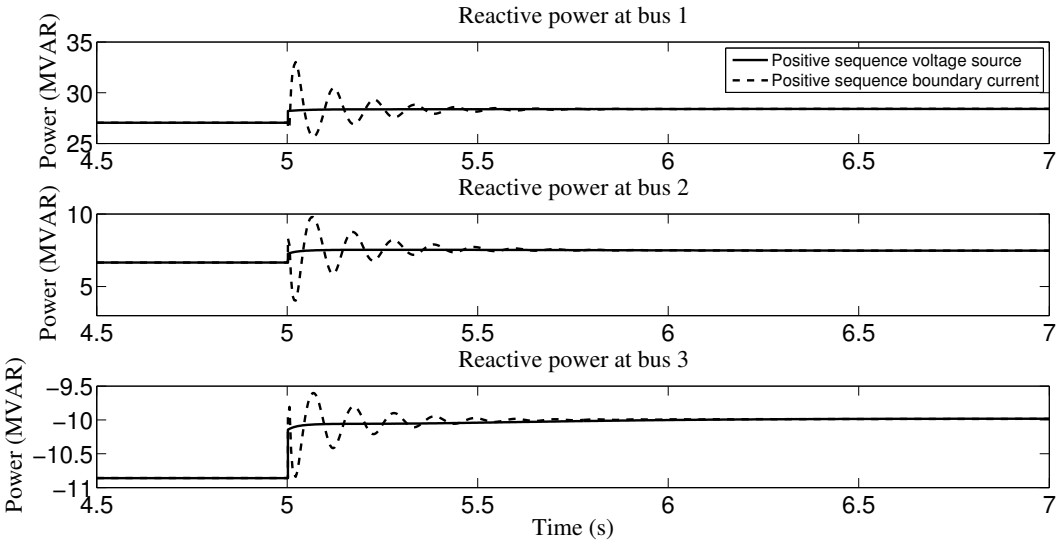

Figure 5.13: Reactive power output of the converters for an all CIG system with increase in active power load

remained unchanged, in an all CIG system. In a synchronous machine, the rotor speed gives an indication of the network frequency. However since converters are static sources, an approximate network frequency is obtained by performing a numerical differentiation of the bus voltage angle. In PSLF, the dynamic model *fmetr* performs this task. With the load change as mentioned, Figure 5.14 shows the frequency response. This response was obtained at bus 5.

The figure shows a large difference in the maximum transient frequency between the two converter representations. Ignoring the oscillatory mode, which is a result of the controller gains, a possible explanation can be as follows: for the boundary current representation of the converter, at the instant of disturbance, the bus voltage angles can experience a step change which upon differentiation can produce a large change in frequency. In the voltage source representation however, the bus voltage angles does not change drastically.

The plot of the voltage magnitude at the terminals of the converters and at the load bus is as shown in Figure 5.15. It can be seen that the drop in voltage magnitude at

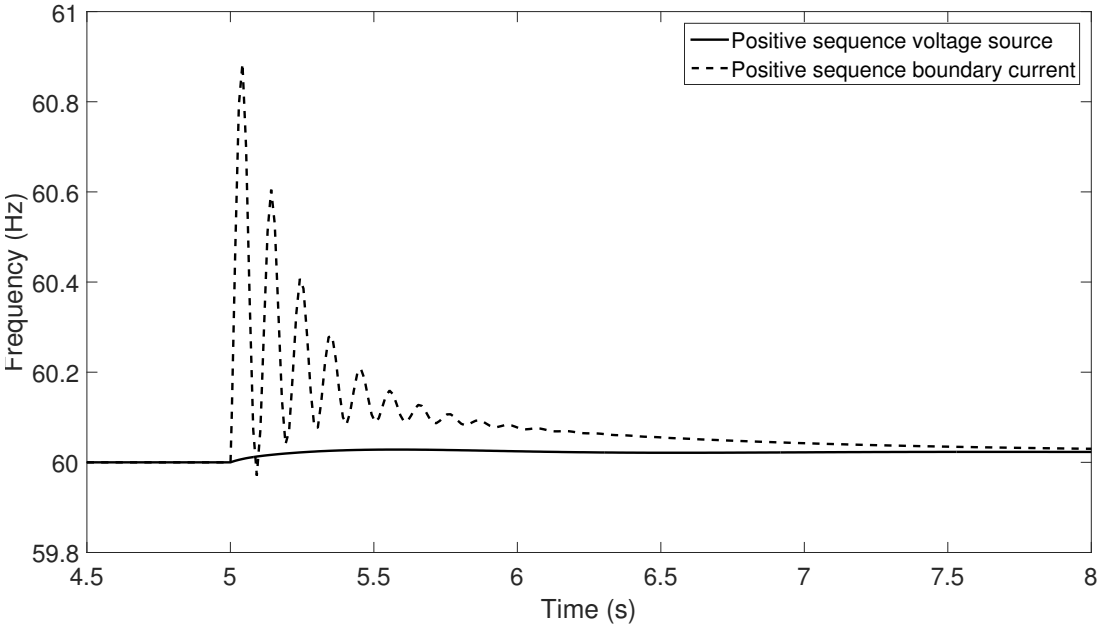

Figure 5.14: Frequency response of an all CIG system with increase in reactive power load

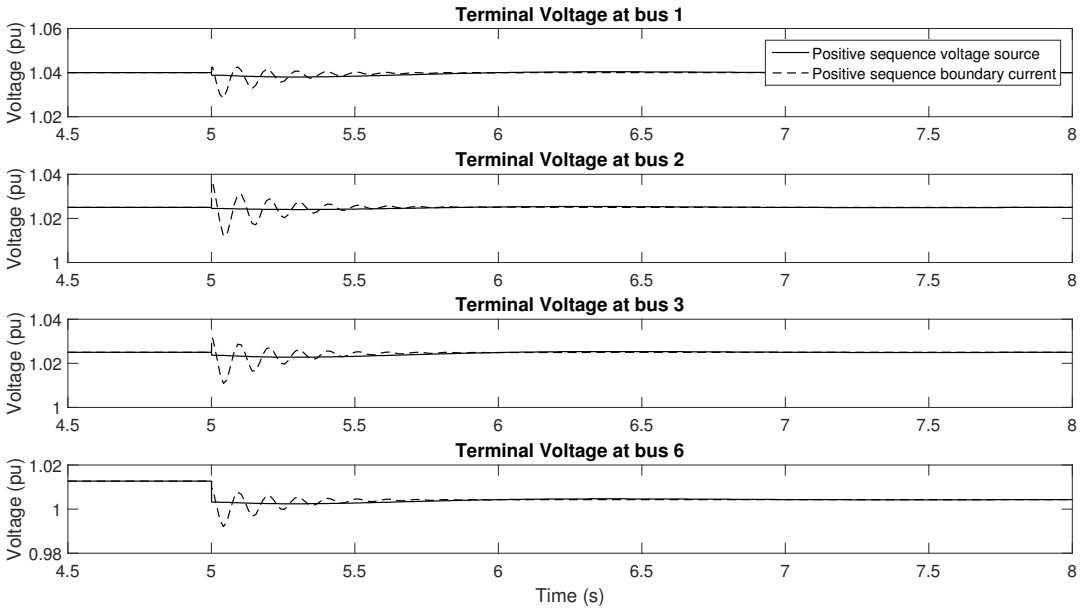

Figure 5.15: Voltage magnitudes of an all CIG system with increase in reactive power load

the terminals of the converters is negligible while the drop at the load bus is around 0.015pu. For a 10 MVAR increase in load, this is a nominal decrease in voltage

magnitude and the fast action of the converters bring the voltage back to the pre-contingency value within 1s. Due to the increase in load, the voltage at the load bus is lower, as expected. The change in active and reactive power of the converters are shown in Figures 5.16 and 5.17 respectively.

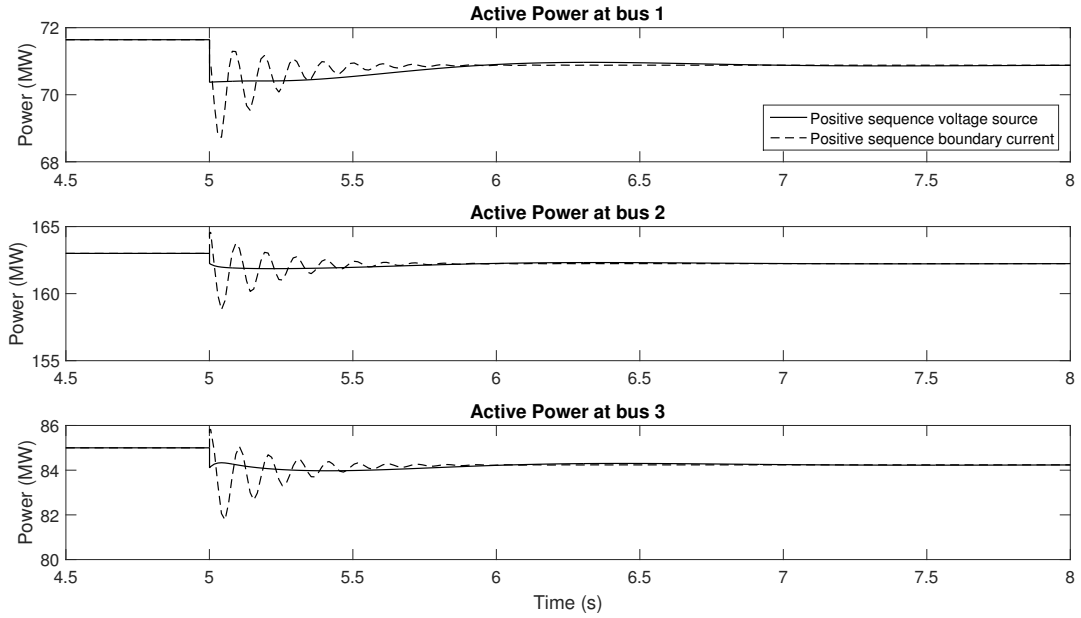

Figure 5.16: Active power output of the converters for an all CIG system with increase in reactive power load

It has thus been established that the voltage source representation of the converter is a more robust representation in positive sequence phasor simulations of large systems.

5.1.3 Large Scale System-Economy of Computation

To ensure that this model is practical in a large scale system, the WECC 2012 system has been used. At this stage, it is important to test the robustness and numerical behavior of the model when large number of converters are present in the system. This system has 18205 buses, 13670 lines and 2592 generators. The total generation is 176 GW while the total load is 169 GW. The power flow pattern of the

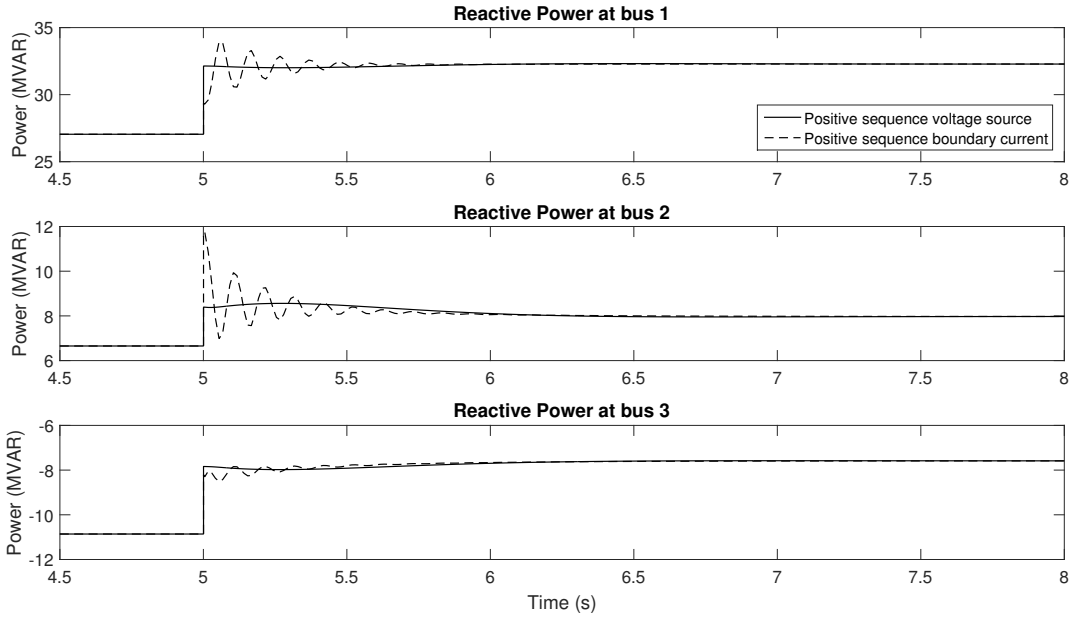

Figure 5.17: Reactive power output of the converters for an all CIG system with increase in reactive power load

system is as shown in Figure 5.18 [88]. To obtain a sizable presence of converters, all the generators in the Arizona and Southern California area (528 units) were replaced with converters represented by the proposed controlled voltage source representation (Section 4.3.3). This accounted for 24.3% of the total system generation with 25.6 GW in Arizona and 17 GW in Southern California.

For a CIG to take part in frequency regulation, a reserve margin has to be present. As per the associated material for the WECC system operating case [88], all areas of the system have a defined amount of headroom available for frequency regulation. This reserve is however not distributed equally among all generators in the area, with few generators operating without a governor. In this dissertation, the maximum active power deliverable by a CIG unit has been assumed to be equal to the MW rating of the turbine of the generator which the CIG replaces while the MVA rating of the CIG has been assumed to be the same as the MVA rating of the generator.

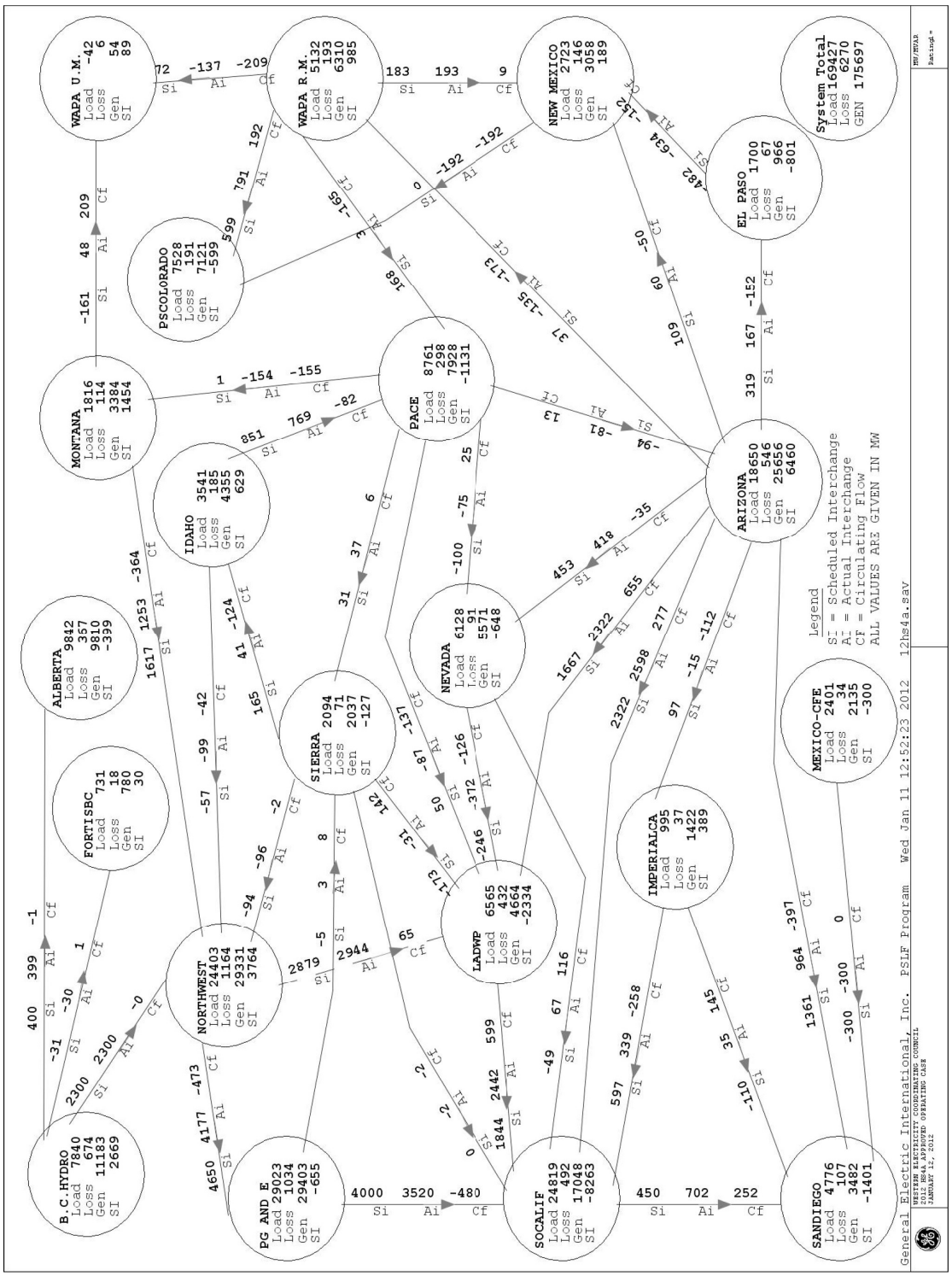

Figure 5.18: Power flow in the WECC system

If the CIG replaces a generator without an associated governor, then it has been assumed that the CIG too cannot take part in frequency regulation.

Thus, with an available headroom on almost all converter interfaced sources, the value of the droop coefficient R_p was taken to be the same as that used by the governor of the synchronous machine it replaced while R_q was taken to be 0.05pu on the converter MVA base. The reactive power PI controller gains of all converters were set to K_p=1.0 and K_i=5.0 while the integral gains K_{ip} and K_{iq} had a value of 10.0 each. The value of R_f and X_f were taken as 0.004pu and 0.05pu on the converter MVA base. The values of all other parameters were kept the same as in Table 5.1.

This initial penetration of 24.3% is used to test the numerical stability of the converter model for three system contingencies.

5.1.3.1 Generation Outage (24.3% CIG penetration)

With reference to the map shown in Figure 5.19, at t=15s, two of the three units at Plant A were tripped resulting in a generation outage of 2755 MW. Figure 5.20 shows the power output from the remaining sources in the Arizona area while the effect on the adjacent area of Southern California has been shown in Figure 5.21. The effect of this generation outage on the flow of power between these two areas is as shown in Figure 5.22. The system frequency plot is shown in Figure 5.23. The fast action of the converters can be observed from the frequency response when compared to the response with all units represented as conventional synchronous machines. The presence of voltage control on all CIG units results in a different steady state loading thus resulting in a different steady state frequency.

In terms of computation time, PSLF took 7:04 minutes to run this 60 second simulation with the first 20 seconds of simulation taking 1:52 minutes. In comparison to this, when all machines were represented in the conventional manner, the same

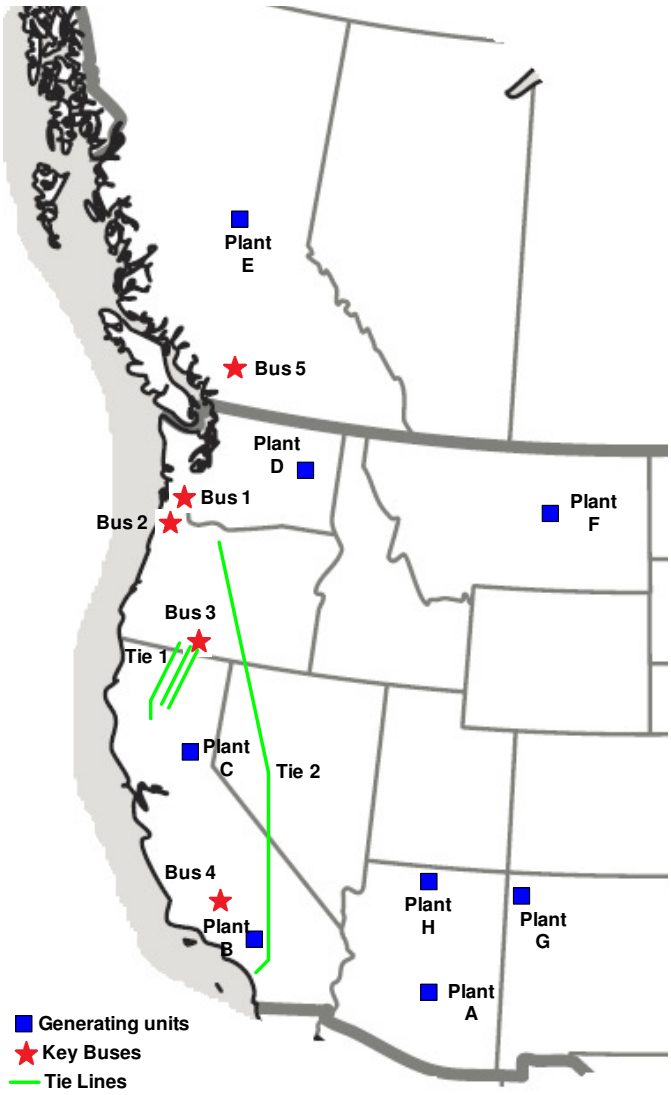

Figure 5.19: Map showing the locations of important generating units, critical buses and tie lines in the WECC system

60 second simulation took 6:41 minutes with the first 20 seconds of simulation being completed in 1:39 minutes. Both simulations were run on a machine with an i7 processor and 16.0 gb of RAM with a simulation time step of 0.0041s.

5.1.3.2 Line Fault followed by Outage (24.3% CIG penetration)

A three phase fault was applied on a tie line between Arizona and Southern California at t=15s. Subsequently, at t=15.05s, the breakers at both ends of the line

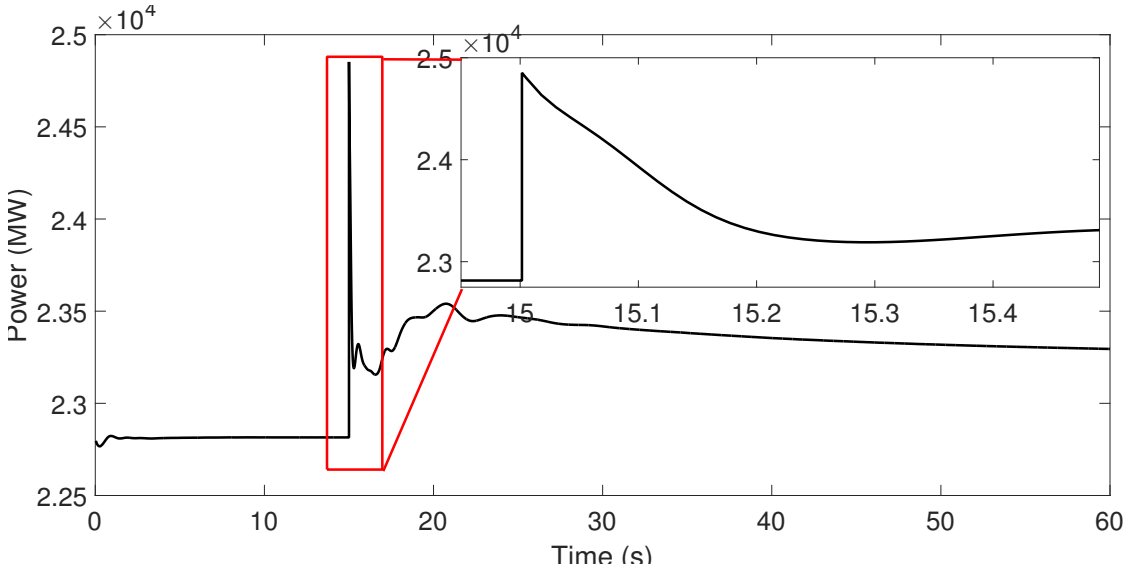

Figure 5.20: Active power generation in the Arizona area due to trip of two Plant A units

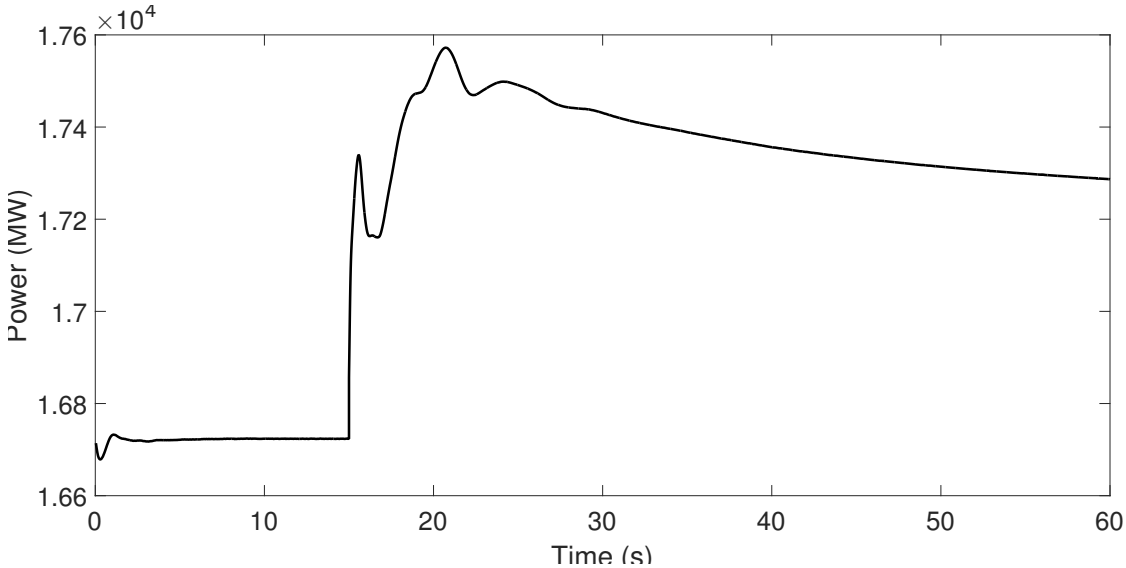

Figure 5.21: Total generation in Southern California area due to trip of two Plant A units

were opened. The initial flow on the line was 1408.6 MW and 134.4 MVAR from the Arizona side. Figures 5.24 and 5.25 show the changes in the power transfer between Southern California and the areas of Arizona, Los Angeles Department of Water and Power (LADWP) and San Diego. Negative values indicate that the power flow is into Southern California while positive values indicate power flow out of the region.

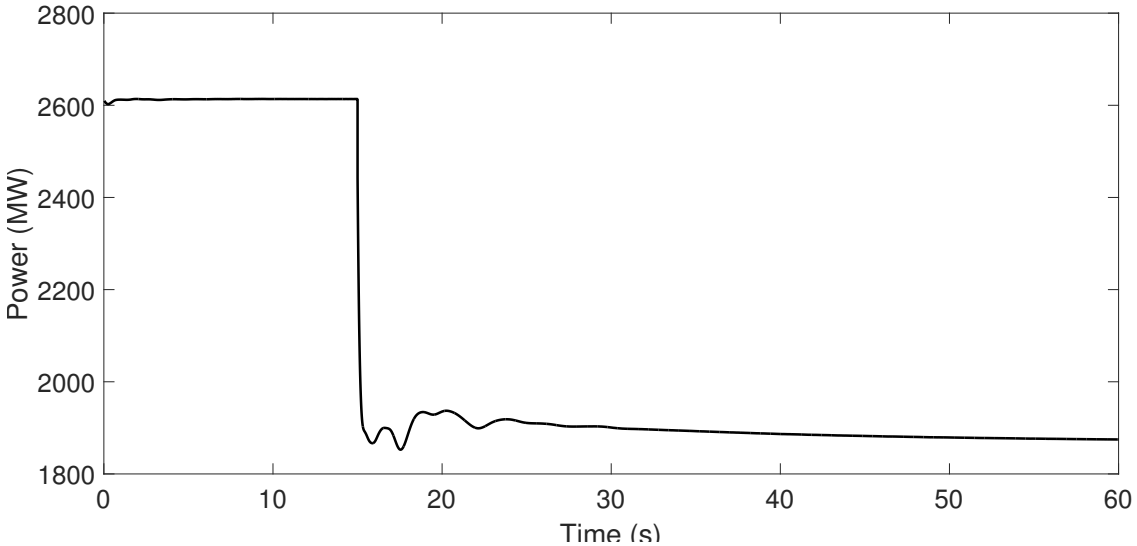

Figure 5.22: Active power flow from Arizona to Southern California due to trip of two Plant A units

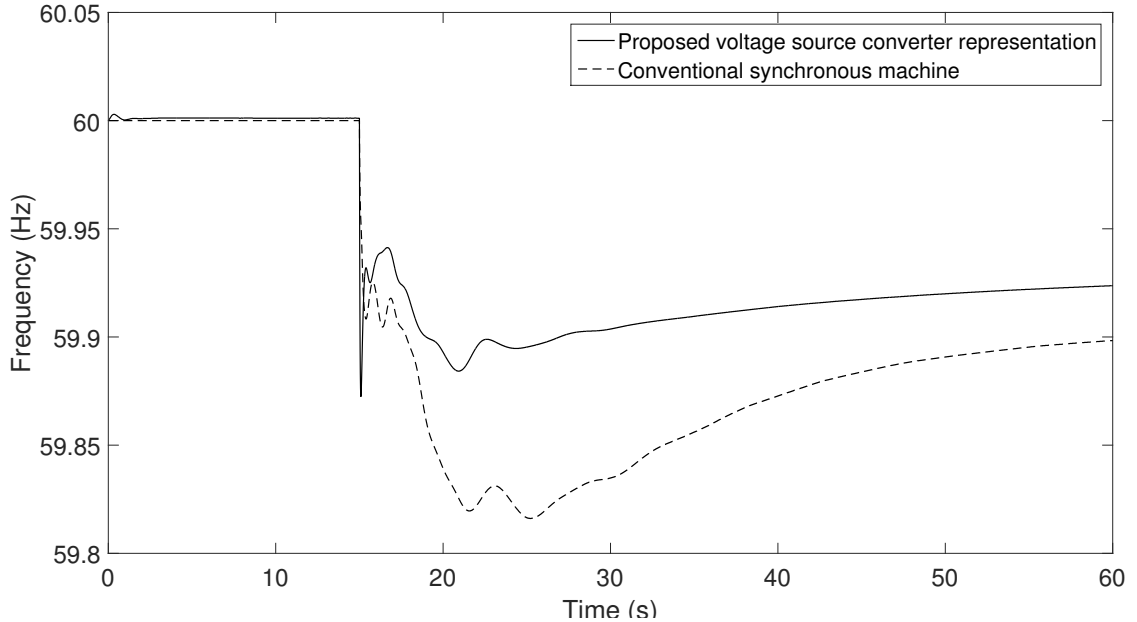

Figure 5.23: System frequency due to trip of two Plant A units

The opening of the line causes a reduction in flow between Arizona and Southern California as expected.

It should be noted that only the voltage source representation of the converter was able to function reliably following the fault. The boundary current representation of the converters resulted in frequent non convergence issues with regard to the network

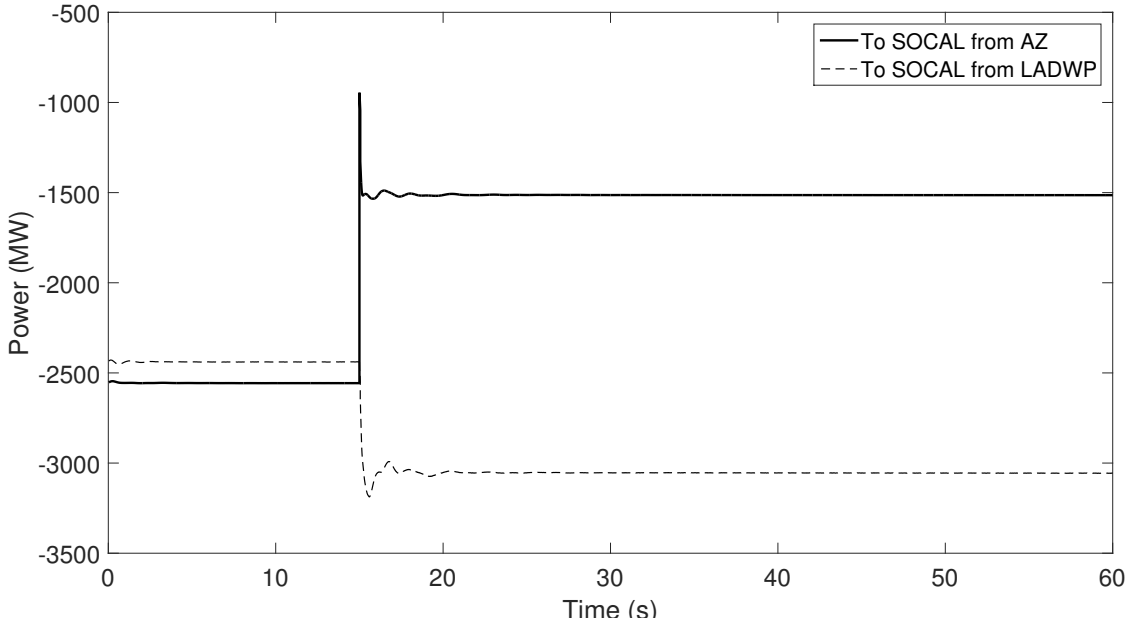

Figure 5.24: Active power flow to Southern California from Arizona and LADWP with the opening of a tie line between Arizona and Southern California following a line fault

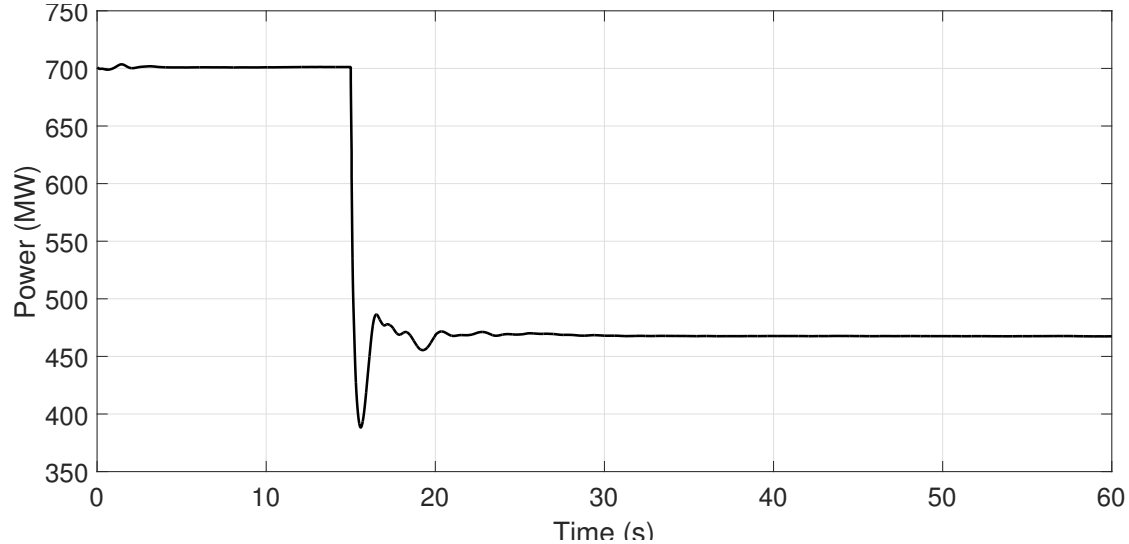

Figure 5.25: Active power flow from Southern California to San Diego with the opening of a tie line between Arizona and Southern California following a line fault

solution following the occurrence of the fault as it was unable to represent the near instantaneous response available from CIG to a disturbance.

5.1.3.3 Bus Fault (24.3% CIG penetration)

The third contingency carried out on the WECC system was applying a bus fault for 0.1s at t=15s at some distance from Plant G. The active power and terminal

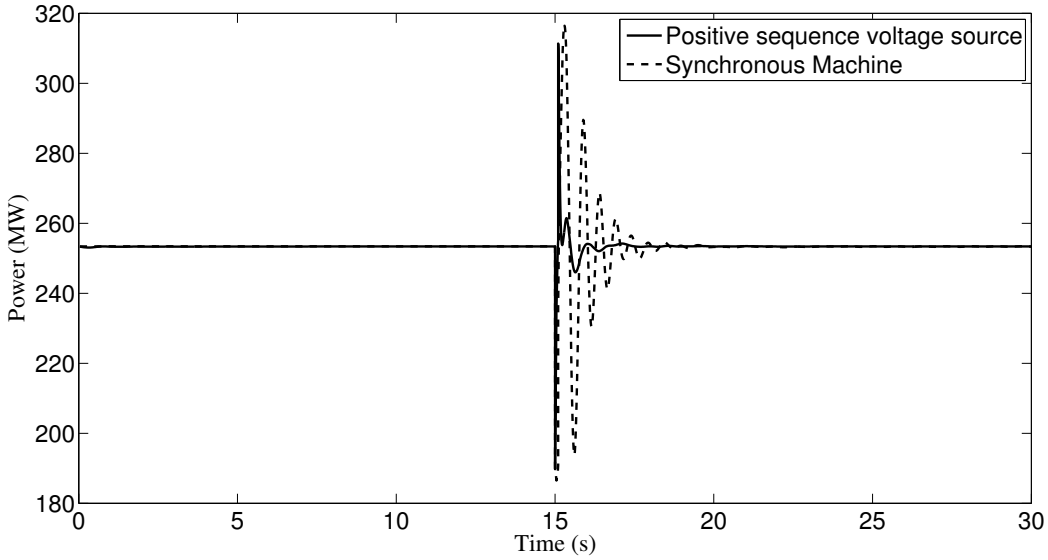

Figure 5.26: Active power output of a unit of Plant G for a bus fault

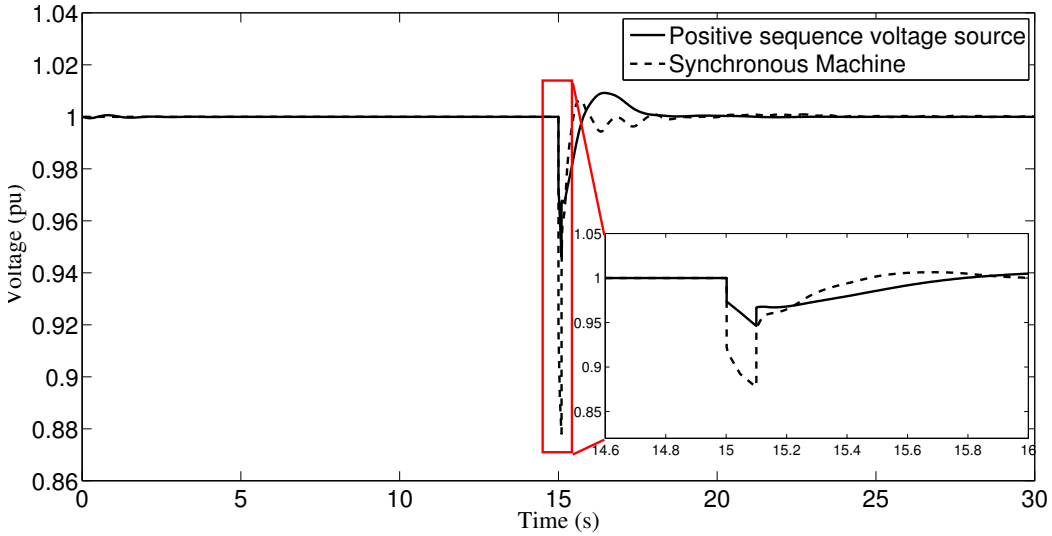

Figure 5.27: Terminal voltage of a unit of Plant G for a bus fault

voltage of one of the units is as shown in Figures 5.26 and 5.27. From the active power plot the familiar damped rotor angle oscillations can be observed from the output of

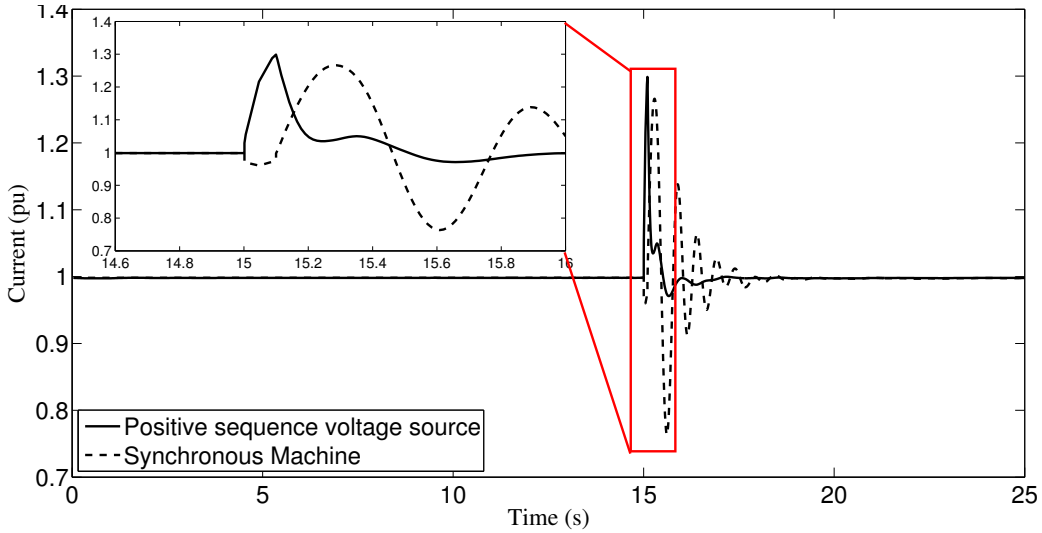

Figure 5.28: Magnitude of converter current for a voltage source representation of the converter for a bus fault

the synchronous machine. In addition, it can also be seen that a large electronic source brings about a highly damped response. However, the voltage dip in the converter response is smaller than that of the corresponding synchronous machine. The value of the coupling inductor X_f along with the absence of a sub-transient capability influences the magnitude of this dip in voltage. The magnitude of the converter current for the voltage source representation is as shown in Figure 5.28. The current is well within its short time current rating of 1.7pu. It has also been observed that for few other significant bus faults, the network solution diverges when the boundary current representation is used.

The performance of the developed controlled voltage source converter model and its associated control structure has been validated for a large system by these three contingencies. The simulation is numerically stable and not computationally intensive.

5.1.4 Note on Boundary Current Representation of Converter

In order to study the effect of large penetration of converter interfaced generation in the power system, it is very important that the computer simulation models have a reliable representation of the converter. Based on the results of the previous section, it has been shown that the boundary current representation is not a suitable representation due to the following reasons:

1. It is unable to capture the near instantaneous response that can be achieved by a CIG following a disturbance.

2. The initial change of the reactive power trajectory does not conform with the expected change.

3. The absence of the coupling inductor results in a larger voltage dip as compared to the voltage source representation and the PLECS response.

4. The network solution fails to converge for simulations of certain contingencies in large systems.

In each case mentioned above, the voltage source representation is consistent with the properties of these devices and is thus a more appropriate approximation of the electromagnetic transient model for positive sequence simulations.

The development of this controlled voltage source model and the corresponding validation results have been published in [98]. In the following section, the behavior of the WECC system will be shown for a 100% CIG penetration with the use of the proposed controlled voltage source model.

5.1.5 All CIG WECC System

In this scenario, all the conventional synchronous machine models in the dynamic file of the WECC system were replaced and represented by the voltage source representation of the converter. With this replacement, the only rotating machines in the system were the induction motor loads and 3 wound rotor induction generators. The 3 induction generators represent 3 wind turbine units. The remaining wind units (33 in number) were represented by the boundary current injection converter model as they were already present in the dynamic file as a converter interfaced source.

Thus, the entire generation set (barring the 3 wound rotor induction generator wind models) were converter interfaced. With a total system generation of 176 GW, the three wound rotor wind generators produce 0.34 GW. The value of the droop coefficient R_p for the converter was taken to be the same as the value of the droop coefficient in the governor of the synchronous machine the converter replaced. This results in a varied value of active droop across the system. The value of coefficient R_q was taken as 0.05pu on a machine MVA base while the PI controller in the reactive power loop had a proportional gain K_p of 1.0 and an integral gain K_i of 5.0. The values of K_{ip} and K_{iq} were chosen as 10.0 for all converters except the three Plant A units. The values of K_{ip} and K_{iq} for the Plant A units were set at 10.0 and 120.0 respectively. In addition, all time constants except T_{frq} had a value of 0.01s. The parameters R_f and X_f were chosen to be 0.004pu and 0.05pu on the converter MVA base respectively. The simulations have been run using PSLF [77].

In the simulations, the electrical frequency is numerically evaluated as the rate of change of the bus voltage phase angle. Further, since the converter controls the magnitude and phase angle of the bus voltage, the frequency can be varied. The $\Delta\omega$ term in Figure 4.5(b) represents the bus frequency recorded by PSLF while T_{frq},

with a value of 0.05s, represents the default time constant used by the software in measuring $\Delta\omega$.

The behavior of this all CIG system has been analyzed for the following contingencies:

5.1.5.1 Generation Outage (100% CIG penetration)

With reference to the map shown in Figure 5.19, two of the three units of Plant A in Arizona were tripped at t=15s resulting is a loss of 2755 MW. Figure 5.29 shows the phase angle at the terminals of the CIG in different areas of the system, relative to Plant D while Figure 5.30 shows the rate of change of the phase angle. The under

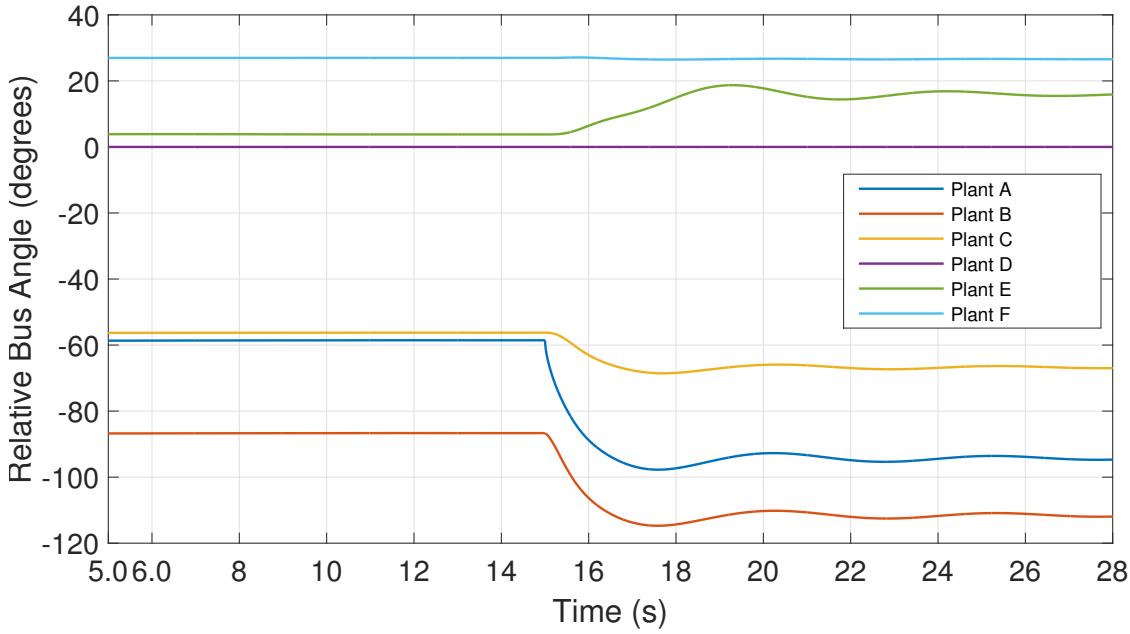

Figure 5.29: Relative change of voltage phase angle for the trip of two Plant A units

frequency trip setting of relays in WECC are set at 59.5 Hz [99]. When all machines are synchronous machines, the frequency response of the entire system is calculated

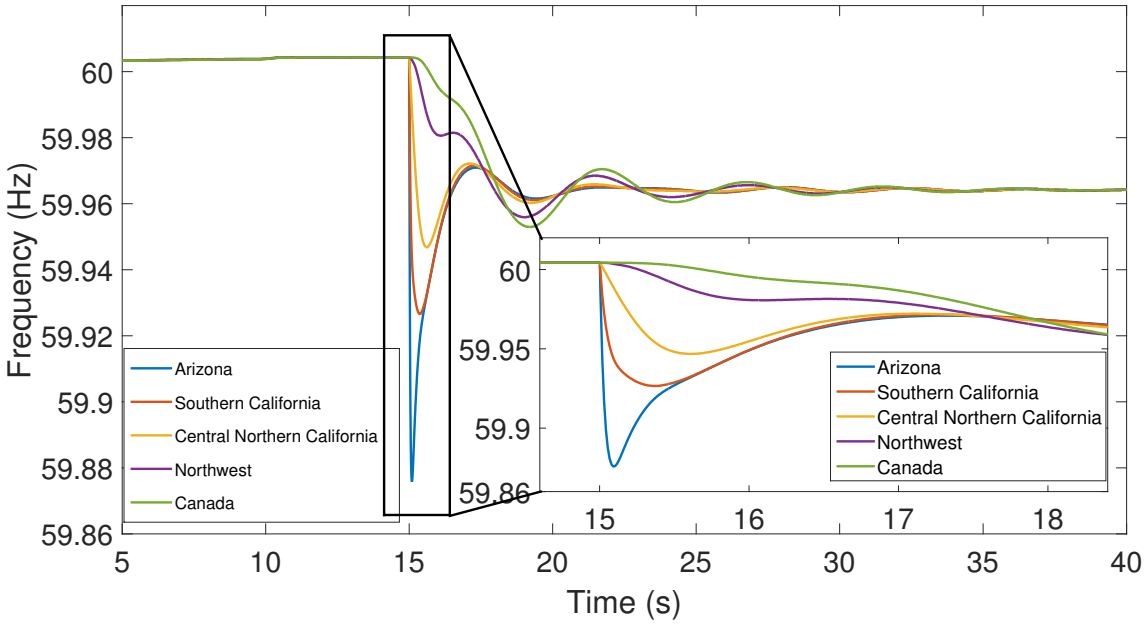

Figure 5.30: Frequency (rate of change of voltage phase angle) in five generation areas for the trip of two Plant A units (droop coefficient of each CIG unit is R_p)

as (5.3) [49],

$$f = \frac{\sum_{i=1}^{n} MVA_i \omega_i}{\sum_{i=1}^{n} MVA_i} \tag{5.3}$$

where MVA_i is the rating of the machine, ω_i is the speed of the machine and n is the number of synchronous machines. However in a system where all sources are interfaced through converters, the speed of rotation of a machine (if present) behind the converter will not give any picture of the system frequency as it is electrically decoupled from the network. Thus an approximate frequency has been obtained by performing a numerical differentiation of the bus voltage angle.

From Figure 5.29, it can be seen that the largest excursion in phase angle is in the Arizona area as expected. Due to the large electrical separation between the north and the south of the WECC system, phase angles in the two regions move away from each other in the first 0.5s after the disturbance as shown by Figure 5.29. However,

with an increased inflow of power from the north as shown by Figure 5.31, the droop control action prevents the system from separating. Figure 5.31 shows the active power flow from the Northwest area to central northern California.

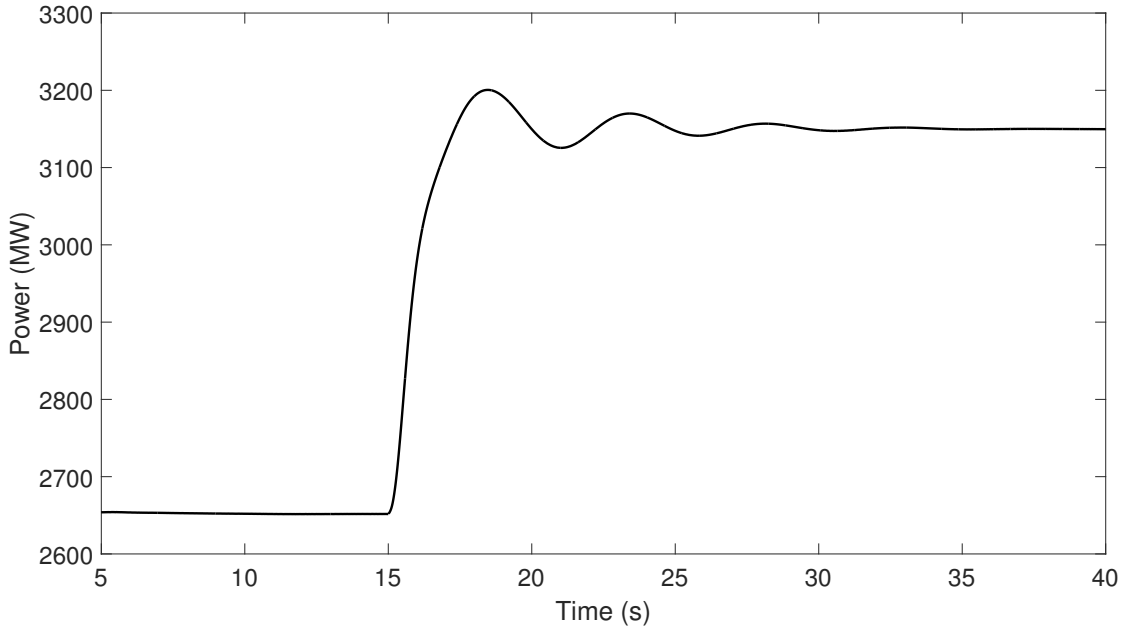

Figure 5.31: Active power flow from the Northwest area to central northern California for the trip of two Plant A units

The voltage magnitude at some key buses in the system were observed as shown in Figure 5.32. It can be seen that as the phase separation between the north and the south increases, the voltage at around the central section of the north-south interface at Bus 3 decreases. However, with the action of the droop control, the voltage stabilizes at a lower value. It can also be seen from this figure that the steady state voltages in the system settle at a lower value following the disturbance. As the majority of the load in the system is voltage dependent, the lower voltage results in a lower loading level of the system.

As all CIG units have a voltage controller with reactive power droop enabled, following the trip of the two units at Plant A(loss of 2755 MW), the final steady state total active power generation in the system is 172300 MW. In comparison, the

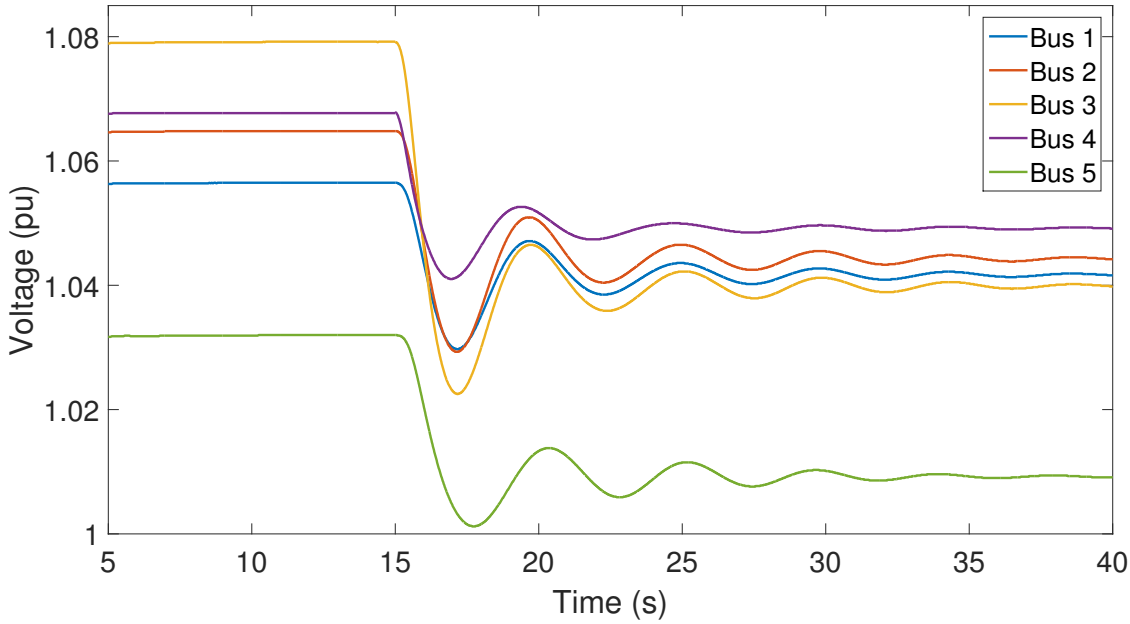

Figure 5.32: Voltage magnitude at few critical buses for the trip of two Plant A units

total pre-disturbance active power generation is 172670 MW. The plots in Figure 5.30 show the calculated frequency in the five major generating areas of the WECC system which account for 63.4% of the total system generation while Figure 5.33 shows the actual active power in four of these areas.

It can be seen that the largest excursion in frequency occurs in the Arizona area as expected. Further, even with the total inertia of the system being close to zero, the frequency nadir is well above the under frequency trip setting. The fast action of the converters and their associated control help in arresting the rate of decrease of frequency and bring about a steady state operation quickly.

As the third unit at Plant A is electrically the closest to the outage, the response of the converter representing this unit is informative. The active power, reactive power, terminal voltage and current of the converter representing the third unit at Plant A is as shown in Figure 5.34. It can be seen that the converter response is quick and none of its limits are violated. The converter current is well within its maximum

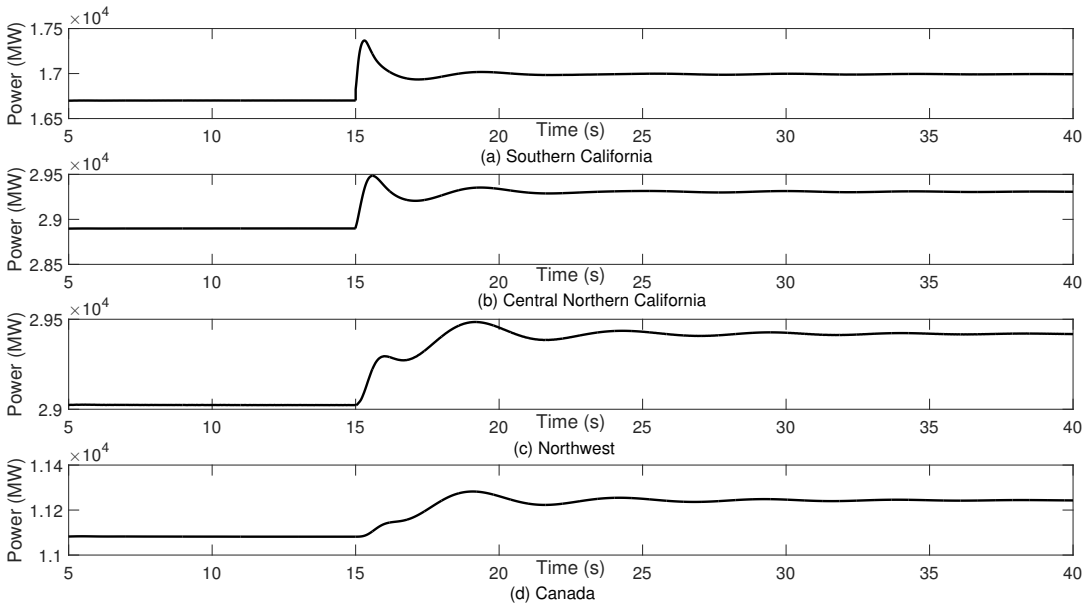

Figure 5.33: Active power output in four areas of WECC for the trip of two Plant A units

rating and the voltage control loop maintains the voltage at the pre-fault value. As the Plant A units are operated close to their maximum active power limit, there is very little reserve margin available.

To observe the effect of the active power droop coefficient, two other simulations were run. In the first case, the values of the droop coefficient were doubled while in the second they were halved. Thus, if we denote R_p as the droop coefficient of each CIG unit for the plot in Figure 5.30, the values of the droop coefficients were made $2R_p$ and $R_p/2$ in order to observe the effect of droop. Individual CIG units may still have different values of droop as the coefficient R_p takes on different values for each unit as mentioned at the start of this section. The rate of change of the voltage phase angle plots of Figures. 5.35 and 5.36 show the performance for the trip of two Plant A units when the values of the droop coefficient were $2R_p$ and $R_p/2$ respectively.

It can be observed that a change in droop coefficient changes the response time to a disturbance in addition to changing the final steady state value of the phase angle.

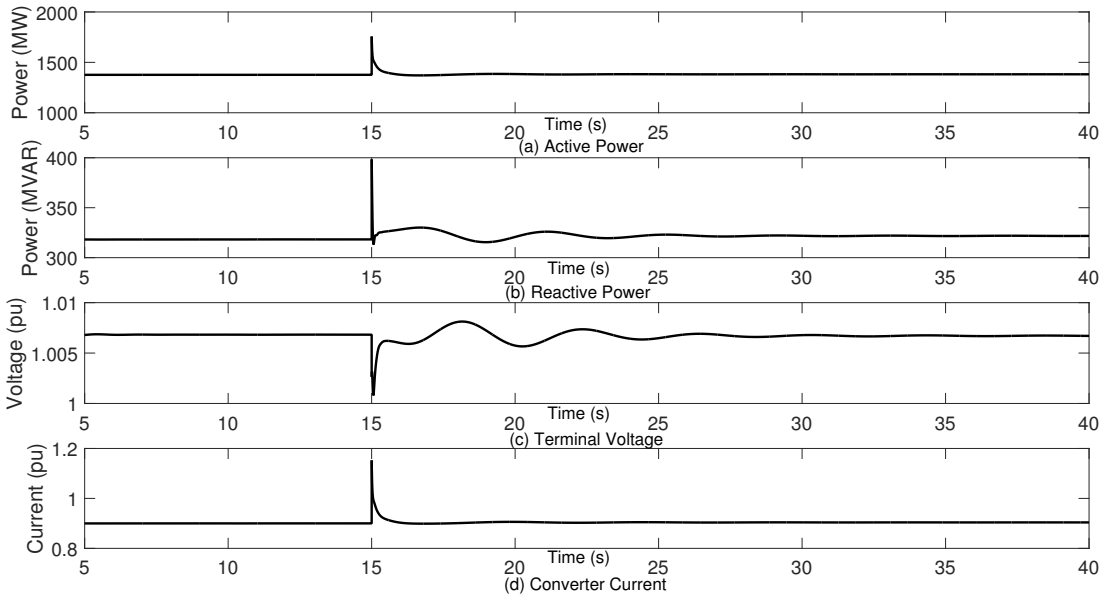

Figure 5.34: Behavior of the third Plant A unit for the trip of two other Plant A units

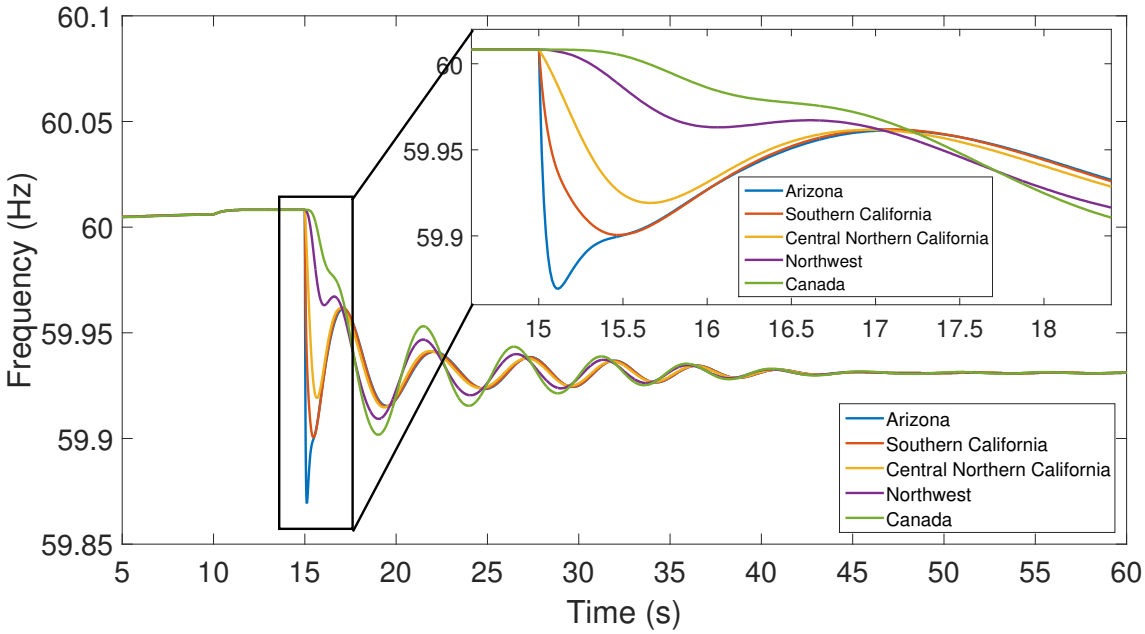

Figure 5.35: Frequency (rate of change of voltage phase angle) in five generation areas for the trip of two Plant A units (droop coefficient of each CIG unit is $2R_p$)

A large value droop has a larger response time while a smaller value of droop has a shorter response time.

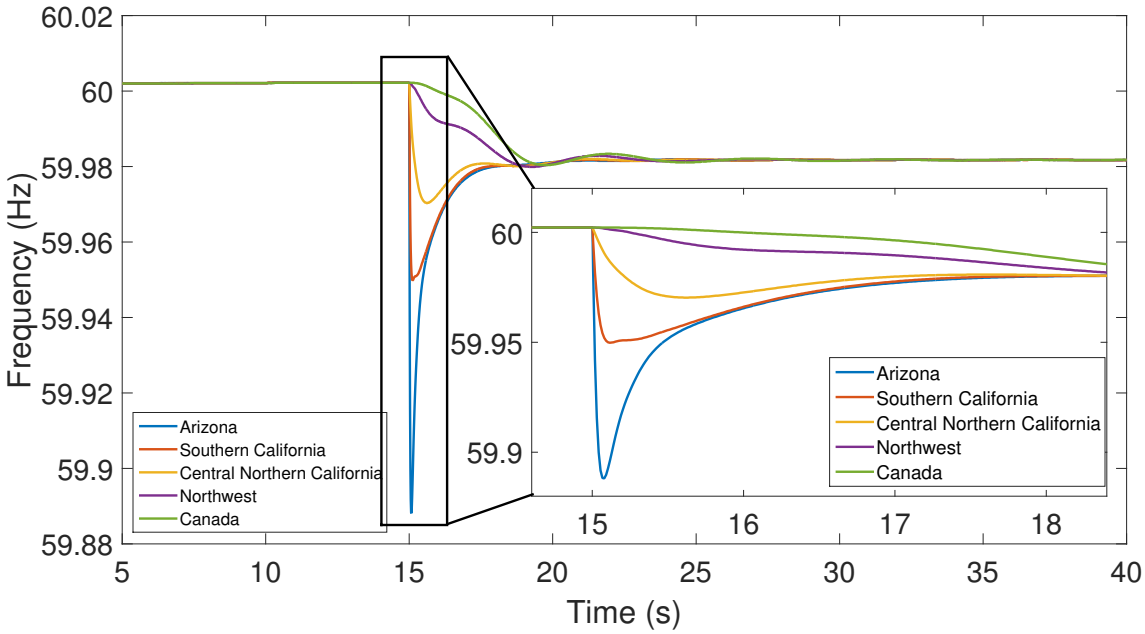

Figure 5.36: Frequency (rate of change of voltage phase angle) in five generation areas for the trip of two Plant A units (droop coefficient of each CIG unit is $R_p/2$)

In addition, this comparison brings to light the fact that although CIG units are fast acting, a finite time is required to bring about a steady state operation as rotating elements are still present in the system in the form of induction motors. The inertia of these motors play a role in the transient behavior of the system. There is also a difference in settling time with different values of droop coefficients and this can be seen from all frequency plots.

To further compare the performance of the system with varying droop coefficients, Figure 5.37 shows the system mean frequency with the droop coefficients of R_p, $2R_p$ and $R_p/2$ while Figure 5.38 shows the voltage magnitude at Bus 3. A larger value of droop ($2R_p$) corresponds to a lower value of gain in the forward path of the frequency control loop (Figure 4.5(b)) while conversely, a small value of droop ($R_p/2$) would correspond to a higher value of gain. However, from the figures of system mean frequency and bus voltage magnitude, it is seen that with the lower value of gain, the response is more oscillatory in nature. The lower value of gain leads to a longer

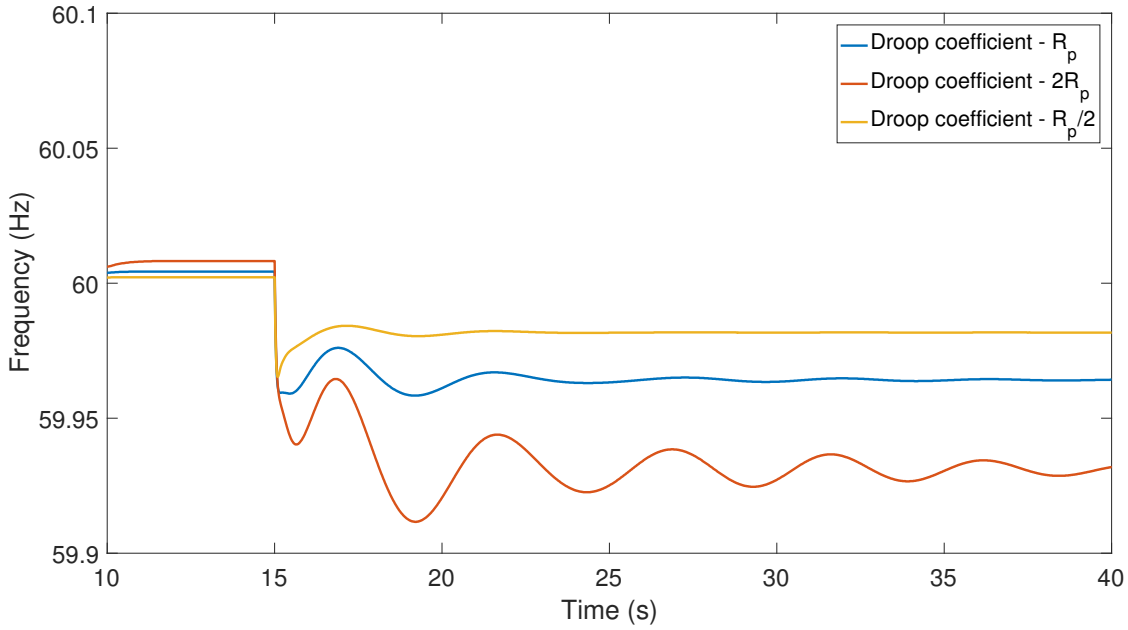

Figure 5.37: Comparison of system mean frequency for the trip of two Plant A units

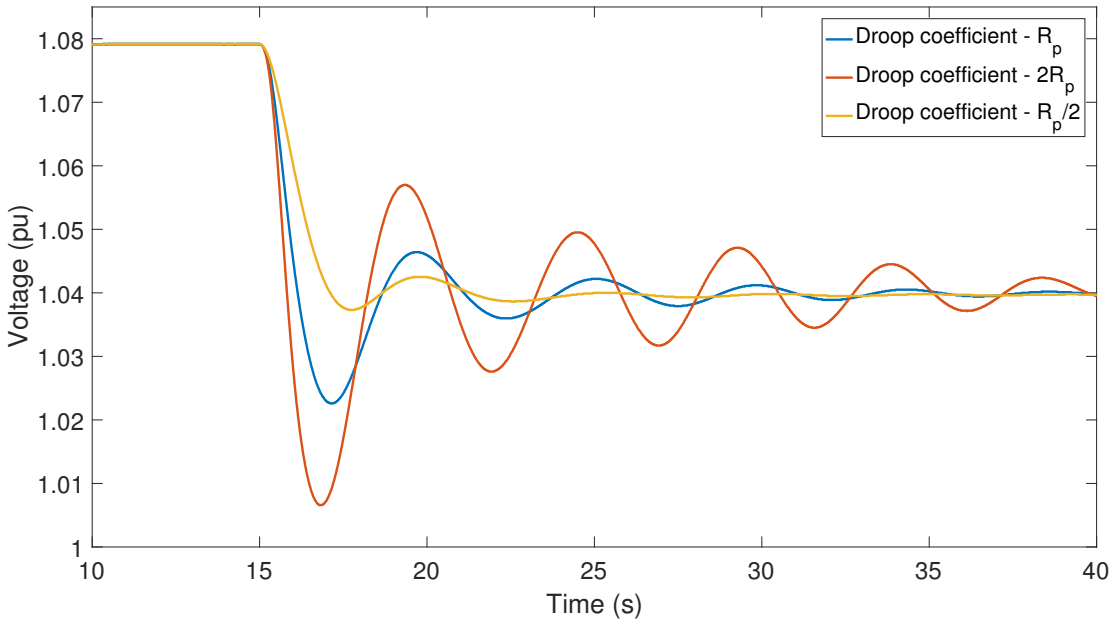

Figure 5.38: Comparison of voltage magnitude at Bus 3 for the trip of two Plant A units

time required to arrest the frequency decline resulting in a larger decrease in voltage magnitude at key system buses. Thus, due to a significant percentage of voltage dependent load in the system (both static and induction motor load), the system

response is more oscillatory in nature. Although, a comprehensive controller tuning exercise could increase the overall damping in the system with this large value of droop, but the topic is beyond the scope of this dissertation.

In all subsequent scenarios, the value of the droop coefficient has been assumed to be R_p.

In terms of computation time, with a droop coefficient R_p, PSLF took 8:10 minutes to run the 40 second simulation of this generation outage scenario with the first 20 seconds of simulation taking 3:52 minutes. The simulation was run on a machine with an i7 processor and 16.0 gb of RAM with a simulation time step of 0.0041s. It can be concluded that an all CIG system is capable of providing a stable frequency response through the fast action of the controllers and the simulation is numerically stable too.

5.1.5.2 dc Voltage Dip and Subsequent Recovery (100% CIG penetration)

In all of the above scenarios, the dc voltage has been assumed to be constant, implying a battery as a source of power. However, even for units of a size as low as 100 MVA, the assumption of a battery as a constant source of power is not realistic. A practical source must be present. Such sources would require a capacitor on the dc bus to maintain a controlled voltage input to the inverter. However, a disturbance in the network would cause fluctuations in the current levels causing the dc voltage across the capacitor to vary. The magnitude of the ac voltage that the converter is able to produce falls generally in proportion to the voltage on its dc bus. It is hence important to study the effect of this variable dc voltage on the system behavior.

At t=15s, two Plant A units are tripped resulting in a generation outage of 2755MW. With a capacitor on the dc link, the immediate response to this contingency would be an increase in the converter current and a decrease in capacitor voltage.

Gradually, as the active power control of the source behind the capacitor reacts, the capacitor voltage will be restored. To simulate this situation, the dc voltage on all CIG units participating in frequency regulation in the Arizona and Southern California areas was reduced by 10%, 20ms after the generation outage. Gradually, over the subsequent 10s, the dc voltage was restored. The relative phase angle plot for this scenario is as shown in Figure 5.39 while Figure 5.40 shows the voltage magnitude at some key buses.

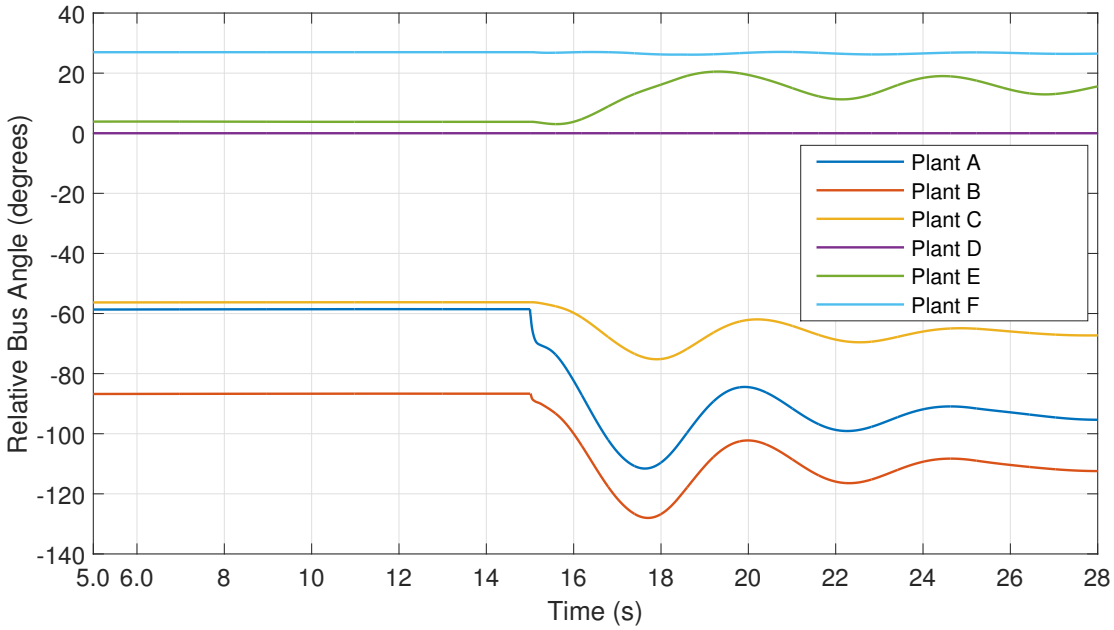

Figure 5.39: Relative change of voltage phase angle for the trip of two Plant A units followed by the reduction in dc voltage by 10% and its subsequent recovery

It can be seen from Figure 5.39 that the drop in dc voltage does not increase the phase separation between the north and south of the system. However from Figure 5.40 it can be seen that the voltage at Bus 3 decreases by a larger amount when compared to the decrease in the voltage shown in Figure 5.32. This reduction in terminal voltage in the south, in addition to the loss of generation, increases the power flow on the interface between the north and south thereby reducing the voltage by a larger amount at Bus 3. In addition, with most of the load being voltage dependent,

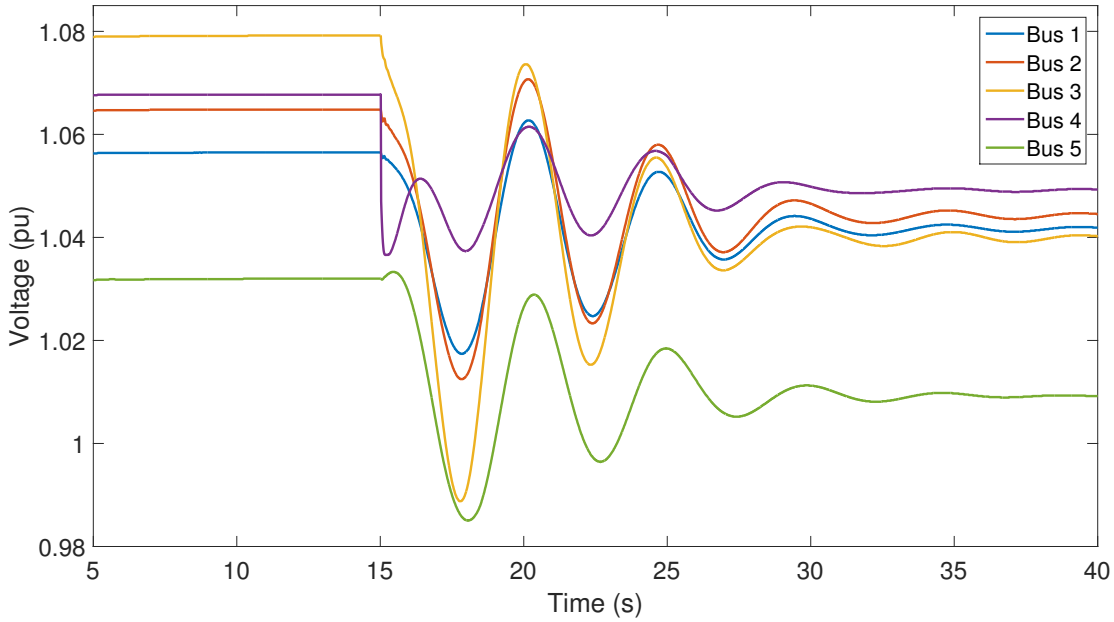

Figure 5.40: Voltage magnitude at few critical buses for the trip of two Plant A units followed by the reduction in dc voltage by 10% and its subsequent recovery

as the dc voltage is ramped up to its pre disturbance value, the load around the system continuously changes resulting in a more pronounced oscillatory behavior.

Under these conditions, Figure 5.41 shows the active power, reactive power, terminal voltage and current of the third Plant A unit.

The results of this scenario are a set of conservative results as the dc voltage has been assumed to drop only on those CIG units in the Arizona and Southern California areas that take part in frequency regulation. In reality, the voltage would drop at all units while the recovery of the voltage is possible only on units that take part in frequency regulation.

In practice, the size of the capacitor at the dc bus would have to be designed so as to restrict the drop in voltage. Additionally, in order to maintain the system reliability, a coordinated, well designed wide area control action may be required.

In the following two contingencies, the dc voltage is assumed to remain constant throughout the entire scenario.

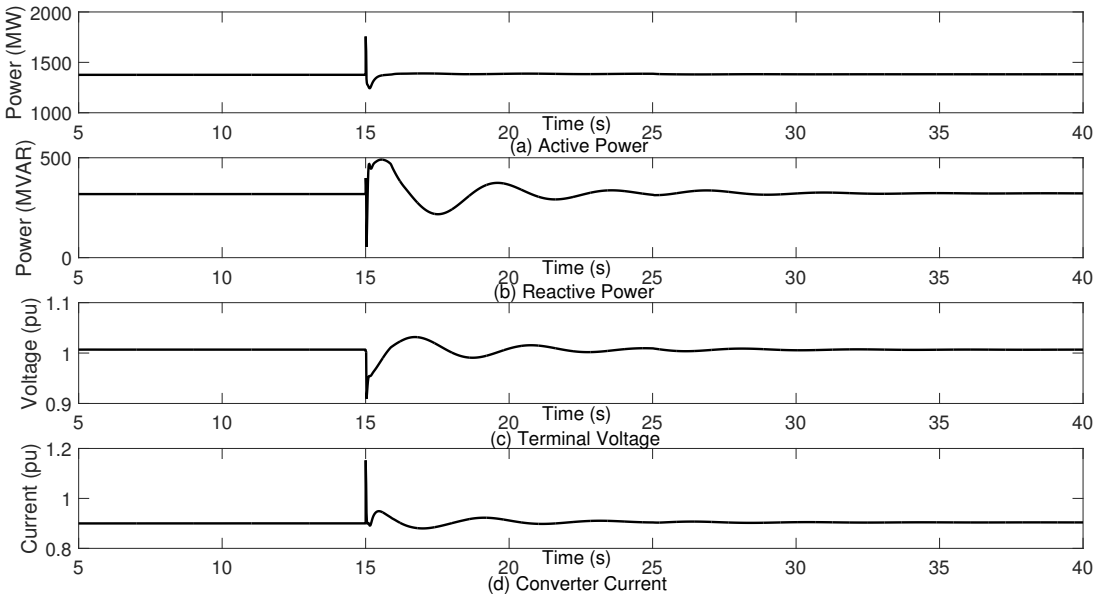

Figure 5.41: Behavior of the third Plant A unit for the trip of two other Plant A units followed by the reduction in dc voltage by 10% and its subsequent recovery

5.1.5.3 Line Fault followed by Outage (100% CIG penetration)

A fault on a transmission line followed by the tripping of the line can be a significant contingency on the system especially if the line is a tie line between two areas and has a considerable amount of power transfer across it. At t=15s a three phase fault was applied for 0.05s at the midpoint of a line between the Arizona and Southern California areas. The line was subsequently tripped at both ends. Modern protection devices are able to clear the fault and isolate the corresponding elements within 4 cycles [100]. The initial flow of power on the line was 1408.6 MW and 134.4 MVAR from the Arizona side. Figures 5.42, 5.43 and 5.44 show the active power generation in the Arizona area, Southern California area and the active power flow between these two areas respectively. The figures show that the response is satisfactory. Again, as the Plant A CIG units are located near the fault, their behavior is informative and will serve as a pointer to the behavior of other CIG units in the system. The active

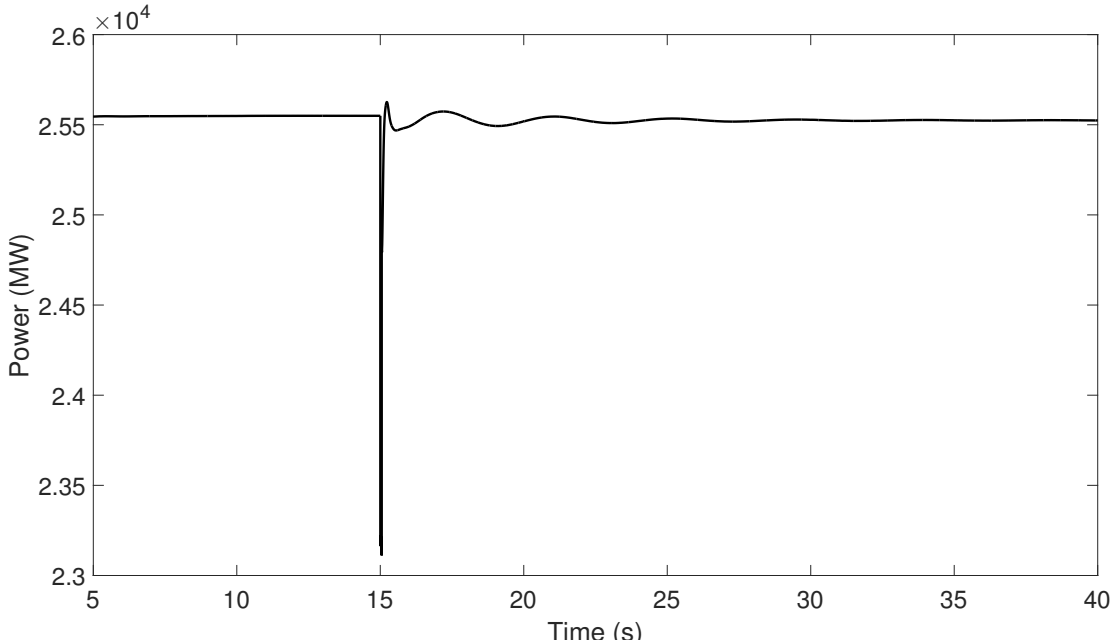

Figure 5.42: Arizona active power generation with the opening of a tie line between Arizona and Southern California following a line fault

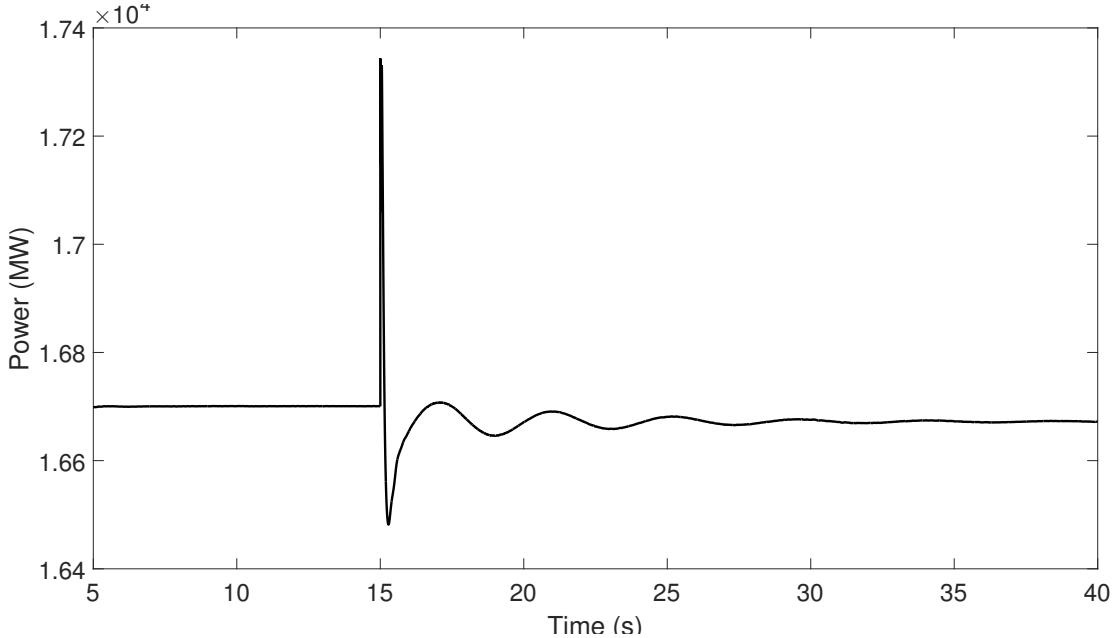

Figure 5.43: Southern California active power generation with the opening of a tie line between Arizona and Southern California following a line fault

power output of the one of the Plant A units is as shown in Figure 5.45 while the terminal voltage and converter current is as in Figures 5.46 and 5.47 respectively.

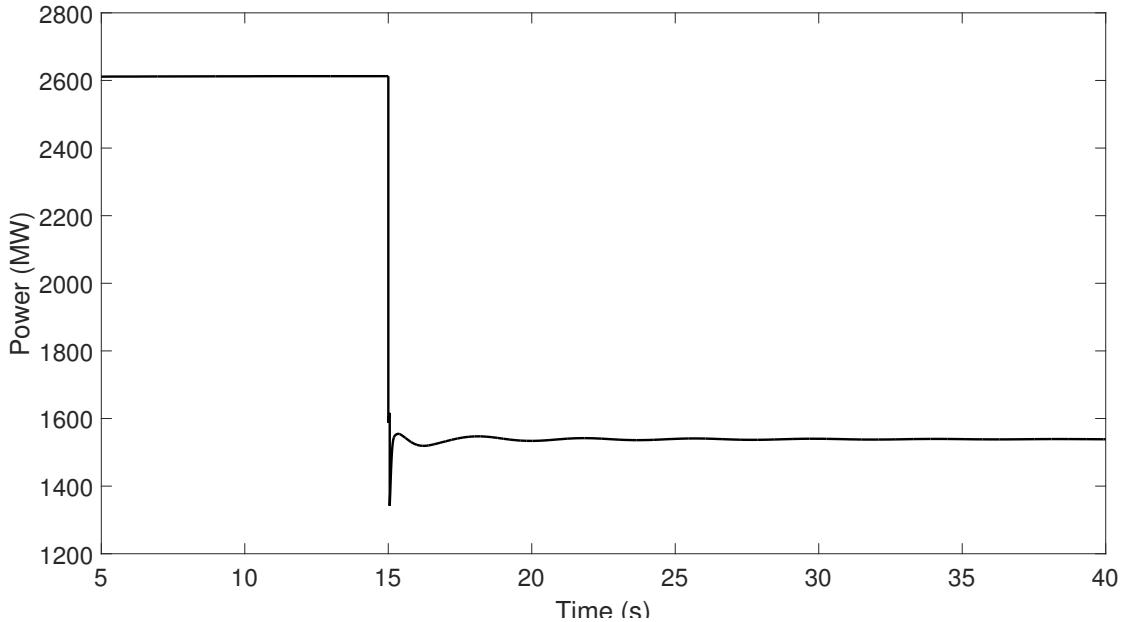

Figure 5.44: Active power flow from Arizona to Southern California with the opening of a tie line between Arizona and Southern California following a line fault

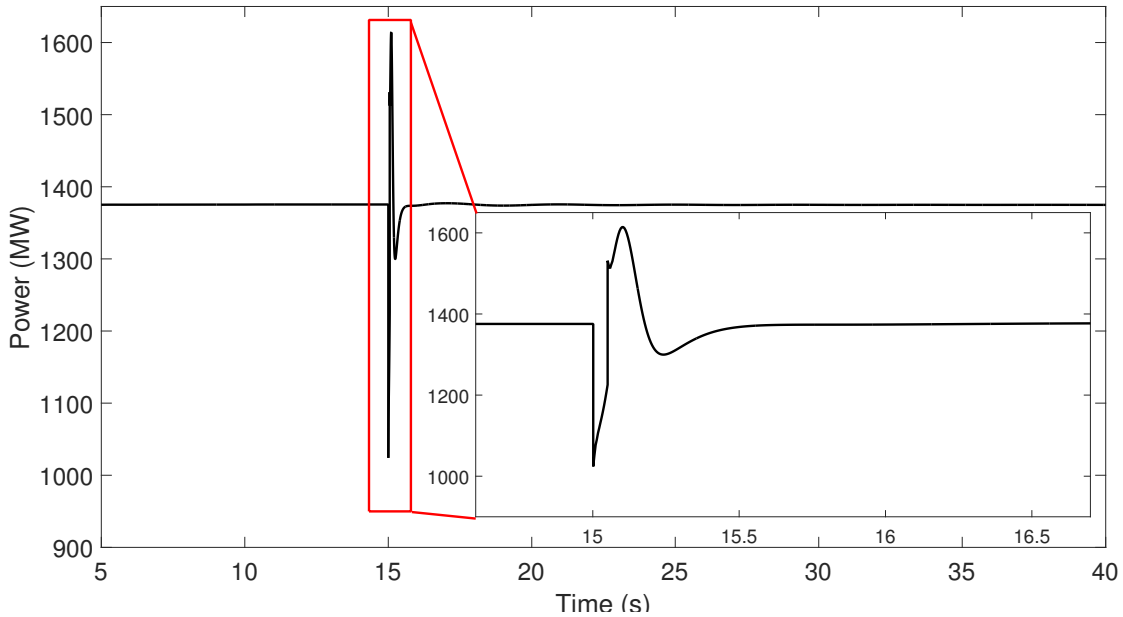

Figure 5.45: Active power output of one Plant A unit for the opening of a tie line between Arizona and Southern California following a line fault

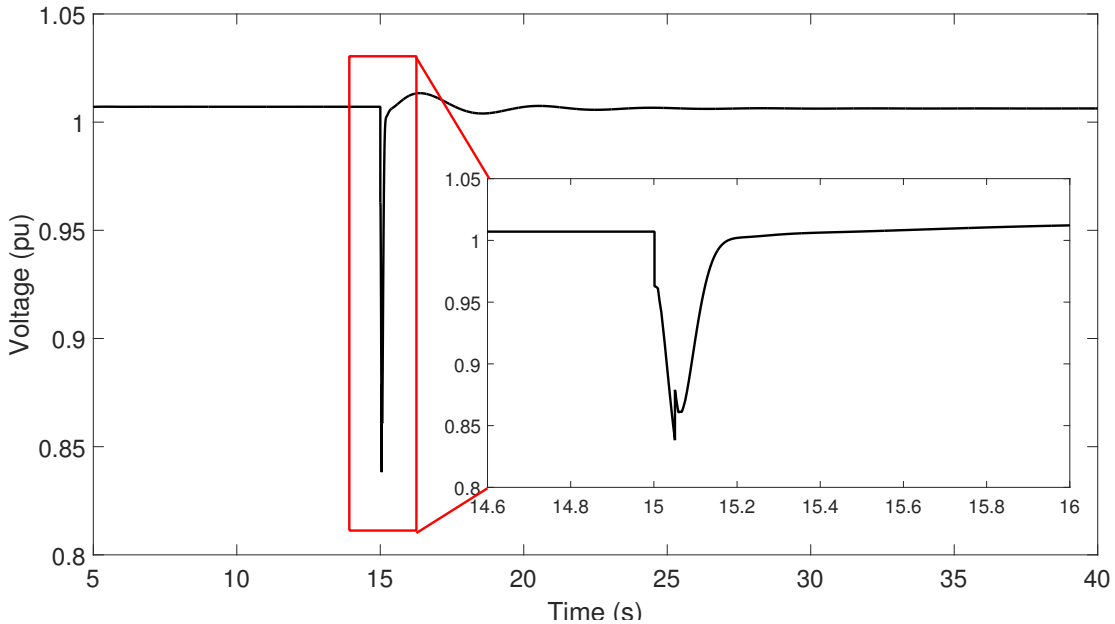

Figure 5.46: Terminal voltage magnitude of one Plant A unit for the opening of a tie line between Arizona and Southern California following a line fault

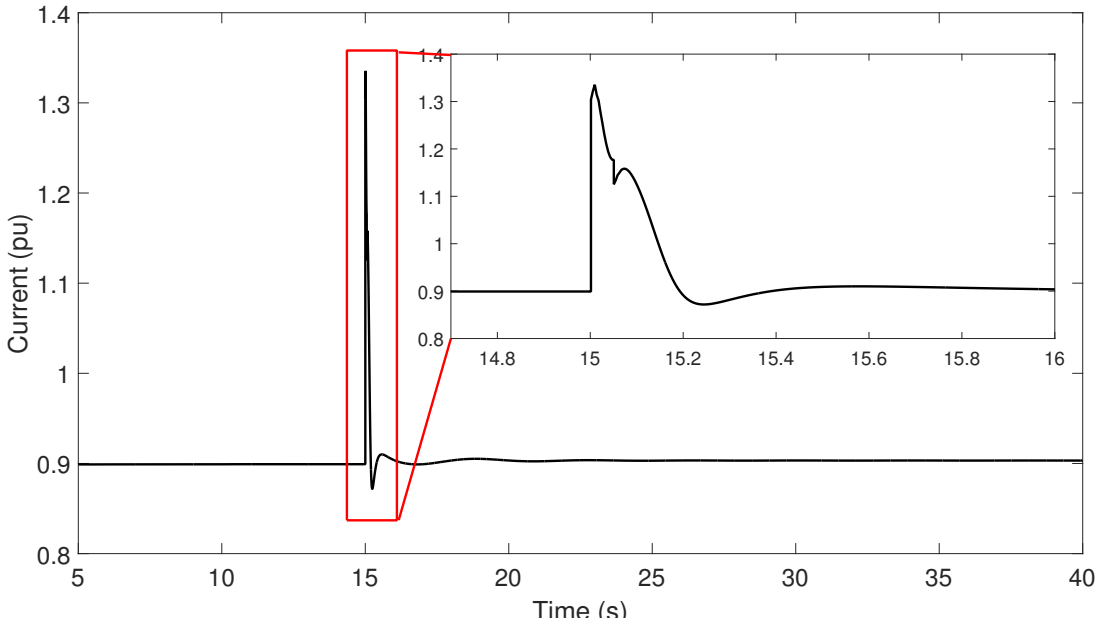

Figure 5.47: Converter current magnitude of one Plant A unit for the opening of a tie line between Arizona and Southern California following a line fault

5.1.5.4 Bus Fault (100% CIG penetration)

A three phase fault for 0.05 seconds at t=15s was applied at a bus at some distance from Plant G. Six converters in the New Mexico area tripped due to overcurrent

upon the occurrence of the fault. The active power, terminal voltage and current of a converter at the generating is as shown in Figures 5.48, 5.49 and 5.50. It can be seen

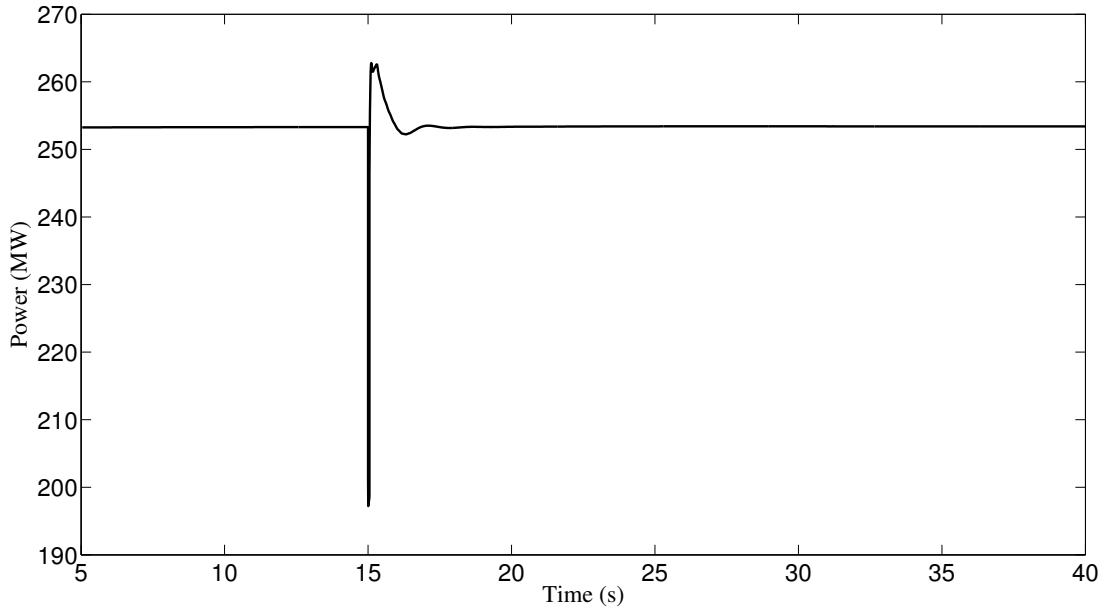

Figure 5.48: Active power of a converter of Plant G for a three phase bus fault

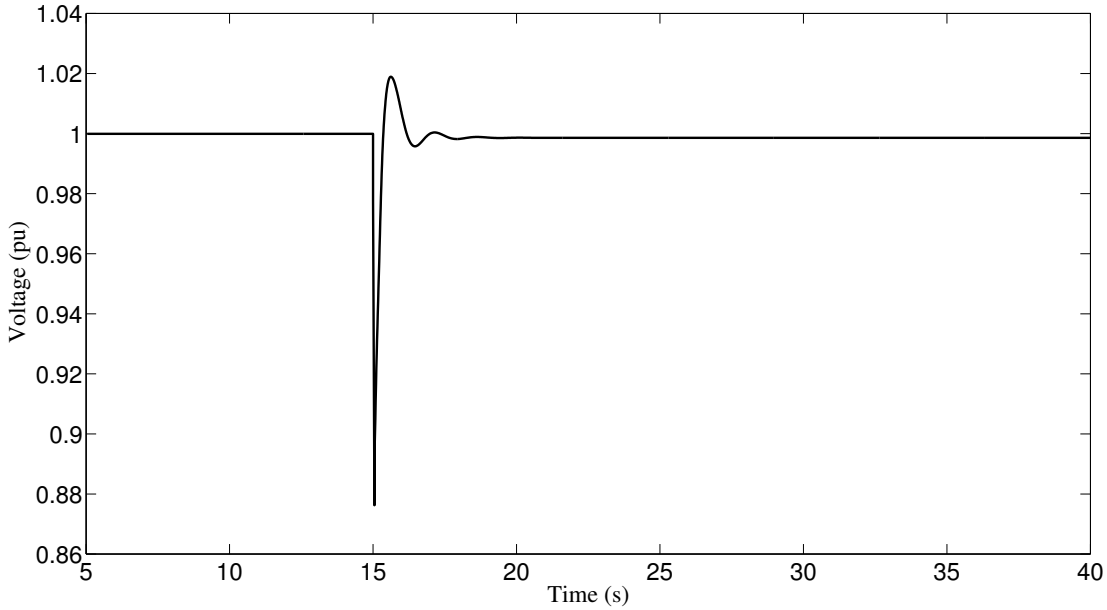

Figure 5.49: Terminal voltage magnitude of a converter of Plant G for a three phase bus fault

from Figure 5.49 that the terminal voltage falls by 0.12pu almost instantaneously

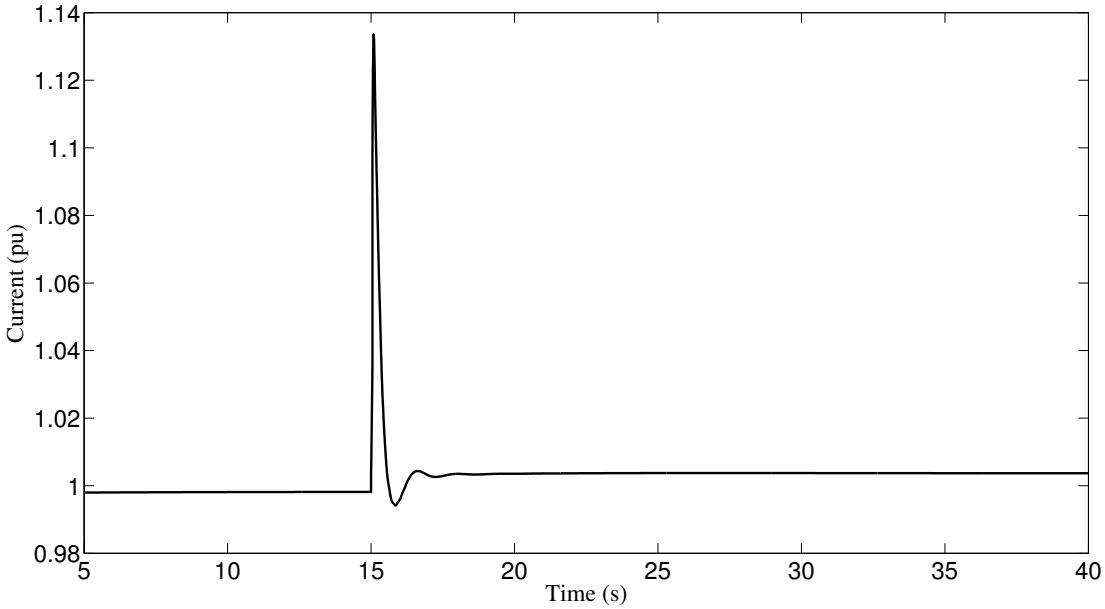

Figure 5.50: Current magnitude of a converter of Plant G for a three phase bus fault

thereby reducing the active power produced at the terminals of the converter by around 50 MW as can be seen from Figure 5.48. However, from the increase in current in Figure 5.50, it can be inferred that the reactive power produced increases to bring the voltage level back to 1.0pu within 3 seconds. The absence of an oscillatory mode for a fault close to a source is a significant observation that can be made from this scenario.

5.1.5.5 Line Reconnection (100% CIG penetration)

The re-closure of a transmission line must be studied to ensure that it does not cause excessive transients of current and voltage.

To observe this scenario, the power flow of the system was solved with a line between two major buses in Arizona outaged, resulting in an angle difference of 40.23 degrees between the buses. During the simulation, at $t = 15$s, the line was closed. With the maximum converter current set as 1.7pu, Figures 5.51 and 5.52 show the converter currents for nearby generating units. From the figures it can be seen that

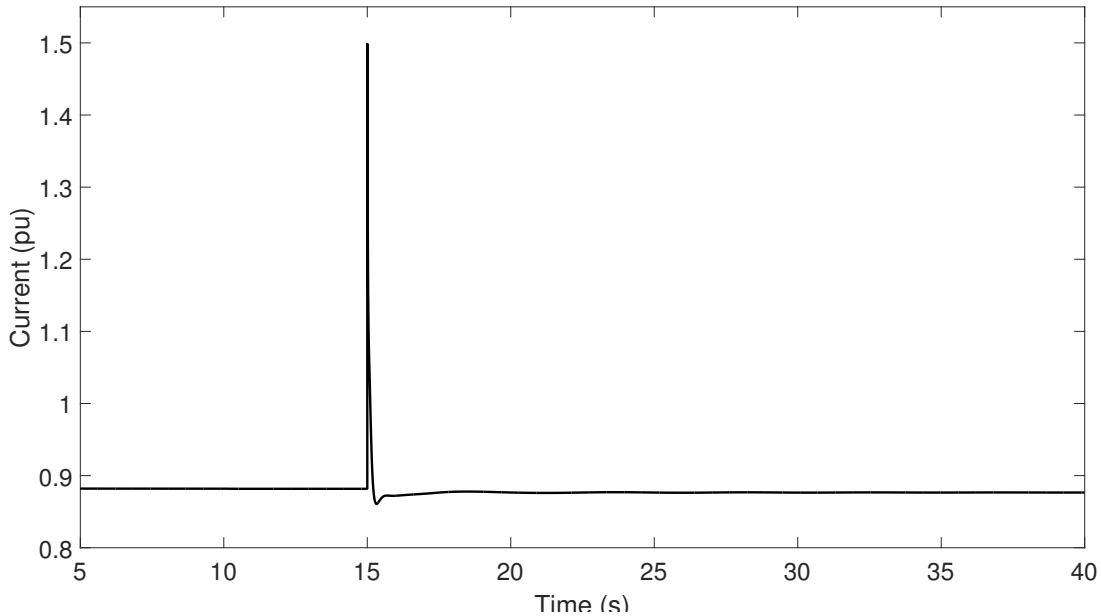

Figure 5.51: Current of a generating unit located close to the line with I_{max}=1.7pu

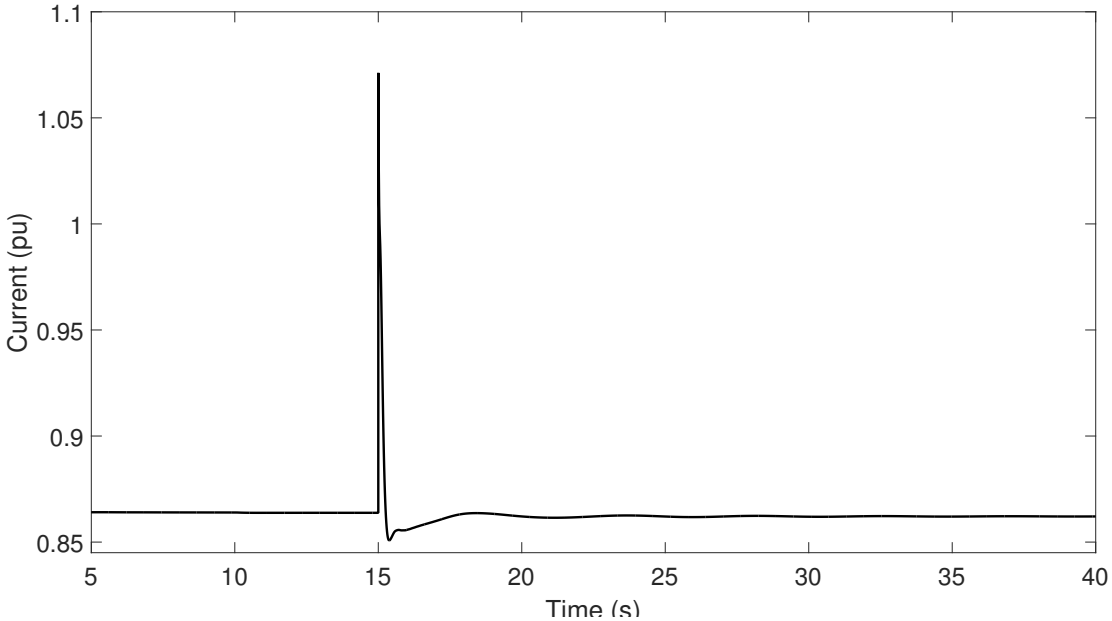

Figure 5.52: Current of a generating unit located one bus away with I_{max}=1.7pu

though there is a large increase in the instantaneous current, the pre-disturbance current value is achieved within 1s. In addition, as expected, the unit located close to the line is affected to a much larger extent. The system however is stable and secure.

In order to observe the behavior with a lower current rating, the maximum current of the nearby units were set as 1.4pu. Due to the lower current setting and due to the over current trip mechanism, the unit located closer to the line would trip while the remaining units pick up the slack. This can be observed from the current of the unit located one bus away as shown in Figure 5.53.

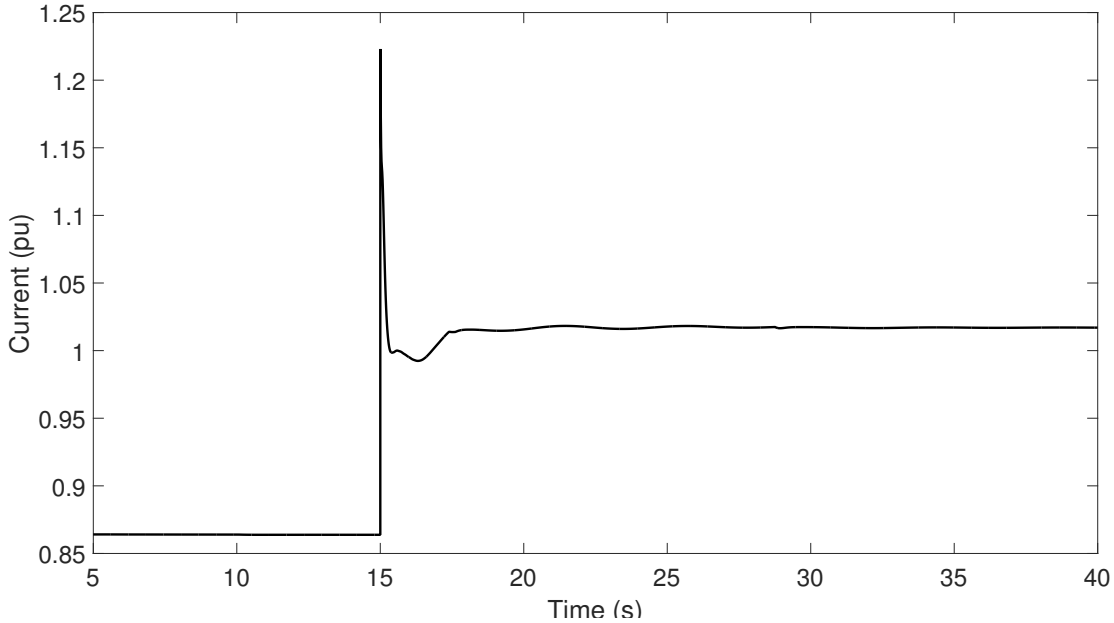

Figure 5.53: Current of a generating unit located one bus away with I_{max}=1.4pu

From the figures, it can be seen that despite the tripping of the unit close to the line, the system is still stable and secure. Thus, with switches of sufficient rating, the converter interfaced system can withstand a line closure with large angle separation between the two ends. This analysis of an all CIG WECC system has been published in [101].

5.1.6 Sensitivity to System Short Circuit Ratio

In grid connected mode, one of the primary concerns regarding the operation of converters is their behavior in relation to varying short circuit capacity (SCC_{MVA}) and short circuit ratio (SCR) at the point of connection [102]. SCR is a metric used to

evaluate the voltage stiffness of the grid. At a bus where a device is to be connected, the short circuit ratio is defined as in (5.4). A larger value of SCR indicates that the system is strong/stiff at the particular bus. Usually, a value of SCR ≥ 4 [22] is considered to indicate a strong system. The short circuit capacity at a bus is defined as the product of the rated bus voltage and short circuit fault current. It can also be mathematically defined as in (5.5).

$$SCR = \frac{\text{Short Circuit Capacity}(SCC_{MVA}) \text{ before device connection}}{\text{Rated MW value of device at the bus}} \tag{5.4}$$

where,

$$SCC_{MVA} = \frac{(\text{Per unit pre-fault bus voltage})^2(\text{Network base MVA})}{\text{per unit Thévenin impedance}} \tag{5.5}$$

The per unit pre-fault bus voltage magnitude is usually assumed to be 1.0pu. In order to evaluate the performance of the proposed converter model for varying SCR at the point of connection, a slightly modified topology of the system of Figure 5.4 was used, as shown in Figure 5.54. The short circuit capacity of the system was varied by varying the value of the X, the per unit reactance between buses 4 and 10. With the loads considered as constant admittance, an assumed 200 MW rating for a converter at bus 1 and value of $R_f + jX_f$=0.0025+j0.06pu on a 247 MVA base, Table 5.2 tabulates the short circuit ratio at bus 1, on a network MVA base of 100 MVA, for the different values of X. For a 10 MW increase in load at bus 6 at t=5s, the active power output and change in reactive power output of the converter at bus 1 is as shown in Figures 5.55 and 5.56 respectively while the change in converter current and voltage magnitude at bus 1 are as shown in Figures 5.57 and 5.58 respectively.

As the short circuit ratio decreases, the near instantaneous rise in the active power output of the converter decreases due to the decrease in the near instantaneous rise in current, while there is a negligible difference in the near instantaneous change in

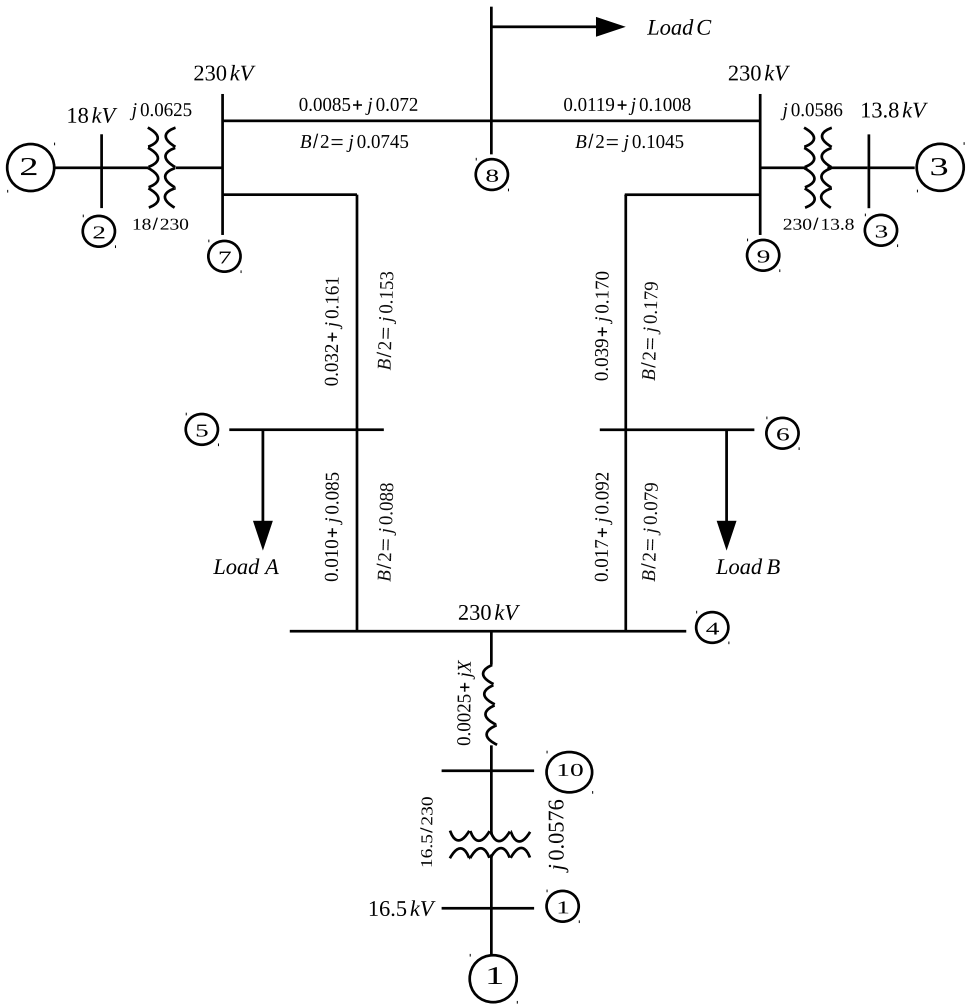

Figure 5.54: Three machine nine bus equivalent system

Table 5.2: Short Circuit Ratio at bus 1

X (pu)	$\mathbf{Z_{11}\angle\theta_{11}^{\circ}}$ **(pu)**	$\mathbf{SCC_{MVA}}$	**SCR**
0.0	$0.2600\angle 70.87$	384.49	1.922
0.1	$0.3552\angle 75.64$	281.5	1.407
0.5	$0.7493\angle 83.25$	133.45	0.667
0.8	$1.0479\angle 85.18$	95.43	0.477
1.0	$1.2473\angle 85.95$	80.17	0.40

reactive power due to the negligible change in terminal voltage magnitude. It can be seen that as the strength of the system decreases, the contribution of the converter

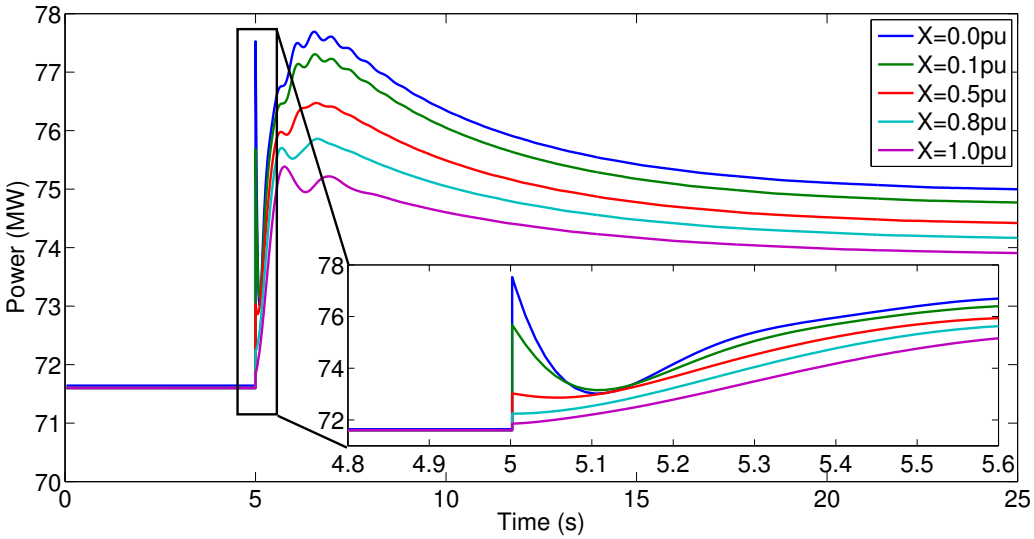

Figure 5.55: Active power output of converter at bus 1 for varying SCR

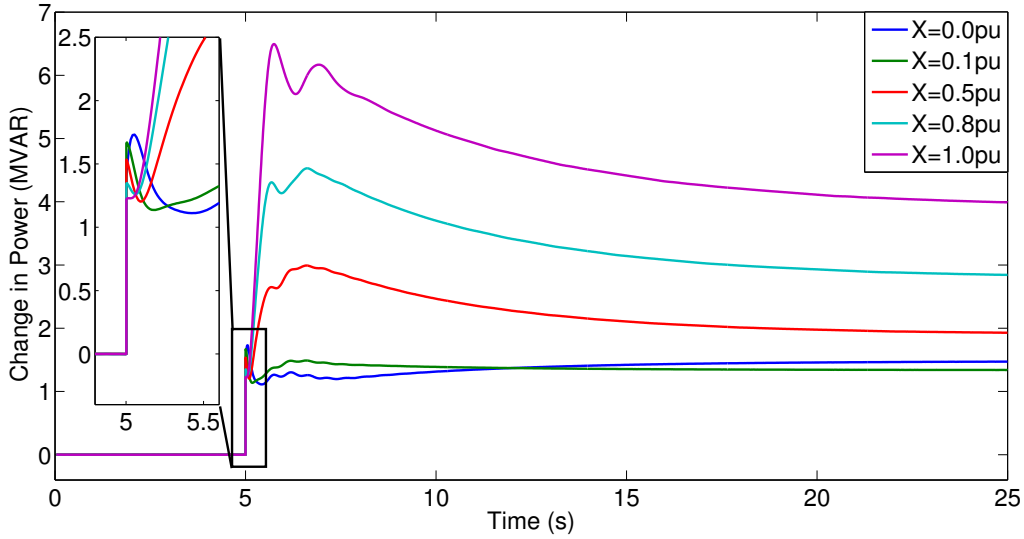

Figure 5.56: Change in reactive power output of converter at bus 1 for varying SCR

to the disturbance, at the instant of disturbance, also decreases resulting in a larger oscillatory transient in the voltage. The electrical distance between the converter and the disturbance location increases with increase in X resulting in a lower contribution at the instant of disturbance. While the converter is still able to act quickly to restore the voltage to the pre-disturbance value, the larger oscillatory component could be a cause for concern in larger systems.

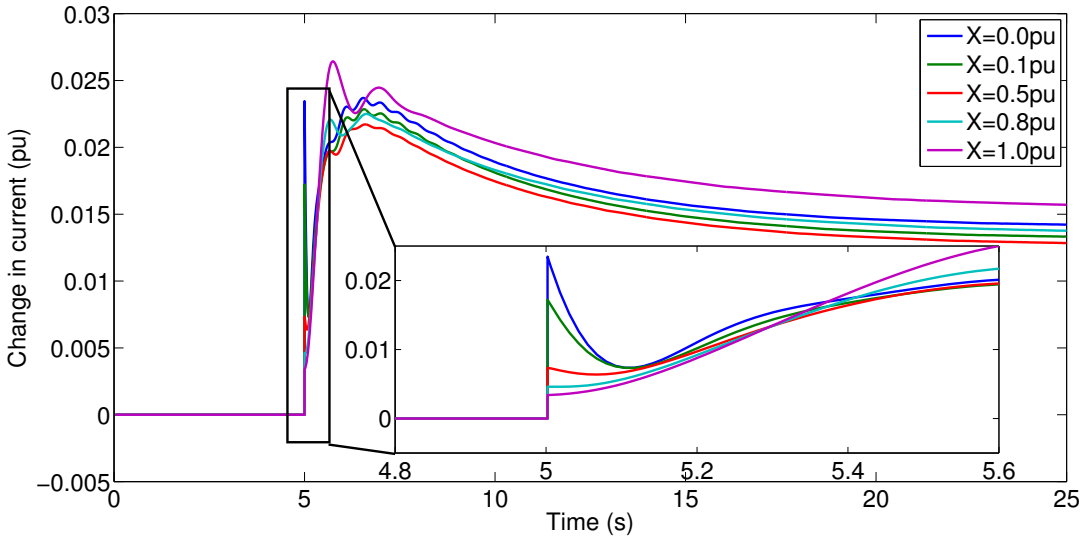

Figure 5.57: Change in current magnitude output of converter at bus 1 for varying SCR

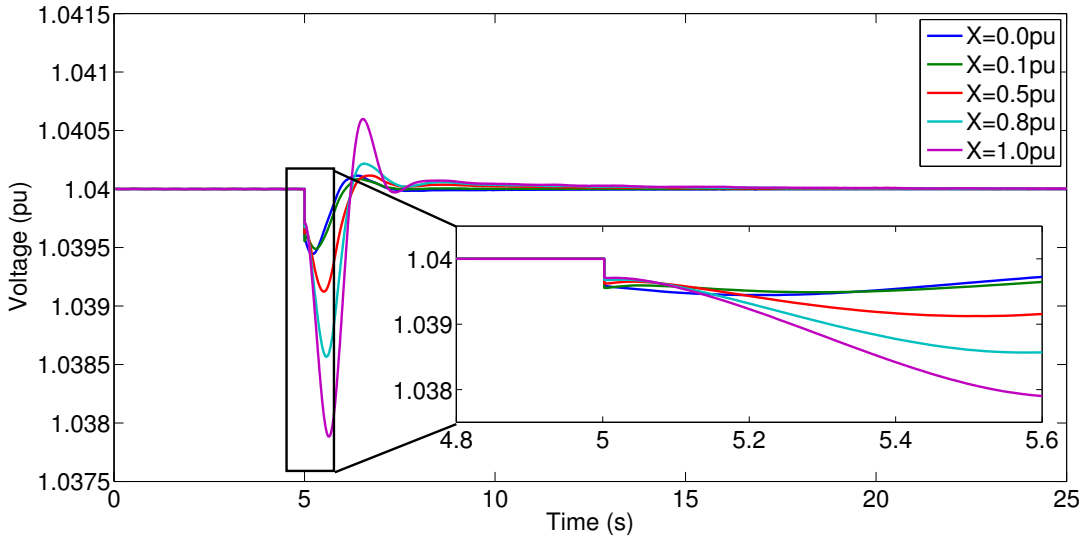

Figure 5.58: Terminal voltage of converter at bus 1 for varying SCR

In order to evaluate the small signal stability of the control loop, the eigen values of a single machine infinite bus equivalent system shown in Figure 5.59, were evaluated. The complete derivation of the state space representation is given in Appendix A while Figure 5.60 shows the trajectory of the eigen values for varying values of X_e.

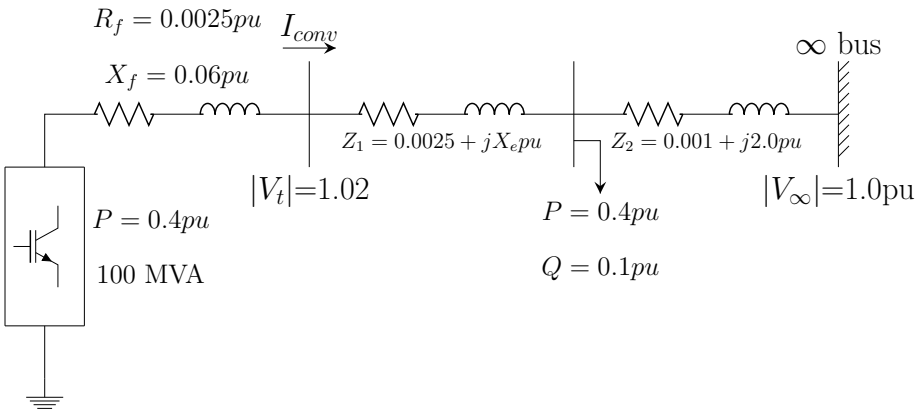

Figure 5.59: Single machine infinite bus equivalent system

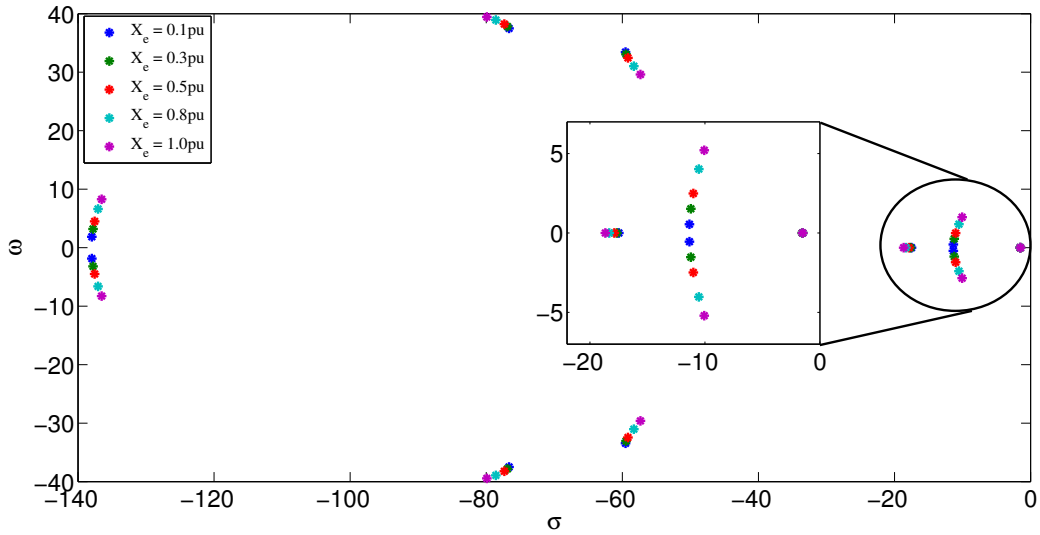

Figure 5.60: Eigen values of controlled voltage source converter model for varying values of X_e

For the analysis of the WECC system, first, the Thévenin impedance and the SCC at every generator bus were calculated using the short circuit analysis module of PSLF. Figure 5.61 shows the SCC in per unit on a 100 MVA base at the generator buses. Subsequently, to evaluate the small signal stability of the controlled voltage source model at each generator bus, the evaluated Thévenin impedance, the active power generation level and the terminal voltage magnitude from the powerflow solution were used in a single machine infinite bus equivalent system as shown in

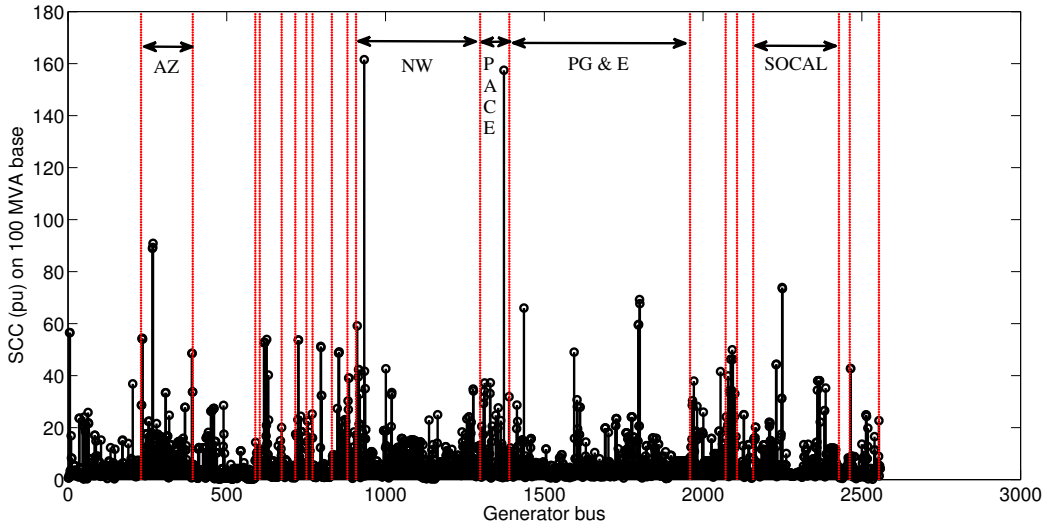

Figure 5.61: SCC in pu on a 100 MVA base at the generator buses of the WECC system

Figure 5.62. The resulting eigen values are shown in Figure 5.63. The eigen value trajectory has a similar trend to that observed for a mini-WECC system in [103], thereby validating the developed small signal state space model. From the results of

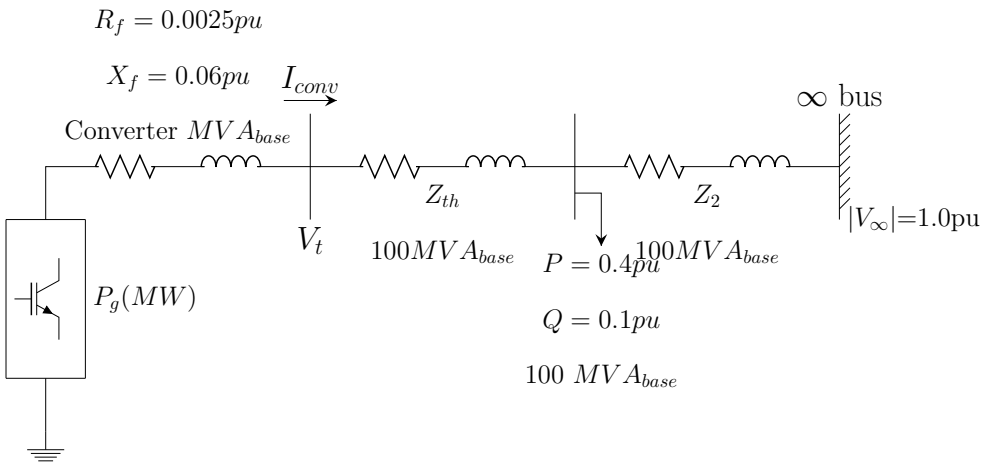

Figure 5.62: Single machine infinite bus equivalent system for analysis of the WECC system

this section it can be concluded that the proposed controlled voltage source converter model and its associated generic control structure is stable for different short circuit

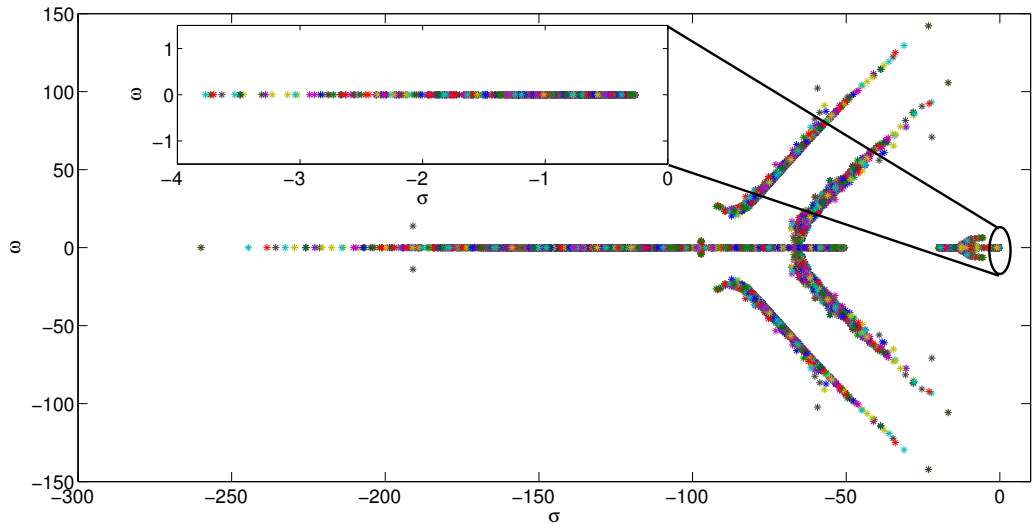

Figure 5.63: Eigen values of controlled voltage source converter model at every generator bus in the WECC system

ratios and the oscillatory modes have a high damping ratio. The examination of the sensitivity and robustness of the converter model to various short circuit ratio has been published in [104].

5.1.7 Performance of Alternate Current Control Structure

The nine bus test system was used to demonstrate the proof of concept of this alternate control structure while the 2012 WECC system was used to demonstrate the economy of computation and comparison with the generic control structure.

5.1.7.1 Three Machine System

The performance of the alternate control structure with explicit representation of the inner current control loop was validated using the three machine nine bus test system [89] with the synchronous machine at bus 1 replaced by a converter described by Figures 4.12 and 4.13.

The values of K_{pp} and K_{pq} were set to 10.0, the values of K_{ip} and K_{iq} were set to 60.0 and the values of K_{fv} and T_{frqv} were set to 1.0 and 0.01s respectively. The values of the remaining parameters were taken to be the same as in the generic controller performance described in the previous sections. For a load increase of 10 MW, Figure 5.64 shows the converter output current magnitude along with the current command. Further, the plot also compares the performance of the generic control structure of the previous sections along with the alternate control structure with the inner current control loop. As the objective of the control structure without the inner

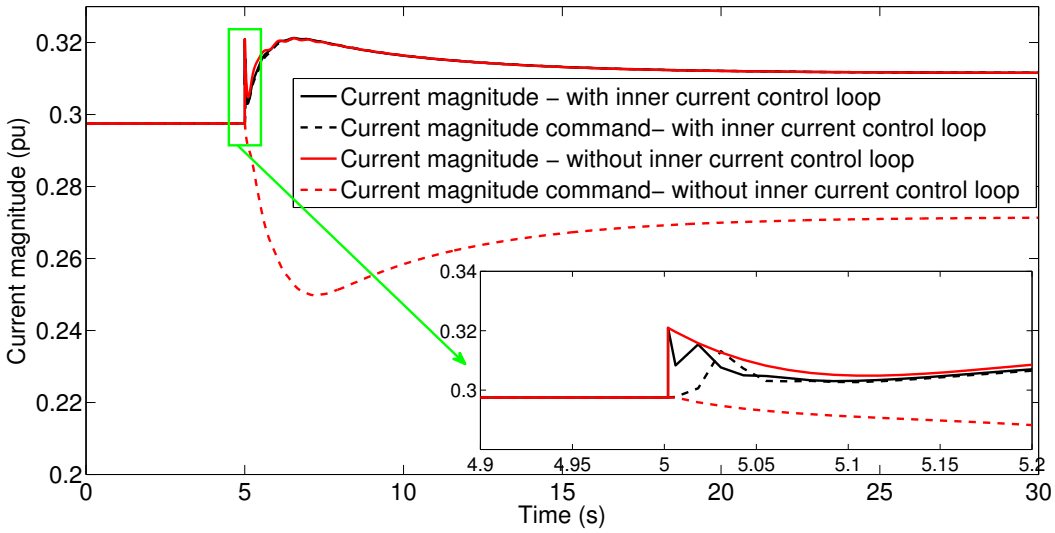

Figure 5.64: Comparison of current magnitude for converter at bus 1 both with and without the inner current control loop

current control loop (Section 4.3.1) was to ensure power control, the generated current commands used in the calculation of the internal voltage ((4.13)) were influenced by the mismatch in power and sought to minimize the mismatch.

In comparison, the alternate control structure has an objective of ensuring current control. Hence, the method of calculating the internal voltage by (4.15) has been modified to be similar to the technique used in point on wave simulations. It can be observed from the figure that with this control structure, the objective of current

control is met and consequently, power control is also obtained as shown in Figure 5.65. The effect of the additional droop component can be observed in the current

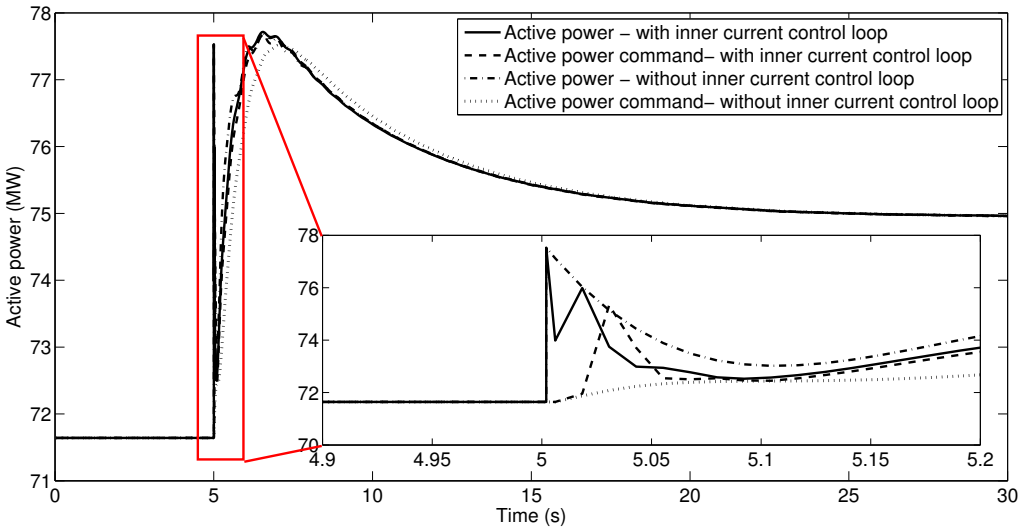

Figure 5.65: Comparison of active power output for converter at bus 1 both with and without the inner current control loop

command when the inner control loop is represented. Due to the limitation on the time step of integration in positive sequence simulations, the current command lags behind the actual current output required by the network at the instant of disturbance. However, point on wave simulations with time steps of the order of micro seconds would not see this lag in the current command. Figure 5.66 shows the comparison of system frequency, with both control structures. It can be seen that from a system behavior point of view, both control structures perform equally well.

5.1.7.2 WECC System

A comparison of the two control methodologies was also carried out using the 2012 WECC high summer case. Again, all conventional synchronous machines were replaced with the converter model and the operating point and reserve margins were maintained as in the previous sections of this dissertation. The values of K_{pp} and

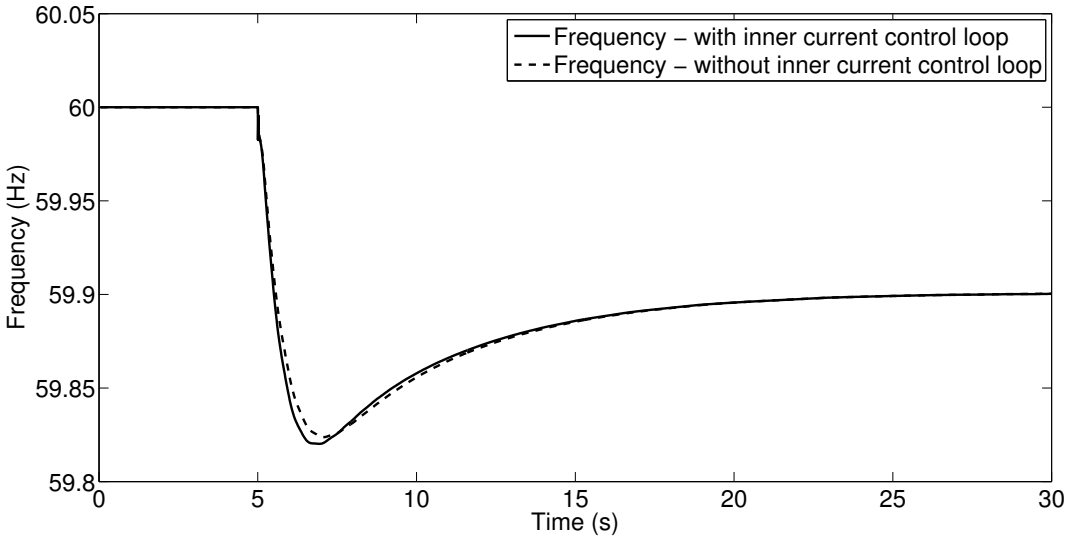

Figure 5.66: Comparison of system frequency both with and without the inner current control loop

K_{pq} were set to 1.0. The behavior of the system for a generation trip of 2755 MW at Plant A was observed. Figure 5.67 compares the interconnection mean frequency obtained with both control structures. It can be seen that with the use of the inner

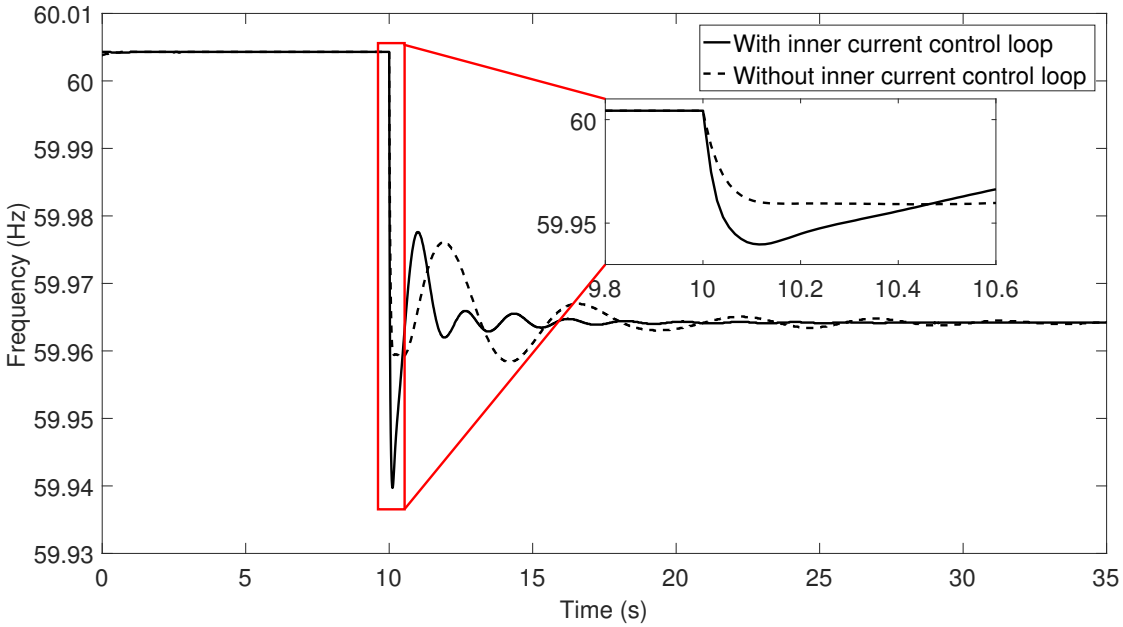

Figure 5.67: Comparison of interconnection mean frequency both with and without the inner current control loop

current control loop, the frequency nadir is slightly lower. A possible explanation can be provided by looking at the plot of voltage magnitude at few key buses shown in Figure 5.68. Due to the explicit representation of the inner current control loop, the

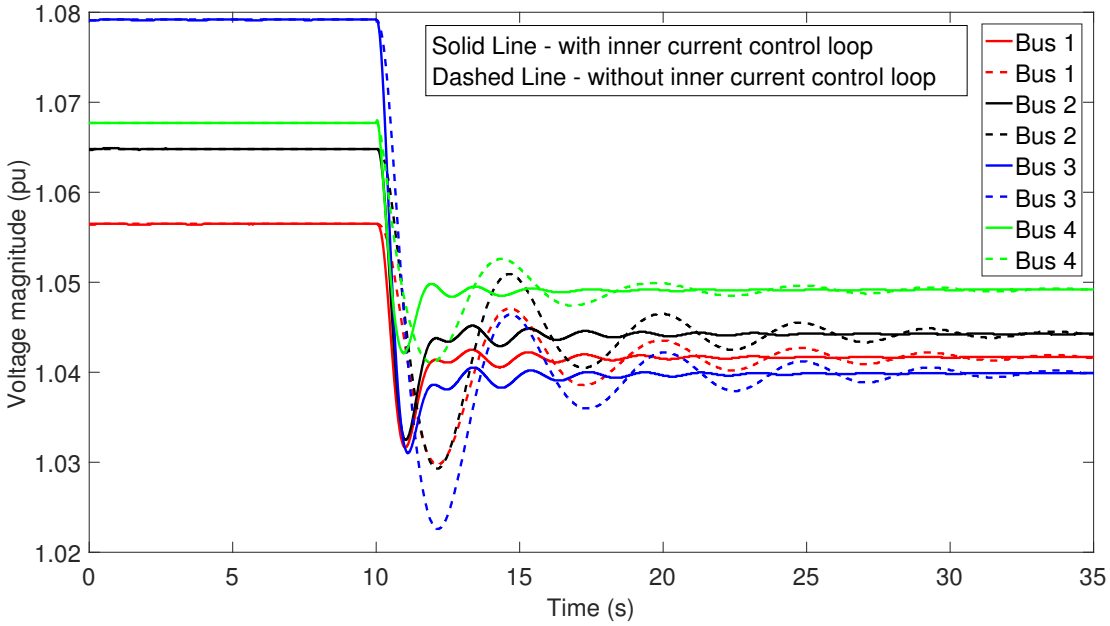

Figure 5.68: Comparison of voltage magnitude at key buses both with and without the inner current control loop

control on current leads to a higher voltage nadir resulting in a higher loading level in the system as a result of the presence of voltage dependent loads. This higher loading level results in a lower frequency nadir. Thus, the current control objective ensures control of both current and power with minimal difference in system performance.

5.1.8 Enforcing a Current Limit on the Output of the Inverter at the Instant of Disturbance

Due to the voltage source representation of the inverter, the value of current injected into the network (I_{grid}) instantaneously upon the occurrence of the disturbance can reach a large value depending on the inverter ac terminal voltage (V_t). This is primarily because the internal voltage $E\angle\psi$ (Figures 4.9 or 4.13) is a function of state

variables and would thus not change instantaneously. Whereas the terminal voltage can change instantaneously with change in network conditions. Further, due to the methodology by which positive sequence transient stability simulations are carried out, with the sequential solution of the differential and algebraic equations, an instantaneous change occurs in the inverter output current for a change in terminal voltage. If the disturbance is applied at time t, this instantaneous change is termed as the solution at time t^+ second. In certain situations, this instantaneous value of current can exceed the maximum current rating of the inverter despite the restricted value of current command.

Practically, or even in point-on-wave simulations, the internal voltage would be controlled rapidly to ensure that the current does not exceed the maximum value. However, due to the relatively large time step of simulation used for positive sequence simulations (generally ≈ 4 ms) iterations with the network solution could be required to ensure that the output current of the inverter does not exceed its maximum value. The flowchart for this process of iterating with the network solution is as shown in Figure 5.71. The simulations described in this section were however not carried out in PSLF and were instead carried out in an independent transient simulation tool developed in-house.

In order to illustrate the effect of this process, the machine at bus 1 in Figure 5.4 was replaced with the converter model shown in Figure 4.9 and the generic control without the inner current loop. The other two synchronous machines were not replaced. A fault with a fault resistance of 0.1pu was applied on bus 4 for a duration of 5 cycles. The output current magnitude of the inverter is as shown in Figure 5.69 while the terminal voltage magnitude is shown in Figure 5.70.

The plots compare the results when no current limit was enforced and when a current limit of 1.7pu and 1.2pu were enforced. It can be seen when the current limit

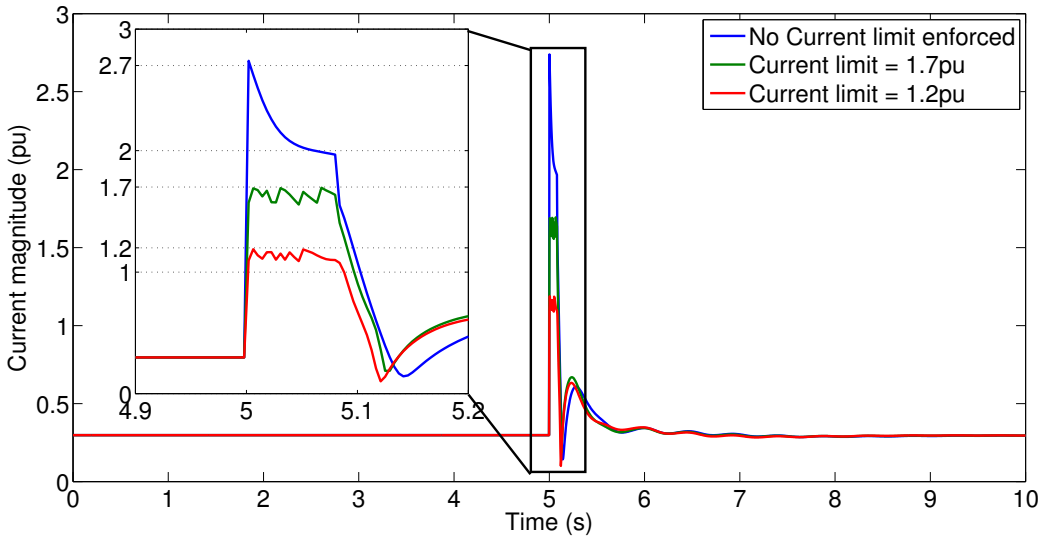

Figure 5.69: Inverter current magnitude for a fault while enforcing a current limit

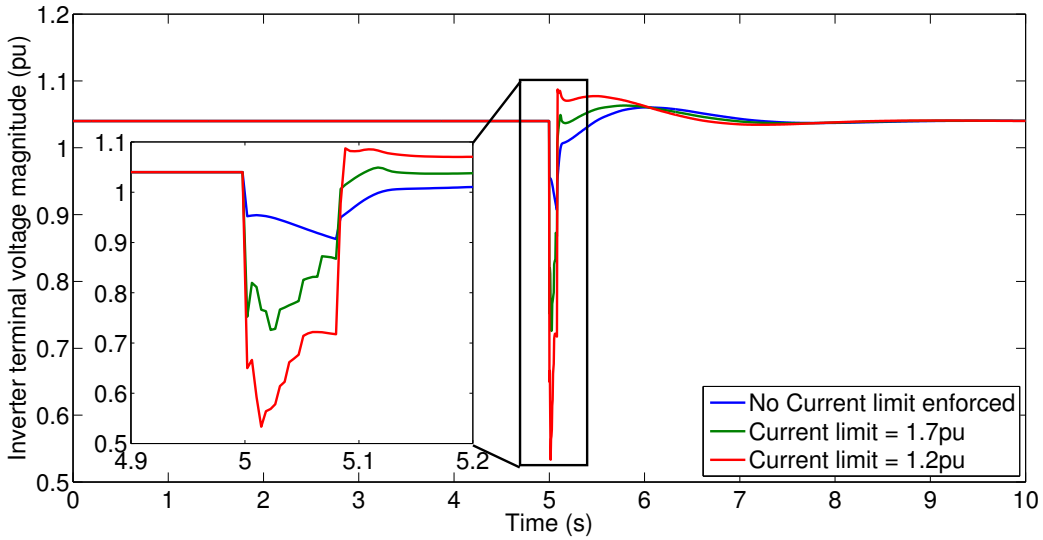

Figure 5.70: Inverter terminal voltage magnitude for a fault while enforcing a current limit

is enforced, the terminal voltage decreases by a larger amount than when the current limit was not enforced. This could have a critical impact on the behavior and recovery of a system following a fault.

To observe the effect of enforcing the current limit on a larger system, a 118 bus system was used. The topology of this system is the same as the IEEE 118 bus

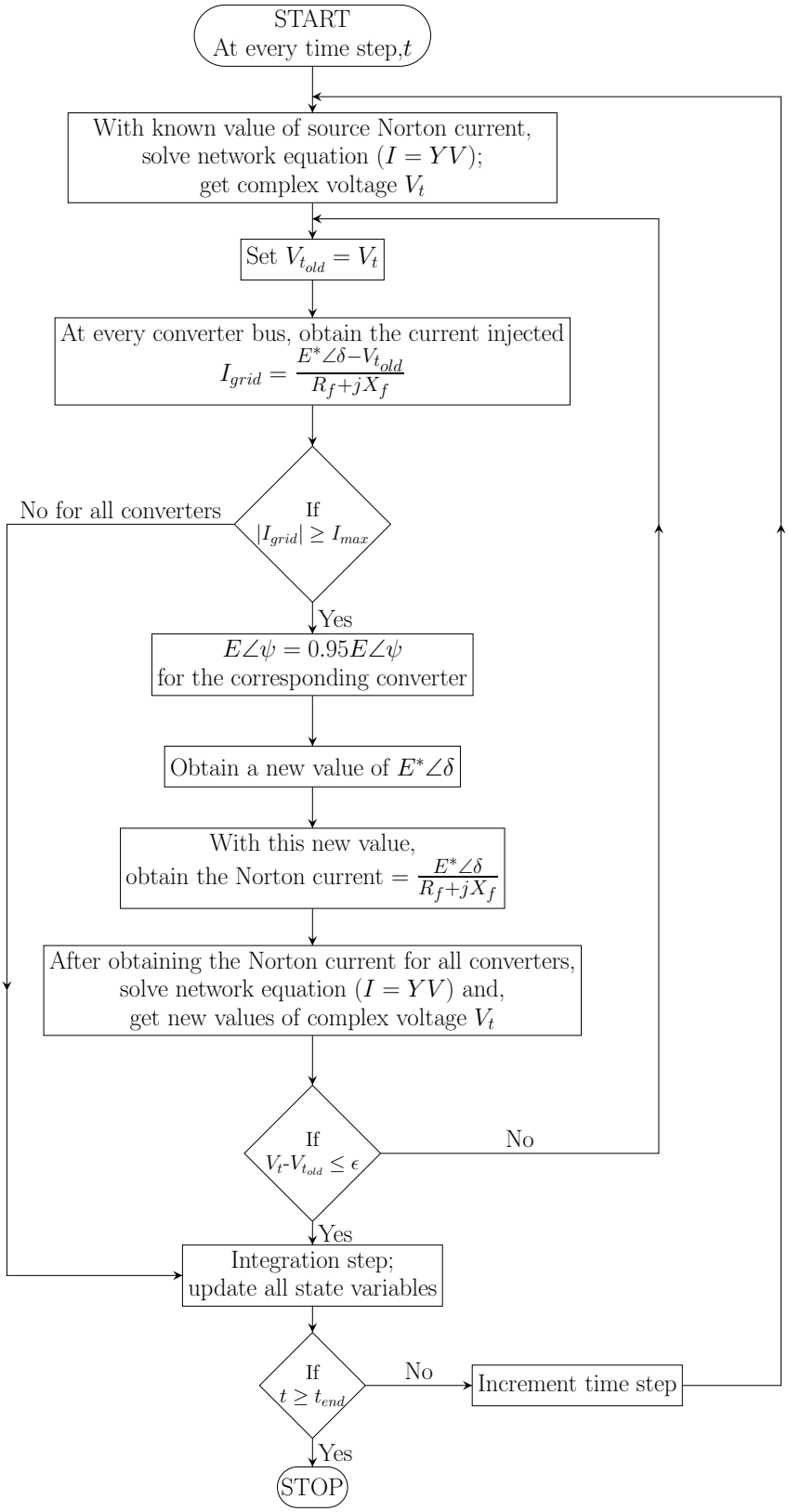

Figure 5.71: Flowchart of the procedure for network iterations in the converter model

system whose data is available at [105]. However, for the purpose of this analysis, the generation and loading level of the system was altered. The input system data and the converged power flow solution are given in Appendix C. The network one line diagram of the system is as shown in Figure 5.72. However, this one line diagram does not have all the generator locations marked.

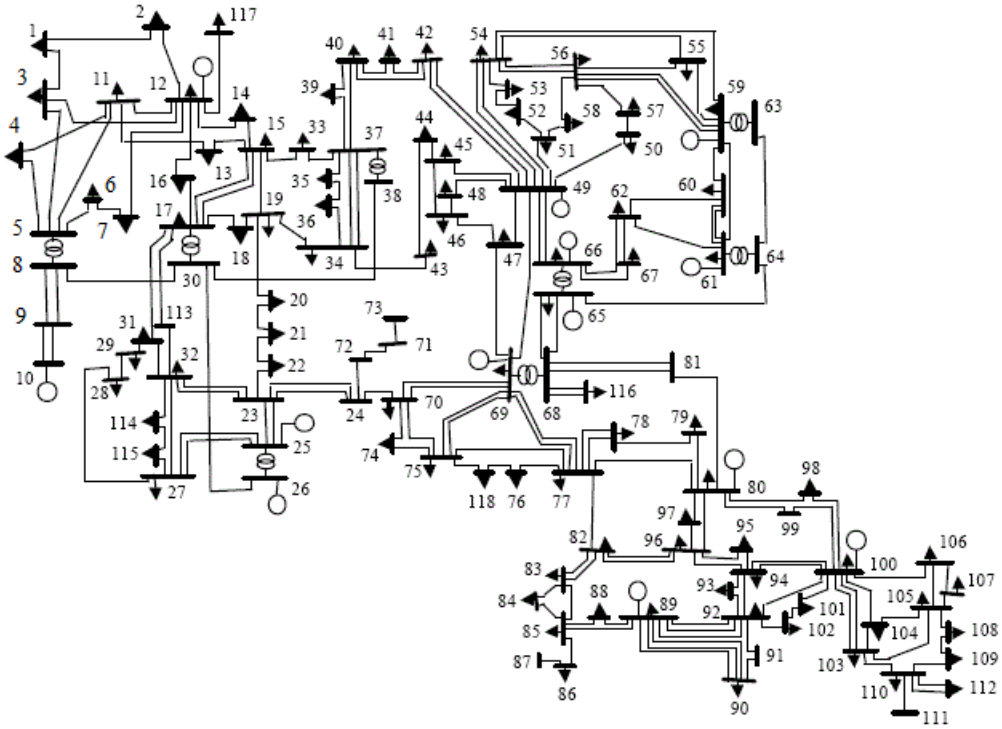

Figure 5.72: Network one line diagram of the 118 bus system

All the generating sources in the system were represented by the converter model shown in Figure 4.9 and the generic control without the inner current loop. The MVA rating of the converters was chosen in accordance to the absolute value of their respective maximum/minimum reactive power and specified active power. The loads were represented as constant impedances. To observe the effect of enforcing the current limit, a fault with a fault resistance of 0.1pu was applied on bus 37 for a duration of 5 cycles. As all the generation sources in the system are converter interfaced, the effect of the fault was observed for two load scenarios; one scenario

where all the load was static load and another scenario where the load on buses 2, 3, 11, 13, 16, 17, 29, 35, 39, 41, 45, 47, 60, 67, 75, 78, 82, 83, 88, 95, 98, 106 and 115 were induction motor load. The location of these induction motor loads was arbitrarily assigned. For the dynamic model of the motor, a single cage motor without implementation of saturation was used, represented by the data in Table A.5

Figure 5.73 compares the system mean frequency for the event while Figure 5.74 compares the voltage magnitude at bus 35 for various current limits while also showing the difference between effect of the static load and induction motor load.

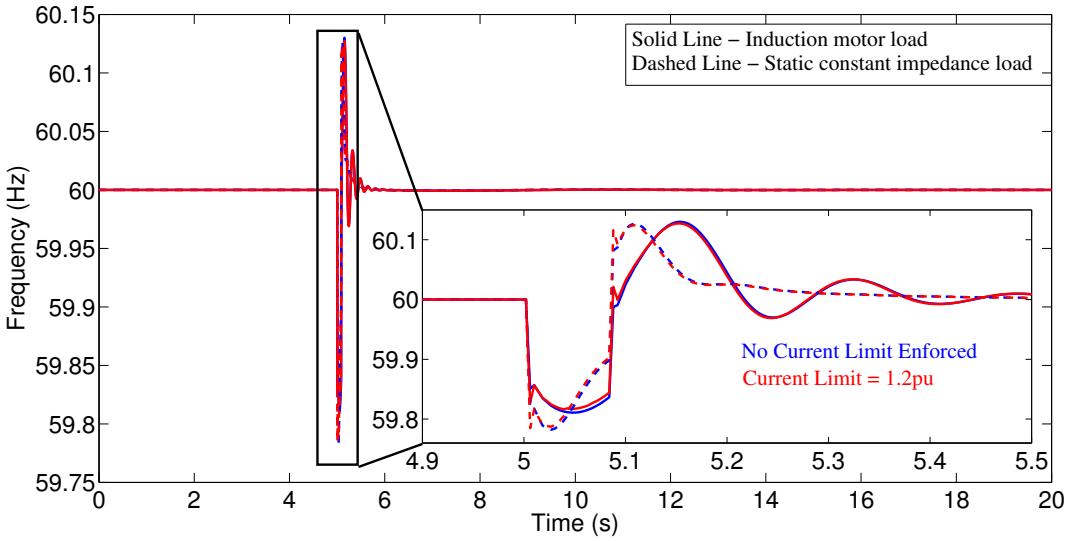

Figure 5.73: Comparison of mean frequency of the 118 bus system for the fault with various converter current limits

For this event, the near instantaneous current magnitude of converters at buses 34 and 36 had to be controlled to ensure that the current limit was not crossed. As expected, it can be seen from the figures that with the presence of the induction motor load, the voltage magnitude at the load bus has a different transient behavior in comparison to the behavior with the presence of static load. With the presence of an induction motor, the enforcement of the current limit decreases the nadir of the voltage magnitude thereby increasing the chances of stalling. However, the enforce-

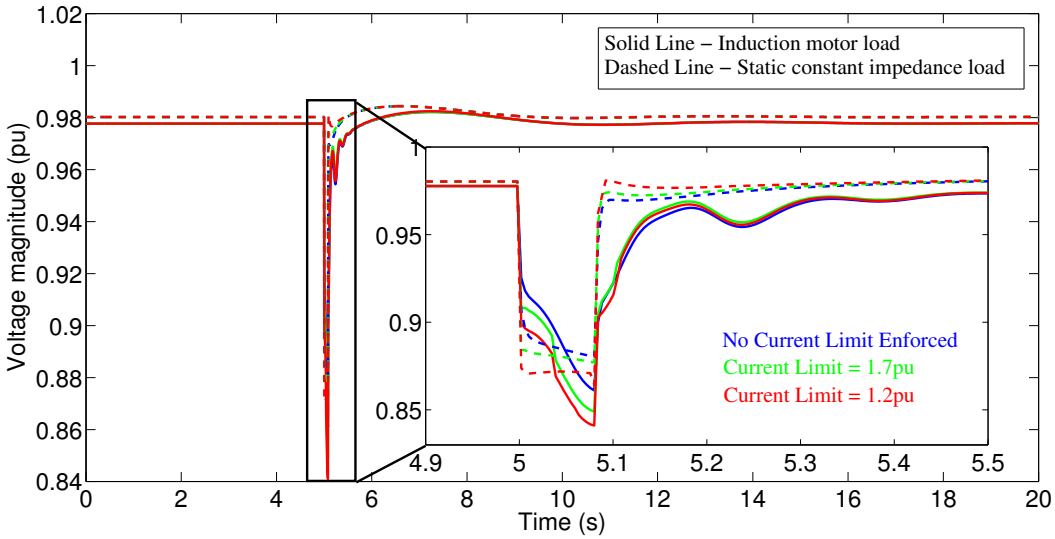

Figure 5.74: Comparison of voltage magnitude at bus 35 of the 118 bus system for the fault with various converter current limits

ment of the converter current limit has minimal impact on the frequency profile of the system both with static load and induction motor load.

While the methodology used to enforce the current limit (Figure 5.71) is still in a preliminary stage of investigation, the impact of the enforced current limit can be clearly observed in the system behavior. In the following section however, for the inverter model, the generic control without the inner current loop has been used and a current limit has not been enforced through network solution iterations.

5.2 Source behind Inverter Model

Using PSLF[3], the behavior of the proposed positive sequence model was first validated using the three machine nine bus equivalent system. Subsequently, its performance on the 18000 bus WECC system was observed.

[3]PSLF Version 18.1_01

5.2.1 Small Scale System: Model Validation

The three machine nine bus equivalent system shown in Figure 5.4 was used to validate the behavior of the model in software. The synchronous machine at bus 1 is replaced by a synchronous generator behind a rectifier-inverter set. The value of C_{dc} was taken to be 7300 μF. On a base voltage of 16.5kV and base MVA of 100 MVA, the energy stored at voltage V_{dc} amounts to 12.1 MWs. The value of τ was taken to be 0.02s.

At t=5s, the load at bus 6 (Figure 5.4) was increased by 50 MW. The values of the controller gains and time constants were as tabulated in Table 5.3. Figure

Table 5.3: Controller gains for source behind inverter

Parameter	**Value**
K_p,K_i	4.0,20.0
K_{ip},K_{iq}	10.0,10.0
T_{frq}	0.05s
R_q	0.0
R_p	0.05pu on 100 MVA
K_a,T_a	200,0.02s
K_{pdc},K_{idc}	0.0,0.1
α_{rect}	15°
K_{gp},K_{gi}	10,1.0s
T_{Gsync}	0.2s
T_1/T_2	3.0/10.0
All other time constants	0.01s

5.75 compares the real power at the inverter ac terminals (P_{conv}) with the real power (P_{gen}) at the generator ac terminal when the dc circuit is represented explicitly (Sec-

tion 4.4.3.1) and is represented approximately (Section 4.4.3.2). The two values are nearly, but not exactly, equal; they differ by the flow of energy into the capacitor supporting the dc bus. The inset in Figure 5.75 shows the extent of the difference as estimated by a detailed simulation of the bus inductance and capacitance, and by using the approximate representation given by (4.30). For the simulation with the detailed representation of the inductor, the values of K_{pdc} and K_{idc} were set as 1.0 and 0.5 respectively. The comparison supports the use of the approximation. This

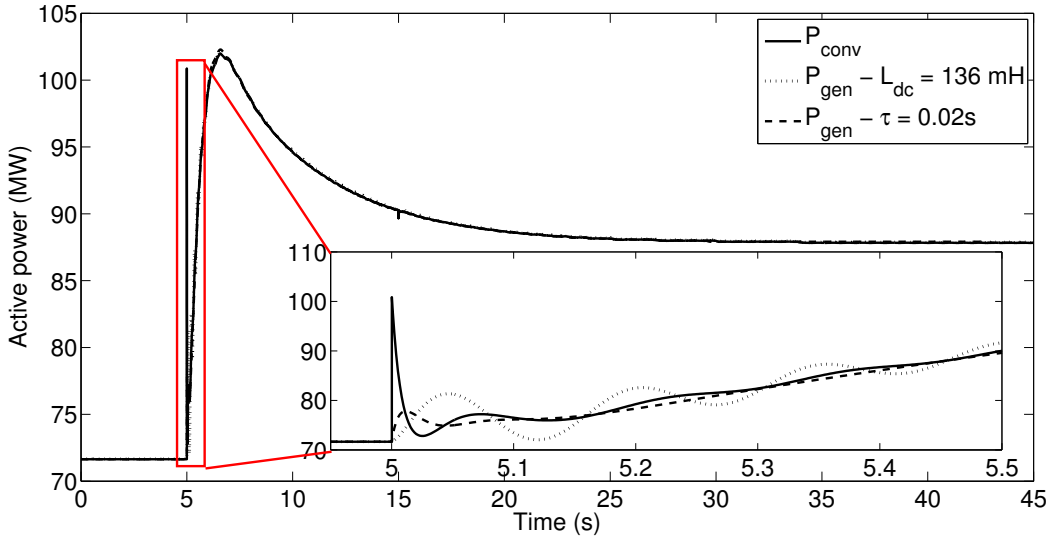

Figure 5.75: Validation for use of τ to approximate the dynamics of L-C circuit on dc bus

is important in large scale grid simulation work because detailed simulation of the dc bus would require very small time steps and would adversely affect computation time. Details of the design and tuning of the dc bus voltage controller could affect the details of the bus response, but the topic is beyond the scope of this dissertation.

Using τ, the active power output of the inverter (P_{conv}) and the active electrical power output of the synchronous generator (P_{gen}) behind the rectifier-inverter set are shown in Figure 5.76. Further, Figure 5.76 also compares P_{gen} of the generator connected electronically with the active power output of the generator if it had been

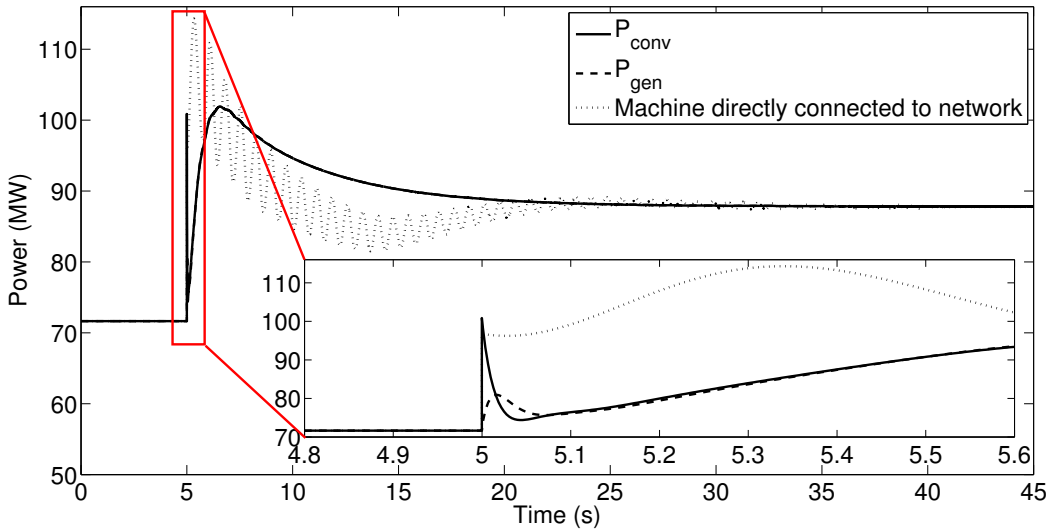

Figure 5.76: Active power output of the unit at bus 1

directly connected to the network. From the figure, two important observations can be made; firstly, the output of the inverter interfaced generator follows the inverter output, and secondly, due to the decoupling of the generator from the electrical network, there is no rotor angle oscillation present.

The system frequency, reactive power output of the inverter (Q_{conv}) and the synchronous machine (Q_{gen}) is shown in Figure 5.77. As the inverter handles the control of its ac terminal voltage, the reactive power demand on the synchronous machine is lower because it only needs to supply the reactive power consumed by the rectifier. This is observed from the figure with the pre-disturbance reactive power output of the machine being 20 MVAR in comparison to the inverter output of 27 MVAR.

Figures 5.78, 5.79 and 5.80 illustrate the importance of recognizing the finite size and control of the dc bus capacitance From (4.19), a smaller value of C_{dc} would result in a larger dip in dc voltage when the inverter power is increased. To practically achieve a near infinite value of capacitance, a very large capacitor would be required. A comparison of the performance of the positive sequence model using different values of C_{dc} was carried out. On a base voltage of 16.5 kV and base MVA of 100 MVA, the

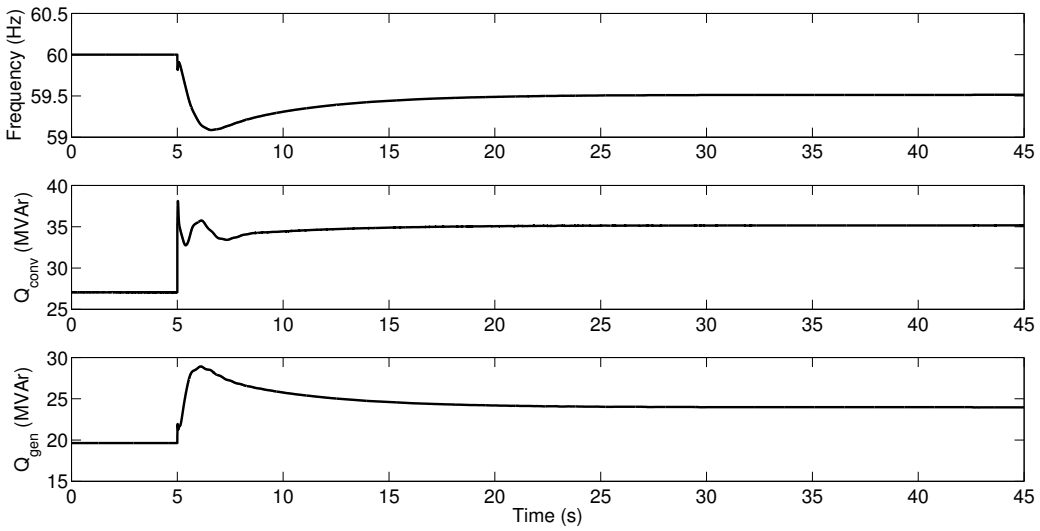

Figure 5.77: System frequency & reactive power output of inverter and synchronous machine

performance with values of C_{dc} as 730 μF, 7300 μF and 73000 μF were compared. The corresponding values for the time constant (τ)(4.19) were 0.002s, 0.02s and 0.2s respectively. The energy in the capacitor at voltage V_{dc} is 1.21 MWs, 12.1 MWs and 120.35 MWs respectively.

For the same 50MW load increase at bus 6, Figure 5.78 shows the variation of the inverter ac terminal voltage. It can be seen the response that to replicate an ideal/infinite dc voltage source, the value of C_{dc} should be 73000 μF. Figure 5.79 shows the variation of the inverter reactive power for the same event while Figure 5.80 shows the dc voltage. From these figures, it is apparent that the existing assumption of modeling the source behind the inverter as an ideal dc voltage in positive sequence simulations, will not be accurate. The large capacitors required to validate this assumption will not be practical. Further, due to the significant reduction in inverter terminal voltage due to the presence of a small capacitance on the dc bus, it is essential to model the dc bus and the source behind the rectifier while studying the dynamic behavior of large systems.

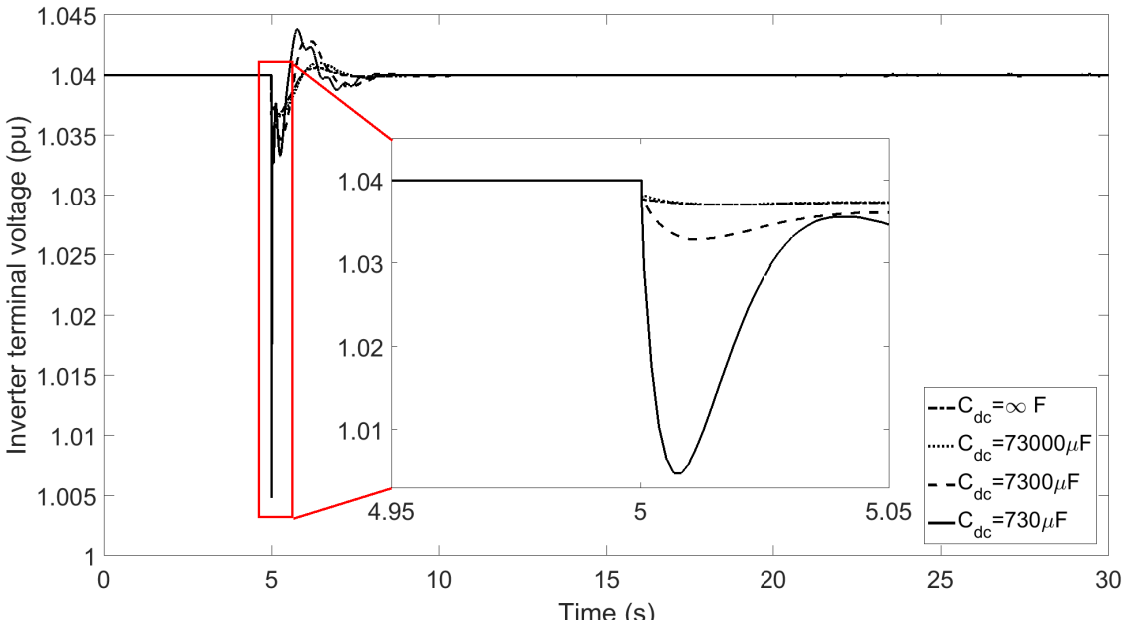

Figure 5.78: Variation of inverter terminal voltage for different values of C_{dc}

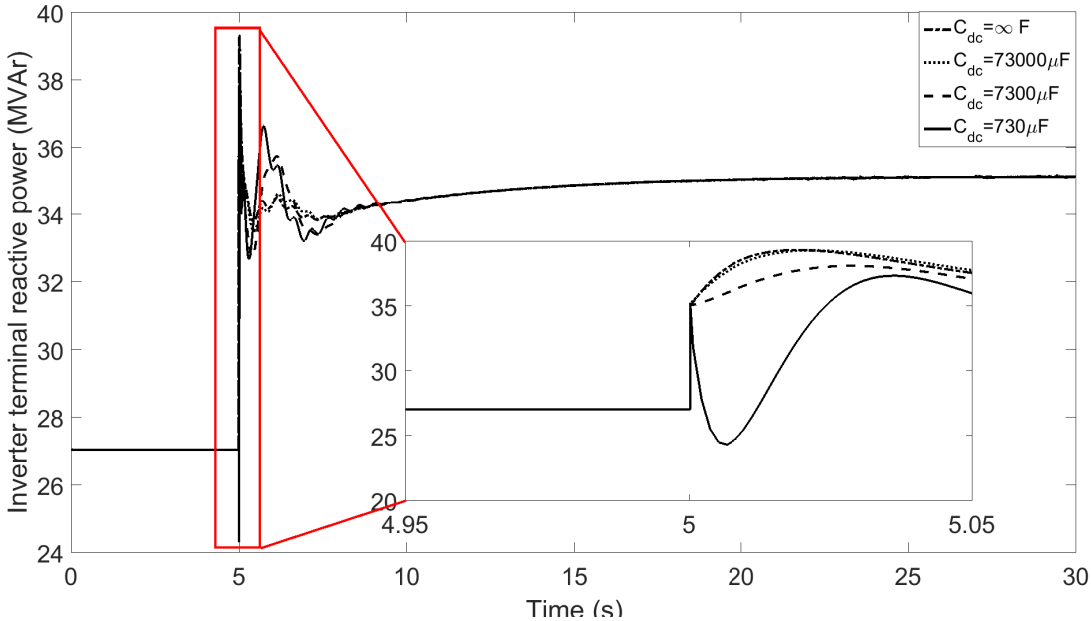

Figure 5.79: Variation of inverter terminal reactive power for different values of C_{dc}

The steady state recovery of the dc voltage is primarily due to the action of the synchronous machine excitation control with the rectifier firing angle control providing minimal support. For the results in Figure 5.80, a strong excitation control was

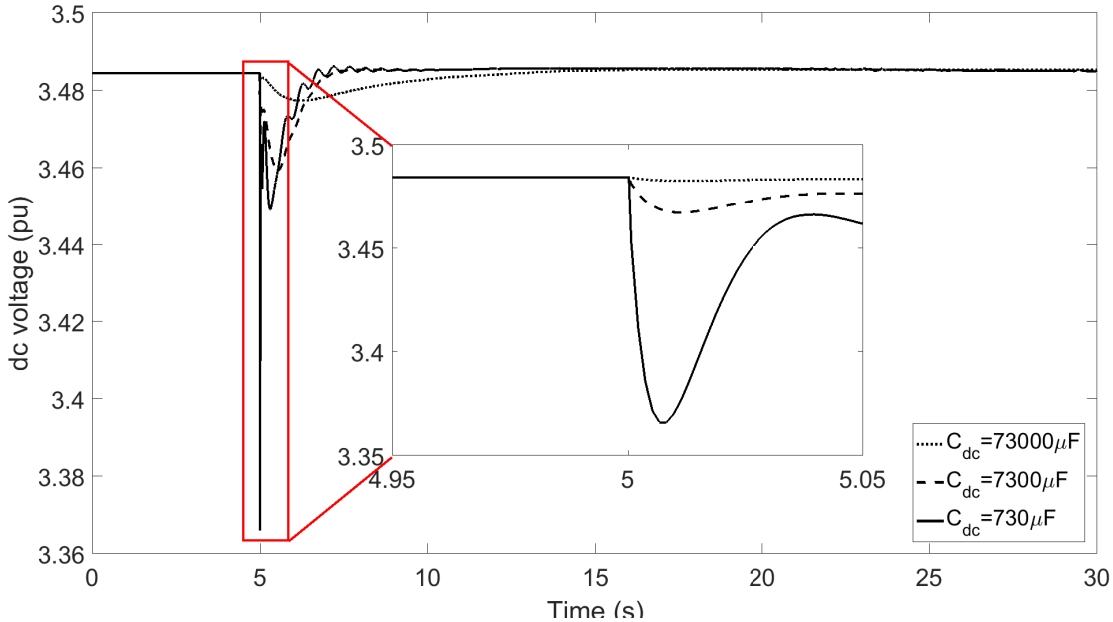

Figure 5.80: Variation of dc voltage for different values of C_{dc}

assumed to be present on the synchronous machine. To compare the performance between a controlled and uncontrolled rectifier, the synchronous machine excitation control gain K_a was reduced to 1.0 thereby weakening the excitation control, while the firing angle control gains K_{pdc} and K_{idc} were increased to 0.1 and 1.0 respectively. The value of the dc capacitance was set at 7300 μF with a time constant of 0.02s. The effect of the weaker synchronous machine excitation control and the rectifier firing angle control on the capacitor voltage is shown in Figure 5.81.

From these set of results it is observable that the reduction in the dc voltage, primarily due to extraction of energy from the capacitor, causes the inverter terminal ac voltage also to reduce. To showcase the difference between using an ideal dc voltage source (converter model of Section 4.3.3) and using the explicit representation of the dynamics of the dc bus and the source behind the rectifier, all machines in Figure 5.4 were replaced with converters. However, the converters at buses 2 and 3 were represented with an ideal dc voltage source while the converter at bus 1 was

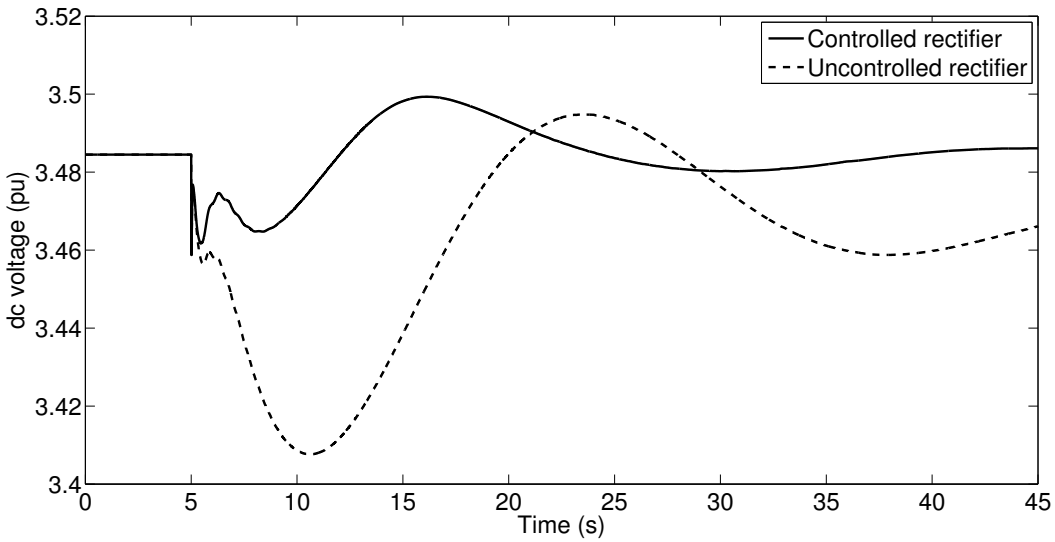

Figure 5.81: Effect of rectifier control on capacitor voltage

represented by the detailed model of the source behind the inverter. In Figure 5.82 the ac side terminal voltage of the converter at bus 1 is shown when the converter at bus 2 was tripped at t=5s. With the proposed detailed model, the inverter at bus 1 responds to the 163 MW generation trip by near instantaneously extracting a large amount of energy from the capacitor causing the dc voltage to reduce by a significant amount thereby resulting in the large drop in ac terminal voltage. However, with the use of the ideal dc voltage source converter model, the energy/power made available for the primary frequency contribution of the inverter is not accounted for on the source side of the inverter and is consequently not accounted for in the ac terminal voltage.

In another scenario, the converters at buses 2 and 3 were prevented from participating in primary frequency response. Figure 5.83 shows the ac side terminal voltage of the converter at bus 1 for a 50 MW load increase at bus 6 at t=5s. With this converter at bus 1 now being solely responsible for frequency response, again the difference between the ideal converter model vs the detailed model can be observed.

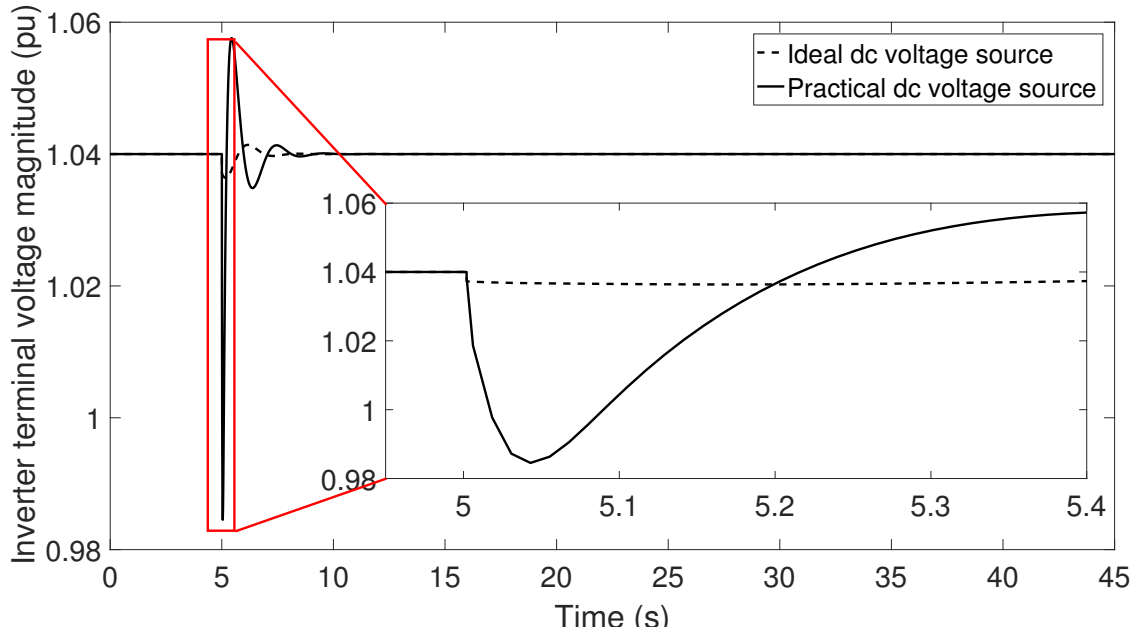

Figure 5.82: Inverter terminal voltage magnitude at bus 1 for converter trip at bus 2

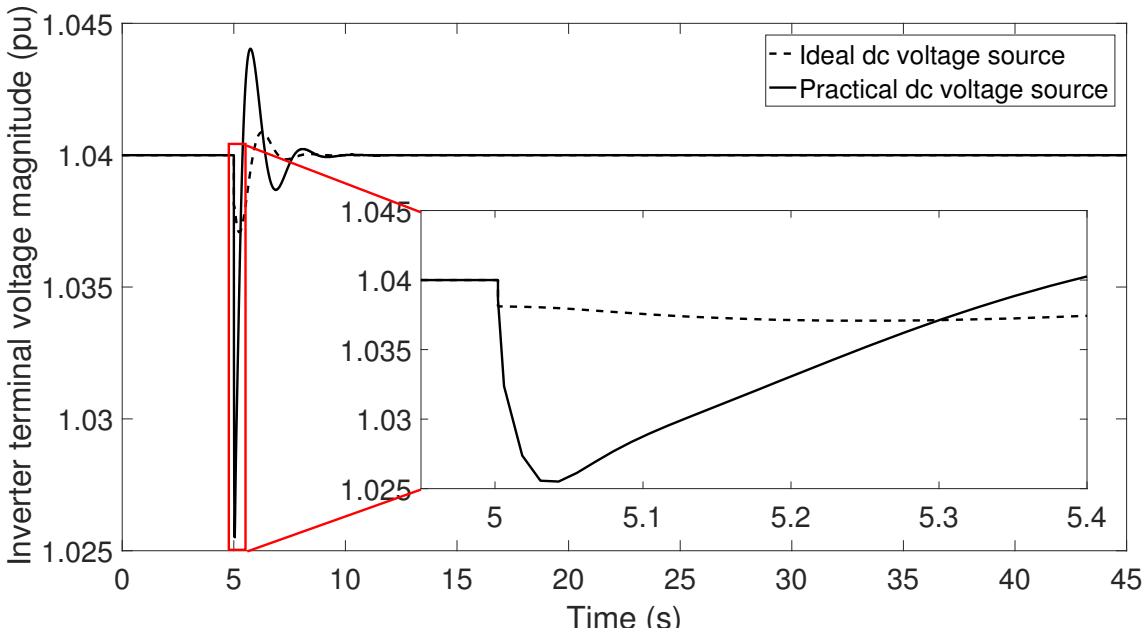

Figure 5.83: Inverter terminal voltage magnitude at bus 1 for constrained primary frequency response

The detailed converter model with representation of the source behind inverter would thus provide a better estimated representation of the system behavior. Further, with lower values of capacitances on the dc bus, it becomes even more important to

look at its effect on the ac side of the system. It can be concluded that the modeling of the actual source behind the inverter, as proposed, is required for the simulation of large systems with significant converter interfaced generation as a detailed point on wave simulation will be computationally burdensome.

5.2.2 Large Scale System: Economy of Computation

Again, the WECC 2012 system has been used to test the behavior of this model in a large scale system. This system has 18205 buses, 13670 lines and 2592 generators. The total generation is 176 GW while the total load is 169 GW. In this section, all active power producing generators in the Arizona area were replaced with the proposed model of the synchronous generator behind a rectifier-inverter set. This amounted to 169 units. The remaining 5 units in the Arizona area act as synchronous condensers and were thus replaced with inverters with an ideal dc voltage. Further, the conventional generation of all other areas were also replaced with inverters with an ideal dc voltage. Thus, again, the entire generation fleet was replaced with converter interfaced generation but in the Arizona area, the source behind the inverter was also modeled.

In the Arizona area, for conventional machines with a rating of more than 200 MVA, the synchronous generator behind the rectifier-inverter set had the same parameters as the conventional generator it replaced. For conventional machines with rating lower than 200 MVA, a standard set of default values were used for the replacement synchronous generator behind the rectifier-inverter [77]. In addition, the value of the active power droop coefficient R_p was taken to be the same as that used in the governor of the conventional machine it replaced. The initial value of α_{rect} was set as 10° while K_p and K_i were set as 1.0 and 5.0 respectively. The values of K_{ip}

and K_{iq} were set as 5.0 each. All other controller gains and time constants remained the same as in Table 5.3.

At t=15s, two units of Plant A were tripped resulting in a generation deficit of 2755 MW. Figure 5.84 shows the collective sum of the active power output of the remaining on line units in Arizona. The solid line shows the collective ac output of the inverters (P_{conv}); the dashed line shows the corresponding collective output of the generator behind the rectifier (P_{gen}). The area between the two curves corresponds to energy from the dc bus capacitance. The frequency in this pure converter interfaced

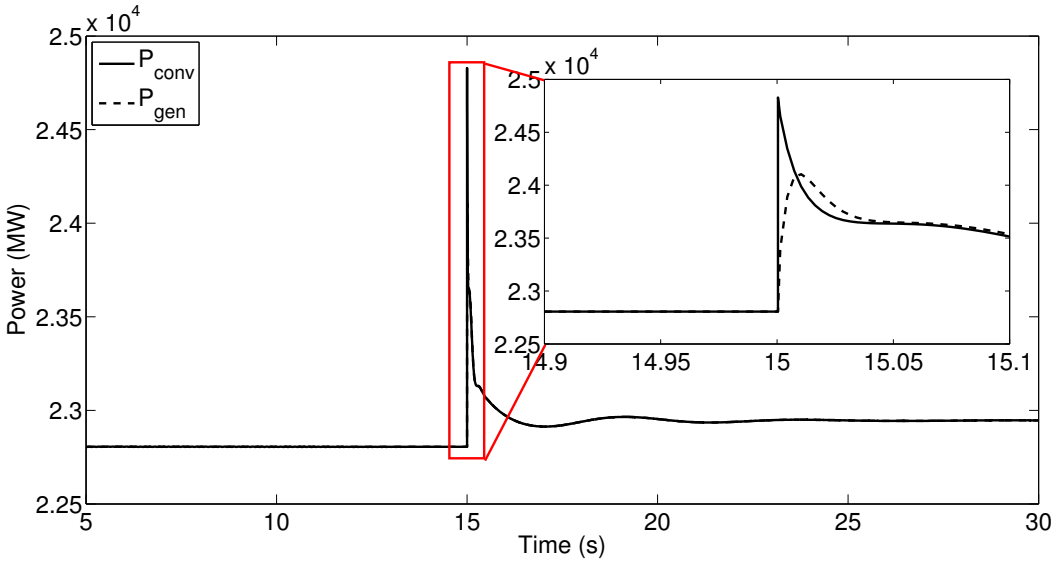

Figure 5.84: Active power output of inverter and synchronous generator behind rectifier in Arizona area for trip of two Plant A units

system is calculated as the rate of change of the terminal bus voltage angle. Figure 5.85 shows the calculated frequency in the Arizona area for the trip of two Plant A units.

It can thus be seen that the simulation with a large presence of detailed models of the source behind the inverter, is numerically stable and the increase in the runtime of the simulation is acceptable when compared to the runtime of the simulation with the source behind the inverter represented as an ideal dc voltage.

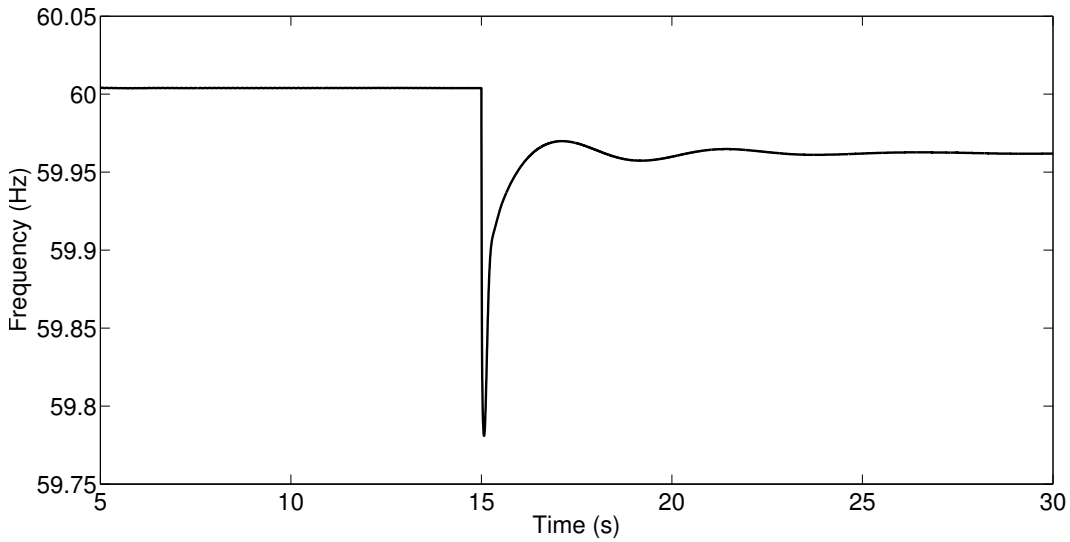

Figure 5.85: Frequency in Arizona area for trip of two Plant A units

Plant H (Figure 5.19) in the Arizona area has three 890 MVA generators at a voltage level of 26 kV. The value of τ was chosen to be 0.005s; correspondingly the value of C_{dc} was 6580 μF which is equivalent to an energy level of 24.1 MWs. The response of a unit of Plant H to the trip of two Plant A units is as shown in Figure 5.86. The figure compares the active power output of the inverter to the active power output of the generator behind the inverter. It can be seen from the figure that the

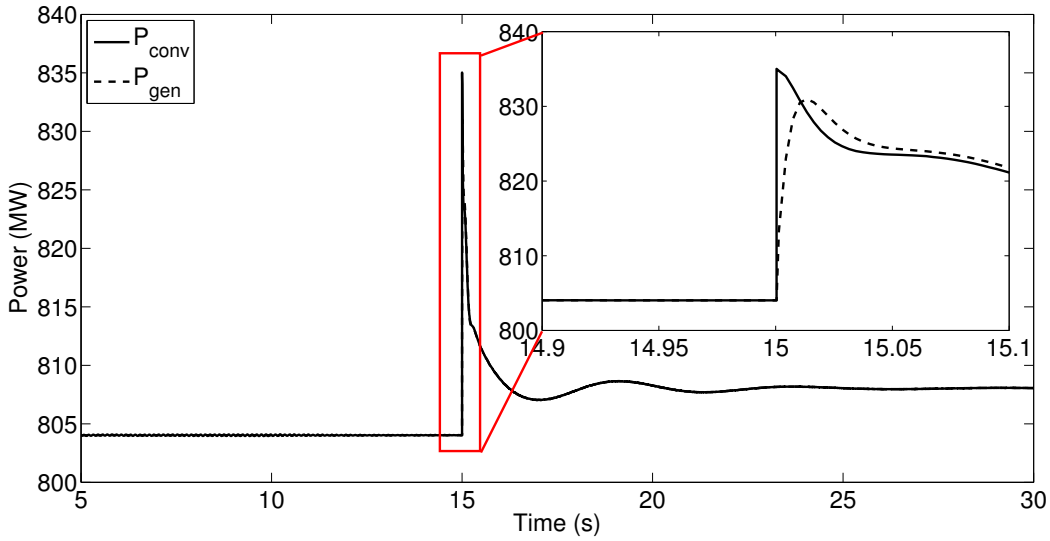

Figure 5.86: Active power response of a unit of Plant H for trip of two Plant A units

inverter, drawing power from the dc capacitor, responds quickly to the generation outage. Due to the presence of the capacitor and its assumed time constant of 5 ms, the synchronous machine behind the rectifier is not loaded immediately and thus the machine response to the outage is smooth.

The withdrawal of power from the capacitor causes the dc voltage and the terminal voltage to drop as shown in Figure 5.87. Though a larger capacitor would reduce

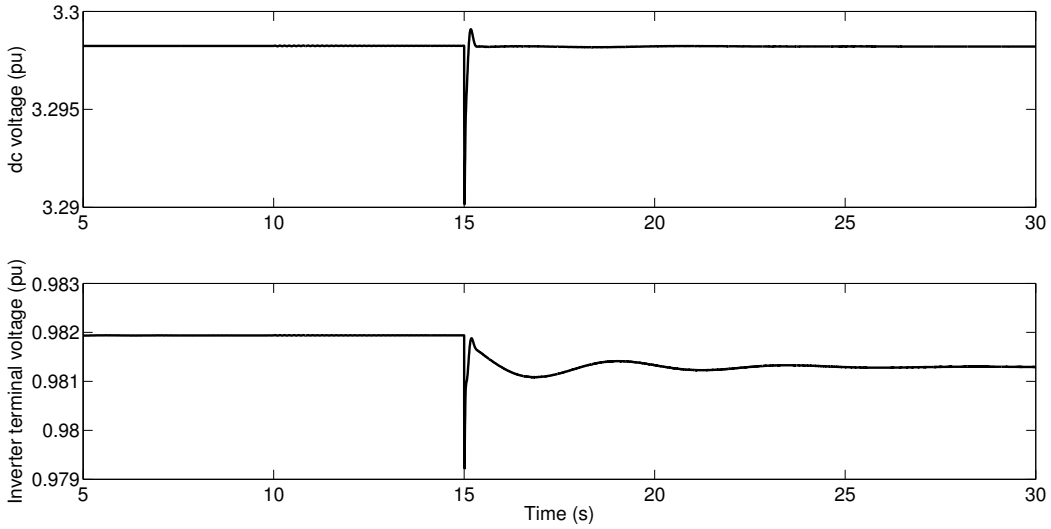

Figure 5.87: Dc voltage and inverter terminal voltage of a unit of Plant H for trip of two Plant A units

the drop in voltage, it would also be a safety hazard due to the large amounts of energy stored and the near instantaneous discharge of energy upon the occurrence of a contingency.

To further illustrate the need for use of this detailed model, primary frequency response participating units in the Southern California area were also replaced by this detailed model. Again, the value of the active power droop coefficient R_p was taken to be the same as that used in the governor of the conventional machine that was replaced. A standard set of default values were used for the replacement synchronous generator behind the rectifier-inverter [77].

With a large renewable energy footprint, at a given time of the day, there could be a possible situation wherein generating sources in multiple areas of the system would not be able to provide primary frequency response. Such a situation can have implications both in the post contingency steady state operating condition and transient behavior of the system. In order to study a possible scenario, units in the Northwest, British Columbia, and other areas in California were blocked from participating in primary frequency response for a generation outage contingency. While conducting a steady state analysis, the lost generation was re-dispatched among the units that were allowed to participate in primary frequency response (not on baseload). A simple re-dispatch based on the size of the unit was implemented with a rudimentary distributed slack bus scheme. Additionally, area interchange control was disabled while re-solving the power flow. The parameters of interest in this analysis were the incremental system wide losses and the increase/decrease of flow on couple of critical tie lines (shown in Figure 5.19) and interfaces. The results are tabulated in Table 5.4 for the trip of two units of Plant A.

It can be seen that there is an increase in system wide losses. Additionally, the post contingency flow on tie line 1 and the North-South California Interface is greater than the steady state rating of the interface. While this may not be an issue for a short amount of time, additional reserves could have to be brought on line in a timely manner to maintain the reliability of the system.

To investigate the transient behavior of the system under the same conditions, at t=15s, two units of Plant A were tripped. Figure 5.88 shows the calculated frequency in the Arizona area and the system mean frequency for the trip of these two units. Also, the frequency plot shows the comparison between use of the ideal dc voltage converter model for all units (including Arizona and Southern California) and use of the detailed model for units in Arizona and Southern California (with the remaining

Table 5.4: Change in tie line power flow and system losses after re-dispatch following a generator contingency

	Base case	After re-dispatch		Rating
	MW	MW	ΔMW	MVA
System Losses	5856.36	6372.26	515.90	
Tie 1	4114.84	4883.00	768.16	4800
Tie 2	3050.06	3050.05	-0.01	3100
Arizona - California Interface	4240.96	2676.89	-1564.07	5700
N-S California Interface	3527.31	5041.74	1514.43	4000

units in the system having an ideal dc voltage). It can be seen that with the repre-

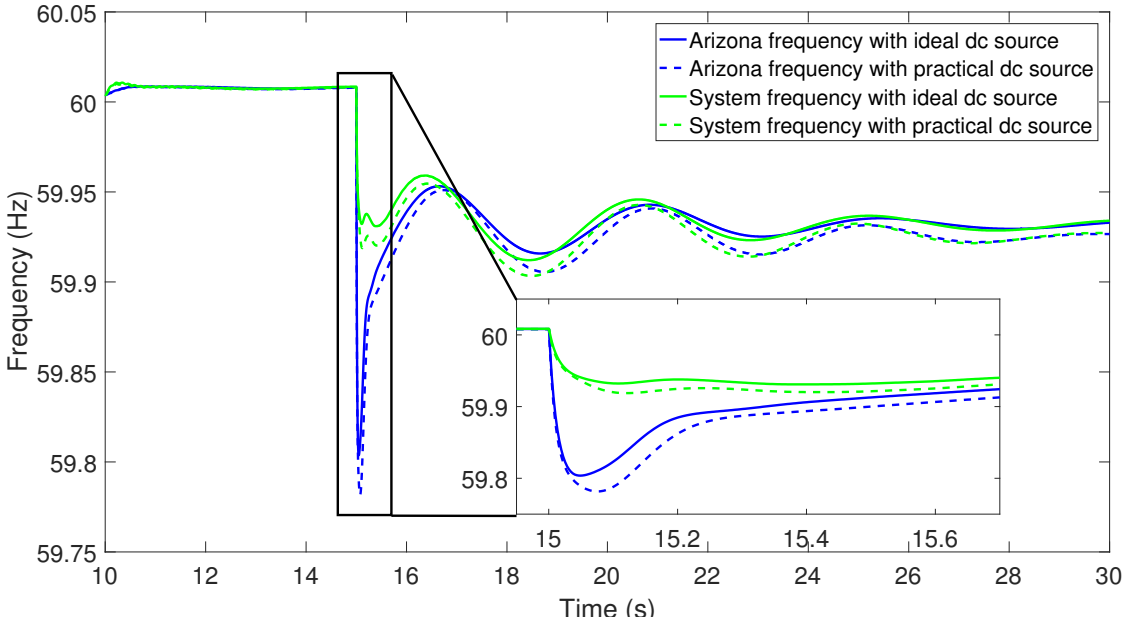

Figure 5.88: System mean frequency and frequency in Arizona area for trip of two Plant A units with limited frequency response capacity

sentation of the source behind the inverter (termed as practical dc source), the nadir of the system frequency is slightly lower while also occurring slightly later.

In terms of computation time, PSLF took 27.14 minutes to run this 30 second simulation. In comparison to this, when all machines were represented as converters with an ideal dc voltage source, PSLF took 25.44 minutes to run the 30 second simulation of this generation outage scenario. All simulations were run on a machine with an i7 processor and 16.0 gb of RAM with a simulation time step of 0.001s.

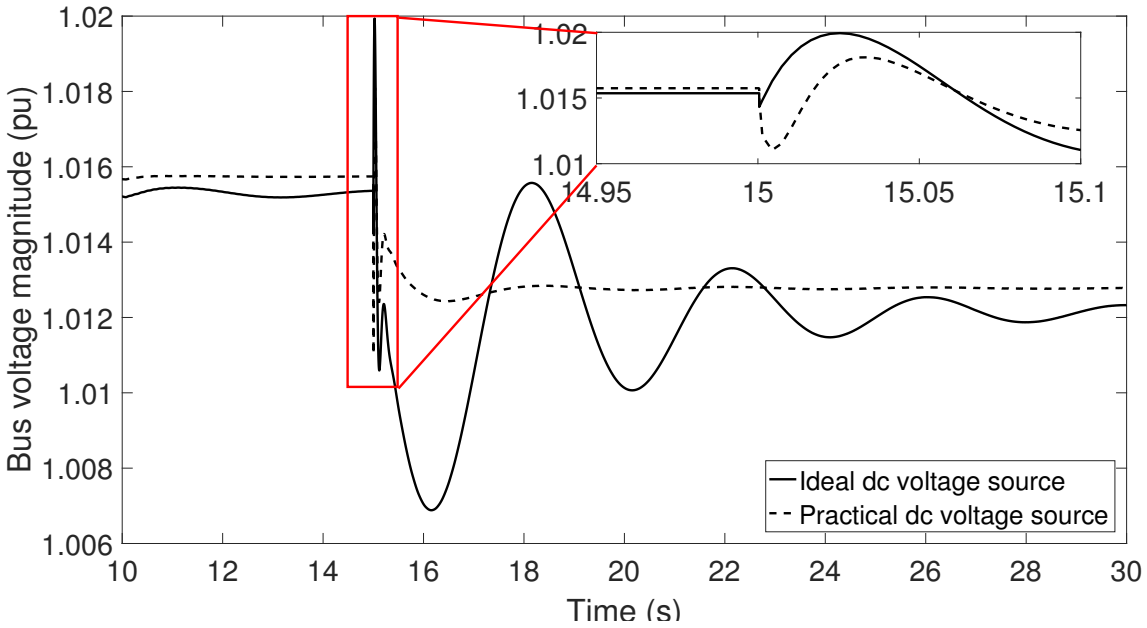

Figure 5.89: Bus voltage magnitude near Plant A

Figures 5.89 and 5.90 show the bus voltage magnitude near Plant A and Plant G respectively. The figures also compare the voltage magnitude between use of the ideal dc voltage converter model and the detailed model with representation of the source behind converter. As before, it can be seen that use of the detailed model provides a more detailed representation of the behavior of the system. As seen from the figures, at the instant of disturbance, the dip in the magnitude of ac terminal voltage is more when using the practical dc voltage source representation. However, when an ideal

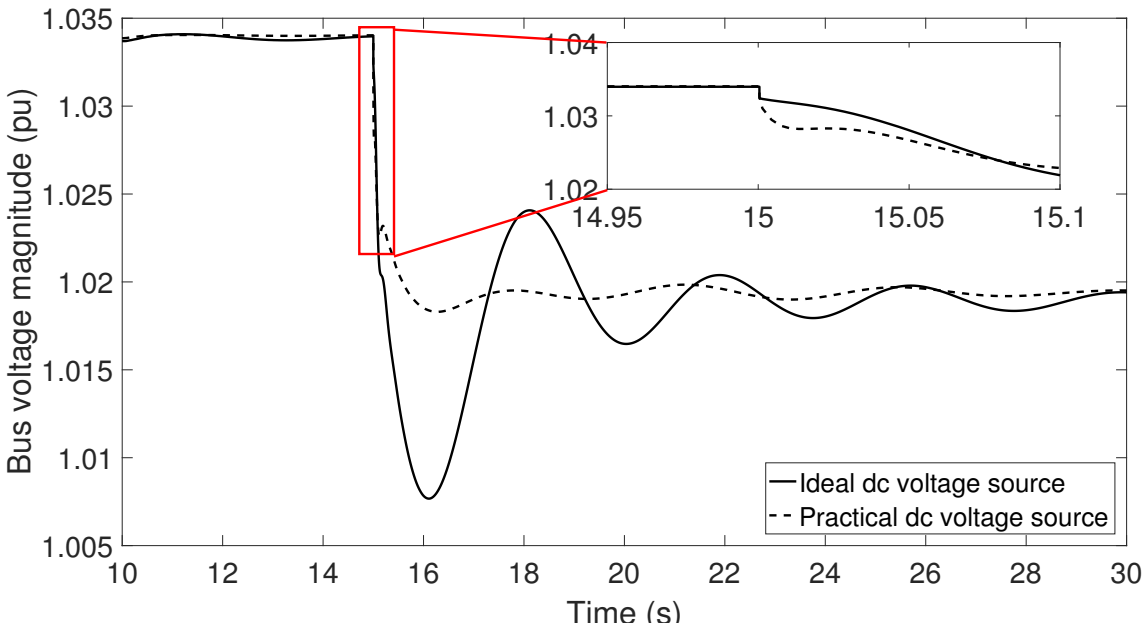

Figure 5.90: Bus voltage magnitude near Plant G

dc voltage source representation is used, the oscillatory behavior is more pronounced. Thus, while these plots concur with the trend of the plots shown in Figure 5.78, it would be difficult to comment on the exact reason for this difference in oscillatory behavior without a detailed small signal analysis.

To further observe the effect of the dc capacitance on the system performance, Figure 5.91 shows the output of the synchronous machine behind the inverter in the Arizona area for two different values of τ. The larger value of τ corresponds to a larger value of capacitance on the dc bus. To meet the immediate requirements of the network following a disturbance, a larger capacitance provides more energy. Thus, the synchronous machine behind the rectifier notices the change in network conditions after a longer duration of time. This can also be surmised from the larger area between the P_{conv} curve and the $P_{gen} - \tau = 0.05s$ curve. In comparison however, the frequency plot (Figure 5.92) for these two values of capacitances does not show much difference in the nadir.

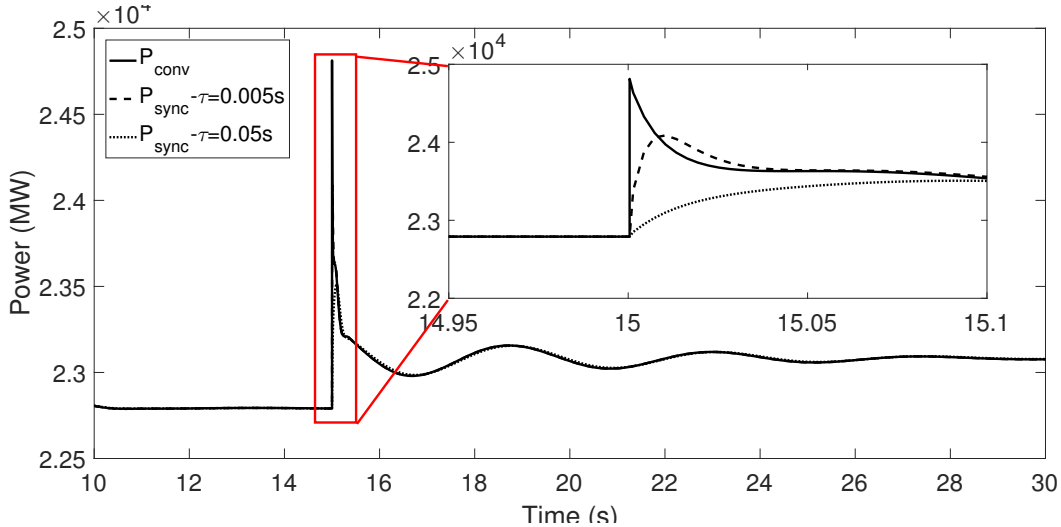

Figure 5.91: Comparison of active power output of synchronous generator behind rectifier in Arizona area for trip of two Plant A units with limited frequency response capacity

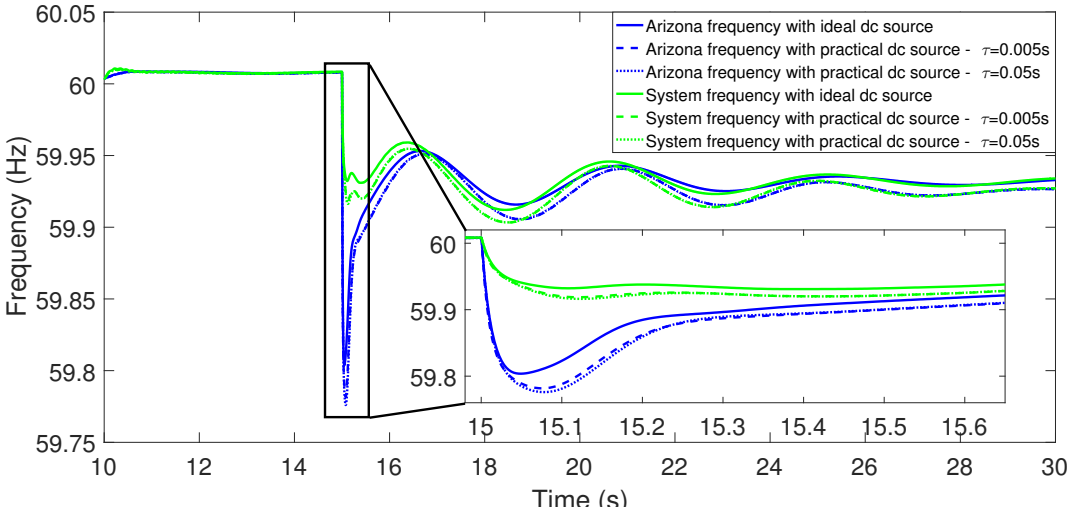

Figure 5.92: Comparison of system mean frequency and frequency in Arizona area for trip of two Plant A units with limited frequency response capacity

Thus, while moving towards a system with large penetration of CIG, with CIG sources participating in primary frequency response, use of this detailed source behind inverter model (rather than the ideal dc voltage source converter model) could give a better estimate of the performance of the system. This simulation has also served

to validate the numerical stability of the model when present in large numbers in the simulation of a large system in a commercial simulation software.

5.3 Induction Motor Drive Model

The performance of the motor drive model was analyzed using two different systems. First, an equivalent transmission system was used to validate the performance. Following this, a sample test distribution feeder was used to observe the performance of the model to changes in the source substation voltage and frequency.

5.3.1 Equivalent Transmission System

The three machine nine bus system as shown in Figure 5.4 was again used to analyze the performance of the speed drive model. The synchronous generators were represented by detailed models with associated thermal governors and static exciters. For the machine models, the parameter values provided in [89] were used. For the governor model, a basic steam turbine governor model (TGOV1 in commercial simulation software) was used with the following parameter values - time constant T_G=0.5s and transient gain reduction T_1/T_2=3.0/10.0. An active power droop of 0.05pu on the system 100MVA base was present on all three governors. The static excitation system was represented by a single gain and time constant with values of 200 and 0.02s respectively. The static load at bus 5 was replaced with an induction motor of inertia constant 0.3s on a 100MVA base and a speed damping factor of 2.0pu. The parameters of the motor are given in Table A.5 in the appendix.

With reference to the speed control block diagram (Fig. 4.21), the values of the controller gains K_{pdrive} and K_{idrive} were taken as 5.0 and 4.0 respectively while the value of $\omega_{sl_{ind}}^{ref}$ was limited to be between 0.15pu and 0.001pu. The following sections describe the various scenarios studied.

5.3.1.1 Static Load Increase

At t=5s, the static load at bus 6 was increased by 10MW. Figure 5.93 shows the speed of the motor both with and without the speed control drive present while Figure 5.94 shows the electrical torque developed by the motor. In order to validate the performance of the independently developed C code, the figures also show the response obtained from PSLF Version 18.1_01 for an induction motor without the presence of the speed control drive. A motor without the presence of a speed control drive represents a directly connected motor. Comparing the responses, it can be observed

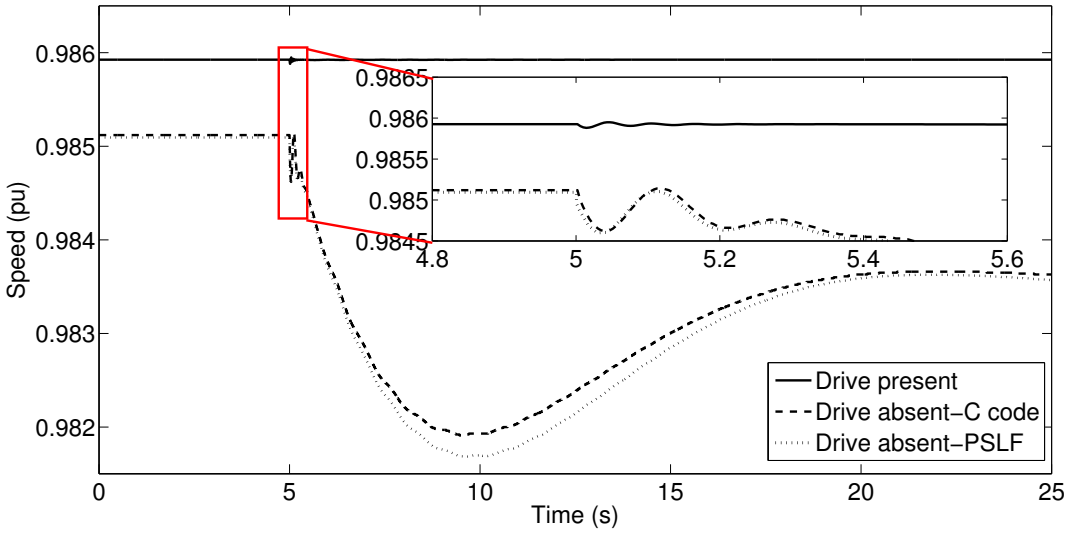

Figure 5.93: Speed of induction motor for a 10MW static load increase

that in the absence of the drive, the performance of the C code emulates the response obtained from PSLF. The difference in the procedure used to evaluate the slip and reactive power consumption results in the slight difference visible from the figures. Further, the speed control drive is successful in maintaining the speed of the motor at the pre-disturbance value. When the drive is present, the pre-disturbance value of speed differs from the pre-disturbance value of speed when the drive is absent due to different motor terminal voltages caused by the different reactive power consumptions

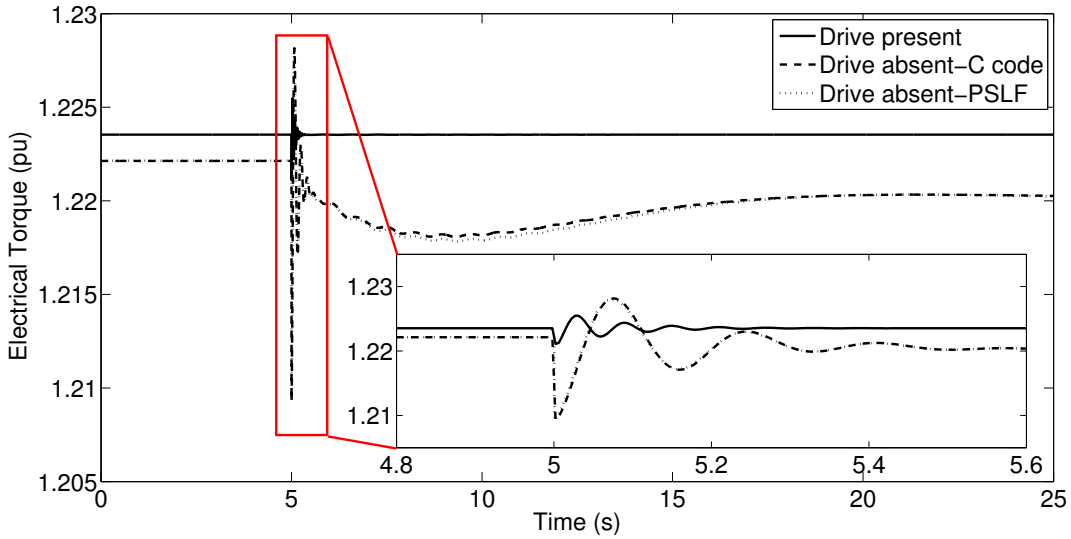

Figure 5.94: Developed electrical torque of induction motor for a 10MW static load increase

at the network terminal. With the speed maintained at the pre-disturbance value following the transient, based on (4.38), the mechanical torque and hence the developed electrical torque are also at their pre-disturbance values as observable from Figure 5.94. As the pre-disturbance value of speed with the drive present is different from that with the drive absent, for the same active power load P_{m0}, the pre-disturbance value of electrical torque differs with the presence and absence of a drive, as shown in Figure 5.94.

The static load increase causes a change in the bus voltages across the system. Figure 5.95 shows the bus voltage magnitude at the induction motor bus, bus 5. Upon the occurrence of the disturbance, it can be seen that the magnitude of the bus voltage first decreases. This decrease in voltage would cause the slip of the motor to increase as is evident from the decrease in speed shown in Figure 5.93. Due to control action of the drive, this decrease in motor speed causes an increase in the reference stator angular speed (ω_s^{ref}) as seen in Figure 5.96. To maintain constant air gap flux within the motor, this increase in ω_s^{ref} has to be accompanied by a proportional

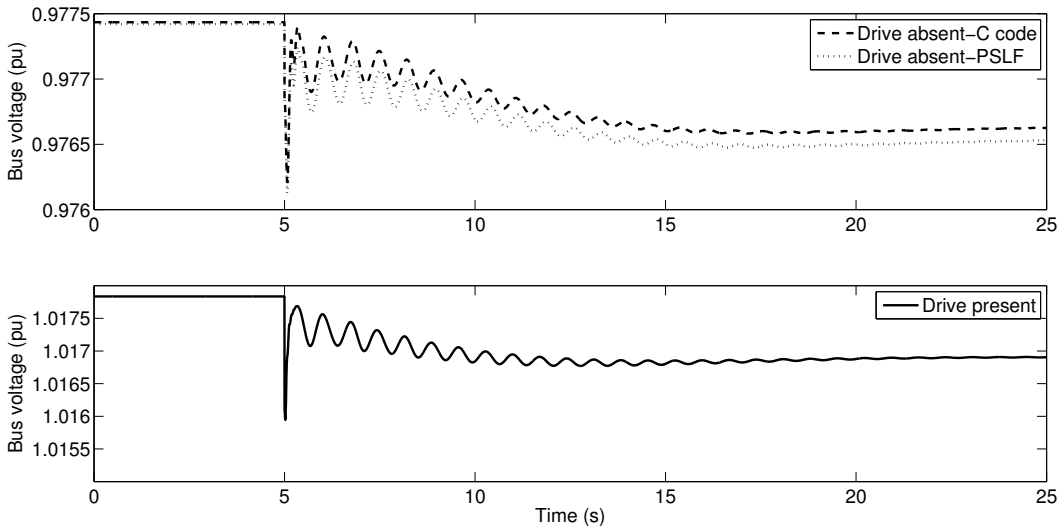

Figure 5.95: Bus voltage magnitude at induction motor bus for a 10MW static load increase

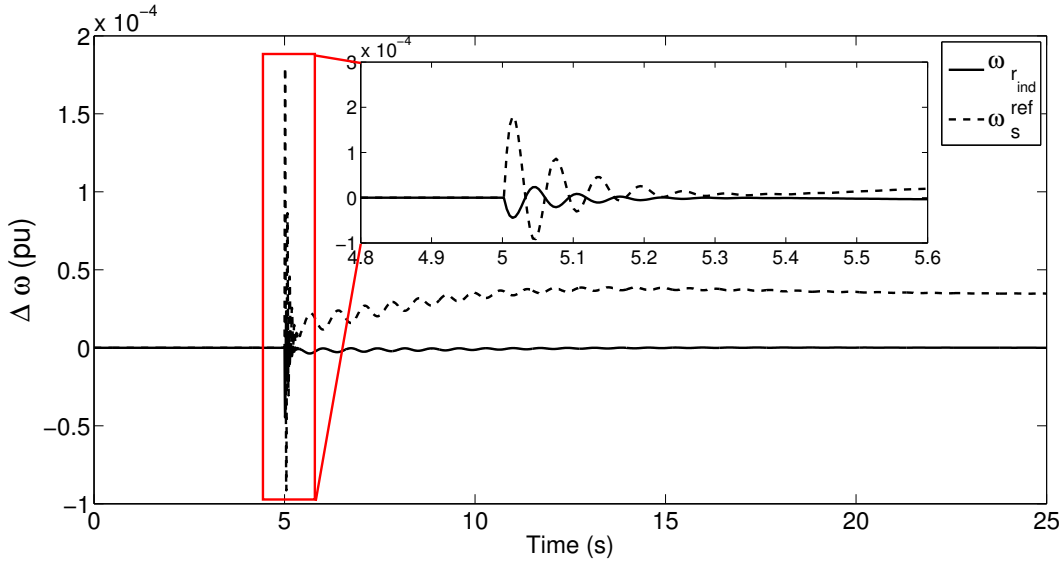

Figure 5.96: Change in rotor speed and reference stator angular speed for a 10MW static load increase

increase in stator voltage magnitude reference (V_s^{ref}) (4.57). In order to maintain constant flux in the motor, an increase in stator frequency would cause the stator voltage magnitude reference (V_s^{ref}) to also increase, represented as an increase in the modulation index m_{ind}, by (4.57).

As the rectifier of the drive is an uncontrolled rectifier, the voltage on the dc side is proportional to the magnitude of voltage on its ac side. Further, as the amplitude modulation index m_{ind} of the inverter has a maximum allowable value of 1.0, the per unit magnitude of voltage on the ac side of the inverter would be lower than the corresponding per unit voltage magnitude on the ac side of the rectifier. As a result, to maintain the same amount of developed electrical torque, the magnitude of current drawn by the motor behind the drive would be higher than the magnitude of current drawn by the motor when the drive is absent. This results in a lower voltage magnitude at the induction motor bus.

With the mechanical load on the motor being constant and the speed held constant by the drive, the active power consumed at the motor bus is also held constant at the pre-disturbance value with the presence of the drive as shown in Figure 5.97. With the drive present, a slight increase in the magnitude of consumed current results in a slight increase in reactive power consumed by the motor to maintain constant flux and this is observable from Figure 5.98. This reactive power demand of the induction motor is met by the inverter. The reactive power consumption of the rectifier is due to the presence of commutation losses resulting in a lagging power factor operation. Thus, the rectifier draws reactive power from the network. Following the transient, the increased current drawn by the motor increases the magnitude of current drawn by the rectifier from the network bus. From (4.46) and (4.48), this increased rectifier current results in a decrease in the power factor, resulting in an increase in reactive power drawn by the rectifier from the network.

With the drive absent, the reactive power consumption decreases slightly as the speed of the motor and the voltage at the terminal is slightly lower than their respective pre-disturbance values.

The active power outputs of the three generators are as shown in Figure 5.99. It

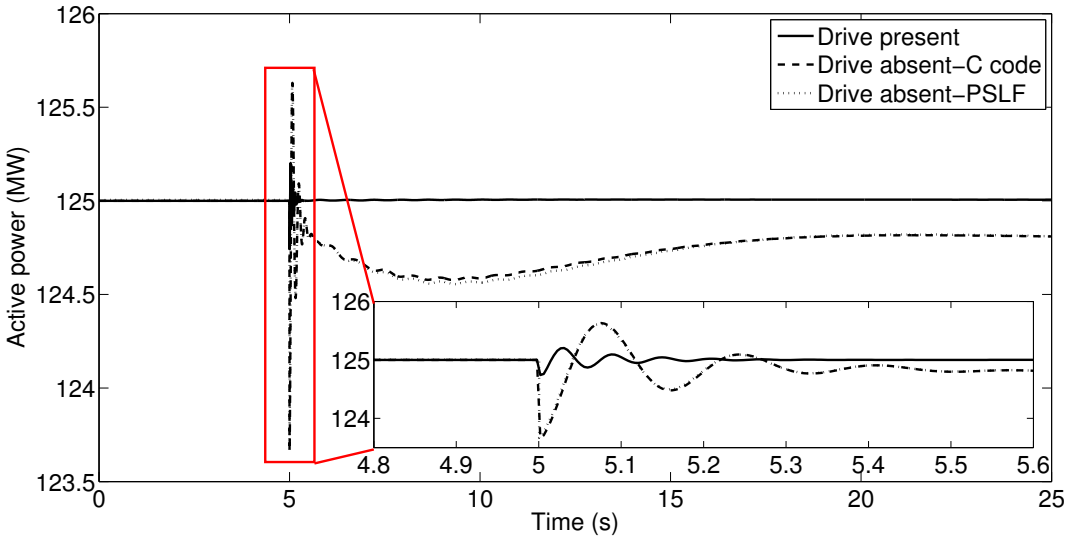

Figure 5.97: Active power consumed by induction motor for a 10MW static load increase

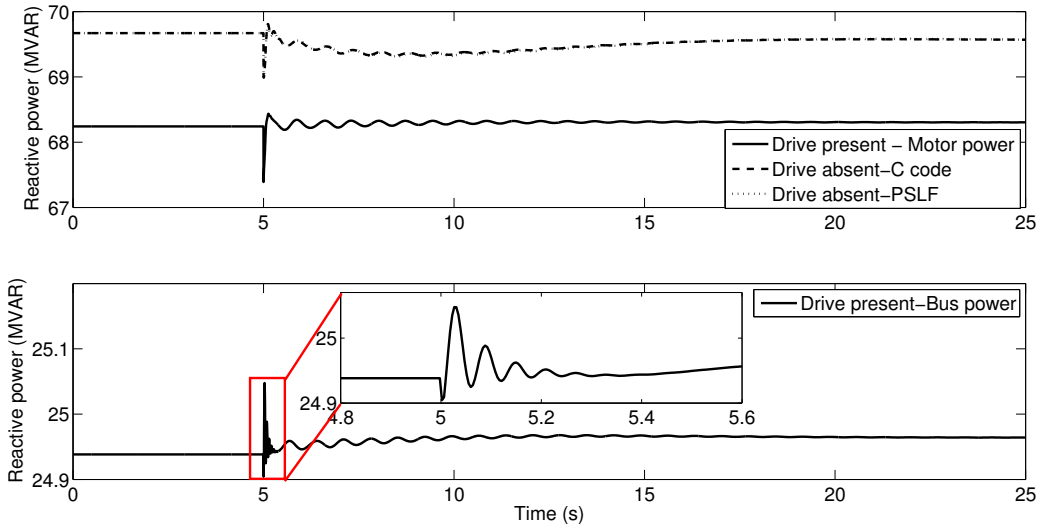

Figure 5.98: Reactive power consumed by induction motor and rectifier for a 10MW static load increase

can be seen from the results of this scenario that with the drive absent, the results from the C code are coincident with the results from PSLF thereby validating the accuracy of the C code for use in the transient stability time domain simulation. Thus, the response from the C code has not been compared with the response from PSLF in the two subsequent scenarios.

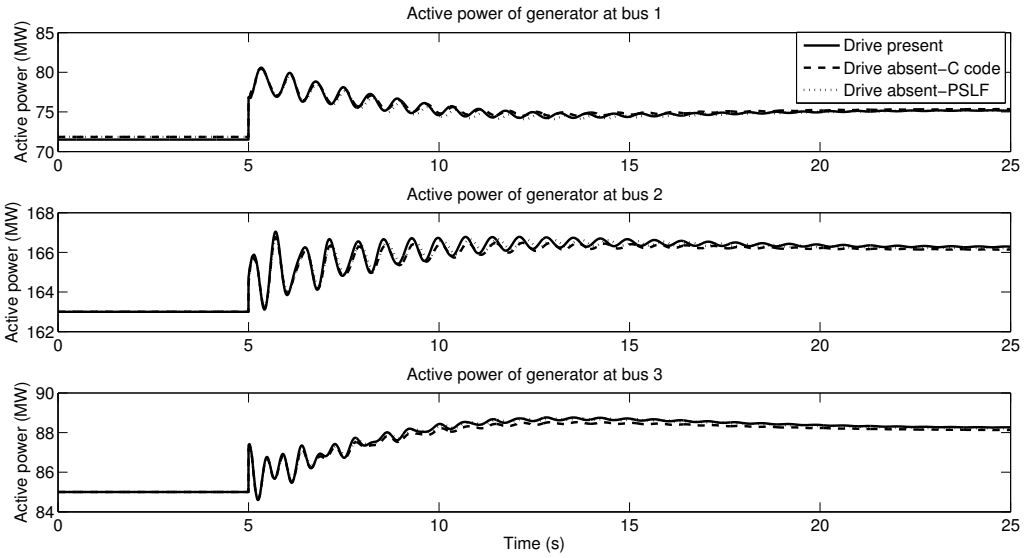

Figure 5.99: Active power output of synchronous machines for a 10MW static load increase with induction motor

5.3.1.2 Induction Motor Load Increase

In this scenario, the active power consumed by the motor is increased by 0.1pu at t=5s. Figure 5.100 shows the speed of the induction motor again both with and without the presence of the drive while Figure 5.101 shows the electrical torque developed by the motor. From Figures 5.100 and 5.101 it can be seen that the speed control drive fulfills the primary objective of maintaining the speed of the motor at the pre-disturbance value while simultaneously ensuring that the load torque is met. Figures 5.104 and 5.105 show the electrical power drawn by the motor at the network bus while Figure 5.102 shows the voltage magnitude at the bus. The control signal from the drive is as shown in Figure 5.103. The increased value of P_{m0} results in an increase in current drawn by the motor, which results in the reactive power increase at the ac terminal of the drive.

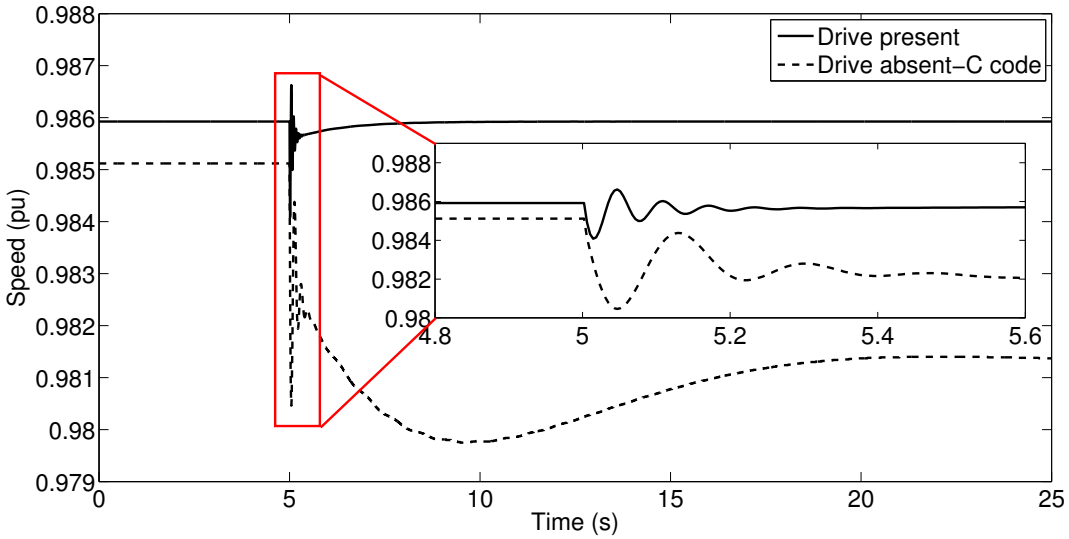

Figure 5.100: Speed of induction motor for a 0.1pu increase in motor load torque

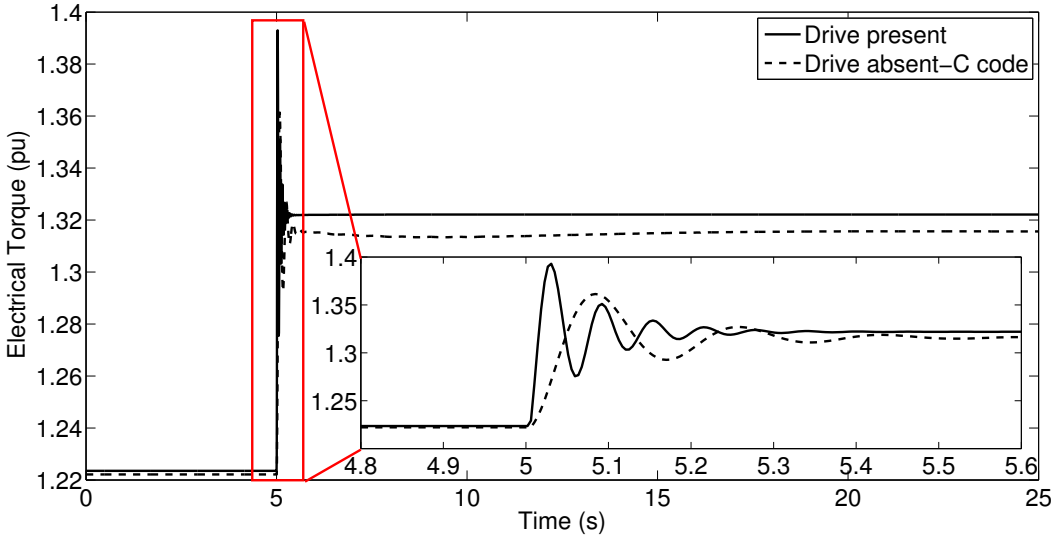

Figure 5.101: Developed electrical torque of induction motor for a 0.1pu increase in motor load torque

5.3.1.3 Change in Reference Rotor Speed

For a constant steady state load of P_{m0}, a need could arise that requires the motor to operate at a different speed. This can be achieved by changing the value of $\omega_{r_{ind}}^{ref}$ of Figure 4.21. In this scenario, at t=5s, the value of $\omega_{r_{ind}}^{ref}$ was increased by 0.01pu. The speed of the motor, as controlled by the drive model, is as shown in Figure 5.106. In

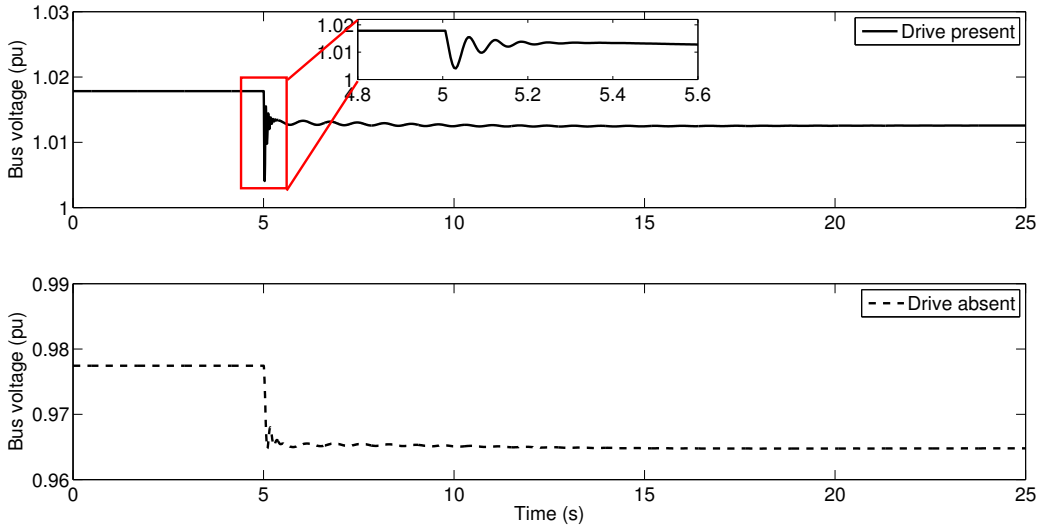

Figure 5.102: Bus voltage magnitude at induction motor bus for a 0.1pu increase in motor load torque

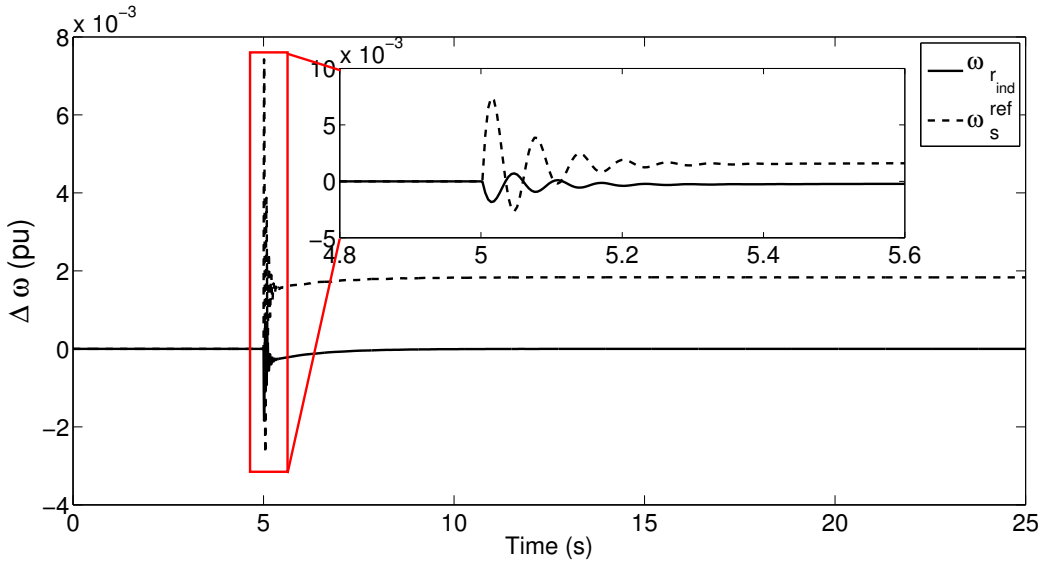

Figure 5.103: Change in rotor speed and reference stator angular speed for a 0.1pu increase in motor load torque

order to accelerate the motor, initially, the electrical torque developed would have to increase thereby increasing the active power drawn from the network. The increase in current will also result in an increase in reactive power drawn from the network. This can be observed from Figures 5.107 and 5.108 respectively. As the motor accelerates,

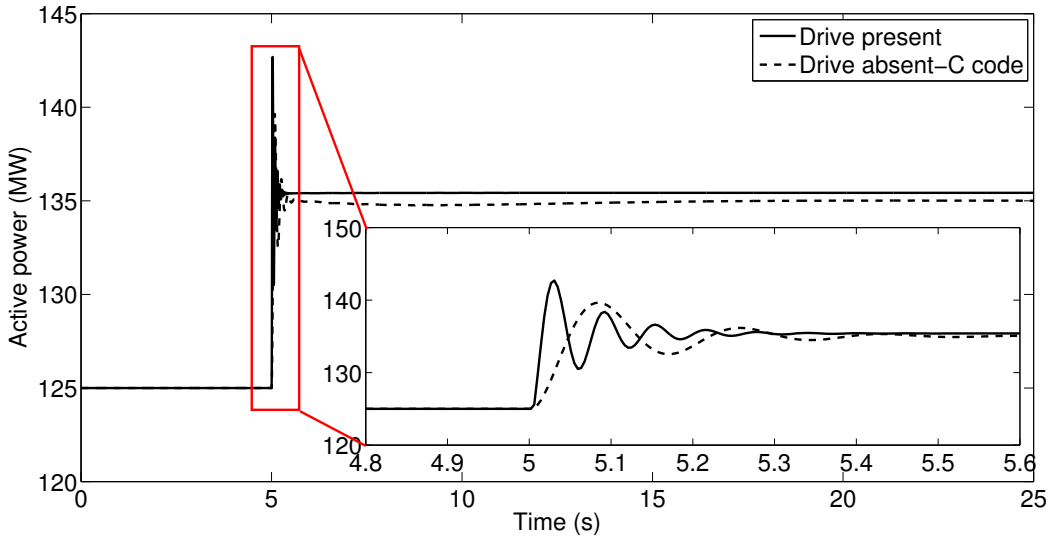

Figure 5.104: Active power consumed by induction motor for a 0.1pu increase in motor load torque

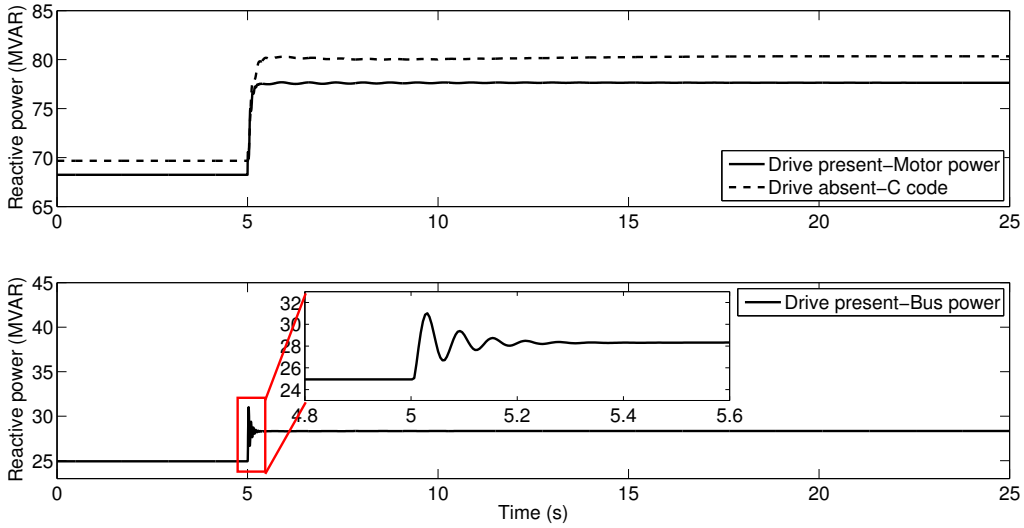

Figure 5.105: Reactive power consumed by induction motor and rectifier for a 0.1pu increase in motor load torque

the slip reduces, thereby transiently reducing the total active power drawn from the network. However, as the steady state load on the motor (P_{m0}) has not changed, the steady state active power settles at the pre-disturbance value while the electrical torque developed varies according to (4.38) to settle at a slightly increased steady state value. This results in a slight increase in the magnitude of current drawn by the

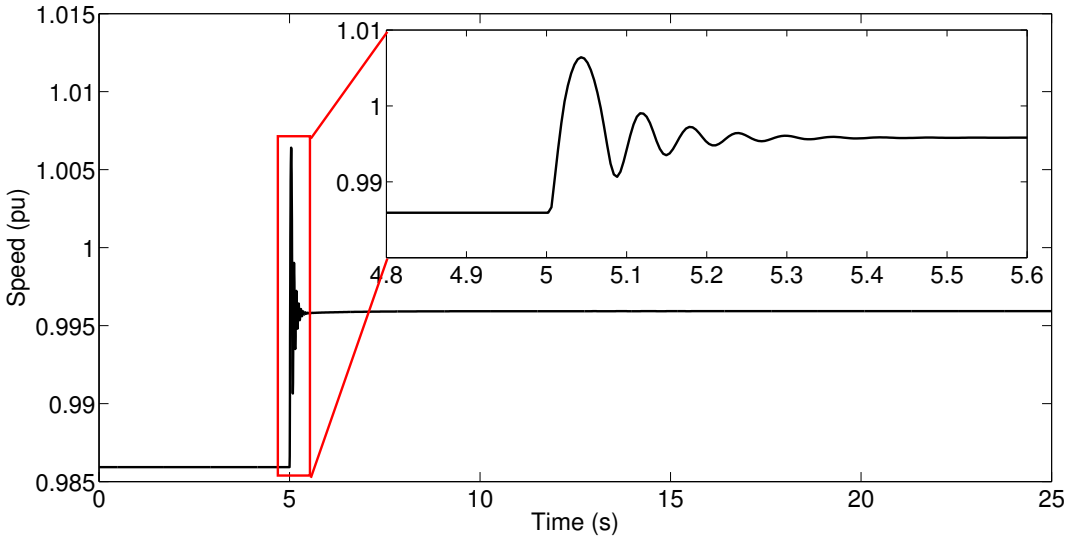

Figure 5.106: Speed of induction motor for a 0.01pu increase in reference rotor speed

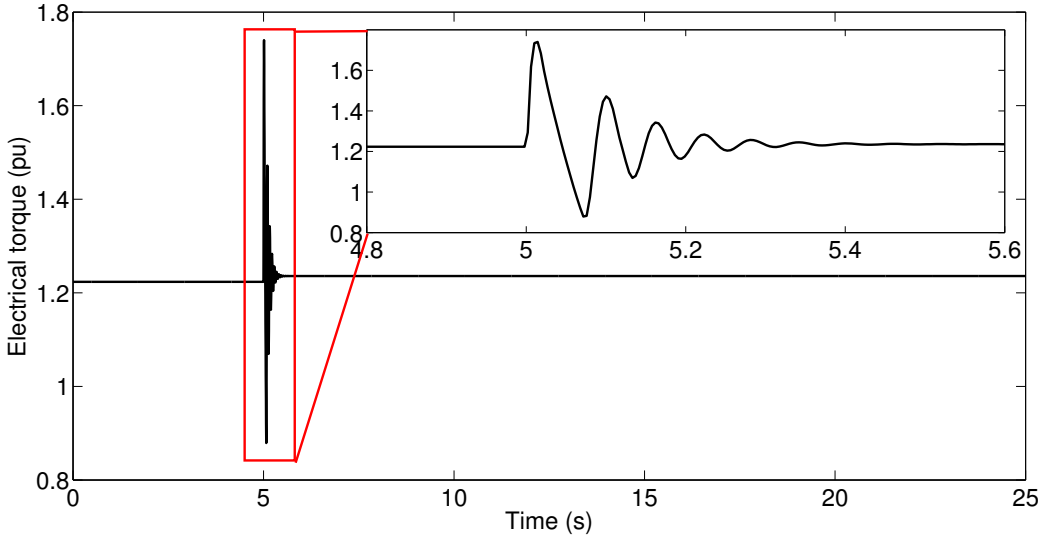

Figure 5.107: Developed electrical torque of induction motor for a 0.01pu increase in reference rotor speed

motor thus, resulting in a marginal increase of reactive power drawn from the network bus, observable from Figure 5.108. The marginal increase in current also manifests as a marginal decrease in the voltage magnitude of the induction motor bus as shown in Figure 5.109.

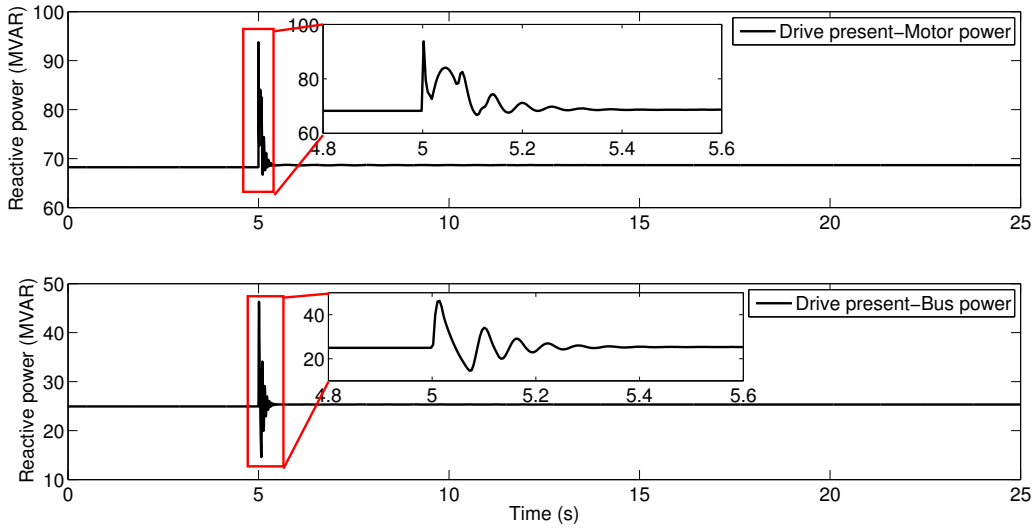

Figure 5.108: Reactive power consumed by induction motor and rectifier for a 0.01pu increase in reference rotor speed

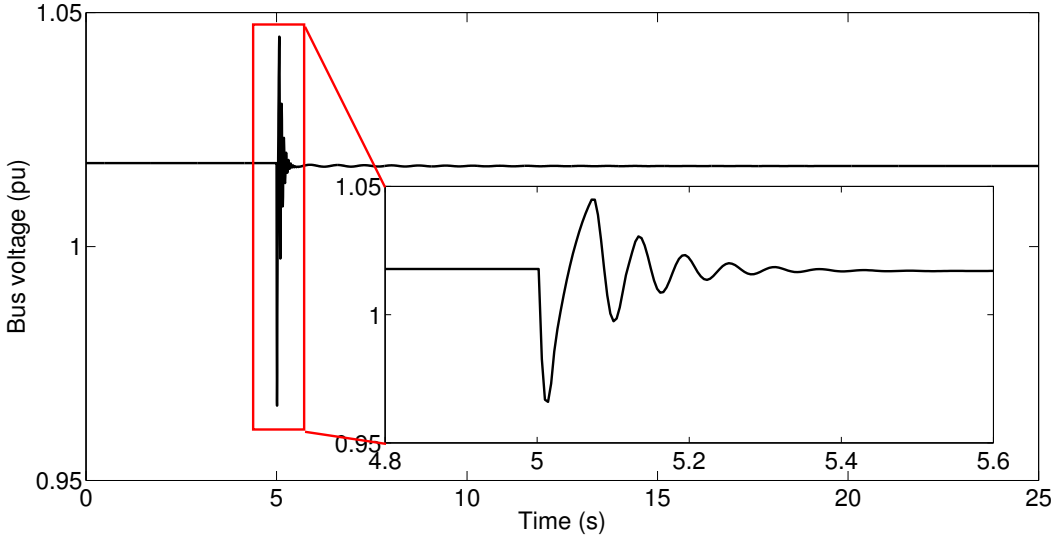

Figure 5.109: Bus voltage magnitude at induction motor bus for a 0.01pu increase in reference rotor speed

The behavior and validation of the performance of the induction motor speed control drive is thus showcased by these results. The following section looks at the performance in a distribution feeder with multiple drive interfaced motors.

5.3.2 Distribution System Feeder

With an increase in penetration of induction motor speed drives in the distribution system, it is important to analyze the performance of multiple motors on a feeder fed from a single substation source. Further, with the single source modeled as a Thévenin source, the performance of the drive model can be captured for controlled changes in the source behavior. The test system constructed is as shown in Figure 5.110. The locations and values of the capacitor banks C_5, C_6 and C_7 and

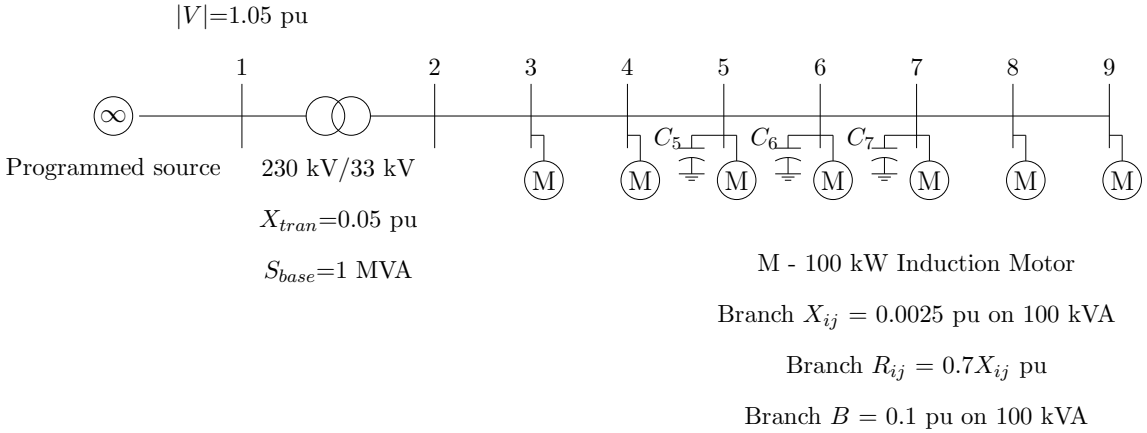

Figure 5.110: Test distribution system feeder

the value of the voltage magnitude at bus 1 were decided to ensure a voltage magnitude between 1.0pu and 1.01pu at bus 9. Additionally, the sum total of all allowed capacitor banks was restricted to a maximum of 300 kVAR. With all motors being identical, the motors parameters in per unit on a 100 kVA base are as given in Table 5.5. The values of the controller gains K_{pdrive} and K_{idrive} (Figure 4.21) were taken as 0.5 and 1.0 respectively while the value of $\omega_{sl_{ind}}^{ref}$ was limited to be between 0.15pu and 0.001pu. The programmed source was represented as a Thévenin voltage whose voltage magnitude and frequency could be controlled.

With the motors directly connected without a drive, the values of the capacitor banks were: C_5=20 kVAR, C_6=20 kVAR, C_7=220 kVAR. With the drive present

Table 5.5: Distribution system induction motor parameters

Parameter	**Value**
X_s	3.5
X'_s	0.17
R_s	0.015
T'_o	0.2s
H_{ind}	0.1s
D_{ind}	2.0
$X_{s\ell}$	0.1

on all motors, the values of the capacitor banks were: C_5=0 kVAR, C_6=0 kVAR, C_7=100 kVAR. The following sections describe the various scenarios studied, with each scenario comparing the behavior of the motors with speed drives present and speed drives absent.

5.3.2.1 Change in Frequency of the Programmable Source

A significant contingency event in the transmission system can cause the frequency in the system to change. At the distribution end of the system, this change in frequency is represented as a change in the frequency of the programmable voltage source. In order to model a drop in frequency, it was assumed that the nadir be around 0.99pu, ten seconds after the occurrence of the event. The final steady state value of the frequency was assumed to be around 0.995pu with a settling time of 40s after the occurrence of the event. With these assumptions, the frequency of the source was modeled as given by (5.6) and shown in Figure 5.111 with the change in

frequency initiated at t=5s.

$$f_{thev}(t) = \begin{cases} 1.0 & \text{if } t \leq 5 \\ 0.9955 + 0.0045e^{-0.099(t-5)}\cos(0.3178(t-5)) & \\ \quad + 0.00141e^{-0.099(t-5)}\sin(0.3178(t-5)) & \text{otherwise} \end{cases} \tag{5.6}$$

The active and reactive power drawn by the motor at the far end of the feeder at

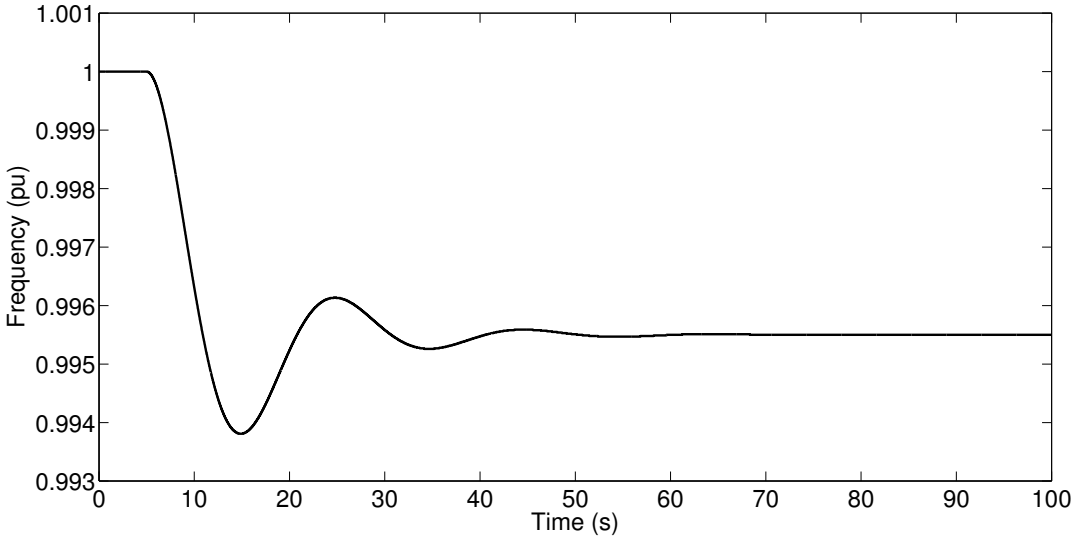

Figure 5.111: Applied frequency change

bus 9 is as shown in Figures 5.112 and 5.113 respectively. The figures compare the performance both with the presence and absence of the speed drive. The total active and reactive power supplied by the source at bus 1 is as shown in Figure 5.114. It can be seen from Figures 5.112, 5.113 and 5.114 that with the reduction in frequency, the active power drawn by the motor from the network and the active power demand on the source reduces when the drive is absent. However, with the presence of the drive, the frequency reduction has no effect on the active power consumed by the motor and the active power demand on the source. Similarly, with the presence of the drive, the reactive power consumed by the motor and rectifier and the reactive power demand on the source remain unchanged. This is due to the fact that the operation of an

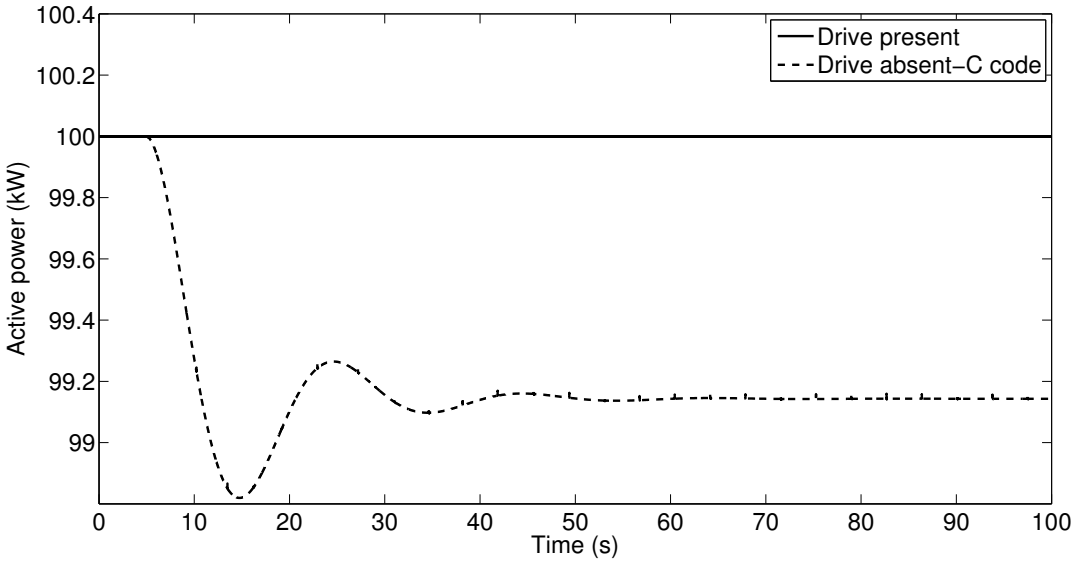

Figure 5.112: Active power consumed by motor at bus 9 for frequency change applied to the voltage source

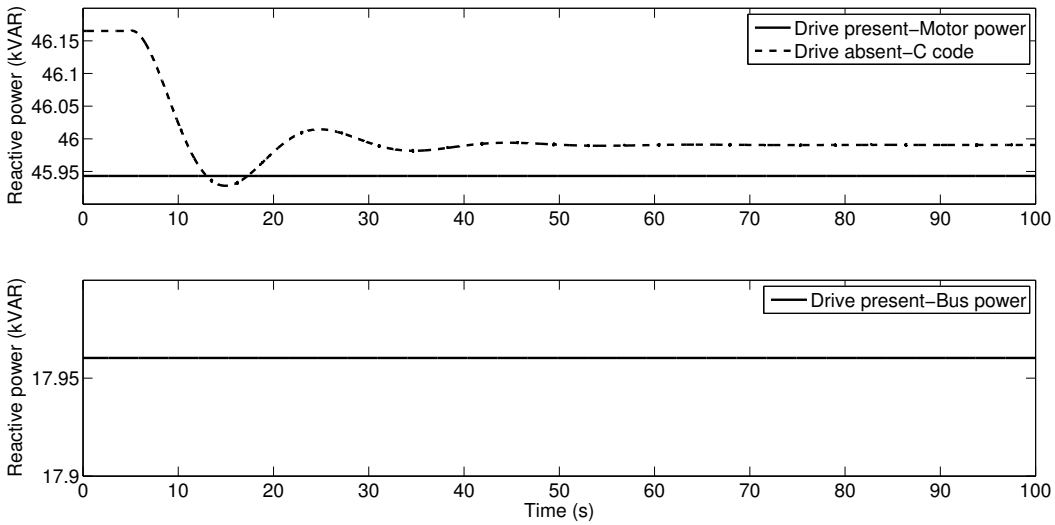

Figure 5.113: Reactive power consumed by motor and rectifier at bus 9 for frequency change applied to the voltage source

uncontrolled rectifier depends only on the magnitude of its ac side voltage and the magnitude of the dc current. A frequency change is essentially a change in the rate of change of phase angle; thus the magnitude of the ac side voltage of the rectifiers remain unchanged as the network reactances are assumed to be frequency invariant.

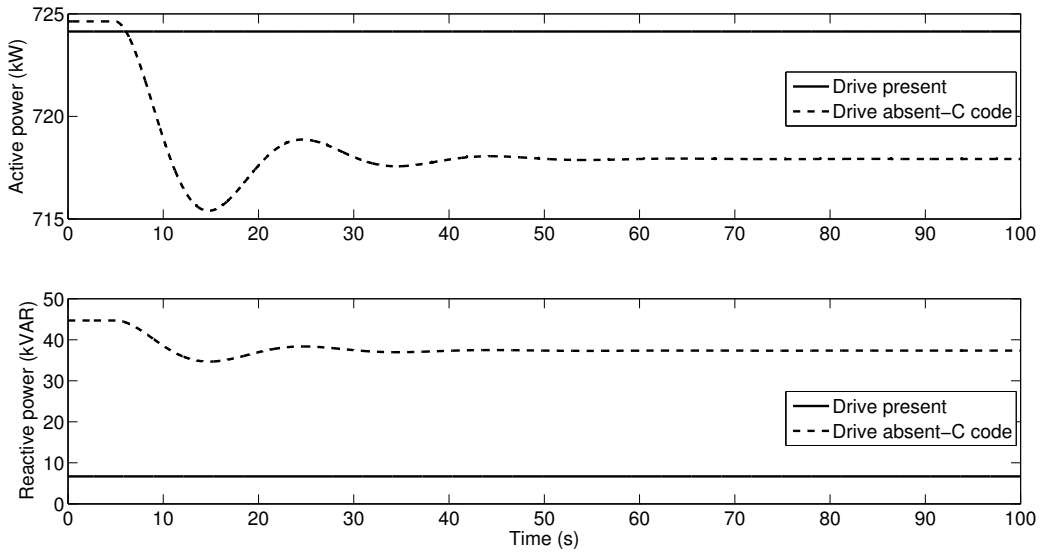

Figure 5.114: Active and reactive power at bus 1 for the applied frequency change

In comparison, when the motor is directly connected to the network without a drive, a change in the phase angle of the ac terminal voltage results in a change in the current drawn by the motor which changes the power drawn by the motor. As the supply frequency reduces, the motor speed reduces as shown in Figure 5.115 thereby reducing the developed electrical torque as shown in Figure 5.116 for constant power load. This causes a reduction in the current drawn by the motor resulting in reduced power drawn from the network. In the absence of the drive, the reduced magnitude of current on the line along with the presence of the capacitor banks results in a higher voltage profile as seen in Figure 5.117.

5.3.2.2 Small Change in Voltage Magnitude of the Programmable Source

Another disturbance that can occur at the distribution system source bus is the reduction of voltage magnitude on the high voltage side of the distribution transformer. This reduction in voltage is modeled by changing the magnitude of the programmable voltage source. If the pre-disturbance value of the magnitude of the voltage source

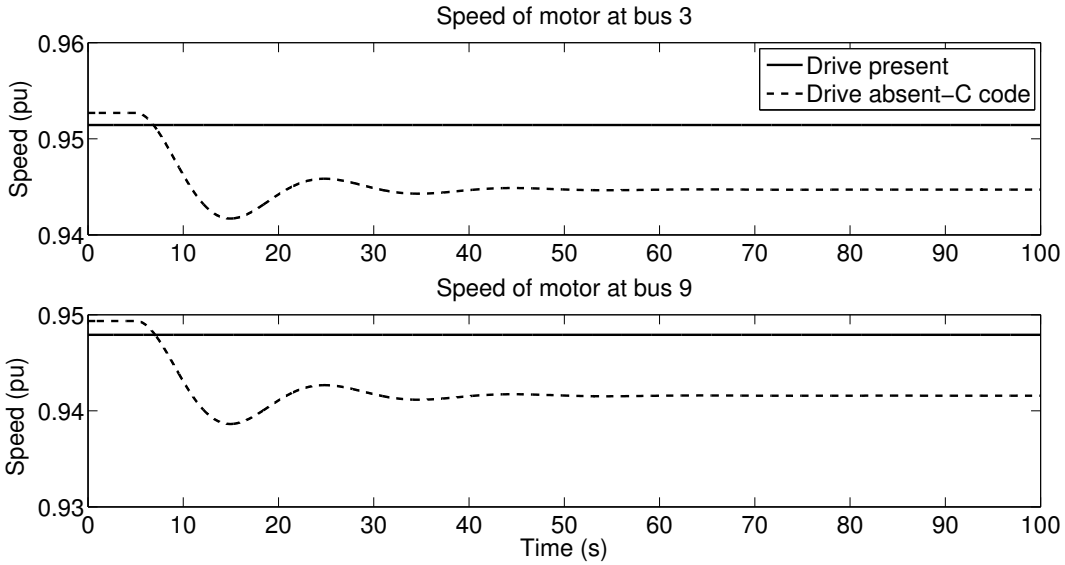

Figure 5.115: Speed of motors at buses 3 and 9 for the applied frequency change

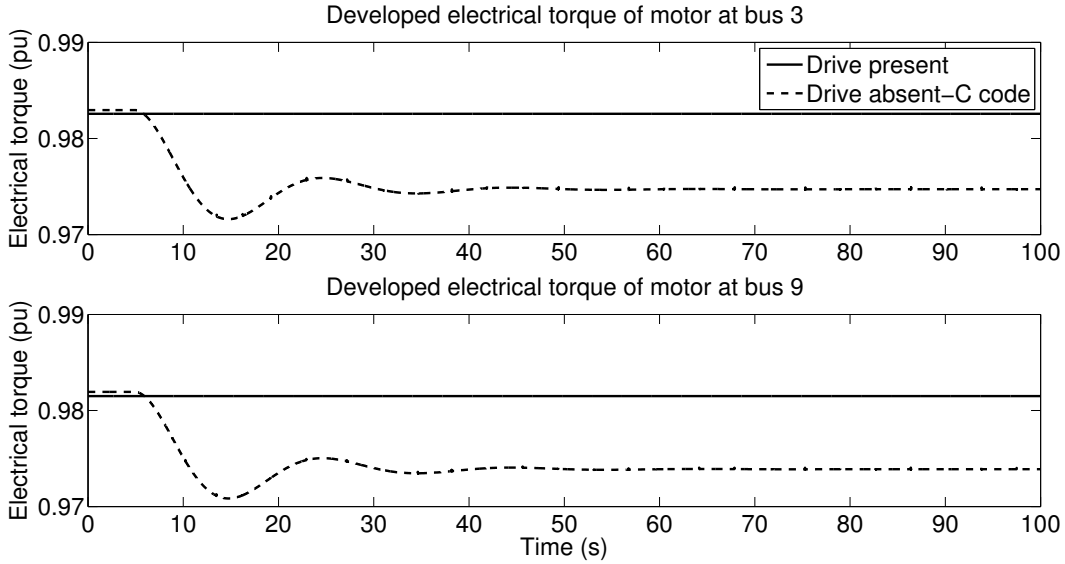

Figure 5.116: Developed electrical torque of motors at buses 3 and 9 for the applied frequency change

is represented as $|E_{thev}|$, then it is assumed that the voltage drops by 1% instantaneously but settles at 98% of $|E_{thev}|$ with a settling time of around 10s following the occurrence of the disturbance. With these assumptions, the voltage magnitude of the source was modeled as given by (5.7) and the voltage at bus 1 is shown in Figure

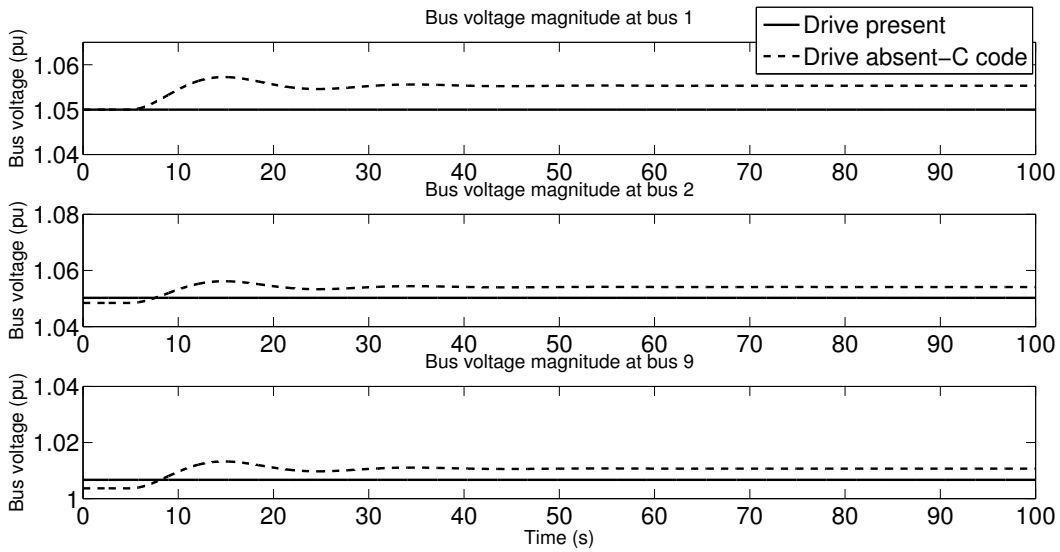

Figure 5.117: Bus voltage magnitude at buses 1, 2 and 9 for the applied frequency change

5.118 with the change in voltage magnitude initiated at t=5s.

$$|E_{thev}|(t) = \begin{cases} |E_{thev}| & \text{if } t \leq 5 \\ (0.98 + 0.01e^{-0.5(t-5.0)})|E_{thev}| & \text{otherwise} \end{cases} \tag{5.7}$$

The active and reactive power consumed by the motor at bus 9 is as shown in Figures

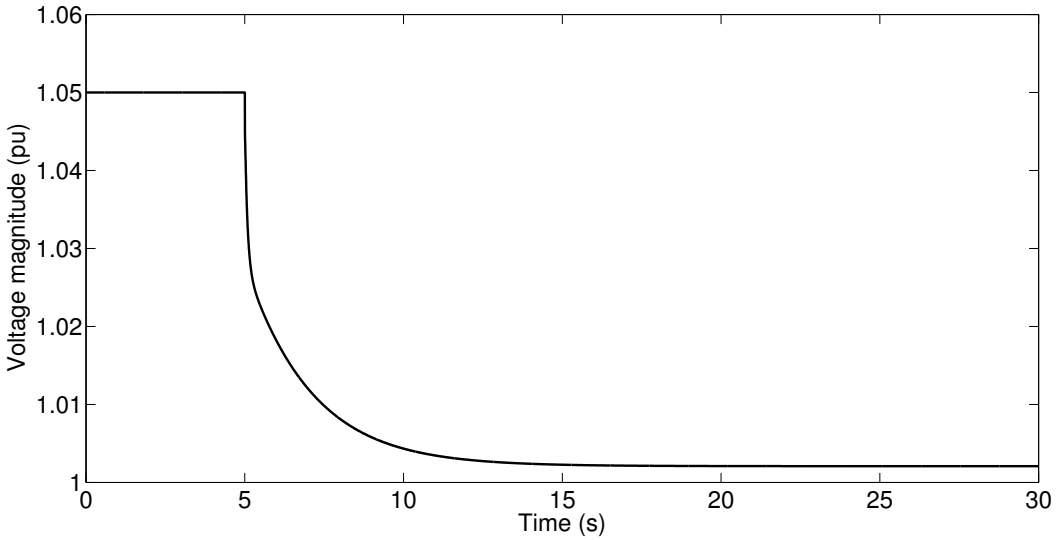

Figure 5.118: Applied small voltage magnitude change

5.119 and 5.120 respectively while the total active and reactive power supplied by

the source at bus 1 is as shown in Figure 5.121. As the load on the motor is

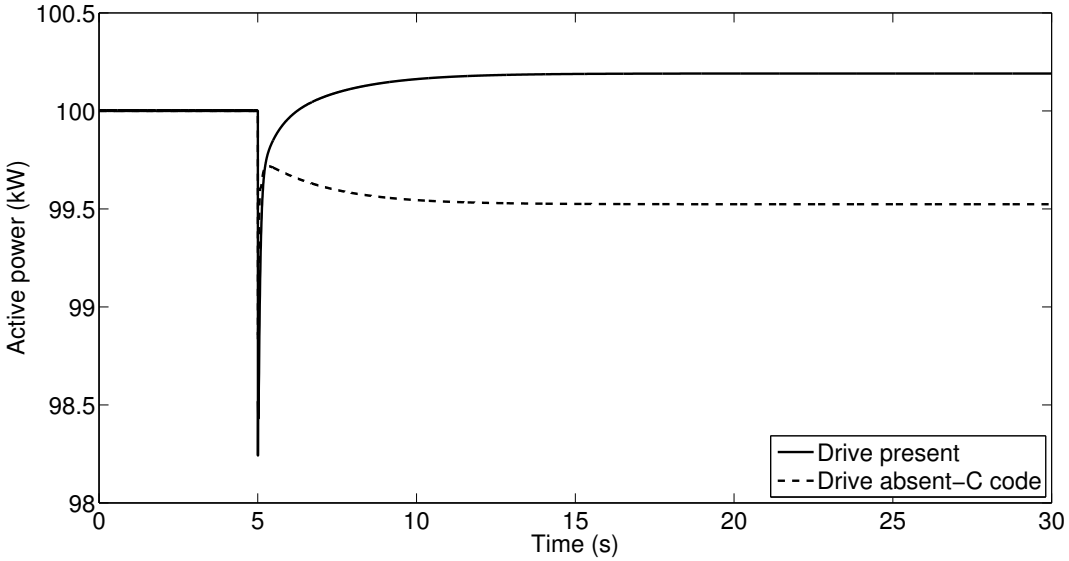

Figure 5.119: Active power consumed by motor at bus 9 for voltage magnitude change applied to the voltage source

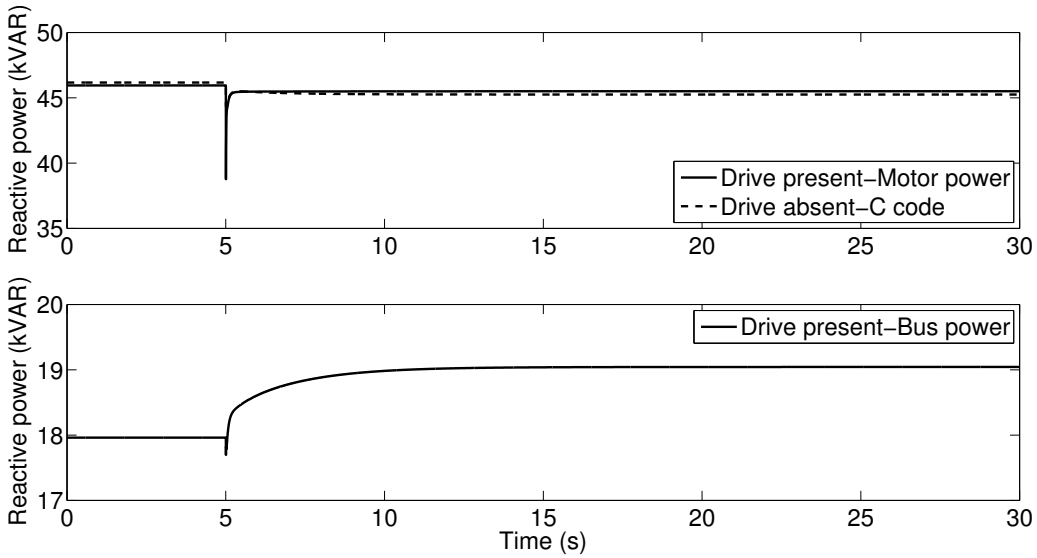

Figure 5.120: Reactive power consumed by motor and rectifier at bus 9 for voltage magnitude change applied to the voltage source

unchanged, a dip in the voltage magnitude of the source results in a larger reactive power demand across the feeder as can be seen from Figure 5.121. With the reduced voltage magnitude, the current drawn by the motor increases to maintain the flux in

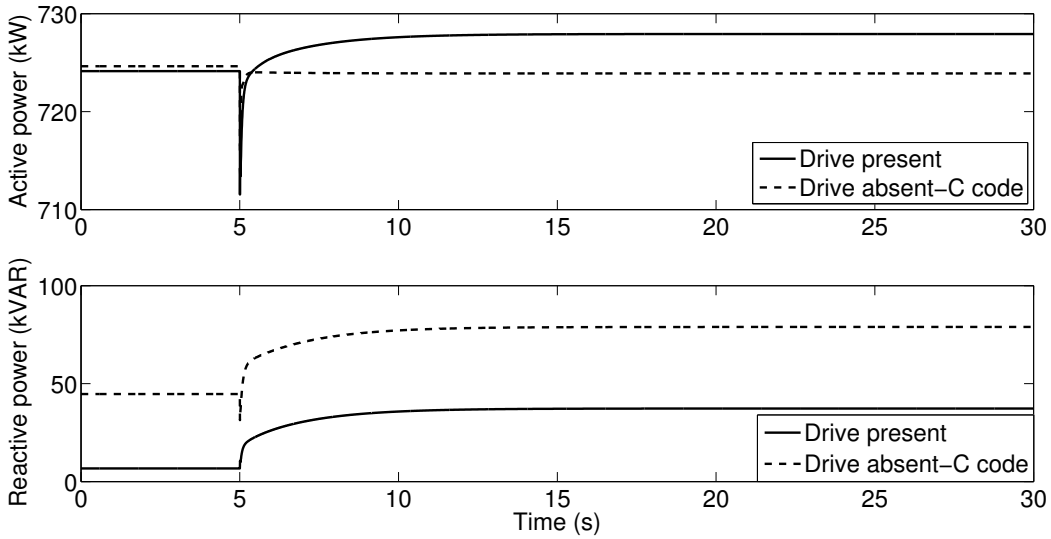

Figure 5.121: Active and reactive power at bus 1 for the applied voltage magnitude change

the motor. The increase in active power consumed by the motor is due to the increase in losses in the motor. As can be seen from the power consumed by the motor, with the presence of a drive, the motor is isolated from the network and thus does not decrease the loading on the source. The power consumed by a directly connected motor however decreases with the decrease in voltage thereby reducing the loading on the source.

The speeds of the motors at bus 3 and bus 9 are as shown in Figure 5.122 while the developed electric torque is shown in Figure 5.123. The voltage profile across the feeder is as shown in Figure 5.124.

5.3.2.3 Large Change in Voltage Magnitude of the Programmable Source

A fault on the substation bus, or a fault in the transmission system, could depress the voltage magnitude at the substation bus by a large amount followed by a slow recovery of the voltage. In this scenario, three simulation runs were carried out with the voltage magnitude of the programmable voltage source reduced to 0.75pu, 0.65pu

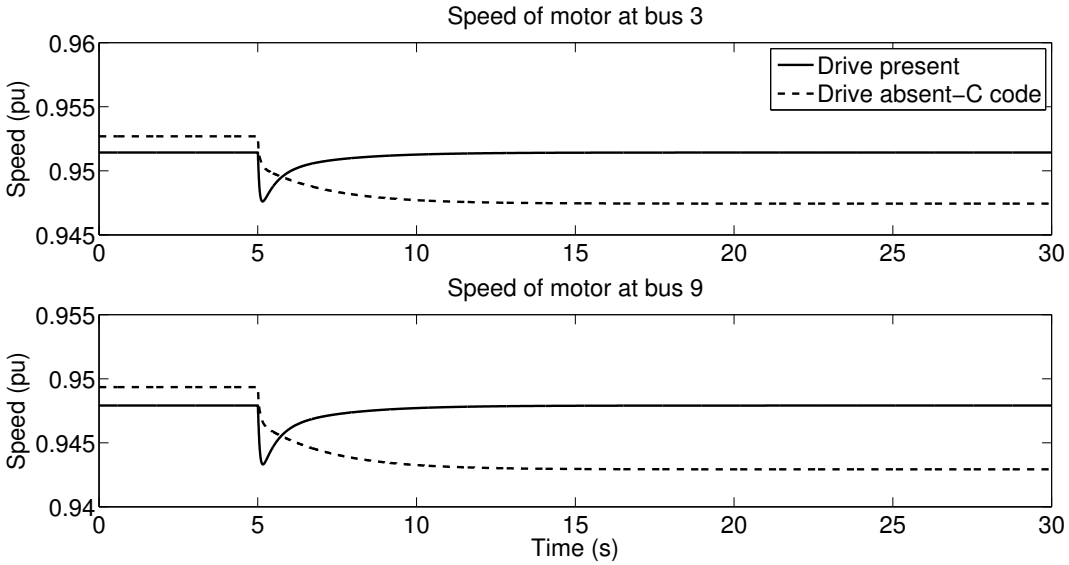

Figure 5.122: Speed of motors at buses 3 and 9 for the applied voltage magnitude change

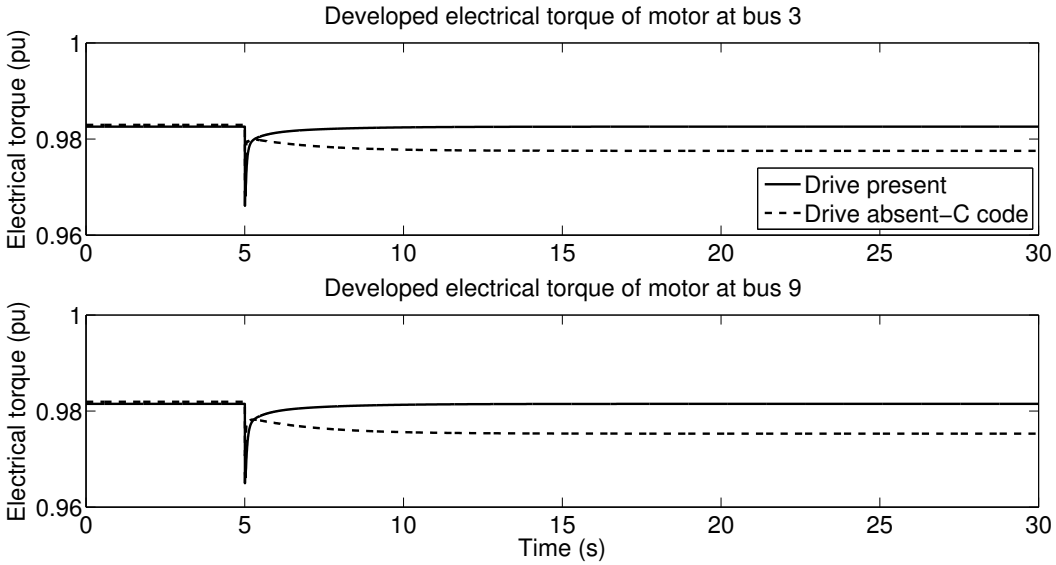

Figure 5.123: Developed electrical torque of motors at buses 3 and 9 for the applied voltage magnitude change

and 0.45pu respectively. In each run, the voltage magnitude recovered to 1.0pu after 5 cycles and then recovered to the pre-disturbance value over the period of one second. The voltage magnitude at bus 1 is as shown in Figure 5.125. For this applied voltage change, the active power drawn at bus 3 is shown in Figures 5.130 and 5.127 when

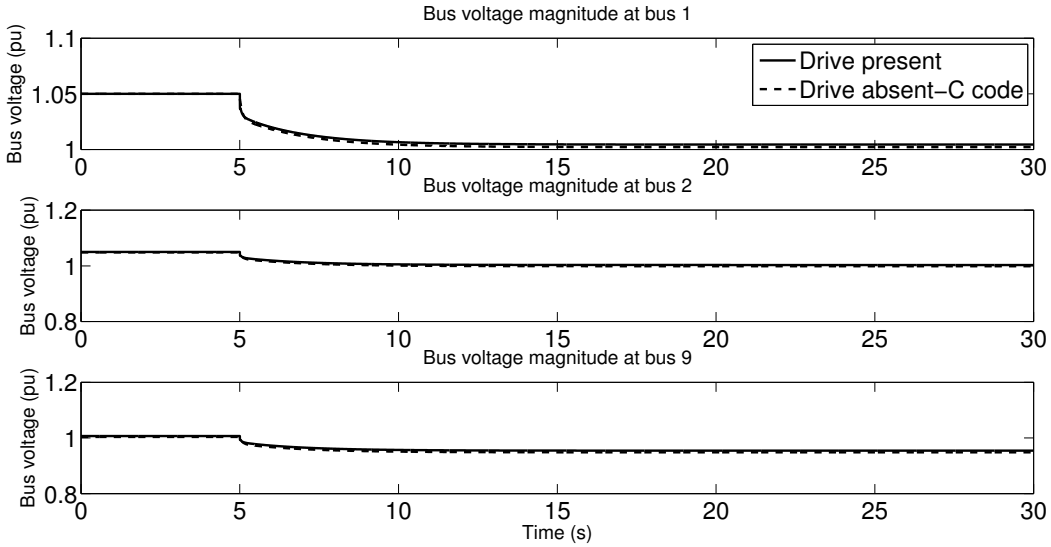

Figure 5.124: Bus voltage magnitude at buses 1, 2 and 9 for the applied voltage magnitude change

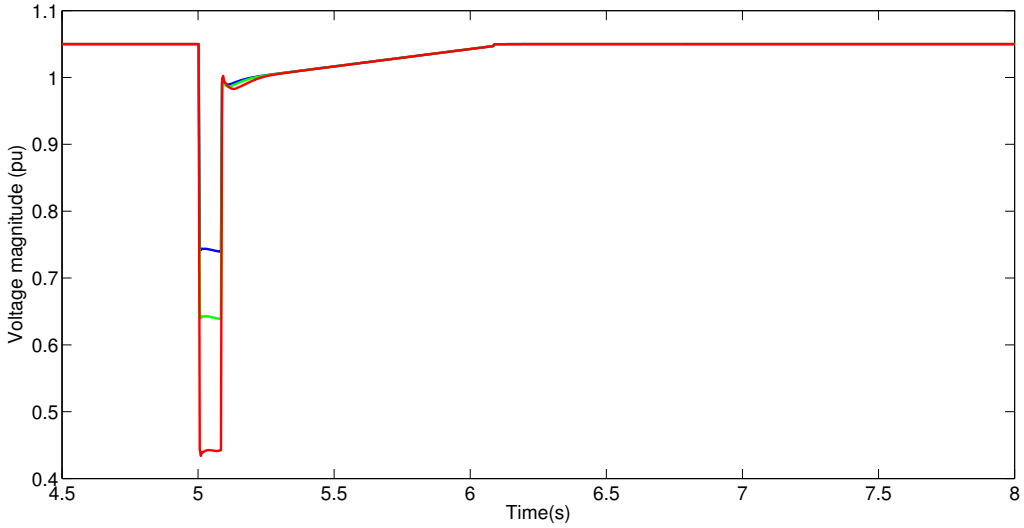

Figure 5.125: Applied large voltage magnitude change

the motor is drive connected and directly connected, respectively. The comparison is also made for the reactive power drawn at the bus as shown by Figures 5.131 and 5.128 respectively. When the voltage magnitude drops, the speed of the directly connected motor, shown in Figure 5.126, reduces to reduce the active power drawn from the network, as shown in Figure 5.127. However, the reactive power consumed,

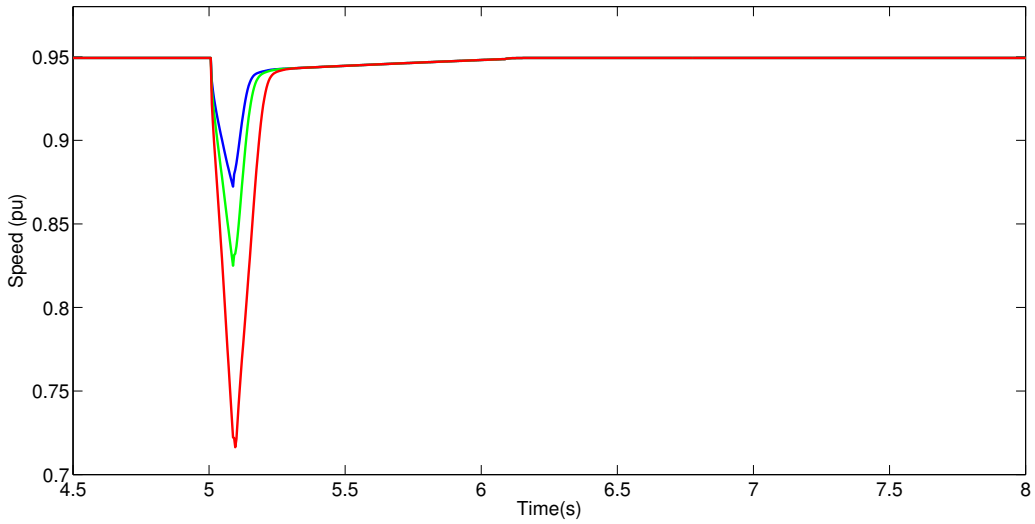

Figure 5.126: Motor speed at bus 3 for the applied large voltage magnitude change with directly connected motor

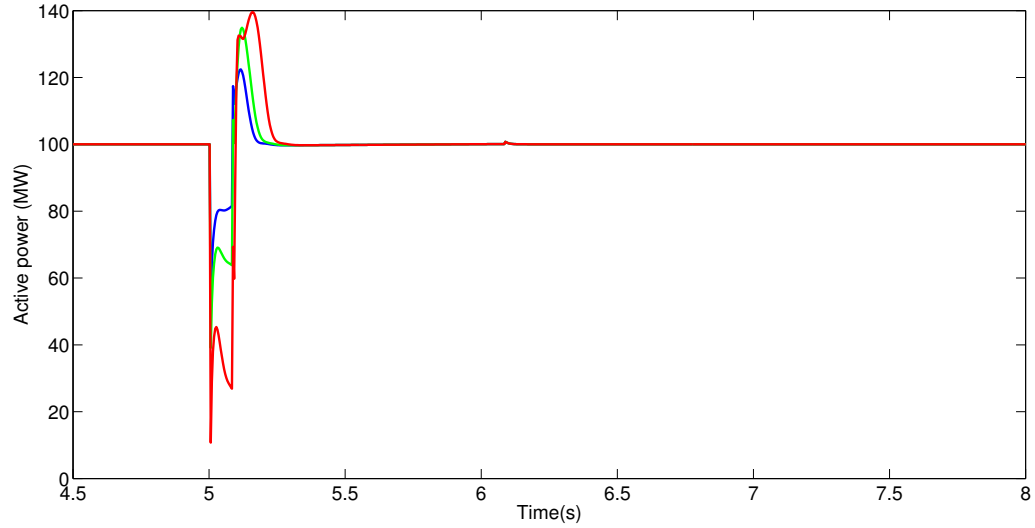

Figure 5.127: Active power drawn at bus 3 for the applied large voltage magnitude change with directly connected motor

shown in Figure 5.128 momentarily increases in order to prevent the flux in the air gap from changing instantaneously. In comparison, when the motor is drive connected, for approximately the same decrease in speed as shown in Figure 5.129, the decrease in active power, shown in Figure 5.130, is also approximately of the same order as the directly connected motor. However, as shown in Figure 5.131, there is no momentary

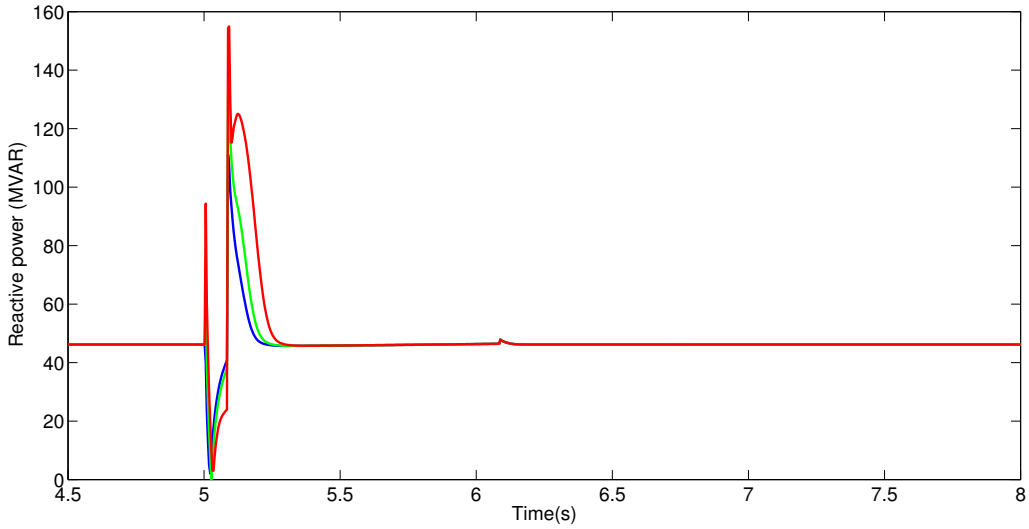

Figure 5.128: Reactive power drawn at bus 3 for applied large voltage magnitude change with directly connected motor

increase in reactive power drawn from the network as the reactive power demands of the motor are met by the inverter. The reactive power drawn from the network is the reactive power consumed by the rectifier. Similarly, as the voltage recovers, the reactive power drawn from the network by the drive connected motor is significantly lower than the reactive power drawn by the directly connected motor.

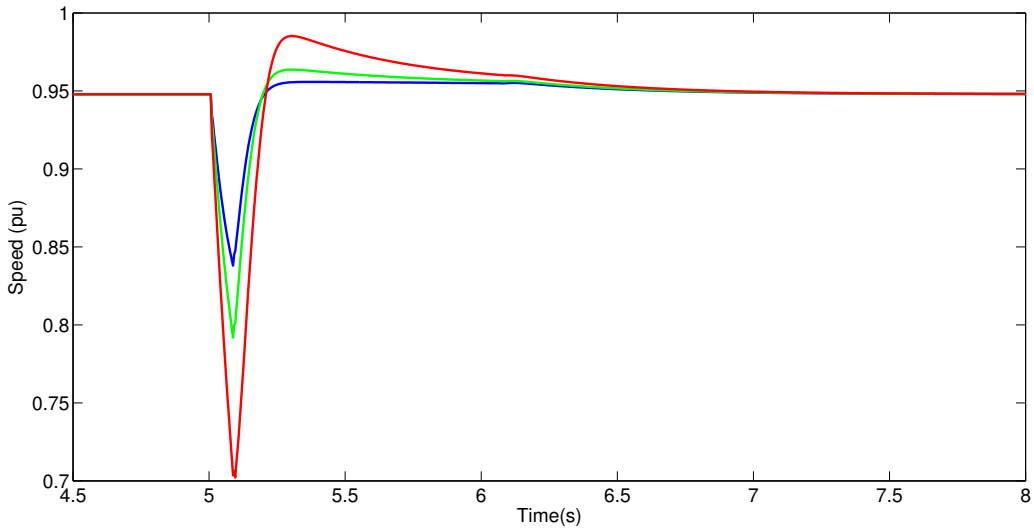

Figure 5.129: Motor speed at bus 3 for the applied large voltage magnitude change with drive connected motor

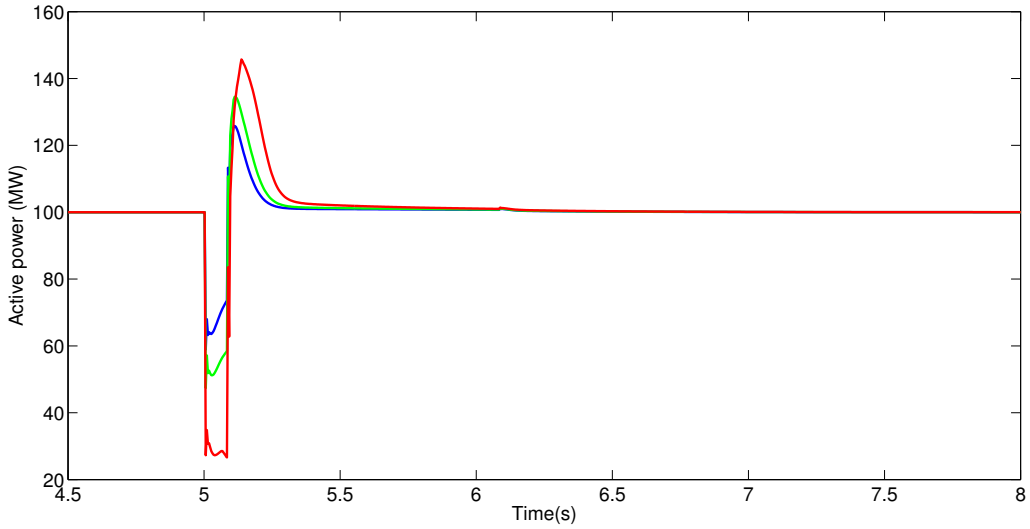

Figure 5.130: Active power drawn at bus 3 for the applied large voltage magnitude change with drive connected motor

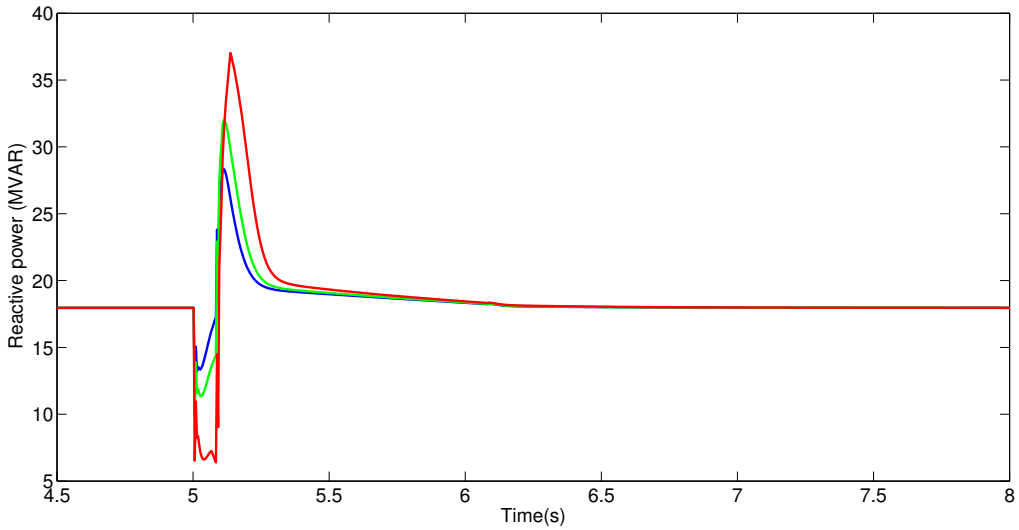

Figure 5.131: Reactive power drawn at bus 3 for the applied large voltage magnitude change with drive connected motor

In a pure CIG network, upon the occurrence of a disturbance, the drop in the dc voltage of a source inverter could result in the widespread dip of voltage magnitude at the load buses. The results of this section show that the presence of speed control drives at the motor terminal could increase the reactive power drawn at the load bus

when the source voltage magnitude is depressed and could aggravate the low voltage situation for a sustained voltage magnitude dip. However, for a significant voltage event, due to the comparatively lower increase in power drawn from the network, the performance of the drive connected motor could be more beneficial to the system than the directly connected motor. Additionally, during a frequency disturbance, the help that is usually provided by an induction motor in terms of lower speed and hence lower power consumption, is reduced with the presence of a drive. Few results are shown in the next section.

5.4 Performance of an all CIG and CIL System

A preliminary analysis was conducted to analyze the performance of a system with both, sources and loads being converter interfaced. Using the modified IEEE 118 bus system discussed in Section 5.1.8, the transient behavior for a load increase event and for a fault event was observed. All generation sources were represented by the ideal dc voltage source converter model without the inner current loop.

The load increase event was the increase of the load at bus 6 by 100 MW. The system mean frequency is as shown in Figure 5.132. For the scenario with a small presence of induction motor load, only the loads at buses 11, 17, 39, 41, 45, 60, 83 and 88 were represented by an induction motor while the scenario with a large presence of induction motor load was the same as in Section 5.1.8.

It can be seen from the figure that when the induction motors are interfaced through a drive, the support from the natural response provided by the induction motor in terms of lower power consumption with reduction in speed is lost thereby increasing the rate of decrease in frequency. With the induction motors directly connected, the rate of decrease in frequency is arrested to a larger extent leading to a higher nadir value. However, with an increase in induction motor presence, the

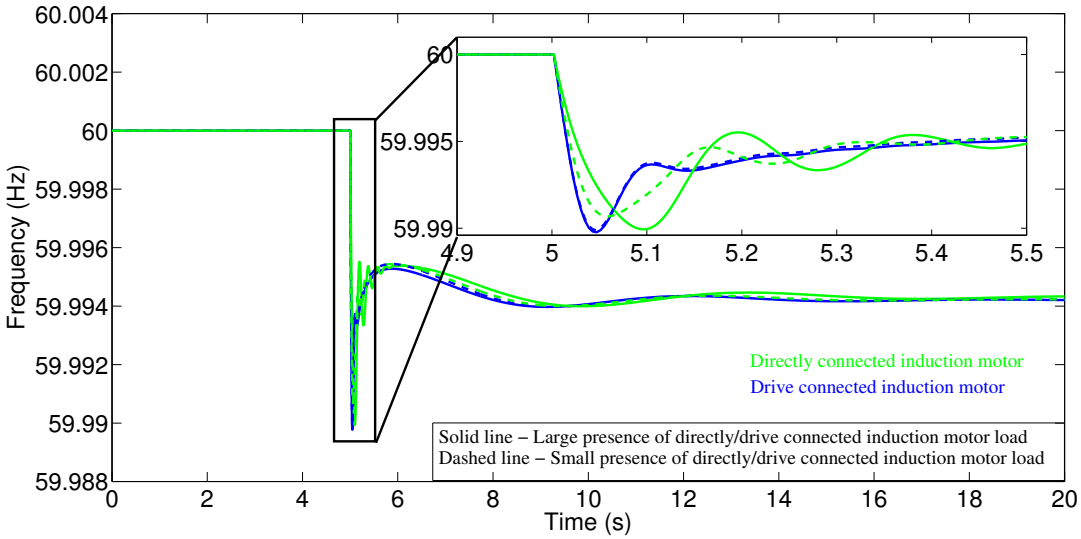

Figure 5.132: Mean frequency of the 118 bus system for a 100 MW load increase event

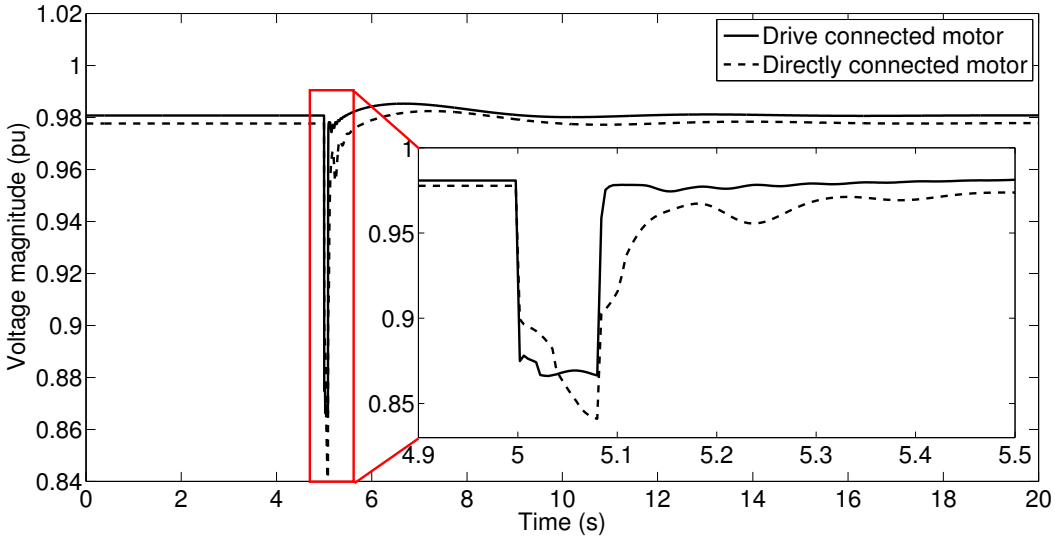

Figure 5.133: Voltage magnitude at bus 35 of the 118 bus system for a fault

value of the nadir is nearly the same both, with directly connected motors and drive connected motors.

In response to a fault, a drive connected motor has a faster voltage recovery when compared to a directly connected motor. This can be seen from Figure 5.133 for a

5 cycle fault applied at bus 37 with a fault resistance of 0.1pu. A converter current limit of 1.2pu was enforced.

Again, as the natural response of the induction motor is isolated from the network, the network sees the drive as a static load and correspondingly the recovery of voltage at the load bus is faster.

While the speed control drive provides a better voltage response to a fault, it worsens the frequency response of the system. Thus, in a system with both generation and load being converter interfaced, the system behavior is quite different from the conventional system behavior and further work needs to be done to study the performance of such a system before a conclusion can be made with regard to whether an all CIG and CIL system performs better or worse than the conventional system.

Chapter 6

DISCUSSION, CONCLUSIONS AND FUTURE RESEARCH

6.1 Discussion

In this dissertation, mathematical models have been developed for converter interfaced generation and load for use in positive sequence time domain simulations. The simulation results portraying the performance and behavior of these mathematical models in the various test networks must however be interpreted with the understanding that there is a difference between the time scale of the simulation and the time scale of actual operation of these devices in the field. In analyzing the positive sequence performance of the bulk power system, the exact characteristics of converter devices are of low interest. However, the trend of the responses from these devices is of high interest and possible concern. In this dissertation, the focus has been on representing this trend more accurately.

With the percentage of penetration of converter devices increasing rapidly, more importance must be placed on developing accurate, while at the same time realistic, mathematical models for simulation and analysis of the bulk power system. Simultaneously, operational policies and practices for the future grid have to be established in order to prevent a case of closing the stable door after the horse has bolted. In this dissertation, an attempt has been made to address these issues of simulation modeling and operational practices. As simulation capability continues to evolve, there could be a possibility to represent these devices and their associated control mechanisms in more detail during the analysis of the bulk power system.

However, there is no single correct mathematical model to represent these converter interfaced devices. Each representation described in this dissertation has its own advantages, applicable scenarios and disadvantages. Good engineering judgment must be used while using these various representations. Use of these mathematical models for bulk power system analysis must however come with the understanding that in positive sequence analysis, certain control characteristics of these converters are ignored and thus, the results of the analysis must be interpreted accordingly.

To summarize the work done in this dissertation, a controlled voltage source mathematical model was developed to represent the converter in positive sequence time-domain commercial software to analyze the behavior of the bulk power system with 100% converter interfaced generation (CIG). The development of this converter model was calibrated by comparison to a detailed electromagnetic transient model. Further, to take into account the dynamics of the dc bus and the physical energy source behind the inverter, a model to represent synchronous generators coupled to transmission through rectifier-inverter links has been developed with recognition of the finite size of the capacitor on the dc bus. The commercially available PSLF and PLECS software were used to run the simulations. At the other end of the spectrum, in order to examine the impact of the presence of converters at the load end, the development and implementation of an induction motor speed control drive in a positive sequence transient simulation has been described. An independently developed C code was used to perform this simulation.

6.2 Conclusions

From the simulation runs, it can be concluded that the developed positive sequence controlled voltage source converter model is numerically robust and behaves satisfactorily in a large realistic system such as the WECC system. Based on the

long proven principle of droop relationships between real power and frequency, reactive power and voltage magnitude, an all converter WECC system could operate in a stable manner for various contingencies and that such a system, if required, could be viable. This result is however contingent on the availability of adequate reserves from CIG sources thereby first requiring the formulation of a dispatch schedule.

Recognition of the characteristics/dynamics of the dc bus and the source behind the inverter becomes important in a system with a large presence of CIG as these sources could play a crucial role in maintaining frequency and voltage. Examples of the use of the source behind rectifier-inverter model have shown the sensitivity of voltage control and complex power flow to the size of the capacitor with only minor increase in computing times. This mathematical model can serve as an essential tool in the simulation analysis of a future power system.

At the load end of the network, it has been shown that during a disturbance, the support that is usually provided by an induction motor in terms of lower speed and hence lower power consumption, is reduced with the presence of a drive. However, the analysis conducted in assessing the impact of this converter interfaced load model is still in the preliminary stages and more work has to be done before a conclusion can be drawn regarding its impact on the power network. Accurate representation of the changing load characteristics for use in analysis of the bulk power system is still an open topic and possibly this converter interfaced load model will help in providing a better representation of the drive interfaced loads in the power network.

It has been seen while converter interfaced generation can provide a quick response to disturbance events, the overall system performance is also influenced by the characteristics of the source behind the converter, the characteristics of the load and the method by which the load is connected to the network. Through this dissertation, a small but important step has been taken in addressing modeling capability issues

and operational practices of a future power system. While the results obtained are promising, it is hoped that they would serve to facilitate a giant leap in research activity on this topic.

6.3 Future Research

During the course of this research work, new questions were raised which can lead to avenues for future research work such as:

1. With a larger drop in the dc voltage of a source inverter upon the occurrence of a contingency, widespread tripping of induction motors due to undervoltage and converters due to overcurrent could occur. It is possible that a well coordinated wide area control strategy could increase the system reliability by bringing voltage support units online quickly.

2. As a planning problem, a capacitor of appropriate size will have to be placed on the dc bus to reduce the voltage drop. Further, it is possible that different locations in the system can withstand different amounts of drop in voltage on the dc bus. This problem would have to be analyzed and addressed as a large sized capacitor could pose a safety hazard.

3. In developing the model for the source behind converter, a single source i.e. the synchronous machine, was assumed. With the realization that it is important of model the source behind the inverter, it is also imperative to identify and mathematically describe the numerous types of sources that can be connected on the dc side of the inverter both individually, and in a combined manner.

4. For large systems, a robust analytical tuning procedure of the controller gains is required. This would ensure the maximum utilization of the converter bandwidth and bring about a healthy system operation.

5. Currently, the stress on the blades of a steam turbine determines the operating frequency range of the system. With an all CIG system, an optimal frequency range is yet to be determined.

6. The effect of generator ramping constraints on the dc bus voltage and ac system behavior will have to be analyzed with synchronous machines interfaced through converters.

7. It is to be determined if the energy stored in the dc capacitor can compensate for the lost kinetic energy of a directly connected rotating machine.

8. The behavior of the induction motor speed drive model has been tested only on a small system. A complete analysis of its behavior and interaction with CIG in a large system is yet to be seen. Further, as induction motor drives can various modes of operation, all these characteristics have to be included in the mathematical model.

REFERENCES

[1] "Electricity in the United States," U.S. Energy Information Administration, April 10, 2013, [Online]: http://www.eia.gov/energyexplained/index.cfm?page=electricity_in_the_united_states [Accessed: August 10, 2014].

[2] I. Kolesnikov, "World Reserves of Fossil Fuels," 2013, [Online]: http://knoema.com/smsfgud/world-reserves-of-fossil-fuels [Accessed: August 10, 2014].

[3] S. Shafiee and E. Topal, "When will fossil fuel reserves be diminished?" *Energy Policy*, vol. 37, no. 1, pp. 181 – 189, 2009.

[4] A. Breidthardt, "German government want nuclear exit by 2022 at latest," Reuters, May 30, 2011, [Online]: http://uk.reuters.com/article/2011/05/30/us-germany-nuclear-idUKTRE74Q2P120110530 [Accessed: August 10, 2014].

[5] "Nuclear Power: When the steam clears," The Economist, March 24, 2011, [Online]: http://www.economist.com/node/18441163 [Accessed: August 10, 2014].

[6] J. Chandler, "Is this the end of the nuclear revival," The Sydney Morning Herald, March 19, 2011, [Online]: http://www.smh.com.au/environment/energy-smart/is-this-the-end-of-the-nuclear-revival-20110318-1c0i9.html [Accessed: August 10, 2014].

[7] D. Gautam, V. Vittal, and T. Harbour, "Impact of increased penetration of DFIG-based wind turbine generators on transient and small signal stability of power systems," *IEEE Trans. Power Syst.*, vol. 24, no. 3, pp. 1426–1434, Aug 2009.

[8] A. Azmy and I. Erlich, "Impact of distributed generation on the stability of electrical power system," in *2005 IEEE Power Engineering Society General Meeting*, June 2005, pp. 1056–1063.

[9] "Clean Power Plan," U.S. Environmental Protection Agency, April 3, 2015, [Online]: http://www2.epa.gov/cleanpowerplan [Accessed: November 17, 2015].

[10] M. Reza, D. Sudarmadi, F. Viawan, W. Kling, and L. van der Sluis, "Dynamic stability of power systems with power electronic interfaced dg," in *2006 IEEE PES Power Systems Conference and Exposition, 2006. PSCE '06.*, Oct 2006, pp. 1423–1428.

[11] F. Gatta, F. Iliceto, S. Lauria, and P. Masato, "Modelling and computer simulation of dispersed generation in distribution networks. measures to prevent disconnection during system disturbances," in *2003 IEEE Bologna Power Tech Conference Proceedings*, vol. 3, Jun 2003, p. 10 pp.

[12] T. Ackermann, *Wind Power in Power Systems*. Wiley, 2012.

[13] R. Kurz, "Gas turbine performance," in *Proceedings of the Thirty-Fourth Turbomachinery Symposium., Houston, TX*, Sep 2005.

[14] J. Sánchez, C. Veganzones, S. Martnez, F. Blázquez, N. Herrero, and J. Wilhelmi, "Dynamic model of wind energy conversion systems with variable speed synchronous generator and full-size power converter for large-scale power system stability studies," *Renewable Energy*, vol. 33, no. 6, pp. 1186 – 1198, 2008.

[15] "The Workhorse of Industry: The Induction Motor," Power Transmission Engineering, Dec 2013, [Online]: http://www.powertransmission.com/articles/1213/The_Workhorse_of_Industry:_The_Induction_Motor [Accessed: November 4, 2015].

[16] B. Bose, "Power electronics and motor drives recent progress and perspective," *IEEE Trans. Ind. Electron.*, vol. 56, no. 2, pp. 581–588, Feb. 2009.

[17] M. Spear, "Adjustable speed drives: Drive up energy efficiency," Chemical Processing, Jun 2005, [Online]: http://www.chemicalprocessing.com/articles/2005/489/?page=1 [Accessed: November 4, 2015].

[18] B. Bose, "The past, present, and future of power electronics [guest introduction]," *IEEE Industrial Electronics Magazine*, vol. 3, no. 2, pp. 7–11, 14, Jun 2009.

[19] H. Storm, "Static Magnetic Exciter for Synchronous Alternators," *Transactions of the American Institute of Electrical Engineers*, vol. 70, no. 1, pp. 1014–1017, July 1951.

[20] L. M. Domeratzky, A. Rubenstein, and M. Temoshok, "A Static Excitation System for Industrial and Utility Steam Turbine-Generators," *Transactions of the American Institute of Electrical Engineers Power Apparatus and Systems, Part III.*, vol. 80, no. 3, pp. 1072–1077, April 1961.

[21] I. Report, "Proposed excitation system definitions for synchronous machines," *IEEE Trans. Power App. Syst.*, vol. PAS-88, no. 8, pp. 1248–1258, Aug 1969.

[22] P. Kundur, *Power System Stability and Control*, N. Balu and M. Lauby, Eds. McGraw-Hill Education, 1994.

[23] S. Mishra, D. Ramasubramanian, and P. Sekhar, "A seamless control methodology for a grid connected and isolated PV-diesel microgrid," *IEEE Trans. Power Syst.*, vol. 28, no. 4, pp. 4393–4404, Nov 2013.

[24] H. Bevrani, A. Ghosh, and G. Ledwich, "Renewable energy sources and frequency regulation: survey and new perspectives," *IET Renewable Power Generation*, vol. 4, no. 5, pp. 438–457, September 2010.

[25] R. de Almeida and J. Peças Lopes, "Participation of doubly fed induction wind generators in system frequency regulation," *IEEE Trans. Power Syst.*, vol. 22, no. 3, pp. 944–950, Aug 2007.

[26] I. Erlich and M. Wilch, "Primary frequency control by wind turbines," in *2010 IEEE Power and Energy Society General Meeting*, July 2010, pp. 1–8.

[27] J. F. Conroy and R. Watson, "Frequency response capability of full converter wind turbine generators in comparison to conventional generation," *IEEE Trans. Power Syst.*, vol. 23, no. 2, pp. 649–656, May 2008.

[28] A. Attya and T. Hartkopf, "Control and quantification of kinetic energy released by wind farms during power system frequency drops," *IET Renewable Power Generation*, vol. 7, no. 3, pp. 210–224, May 2013.

[29] T. Vandoorn, B. Meersman, J. De Kooning, and L. Vandevelde, "Transition from islanded to grid-connected mode of microgrids with voltage-based droop control," *IEEE Trans. Power Syst.*, vol. 28, no. 3, pp. 2545–2553, Aug 2013.

[30] K. Vidyanandan and N. Senroy, "Primary frequency regulation by deloaded wind turbines using variable droop," *IEEE Trans. Power Syst.*, vol. 28, no. 2, pp. 837–846, May 2013.

[31] R. Majumder, B. Chaudhuri, A. Ghosh, R. Majumder, G. Ledwich, and F. Zare, "Improvement of stability and load sharing in an autonomous microgrid using supplementary droop control loop," *IEEE Trans. Power Syst.*, vol. 25, no. 2, pp. 796–808, May 2010.

[32] Y. A. R. I. Mohamed and E. El-Saadany, "Adaptive decentralized droop controller to preserve power sharing stability of paralleled inverters in distributed generation microgrids," *IEEE Trans. Power Electron.*, vol. 23, no. 6, pp. 2806–2816, Nov 2008.

[33] E. Barklund, N. Pogaku, M. Prodanovic, C. Hernandez-Aramburo, and T. Green, "Energy management in autonomous microgrid using stability-constrained droop control of inverters," *IEEE Trans. Power Electron.*, vol. 23, no. 5, pp. 2346–2352, Sept 2008.

[34] S. Ashabani and Y.-R. Mohamed, "General interface for power management of micro-grids using nonlinear cooperative droop control," *IEEE Trans. Power Syst.*, vol. 28, no. 3, pp. 2929–2941, Aug 2013.

[35] G. Diaz, C. Gonzalez-Moran, J. Gomez-Aleixandre, and A. Diez, "Scheduling of droop coefficients for frequency and voltage regulation in isolated microgrids," *IEEE Trans. Power Syst.*, vol. 25, no. 1, pp. 489–496, Feb 2010.

[36] H. Xin, Y. Liu, Z. Wang, D. Gan, and T. Yang, "A new frequency regulation strategy for photovoltaic systems without energy storage," *IEEE Trans. Sustain. Energy*, vol. 4, no. 4, pp. 985–993, Oct 2013.

[37] W. Omran, M. Kazerani, and M. Salama, "Investigation of methods for reduction of power fluctuations generated from large grid-connected photovoltaic systems," *IEEE Trans. Energy Convers.*, vol. 26, no. 1, pp. 318–327, March 2011.

[38] M. Datta, T. Senjyu, A. Yona, T. Funabashi, and C.-H. Kim, "A frequency-control approach by photovoltaic generator in a PV-diesel hybrid power system," *IEEE Trans. Energy Convers.*, vol. 26, no. 2, pp. 559–571, June 2011.

[39] N. Kakimoto, S. Takayama, H. Satoh, and K. Nakamura, "Power modulation of photovoltaic generator for frequency control of power system," *IEEE Trans. Energy Convers.*, vol. 24, no. 4, pp. 943–949, Dec 2009.

[40] M. Morjaria and D. Anichkov, ""Grid Friendly" utility-scale PV plants," White Paper, First Solar, Aug 2013.

[41] "Wind integration," MISO Energy, [Available Online:] https://www.misoenergy.org/WhatWeDo-/StrategicInitiatives/Pages/WindIntegration.aspx.

[42] M. A. Eltawil and Z. Zhao, "Grid-connected photovoltaic power systems: Technical and potential problemsa review," *Renewable and Sustainable Energy Reviews*, vol. 14, no. 1, pp. 112 – 129, January 2010.

[43] E. Vittal, M. O'Malley, and A. Keane, "Rotor angle stability with high penetrations of wind generation," *IEEE Trans. Power Syst.*, vol. 27, no. 1, pp. 353–362, Feb 2012.

[44] J. Slootweg and W. Kling, "Impacts of distributed generation on power system transient stability," in *2002 IEEE Power Engineering Society Summer Meeting*, vol. 2, July 2002, pp. 862–867.

[45] R. Pearmine, Y. H. Song, and A. Chebbo, "Influence of wind turbine behaviour on the primary frequency control of the British transmission grid," *IET Renewable Power Generation*, vol. 1, no. 2, pp. 142–150, June 2007.

[46] D. Gautam, L. Goel, R. Ayyanar, V. Vittal, and T. Harbour, "Control strategy to mitigate the impact of reduced inertia due to doubly fed induction generators on large power systems," *IEEE Trans. Power Syst.*, vol. 26, no. 1, pp. 214–224, Feb 2011.

[47] S. Eftekharnejad, V. Vittal, G. Heydt, B. Keel, and J. Loehr, "Impact of increased penetration of photovoltaic generation on power systems," *IEEE Trans. Power Syst.*, vol. 28, no. 2, pp. 893–901, May 2013.

[48] J. Quintero, V. Vittal, G. Heydt, and H. Zhang, "The impact of increased penetration of converter control-based generators on power system modes of oscillation," *IEEE Trans. Power Syst.*, vol. 29, no. 5, pp. 2248–2256, Sept 2014.

[49] N. W. Miller, M. Shao, S. Pajic, and R. D'Aquila, "Western wind and solar integration study phase 3 - frequency response and transient stability," NREL, Tech. Rep. NREL Report No. SR-5D00-62906, Dec 2014.

[50] "WECC second generation wind turbine models," Western Electricity Coordinating Council, Tech. Rep., 2014, [Available Online:] https://www.wecc.biz/Reliability/WECC-Second-Generation-Wind-Turbine-Models-012314.pdf.

[51] J. Jatskevich, S. Pekarek, and A. Davoudi, "Parametric average-value model of synchronous machine-rectifier systems," *IEEE Trans. Energy Convers.*, vol. 21, no. 1, pp. 9–18, Mar 2006.

[52] S. Pekarek, O. Wasynczuk, and H. Hegner, "An efficient and accurate model for the simulation and analysis of synchronous machine/converter systems," *IEEE Trans. Energy Convers.*, vol. 13, no. 1, pp. 42–48, Mar 1998.

[53] J. Jatskevich, S. Pekarek, and A. Davoudi, "Fast procedure for constructing an accurate dynamic average-value model of synchronous machine-rectifier systems," *IEEE Trans. Energy Convers.*, vol. 21, no. 2, pp. 435–441, Jun 2006.

[54] S. Sudhoff, S. Glover, P. Lamm, D. Schmucker, and D. Delisle, "Admittance space stability analysis of power electronic systems," *IEEE Trans. Aerospace and Electronic Systems*, vol. 36, no. 3, pp. 965–973, Jul 2000.

[55] I. Jadric, D. Borojevic, and M. Jadric, "Modeling and control of a synchronous generator with an active dc load," *IEEE Trans. Power Electron.*, vol. 15, no. 2, pp. 303–311, Mar 2000.

[56] J. Hu, Y. Huang, D. Wang, H. Yuan, and X. Yuan, "Modeling of grid-connected dfig-based wind turbines for dc-link voltage stability analysis," *IEEE Trans. Sustain. Energy*, vol. 6, no. 4, pp. 1325–1336, Oct 2015.

[57] H. Yuan, X. Yuan, and J. Hu, "Modeling and large-signal stability of dfig wind turbine in dc-voltage control time scale," in *2016 IEEE Power and Energy Society General Meeting (PESGM)*, July 2016, pp. 1–5.

[58] A. Grauers, "Efficiency of three wind energy generator systems," *IEEE Trans. Energy Convers.*, vol. 11, no. 3, pp. 650–657, Sep 1996.

[59] E. Spooner and A. Williamson, "Direct coupled, permanent magnet generators for wind turbine applications," *IEE Proceedings-Electric Power Applications*, vol. 143, no. 1, pp. 1–8, Jan 1996.

[60] M. Chinchilla, S. Arnaltes, and J. Burgos, "Control of permanent-magnet generators applied to variable-speed wind-energy systems connected to the grid," *IEEE Trans. Energy Convers.*, vol. 21, no. 1, pp. 130–135, March 2006.

[61] K. Zhang, H. Kojabadi, P. Wang, and L. Chang, "Modeling of a converter-connected six-phase permanent magnet synchronous generator," in *International Conference on Power Electronics and Drives Systems, 2005. PEDS 2005.*, vol. 2, Nov 2005, pp. 1096–1100.

[62] H. Hegner, P. Krause, O. Wasynczuk, E. Walters, and S. Pekarek, "Parameter measurement of a six-phase synchronous machine for simulation of machine/-converter systems," in *Proceedings of the 31st Intersociety Energy Conversion Engineering Conference, 1996. IECEC 96.*, vol. 3, Aug 1996, pp. 1792–1797.

[63] "Reasons for projected natural gas-fired generation growth vary by region," U.S. Energy Information Administration, August 15, 2014, [Online]: http://www.eia.gov/todayinenergy/detail.cfm?id=17571 [Accessed: November 19, 2015].

[64] "Natural gas, renewables projected to provide larger shares of electricity generation," U.S. Energy Information Administration, May 4, 2015, [Online]: http://www.eia.gov/todayinenergy/detail.cfm?id=21072 [Accessed: November 19, 2015].

[65] W. Li, C. Abbey, and G. Joos, "Control and performance of wind turbine generators based on permanent magnet synchronous machines feeding a diode rectifier," in *37th IEEE Power Electronics Specialists Conference, 2006. PESC '06.*, Jun 2006, pp. 1–6.

[66] J. Slootweg, H. Polinder, and W. Kling, "Dynamic modelling of a wind turbine with direct drive synchronous generator and back to back voltage source converter and its controls," in *European Wind Energy Conference EWEC-2001*, Jul 2001.

[67] S.-H. Song, S. il Kang, and N. kun Hahm, "Implementation and control of grid connected ac-dc-ac power converter for variable speed wind energy conversion system," in *Eighteenth Annual IEEE Applied Power Electronics Conference and Exposition, 2003. APEC '03.*, vol. 1, Feb 2003, pp. 154–158.

[68] S. Achilles and M. Pöller, "Direct drive synchronous machine models for stability assessment of wind farms," in *4th International Workshop on Large-scale Integration of Wind Power and Transmission Networks for Offshore Wind Farms*, Oct 2003, pp. 1–9.

[69] P. Pourbeik, "Proposed changes to the WECC WT4 generic model for type 4 wind turbine generators," EPRI, Tech. Rep., 2013.

[70] J. F. Conroy and R. Watson, "Low-voltage ride-through of a full converter wind turbine with permanent magnet generator," *IET Renewable Power Generation*, vol. 1, no. 3, pp. 182–189, Sep 2007.

[71] M. F. M. Arani and Y. A. R. I. Mohamed, "Assessment and enhancement of a full-scale pmsg-based wind power generator performance under faults," *IEEE Trans. Energy Convers.*, vol. 31, no. 2, pp. 728–739, Jun 2016.

[72] D. Xiang, J. Turu, S. Muratel, and T. Wang, "On-site LVRT testing method for full power converter wind turbines," *IEEE Trans. Sustain. Energy*, vol. PP, no. 99, pp. 1–1, 2016.

[73] Z. Wu, W. Gao, D. Yang, and Y. Shi, "Comprehensive modeling and analysis of permanent magnet synchronous generator-wind turbine system with enhanced low voltage ride through capability," in *2012 IEEE Energy Conversion Congress and Exposition (ECCE)*, Sept 2012, pp. 2091–2098.

[74] N. De and P. Sen, *Electric Drives*. PHI Learning, 1999.

[75] W. Leonhard, *Control of Electrical Drives*. Springer Berlin Heidelberg, 2012.

[76] "PSS®E," Siemens PTI, http://w3.siemens.com/smartgrid/global/en/products-systems-solutions/software-solutions/planning-data-management-software/planning-simulation/pages/pss-e.aspx.

[77] "PSLF," GE Energy Consulting, http://www.geenergyconsulting.com/practice-area/software-products/pslf.

[78] N. Bottrell, M. Prodanovic, and T. Green, "Dynamic stability of a microgrid with an active load," *IEEE Trans. Power Electron.*, vol. 28, no. 11, pp. 5107–5119, Nov 2013.

[79] N. Mohan, T. Undeland, and W. Robbins, *Power Electronics: Converters, Applications and Design*, 3rd ed. Wiley, 2003.

[80] S. Cole and B. Haut, "Robust modeling against model-solver interactions for high-fidelity simulation of VSC HVDC systems in EUROSTAG," *IEEE Trans. Power Syst.*, vol. 28, no. 3, pp. 2632–2638, Aug 2013.

[81] S. Rosado, R. Burgos, S. Ahmed, F. Wang, and D. Boroyevich, "Modeling of power electronics for simulation based analysis of power systems," in *Proceedings of the 2007 Summer Computer Simulation Conference*, ser. SCSC '07. Society for Computer Simulation International, 2007, pp. 19–26.

[82] B. K. Johnson, "Hvdc models used in stability studies," *IEEE Trans. Power Del.*, vol. 4, no. 2, pp. 1153–1163, Apr 1989.

[83] K. Clark, R. Walling, and N. Miller, "Solar photovoltaic (PV) plant models in pslf," in *2011 IEEE Power and Energy Society General Meeting*, July 2011, pp. 1–5.

[84] K. Clark, N. W. Miller, and R. Walling, "Modeling of GE solar photovoltaic plants for grid studies," GE Energy, Tech. Rep. 1.1, April 2010.

[85] N. W. Miller, W. W. Price, and J. J. Sanchez-Gasca, "Dynamic modeling of GE 1.5 and 3.6 wind turbine-generators," GE Power Systems, Tech. Rep. 3.0, October 2003.

[86] "TSAT," Powertech Labs Inc., http://www.dsatools.com/html/prod_tsat.php.

[87] "Technical update - wind and solar pv modeling and model validation," EPRI,Palo Alto, CA, Tech. Rep. 1025475, 2012.

[88] "Associated material for 2012 HS4A approved operating case," Western Electricity Coordinating Council, January 2012.

[89] P. Anderson and A. Fouad, *Power System Control and Stability*. IEEE Press, 2003.

[90] J. M. Undrill, "Structure in the Computation of Power-System Nonlinear Dynamical Response," *IEEE Trans. Power App. Syst.*, vol. PAS-88, no. 1, pp. 1–6, January 1969.

[91] *PSLF User's Manual*, General Electric International, Inc., 2013.

[92] A. Ghoshal and V. John, "Anti-windup schemes for proportional integral and proportional resonant controller," in *National Power Electronic Conference*, 2010.

[93] B. K. Bose, *Modern Power Electronics and AC Drives.* Prentice Hall PTR, 2002.

[94] S. Yang, Q. Lei, F. Peng, and Z. Qian, "A robust control scheme for grid-connected voltage-source inverters," *IEEE Trans. Ind. Electron.*, vol. 58, no. 1, pp. 202–212, Jan 2011.

[95] B. Johnson, F. de Mello, and J. Undrill, "Comparing fundamental frequency and differential equation representation of ac/dc," *IEEE Trans. Power Apparatus and Systems*, vol. PAS-101, no. 9, pp. 3379–3384, Sep 1982.

[96] J. Machowski, J. Bialek, and J. Bumby, *Power System Dynamics and Stability.* Wiley, 1997.

[97] D. Ruiz-Vega, T. Asiain Olivares, and D. Olguin Salinas, "An approach to the initialization of dynamic induction motor models," *IEEE Trans. Power Syst.*, vol. 17, no. 3, pp. 747 – 751, Aug 2002.

[98] D. Ramasubramanian, Z. Yu, R. Ayyanar, V. Vittal, and J. Undrill, "Converter model for representing converter interfaced generation in large scale grid simulations," *IEEE Trans. Power Syst.*, vol. 32, no. 1, pp. 765–773, Jan 2017.

[99] "Frequency response initiative report - the reliability role of frequency response," NERC, Atlanta, GA, Tech. Rep., Oct 2012.

[100] M. Seelig, "Impact of new generator circuit-breaker technologies on power plant availability and profitability," *Proceedings CEPSI*, 2000.

[101] D. Ramasubramanian, V. Vittal, and J. M. Undrill, "Transient stability analysis of an all converter interfaced generation wecc system," in *2016 Power Systems Computation Conference (PSCC)*, June 2016, pp. 1–7.

[102] "Essential reliability services task force measures framework report," NERC, Atlanta, GA, Tech. Rep., Dec 2015.

[103] R. Concepcion, M. Donnelly, R. Elliott, and J. Sanchez-Gasca, "Extended-term dynamic simulations with high penetrations of photovoltaic generation," Sandia National Laboratories, Albuquerque, NM, Tech. Rep. SAND2016-0065, Jan 2016.

[104] D. Ramasubramanian and V. Vittal, "Small signal stability analysis of controlled voltage source converter model for positive sequence time domain simulations," in *2016 North American Power Symposium (NAPS)*, Sept 2016, pp. 1–6.

[105] "Power Systems Test Case Archive," University of Washington, Electrical Engineering, May 1993, [Online]: http://www2.ee.washington.edu/research/pstca/pf118/pg_tca118bus.htm [Accessed: December 29, 2016].

APPENDIX A

THREE GENERATOR EQUIVALENT SYSTEM DATA

A.1 Power Flow Solution

The power flow solution along with the power demand and generation at each bus is as tabulated in Table A.1.

Table A.1: Power flow solution for the three generator equivalent system

Bus	**V(pu)**	**Ang(deg)**	$\mathbf{P_d}$**(MW)**	$\mathbf{Q_d}$**(MVAR)**	$\mathbf{P_g}$**(MW)**	$\mathbf{Q_g}$**(MVAR)**
1	1.040	0.0	0.0	0.0	71.6	27.0
2	1.025	9.3	0.0	0.0	163.0	6.7
3	1.025	4.7	0.0	0.0	85.0	-10.9
4	1.026	-2.2	0.0	0.0	0.0	0.0
5	0.996	-4.0	125.0	50.0	0.0	0.0
6	1.013	-3.7	90.0	30.0	0.0	0.0
7	1.026	3.7	0.0	0.0	0.0	0.0
8	1.016	0.7	100.0	35.0	0.0	0.0
9	1.032	2.0	0.0	0.0	0.0	0.0

A.2 Dynamic Data

The generator, exciter and governor data is as given as in Tables A.2, A.3 and A.4 respectively. The reactances in the generator data are given in *pu* on a 100 MVA base while the time constants and the inertia constant are in seconds. The machine at bus 1 was modeled using the GENSAL model while the other two machines were modeled using the GENROU models. The induction motor data is given in Table A.5. A static exciter EXST1 was used on all machines while the governor model

Table A.2: Generator dynamic data for the three generator equivalent system

Bus	**MVA**	**kV**	$\mathbf{x_d}$	$\mathbf{x'_d}$	$\mathbf{x_q}$	$\mathbf{x'_q}$	$\mathbf{x_\ell}$	$\tau'_{\mathbf{d0}}$	$\tau'_{\mathbf{q0}}$	**H**
1	247.5	16.5	0.1460	0.0608	0.0969	0.0969	0.0336	8.96	0	23.64
2	192.0	18.0	0.8958	0.1198	0.8645	0.1969	0.0521	6.00	0.535	6.4
3	128.0	13.8	1.3125	0.1813	1.2578	0.25	0.0742	5.89	0.6	3.01

TGOV1 was used as a governor on all machines.

Table A.3: Exciter dynamic data for the three generator equivalent system

Bus	$\mathbf{T_r}$	$\mathbf{V_{imax}}$	$\mathbf{V_{imin}}$	$\mathbf{T_c}$	$\mathbf{T_b}$	$\mathbf{K_a}$	$\mathbf{T_a}$	$\mathbf{V_{rmax}}$	$\mathbf{V_{rmin}}$	$\mathbf{K_c}$	$\mathbf{K_f}$	$\mathbf{T_f}$	$\mathbf{T_{c1}}$	$\mathbf{T_{b1}}$	$\mathbf{V_{amax}}$	$\mathbf{V_{amin}}$	$\mathbf{X_e}$	$\mathbf{I_{lr}}$	$\mathbf{K_{lr}}$
1	0.0	0.1	-0.1	1.0	10.0	200.0	0.02	5.0	-5.0	0.05	0.0	1.0	1.0	1.0	5.0	-5.0	0.04	2.8	5.0
2	0.0	0.1	-0.1	1.0	10.0	200.0	0.02	5.0	-5.0	0.05	0.0	1.0	1.0	1.0	5.0	-5.0	0.04	2.8	5.0
3	0.0	0.1	-0.1	1.0	10.0	200.0	0.02	5.0	-5.0	0.05	0.0	1.0	1.0	1.0	5.0	-5.0	0.04	2.8	5.0

Table A.4: Governor dynamic data for the three generator equivalent system

Bus	**MWcap**	**R**	$\mathbf{T_1}$	$\mathbf{V_{max}}$	$\mathbf{V_{min}}$	$\mathbf{T_2}$	$\mathbf{T_3}$	$\mathbf{D_t}$
1	247.5	0.05	0.5	1.0	0.01	1.0	10.0	0.0
2	192.0	0.05	0.5	1.0	0.01	1.0	10.0	0.0
3	128.0	0.05	0.5	1.0	0.01	1.0	10.0	0.0

Table A.5: Induction motor data

Parameter	**Value**
X_s	3.97
X'_s	0.236
R_s	0.013
T'_o	1.139s
H_{ind}	0.3s
D_{ind}	2.0
$X_{s\ell}$	0.17

APPENDIX B

DERIVATION OF STATE SPACE REPRESENTATION OF CONTROLLED VOLTAGE SOURCE CONVERTER CONTROL MODEL

With reference to Figures 4.5 and 4.9, and (4.13), the equations representing the controller and converter are linearized as below,

Ⓘ

$$\frac{ds_1}{dt} = K_i \left[V_{ref} - s_2 - R_q Q_g\right] \tag{B.1}$$

$$\Rightarrow \Delta\dot{s}_1 = K_i \Delta V_{ref} - K_i \Delta s_2 - R_q K_i \Delta Q_g$$

$$\text{but } Q_g = V_{t_q} i_d - V_{t_d} i_q \rightarrow Q_g = V_{t_q} s_7 - V_{t_d} s_6$$

$$\therefore \Delta Q_g = V_{t_{q0}} \Delta s_7 + i_{d_0} \Delta V_{t_q} - V_{t_{d0}} \Delta s_6 - i_{q_0} \Delta V_{t_d}$$

$$\therefore \boxed{\begin{aligned}\Delta\dot{s}_1 = K_i \Delta V_{ref} - K_i \Delta s_2 - K_i R_q V_{t_{q0}} \Delta s_7 - K_i R_q i_{d_0} \Delta V_{t_q} + K_i R_q V_{t_{d0}} \Delta s_6 \\ + K_i R_q i_{q_0} \Delta V_{t_d}\end{aligned}}$$

Ⓘⓘ

$$\frac{ds_2}{dt} = (1/T_r) * \left[V_t - s_2\right] \tag{B.2}$$

$$\Rightarrow \Delta\dot{s}_2 = (1/T_r) \left[\Delta V_t - \Delta s_2\right]$$

$$\text{but } V_t^2 = V_{t_d}^2 + V_{t_q}^2 \Rightarrow 2V_{t_0} \Delta V_t = 2V_{t_{d0}} \Delta V_{t_d} + 2V_{t_{q0}} \Delta V_{t_q}$$

$$\therefore \Delta V_t = \frac{V_{t_{d0}}}{V_{t_0}} \Delta V_{t_d} + \frac{V_{t_{q0}}}{V_{t_0}} \Delta V_{t_q}$$

$$\therefore \boxed{\Delta\dot{s}_2 = \frac{V_{t_{d0}}}{T_r V_{t_0}} \Delta V_{t_d} + \frac{V_{t_{q0}}}{T_r V_{t_0}} \Delta V_{t_q} - \frac{1}{T_r} \Delta s_2}$$

Ⓘⓘⓘ

$$\frac{ds_3}{dt} = (1/T_{Gpv}) * \left[P_{ref} - (\Delta\omega/R_p) - s_3\right] \tag{B.3}$$

$$\Rightarrow \Delta\dot{s}_3 = (1/T_{Gpv}) \left[\Delta P_{ref} - (\Delta\omega/R_p) - \Delta s_3\right]$$

with $\Delta\omega = \omega - \omega_s$. For a converter, the frequency (ω) is obtained as the rate of change of the bus voltage angle (δ) at the point of connection. In PSLF, internally, a numerical differentiation of the bus voltage angle is performed. The bus frequency is then obtained by passing the result of the numerical differentiation through a filter with a time constant denoted by T_{frq}=0.05s. During linearization, the change in frequency for the active power droop equation is obtained as shown in Figure B.1. The bus voltage angle can be defined as,

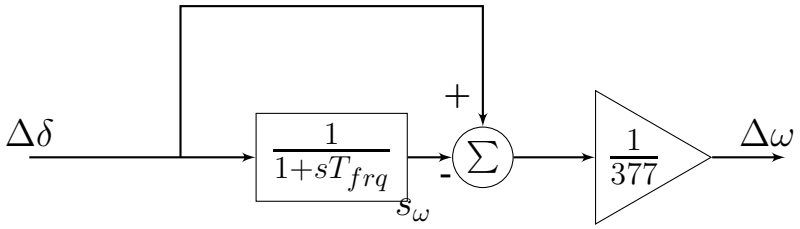

Figure B.1: Block diagram for obtaining $\Delta\omega$ for linearization of active power droop equation

$$\tan\delta = V_{t_q}/V_{t_d}$$

$$\Rightarrow \frac{d(\tan\delta)}{dt} = \frac{V_{t_{d0}}\Delta V_{t_q} - V_{t_{q0}}\Delta V_{t_d}}{V_{t_{d0}}^2}$$

$$\Rightarrow \sec^2\delta_0\Delta\delta = \frac{\Delta\delta}{\cos^2\delta_0} = \frac{V_{t_{d0}}\Delta V_{t_q} - V_{t_{q0}}\Delta V_{t_d}}{V_{t_{d0}}^2}$$

but $\cos\delta_0 = V_{t_{d0}}/V_{t_0}$

$$\Rightarrow \Delta\delta = \frac{V_{t_{d0}}}{V_{t_0}^2}\Delta V_{t_q} - \frac{V_{t_{q0}}}{V_{t_0}^2}\Delta V_{t_d}$$

but $\Delta\omega = \Delta\dot{s}_\omega/377$ where $\Delta\dot{s}_\omega$ is defined by (B.10)

$$\therefore \Delta\omega = -\frac{1}{377T_{frq}}\Delta s_\omega + \frac{V_{t_{d0}}}{377T_{frq}V_{t_0}^2}\Delta V_{t_q} - \frac{V_{t_{q0}}}{377T_{frq}V_{t_0}^2}\Delta V_{t_d}$$

$$\therefore \boxed{\Delta\dot{s}_3 = \frac{\Delta P_{ref}}{T_{Gpv}} - \frac{1}{T_{Gpv}}\Delta s_3 + \frac{1}{377T_{frq}R_pT_{Gpv}}\Delta s_\omega - \frac{V_{t_{d0}}}{377T_{frq}R_pT_{Gpv}V_{t_0}^2}\Delta V_{t_q} + \frac{V_{t_{q0}}}{377T_{frq}R_pT_{Gpv}V_{t_0}^2}\Delta V_{t_d}}$$

(IV)

$$\frac{ds_4}{dt} = K_{ip}\left[s_3 - P_g\right] \tag{B.4}$$

$$\Rightarrow \Delta\dot{s}_4 = K_{ip}\Delta s_3 - K_{ip}\Delta P_g$$

but $P_g = V_d i_d + V_q i_q \rightarrow P_g = V_d s_7 + V_q s_6$

$$\therefore \Delta P_g = V_{t_{d0}}\Delta s_7 + i_{d_0}\Delta V_{t_d} + V_{t_{q0}}\Delta s_6 + i_{q_0}\Delta V_{t_q}$$

$$\therefore \boxed{\Delta\dot{s}_4 = K_{ip}\Delta s_3 - K_{ip}V_{t_{d0}}\Delta s_7 - K_{ip}i_{d_0}\Delta V_{t_d} - K_{ip}V_{t_{q0}}\Delta s_6 - K_{ip}i_{q_0}\Delta V_{t_q}}$$

(V)

$$\frac{ds_5}{dt} = K_{iq}\left[Q_{cmd} - Q_g\right] \tag{B.5}$$

$$\Rightarrow \Delta\dot{s}_5 = K_{iq}\Delta Q_{cmd} - K_{iq}\Delta Q_g$$

$$\text{but } \Delta Q_{cmd} = \Delta s_1 + K_p\Delta V_{ref} - K_p\Delta s_2 - K_pR_q\Delta Q_g$$

$$\therefore \Delta\dot{s}_5 = K_{iq}\Delta s_1 + K_{iq}K_p\Delta V_{ref} - K_{iq}K_p\Delta s_2 - K_{iq}\left(K_pR_q + 1\right)\Delta Q_g$$

$$\text{but } \Delta Q_g = V_{t_{q0}}\Delta s_7 + i_{d_0}\Delta V_{t_q} - V_{t_{d0}}\Delta s_6 - i_{q_0}\Delta V_{t_d}$$

$$\therefore \boxed{\begin{aligned}\Delta\dot{s}_5 = {} & K_{iq}\Delta s_1 + K_{iq}K_p\Delta V_{ref} - K_{iq}K_p\Delta s_2 - K_{iq}V_{t_{q0}}\left(K_pR_q + 1\right)\Delta s_7 \\ & - K_{iq}i_{d_0}\left(K_pR_q + 1\right)\Delta V_{t_q} + K_{iq}V_{t_{d0}}\left(K_pR_q + 1\right)\Delta s_6 \\ & + K_{iq}i_{q_0}\left(K_pR_q + 1\right)\Delta V_{t_d}\end{aligned}}$$

(VI)

$$\frac{ds_6}{dt} = \frac{1}{T_Q}\left[-I_{Qcmd} - s_6\right] \tag{B.6}$$

$$\Rightarrow \Delta\dot{s}_6 = -\frac{1}{T_Q}\Delta I_{Qcmd} - \frac{1}{T_Q}\Delta s_6$$

$$\text{but } I_{Qcmd} = \frac{Q_{cmd}}{V_t} + s_5$$

$$\therefore \Delta I_{Qcmd} = \frac{\Delta Q_{cmd}}{V_{t_0}} - \frac{Q_{cmd_0}}{V_{t_0}^2}\Delta V_t + \Delta s_5$$

$$\text{but } Q_{cmd} = s_1 + K_p\left[V_{ref} - s_2 - R_qQ_g\right]$$

$$\therefore \Delta Q_{cmd} = \begin{aligned}& \Delta s_1 + K_p\Delta V_{ref} - K_p\Delta s_2 - K_pR_qV_{t_{q0}}\Delta s_7 \\ & - K_pR_qi_{d_0}\Delta V_{t_q} + K_pR_qV_{t_{d0}}\Delta s_6 + K_pR_qi_{q_0}\Delta V_{t_d}\end{aligned}$$

$$\text{also } \Delta V_t = \frac{V_{t_{d0}}}{V_{t_0}}\Delta V_{t_d} + \frac{V_{t_{q0}}}{V_{t_0}}\Delta V_{t_q}$$

$$\therefore \boxed{\begin{aligned}\Delta\dot{s}_6 =& \frac{-1}{T_Q V_{t_0}}\Delta s_1 - \frac{K_p}{T_Q V_{t_0}}\Delta V_{ref} + \frac{K_p}{T_Q V_{t_0}}\Delta s_2 + \frac{K_p R_q V_{t_{q0}}}{T_Q V_{t_0}}\Delta s_7 \\ &+ \left[\frac{K_p R_q i_{d_0}}{T_Q V_{t_0}} + \frac{Q_{cmd_0} V_{t_{q0}}}{T_Q V_{t_0}^3}\right]\Delta V_{t_q} - \left[\frac{K_p R_q V_{t_{d0}}}{T_Q V_{t_0}} + \frac{1}{T_Q}\right]\Delta s_6 \\ &- \left[\frac{K_p R_q i_{q_0}}{T_Q V_{t_0}} - \frac{Q_{cmd_0} V_{t_{d0}}}{T_Q V_{t_0}^3}\right]\Delta V_{t_d} - \frac{1}{T_Q}\Delta s_5\end{aligned}}$$

(VII)

$$\frac{ds_7}{dt} = \frac{1}{T_D}\left[I_{Pcmd} - s_7\right] \tag{B.7}$$

$$\Rightarrow \Delta\dot{s}_7 = \frac{1}{T_D}\Delta I_{Pcmd} - \frac{1}{T_D}\Delta s_7$$

$$\text{but } I_{Pcmd} = \frac{s_3}{V_t} + s_4$$

$$\therefore \Delta I_{Pcmd} = \frac{\Delta s_3}{V_{t_0}} - \frac{P_{cmd_0}}{V_{t_0}^2}\Delta V_t + \Delta s_4$$

$$\Rightarrow \Delta I_{Pcmd} = \frac{\Delta s_3}{V_{t_0}} - \frac{P_{cmd_0} V_{t_{d0}}}{V_{t_0}^3}\Delta V_{t_d} - \frac{P_{cmd_0} V_{t_{q0}}}{V_{t_0}^3}\Delta V_{t_q} + \Delta s_4$$

$$\therefore \boxed{\Delta\dot{s}_7 = \frac{1}{T_D V_{t_0}}\Delta s_3 - \frac{P_{cmd_0} V_{t_{d0}}}{T_D V_{t_0}^3}\Delta V_{t_d} - \frac{P_{cmd_0} V_{t_{q0}}}{T_D V_{t_0}^3}\Delta V_{t_q} + \frac{1}{T_D}\Delta s_4 - \frac{1}{T_D}\Delta s_7}$$

(VIII)

$$\frac{ds_8}{dt} = \frac{1}{T_{ed}}\left[E_d - s_8\right] \tag{B.8}$$

$$\Rightarrow \Delta\dot{s}_8 = \frac{1}{T_{ed}}\Delta E_d - \frac{1}{T_{ed}}\Delta s_8$$

$$\text{but } E_d = V_{t_{d0}} + i_d R_f - i_q X_f \Rightarrow E_d = V_{t_{d0}} + s_7 R_f - s_6 X_f$$

$$\therefore \Delta E_d = R_f \Delta s_7 - X_f \Delta s_6$$

$$\therefore \boxed{\Delta\dot{s}_8 = \frac{R_f}{T_{ed}}\Delta s_7 - \frac{X_f}{T_{ed}}\Delta s_6 - \frac{1}{T_{ed}}\Delta s_8}$$

(IX)

$$\frac{ds_9}{dt} = \frac{1}{T_{eq}}\left[E_q - s_9\right] \tag{B.9}$$

$$\Rightarrow \Delta\dot{s}_9 = \frac{1}{T_{eq}}\Delta E_q - \frac{1}{T_{eq}}\Delta s_9$$

$$\text{but } E_q = V_{t_{q0}} + i_q R_f + i_d X_f \Rightarrow E_q = V_{t_{q0}} + s_6 R_f + s_7 X_f$$

$$\therefore \Delta E_q = R_f \Delta s_6 + X_f \Delta s_7$$

$$\therefore \boxed{\Delta\dot{s}_9 = \frac{R_f}{T_{eq}}\Delta s_6 + \frac{X_f}{T_{eq}}\Delta s_7 - \frac{1}{T_{eq}}\Delta s_9}$$

(X)

$$\frac{ds_\omega}{dt} = \frac{1}{T_{frq}}\left[\Delta\delta - s_\omega\right] \tag{B.10}$$

$$\therefore \boxed{\Delta\dot{s}_\omega = \frac{-1}{T_{frq}}\Delta s_\omega + \frac{V_{t_{d0}}}{T_{frq}V_{t_0}^2}\Delta V_{t_q} - \frac{V_{t_{q0}}}{T_{frq}V_{t_0}^2}\Delta V_{t_d}}$$

The state equations of the device will be represented in the following form:

$$\begin{aligned} \Delta\dot{x} &= A_d\Delta x + B_d\left[\Delta V_{t_d}\ \Delta V_{t_q}\right]^T + F_d\left[\Delta V_{ref}\ \Delta P_{ref}\right]^T \\ \left[\Delta i_d\ \Delta i_q\right]^T &= C_d\Delta x + D_d\left[\Delta V_{t_d}\ \Delta V_{t_q}\right]^T \end{aligned} \tag{B.11}$$

where,

$$A_d = \begin{bmatrix} 0 & -K_i & 0 & 0 & 0 & K_iR_qV_{t_{d0}} & -K_iR_qV_{t_{q0}} & 0 & 0 & 0 \\ 0 & \frac{-1}{T_r} & 0 & 0 & 0 & 0 & 0 & 0 & 0 & 0 \\ 0 & 0 & \frac{-1}{T_{Gpv}} & 0 & 0 & 0 & 0 & 0 & 0 & \frac{1}{377T_{frq}R_pT_{Gpv}} \\ 0 & 0 & K_{ip} & 0 & 0 & -K_{ip}V_{t_{q0}} & -K_{ip}V_{t_{d0}} & 0 & 0 & 0 \\ K_{iq} & -K_{iq}K_p & 0 & 0 & 0 & K_{iq}V_{t_{d0}}(K_pR_q{+}1) & K_{iq}V_{t_{q0}}(K_pR_q{+}1) & 0 & 0 & 0 \\ \frac{-1}{T_QV_{t_0}} & \frac{K_p}{T_QV_{t_0}} & 0 & 0 & \frac{-1}{T_Q} & -\left[\frac{K_pR_qV_{t_{d0}}}{T_QV_{t_0}}+\frac{1}{T_Q}\right] & \frac{K_pR_qV_{t_{q0}}}{T_QV_{t_0}} & 0 & 0 & 0 \\ 0 & 0 & \frac{1}{T_DV_{t_0}} & \frac{1}{T_D} & 0 & 0 & \frac{-1}{T_D} & 0 & 0 & 0 \\ 0 & 0 & 0 & 0 & 0 & \frac{-X_f}{T_{ed}} & \frac{R_f}{T_{ed}} & \frac{-1}{T_{ed}} & 0 & 0 \\ 0 & 0 & 0 & 0 & 0 & \frac{R_f}{T_{eq}} & \frac{X_f}{T_{eq}} & 0 & \frac{-1}{T_{eq}} & 0 \\ 0 & 0 & 0 & 0 & 0 & 0 & 0 & 0 & 0 & \frac{-1}{T_{frq}} \end{bmatrix}$$

$$B_d = \begin{bmatrix} K_i R_q i_{q_0} & -K_i R_q i_{d_0} \\ \frac{V_{t_{d0}}}{T_r V_{t_0}} & \frac{V_{t_{q0}}}{T_r V_{t_0}} \\ \frac{V_{t_{q0}}}{377 R_p T_{Gpv} T_{frq} V_{t_0}^2} & \frac{-V_{t_{d0}}}{377 R_p T_{Gpv} T_{frq} V_{t_0}^2} \\ -K_{ip} i_{d_0} & -K_{ip} i_{q_0} \\ K_{iq} i_{q_0} (K_p R_q + 1) & -K_{iq} i_{d_0} (K_p R_q + 1) \\ -\left[\frac{K_p R_q i_{q_0}}{T_Q V_{t_0}} - \frac{Q_{cmd_0} V_{t_{d0}}}{T_Q V_{t_0}^3}\right] & \left[\frac{K_p R_q i_{d_0}}{T_Q V_{t_0}} + \frac{Q_{cmd_0} V_{t_{q0}}}{T_Q V_{t_0}^3}\right] \\ \frac{-P_{cmd_0} V_{t_{d0}}}{T_D V_{t_0}^3} & \frac{-P_{cmd_0} V_{t_{q0}}}{T_D V_{t_0}^3} \\ 0 & 0 \\ 0 & 0 \\ \frac{-V_{t_{q0}}}{T_{frq} V_{t_0}^2} & \frac{V_{t_{d0}}}{T_{frq} V_{t_0}^2} \end{bmatrix}$$

$$F_d = \begin{bmatrix} K_i & 0 \\ 0 & 0 \\ 0 & \frac{1}{T_{Gpv}} \\ 0 & 0 \\ K_{iq} K_p & 0 \\ \frac{-K_p}{T_Q V_{t_0}} & 0 \\ 0 & 0 \\ 0 & 0 \\ 0 & 0 \\ 0 & 0 \end{bmatrix} \qquad C_d = \begin{bmatrix} 0 & 0 & 0 & 0 & 0 & 0 & 1 & 0 & 0 & 0 \\ 0 & 0 & 0 & 0 & 0 & 0 & 1 & 0 & 0 & 0 \end{bmatrix}$$

$$D_d = \begin{bmatrix} 0 & 0 \\ 0 & 0 \end{bmatrix}$$

To obtain the system A matrix, the converter is connected to an infinite bus as shown in Figure 5.59 and the network equations are derived. From (4.13) and Figure 4.9, the equation for the terminal voltage can be written as,

$$\left(V_{t_d} + jV_{t_q}\right) = (s_8 + js_9) - (i_d + ji_q)(R_f + jX_f) \tag{B.12}$$

where, i_d and i_q are the components of the converter current I_{conv} along the network dq axis. By treating the load as a constant admittance load $Y_L = G_L + jB_L$, the equation for current can be written as,

$$i_d + ji_q = (s_8 + js_9)(G + jB) - (s_8 + js_9)\frac{(G + jB)^2}{(G_x + jB_x)} - (V_\infty + j0)\frac{(G_2 + jB_2)(G + jB)}{(G_x + jB_x)} \tag{B.13}$$

where, $G + jB = 1/(Z_1 + R_f + jX_f)$, $G_2 + jB_2 = 1/Z_2$ and $G_x + jB_x = (G + jB) + (G_L + jB_L) + (G_2 + jB_2)$. Substituting for $i_d + ji_q$ in (B.12) by using the expression

in (B.13), the expression for the terminal voltage of the converter can be obtained as,

$$\begin{aligned}\left(V_{t_d}+jV_{t_q}\right) &= \left(s_8+js_9\right)\left[1-\left(R_f+jX_f\right)\left(G+jB\right)+\frac{\left(R_f+jX_f\right)\left(G+jB\right)^2}{\left(G_x+jB_x\right)}\right] \\ &\quad +\left(V_\infty+j0\right)\left[\frac{\left(R_f+jX_f\right)\left(G_2+jB_2\right)\left(G+jB\right)}{\left(G_x+jB_x\right)}\right] \\ \Rightarrow \left(V_{t_d}+jV_{t_q}\right) &= \left(s_8+js_9\right)\left(Y_A+jY_B\right)+\left(V_\infty+j0\right)\left(Y_C+jY_D\right)\end{aligned} \tag{B.14}$$

where,

$$\begin{aligned}Y_A &= \mathbb{R}\left[1-\left(R_f+jX_f\right)\left(G+jB\right)+\frac{\left(R_f+jX_f\right)\left(G+jB\right)^2}{\left(G_x+jB_x\right)}\right] \\ Y_B &= \mathbb{I}\left[1-\left(R_f+jX_f\right)\left(G+jB\right)+\frac{\left(R_f+jX_f\right)\left(G+jB\right)^2}{\left(G_x+jB_x\right)}\right] \\ Y_C &= \mathbb{R}\left[\frac{\left(R_f+jX_f\right)\left(G_2+jB_2\right)\left(G+jB\right)}{\left(G_x+jB_x\right)}\right] \\ Y_D &= \mathbb{I}\left[\frac{\left(R_f+jX_f\right)\left(G_2+jB_2\right)\left(G+jB\right)}{\left(G_x+jB_x\right)}\right]\end{aligned} \tag{B.15}$$

Linearizing (B.14),

$$\boxed{\Delta V_{t_d}=Y_A\Delta s_8-Y_B\Delta s_9;\ \Delta V_{t_q}=Y_B\Delta s_8+Y_A\Delta s_9}$$

Thus, the network matrix relating the converter terminal voltage to the state variables can be written as,

$$Y_d=\left[\begin{smallmatrix}0&0&0&0&0&0&0&Y_A&-Y_B&0\\0&0&0&0&0&0&0&Y_B&Y_A&0\end{smallmatrix}\right]$$

The final state space representation of the system of Fig. 5.59 can be written as,

$$\begin{aligned}\Delta\dot{x} &= A_{sys}\Delta x+B_{sys}\left[\Delta V_{ref}\ \Delta P_{ref}\right]^T \\ \Delta y &= C_{sys}\Delta x+D_{sys}\left[\Delta V_{ref}\ \Delta P_{ref}\right]^T\end{aligned} \tag{B.16}$$

where,

$$A_{sys}=A_d+B_dY_d \text{ and } B_{sys}=F_d \tag{B.17}$$

The terminal voltage of the converter (V_t) and the frequency (ω) are taken as the output variables. Hence,

$$C_{sys}=\left[\begin{smallmatrix}0&0&0&0&0&0&0&\frac{V_{t_{d0}}}{V_{t_0}}Y_A+\frac{V_{t_{q0}}}{V_{t_0}}Y_B&\frac{-V_{t_{d0}}}{V_{t_0}}Y_B+\frac{V_{t_{q0}}}{V_{t_0}}Y_A&0\\0&0&0&0&0&0&0&\frac{V_{t_{d0}}}{377T_{frq}V_{t_0}^2}Y_B-\frac{V_{t_{q0}}}{377T_{frq}V_{t_0}^2}Y_A&\frac{V_{t_{d0}}}{377T_{frq}V_{t_0}^2}Y_A+\frac{V_{t_{q0}}}{377T_{frq}V_{t_0}^2}Y_B&\frac{-1}{377T_{frq}}\end{smallmatrix}\right]$$

and, $D_{sys}=\left[\begin{smallmatrix}0&0\\0&0\end{smallmatrix}\right]$ (B.18)

APPENDIX C

118 BUS SYSTEM DATA AND CONVERGED POWER FLOW SOLUTION

C.1 Input Data for Power Flow Program

NRLF Program

System Specification

Total number of buses: 118

Total number of branches: 186

Slack Bus

Bus	Vspec(pu)	Pd(MW)	Qd(MVAR)
69	1.03500	0.00000	0.00000

PV Buses

Total Number of PV Buses: 53

Bus	Vspec(pu)	Pg(MW)	Pd(MW)	Qd(MVAR)	Qmax(MVAR)	Qmin(MVAR)
1	0.9550	0.00	61.20	27.00	15.00	−5.00
4	0.9980	9.00	36.00	12.00	300.00	−300.00
6	0.9900	0.00	62.40	22.00	50.00	−13.00
8	1.0150	28.00	0.00	0.00	300.00	−300.00
10	1.0500	450.00	0.00	0.00	200.00	−147.00
12	0.9900	85.00	56.40	10.00	120.00	−35.00
15	0.9700	0.00	108.00	30.00	30.00	−10.00
18	0.9730	0.00	72.00	34.00	50.00	−16.00
19	0.9620	0.00	54.00	25.00	24.00	−8.00
24	0.9920	13.00	0.00	0.00	300.00	−300.00
25	1.0500	220.00	0.00	0.00	140.00	−47.00
26	1.0150	314.00	0.00	0.00	1000.00	−1000.00
27	0.9680	9.00	74.40	13.00	300.00	−300.00
31	0.9670	7.00	51.60	27.00	300.00	−300.00
32	0.9630	0.00	70.80	23.00	42.00	−14.00
34	0.9840	0.00	70.80	26.00	24.00	−8.00
36	0.9800	0.00	37.20	17.00	24.00	−8.00
40	0.9700	46.00	24.00	23.00	300.00	−300.00
42	0.9850	59.00	44.40	23.00	300.00	−300.00
46	1.0050	19.00	33.60	10.00	100.00	−100.00
49	1.0250	204.00	104.40	30.00	210.00	−85.00
54	0.9550	48.00	135.60	32.00	300.00	−300.00
55	0.9520	0.00	75.60	22.00	23.00	−8.00
56	0.9540	0.00	100.80	18.00	15.00	−8.00
59	0.9850	155.00	332.40	113.00	180.00	−60.00
61	0.9950	160.00	0.00	0.00	300.00	−100.00
62	0.9980	0.00	92.40	14.00	20.00	−20.00
65	1.0050	391.00	0.00	0.00	200.00	−67.00
66	1.0500	392.00	46.80	18.00	200.00	−67.00
70	0.9840	0.00	79.20	20.00	32.00	−10.00
72	0.9800	12.00	0.00	0.00	100.00	−100.00
73	0.9910	6.00	0.00	0.00	100.00	−100.00
74	0.9580	0.00	81.60	27.00	9.00	−6.00

76	0.9430	0.00	81.60	36.00	23.00	−8.00
77	1.0060	0.00	73.20	28.00	70.00	−20.00
80	1.0400	477.00	156.00	26.00	280.00	−165.00
85	0.9850	0.00	28.80	15.00	23.00	−8.00
87	1.0150	4.00	0.00	0.00	1000.00	−100.00
89	1.0050	607.00	0.00	0.00	300.00	−210.00
90	0.9850	85.00	93.60	42.00	300.00	−300.00
91	0.9800	10.00	0.00	0.00	100.00	−100.00
92	0.9900	0.00	78.00	10.00	9.00	−3.00
99	1.0100	42.00	0.00	0.00	100.00	−100.00
100	1.0170	252.00	44.40	18.00	155.00	−50.00
103	1.0100	40.00	27.60	16.00	40.00	−15.00
104	0.9710	0.00	45.60	25.00	23.00	−8.00
105	0.9650	0.00	37.20	26.00	23.00	−8.00
107	0.9520	22.00	33.60	12.00	200.00	−200.00
110	0.9730	0.00	46.80	30.00	23.00	−8.00
111	0.9800	36.00	0.00	0.00	1000.00	−100.00
112	0.9750	43.00	30.00	13.00	1000.00	−100.00
113	0.9930	6.00	0.00	0.00	200.00	−100.00
116	1.0050	184.00	0.00	0.00	1000.00	−1000.00

PQ Buses

Bus	Pd(MW)	Qd(MVAR)	Bus	Pd(MW)	Qd(MVAR)
2	24.00000	9.00000	3	46.80000	10.00000
5	0.00000	0.00000	7	22.80000	2.00000
9	0.00000	0.00000	11	84.00000	23.00000
13	40.80000	16.00000	14	16.80000	1.00000
16	30.00000	10.00000	17	13.20000	3.00000
20	21.60000	3.00000	21	16.80000	8.00000
22	12.00000	5.00000	23	8.40000	3.00000
28	20.40000	7.00000	29	28.80000	4.00000
30	0.00000	0.00000	33	27.60000	9.00000
35	39.60000	9.00000	37	0.00000	0.00000
38	0.00000	0.00000	39	32.40000	11.00000
41	44.40000	10.00000	43	21.60000	7.00000
44	19.20000	8.00000	45	63.60000	22.00000
47	40.80000	0.00000	48	24.00000	11.00000
50	20.40000	4.00000	51	20.40000	8.00000
52	21.60000	5.00000	53	27.60000	11.00000
57	14.40000	3.00000	58	14.40000	3.00000
60	93.60000	3.00000	63	0.00000	0.00000
64	0.00000	0.00000	67	33.60000	7.00000
68	0.00000	0.00000	71	0.00000	0.00000
75	56.40000	11.00000	78	85.20000	26.00000
79	46.80000	32.00000	81	0.00000	0.00000
82	64.80000	27.00000	83	24.00000	10.00000
84	13.20000	7.00000	86	25.20000	10.00000
88	57.60000	10.00000	93	14.40000	7.00000
94	36.00000	16.00000	95	50.40000	31.00000

96	45.60000	15.00000	97	18.00000	9.00000
98	40.80000	8.00000	101	26.40000	15.00000
102	6.00000	3.00000	106	51.60000	16.00000
108	2.40000	1.00000	109	9.60000	3.00000
114	9.60000	3.00000	115	26.40000	7.00000
117	24.00000	8.00000	118	39.60000	15.00000

Bus Shunt Data

Bus	GShunt(pu)	BShunt(pu)	Bus	GShunt(pu)	BShunt(pu)
34	0.00000	0.14000	44	0.00000	0.10000
45	0.00000	0.10000	46	0.00000	0.10000
48	0.00000	0.15000	74	0.00000	0.12000
79	0.00000	0.20000	82	0.00000	0.20000
83	0.00000	0.10000	105	0.00000	0.20000
107	0.00000	0.06000	110	0.00000	0.06000

Line Data

FB	TB	G(pu)	B(pu)	Bch(pu)
1	2	−2.78030	9.16674	0.02540
1	3	−6.56766	21.58673	0.01082
4	5	−26.35599	119.50043	0.00210
3	5	−1.96818	8.82006	0.02840
5	6	−3.89193	17.66085	0.01426
6	7	−10.11664	45.84445	0.00550
8	9	−2.60627	32.57838	1.16200
9	10	−2.47246	30.85780	1.23000
4	11	−4.04236	13.30690	0.01748
5	11	−4.00922	13.46940	0.01738
11	12	−14.18144	46.71533	0.00502
2	12	−4.51228	14.86397	0.01572
3	12	−1.73212	5.72603	0.04060
7	12	−7.00640	27.63544	0.00874
11	13	−3.81080	12.51997	0.01876
12	14	−3.93720	12.94696	0.01816
13	15	−1.13994	3.74463	0.06268
14	15	−1.43148	4.69142	0.05020
12	16	−2.86293	11.26266	0.02140
15	17	−6.33419	20.96999	0.04440
16	17	−1.31605	5.22072	0.04660
17	18	−4.55296	18.69304	0.01298
18	19	−4.37844	19.29017	0.01142
19	20	−1.75928	8.16809	0.02980
15	19	−7.07397	23.22620	0.01010
20	21	−2.42612	11.25562	0.02160
21	22	−2.12273	9.85191	0.02460
22	23	−1.29297	6.01120	0.04040
23	24	−5.18654	18.90207	0.04980
23	25	−2.34821	12.04210	0.08640
25	27	−1.15300	5.91003	0.17640
27	28	−2.49212	11.13831	0.02160
28	29	−2.50683	9.97442	0.02380
8	30	−1.68443	19.69722	0.51400
26	30	−1.07107	11.52840	0.90800
17	31	−1.77685	5.85910	0.03990
29	31	−8.90905	27.30460	0.00830
23	32	−2.21694	8.06351	0.11730
31	32	−2.81390	9.30097	0.02510
27	32	−3.67892	12.12918	0.01926
15	33	−2.24595	7.35252	0.03194
19	34	−1.12804	3.70515	0.06320
35	36	−20.53960	93.52856	0.00268
35	37	−4.24532	19.18112	0.01318
33	37	−1.89617	6.48809	0.03660
34	36	−10.96834	33.74872	0.00568
34	37	−26.97190	99.03744	0.00984
37	39	−2.61690	8.64149	0.02700
37	40	−1.86828	5.29292	0.04200
30	38	−1.57956	18.38279	0.42200
39	40	−4.60137	15.12950	0.01552
40	41	−5.61593	18.86179	0.01222
40	42	−1.51767	5.00420	0.04660
41	42	−2.05968	6.78187	0.03440
43	44	−0.95122	3.83931	0.06068
34	43	−1.37835	5.61020	0.04226
44	45	−2.59868	10.45272	0.02240
45	46	−2.00126	6.78429	0.03320
46	47	−2.16241	7.22700	0.03160
46	48	−1.52798	4.80512	0.04720
47	49	−4.47196	14.63337	0.01604
42	49	−0.65332	2.95136	0.08600

42	49	−0.65332	2.95136	0.08600
45	49	−1.74159	4.73589	0.04440
48	49	−6.23550	17.59177	0.01258
49	50	−4.19289	11.80918	0.01874
49	51	−2.29994	6.48338	0.03420
51	52	−5.24612	15.19564	0.01396
52	53	−1.42744	5.76262	0.04058
53	54	−1.68853	7.83272	0.03100
49	54	−0.82161	3.25267	0.07380
49	54	−0.94218	3.15507	0.07300
54	55	−3.19827	13.37976	0.02020
54	56	−27.84387	96.69417	0.00732
55	56	−19.37858	59.96242	0.00374
56	57	−3.26416	9.19295	0.02420
50	57	−2.34621	6.63276	0.03320
56	58	−3.26416	9.19295	0.02420
51	58	−4.38155	12.35425	0.01788
54	59	−0.91274	4.16088	0.05980
56	59	−1.18183	3.59562	0.05690
56	59	−1.26319	3.75969	0.05360
55	59	−0.97080	4.42073	0.05646
59	60	−1.43895	6.58197	0.03760
59	61	−1.39125	6.36245	0.03880
60	61	−13.95204	71.34567	0.01456
60	62	−3.72897	17.00773	0.01468
61	62	−5.56134	25.37698	0.00980
63	64	−4.26843	49.63291	0.21600
38	65	−0.91909	10.05800	1.04600
64	65	−2.92622	32.85194	0.38000
49	66	−2.05254	10.47937	0.02480
49	66	−2.05254	10.47937	0.02480
62	66	−0.96695	4.37336	0.05780
62	67	−1.79733	8.15067	0.03100
66	67	−2.07330	9.39466	0.02682
65	68	−5.35082	62.03849	0.63800
47	69	−1.00123	3.29552	0.07092
49	69	−0.85892	2.82530	0.08280
69	70	−1.76170	7.45787	0.12200
24	70	−0.01305	2.43006	0.10198
70	71	−6.59172	26.53130	0.00878
24	72	−1.19615	4.80422	0.04880
71	72	−1.29692	5.23421	0.04444
71	73	−4.05401	21.25313	0.01178
70	74	−2.09824	6.92261	0.03368
70	75	−1.97118	6.49385	0.03600
69	75	−2.45094	7.38309	0.12400
74	75	−6.83466	22.55994	0.01034
76	77	−1.85966	6.19886	0.03680
69	77	−2.76986	9.05358	0.10380
75	77	−1.37933	4.58781	0.04978
77	78	−22.39460	73.85454	0.01264
78	79	−8.73360	39.02928	0.00648
77	80	−6.43635	18.36252	0.04720
77	80	−2.47280	8.83143	0.02280
79	80	−3.00028	13.53971	0.01870
68	81	−4.25685	49.13616	0.80800
77	82	−3.65011	10.44814	0.08174
82	83	−7.62599	24.95468	0.03796
83	84	−2.93011	6.18839	0.02580
83	85	−1.81030	6.23079	0.03480
84	85	−6.01492	12.76676	0.01234
85	86	−2.14015	7.52110	0.02760
86	87	−0.64545	4.73359	0.04450
85	88	−1.85117	9.44095	0.02760
85	89	−0.78360	5.67209	0.04700
88	89	−2.64125	13.52931	0.01934
89	90	−1.36218	4.94382	0.05280
89	90	−2.26526	9.48934	0.10600
90	91	−3.32717	10.95084	0.02140
89	92	−3.73830	19.06912	0.05480
89	92	−1.48078	5.95702	0.04140
91	92	−2.18922	7.19558	0.03268
92	93	−3.28383	10.79336	0.02180
92	94	−1.76335	5.79230	0.04060
93	94	−3.80837	12.50100	0.01876
94	95	−6.41462	21.09048	0.01110
80	96	−1.03514	5.29203	0.04940
82	96	−5.27440	17.25575	0.05440
94	96	−3.25067	10.50123	0.02300
80	97	−2.02021	10.31081	0.02540
80	98	−1.94596	8.83043	0.02860
80	99	−1.02029	4.62951	0.05460
92	100	−0.71034	3.23380	0.04720
94	100	−4.83585	15.75727	0.06040
95	96	−5.20627	16.65398	0.01474
96	97	−2.12752	10.88355	0.02400
98	100	−1.18095	5.32467	0.04760
99	100	−2.59602	11.72536	0.02160
100	101	−1.65931	7.55972	0.03280
92	102	−3.75446	17.06297	0.01464
101	102	−1.87084	8.51765	0.02940
100	103	−5.31164	17.42883	0.05360
100	104	−1.03322	4.67354	0.05410
103	104	−1.70933	5.81026	0.04070
103	105	−1.82790	5.55204	0.04080
100	106	−1.07841	4.08191	0.06200
104	105	−6.50675	24.74399	0.00986

105	106	−4.39134	17.15761	0.01434
105	107	−1.46014	5.04160	0.04720
105	108	−4.64140	12.50156	0.01844
106	107	−1.46014	5.04160	0.04720
108	109	−11.17390	30.64841	0.00760
103	110	−1.13562	5.27106	0.04610
109	110	−4.22539	11.58181	0.02020
110	111	−3.55742	12.20843	0.02000
110	112	−5.24852	13.59940	0.06200
17	113	−9.22812	30.42350	0.00768
32	113	−1.36693	4.51199	0.05180
32	114	−3.43713	15.58168	0.01628
27	115	−2.84734	12.86510	0.01972
114	115	−20.27325	91.67034	0.00276
68	116	−20.58348	245.18558	0.16400
12	117	−1.59072	6.76904	0.03580
75	118	−5.74517	19.05811	0.01198
76	118	−5.08004	16.85087	0.01356

Transformer Data

FB	TB	G(pu)	B(pu)	Tap Ratio
8	5	−0.00000	37.45318	0.98500
26	25	−0.00000	26.17801	0.96000
30	17	−0.00000	25.77320	0.96000
38	37	−0.00000	26.66667	0.93500
63	59	−0.00000	25.90674	0.96000
64	61	−0.00000	37.31343	0.98500
65	66	−0.00000	27.02703	0.93500
68	69	−0.00000	27.02703	0.93500
81	80	−0.00000	27.02703	0.93500

CONVERGED SOLUTION

The number of iterations for convergence: 7

The largest mismatch is: 0.000000

Bus Voltages

Bus	V(pu)	Ang(deg)	Bus	V(pu)	Ang(deg)
1	0.95500	−18.47446	2	0.97085	−17.78221
3	0.96702	−17.34437	4	0.99800	−12.65515
5	1.00212	−12.19590	6	0.99000	−15.55254
7	0.98922	−16.10603	8	1.01500	−6.37423
9	1.04292	0.87986	10	1.05000	8.46075
11	0.98414	−15.87095	12	0.99000	−16.56790
13	0.96628	−17.38804	14	0.98315	−17.21691
15	0.97000	−16.99274	16	0.98305	−16.74683
17	0.99525	−14.14625	18	0.97300	−16.69244
19	0.96225	−17.11274	20	0.95493	−16.37046
21	0.95482	−14.68254	22	0.96602	−11.83959
23	0.99846	−6.28277	24	0.99200	−5.67337
25	1.05000	0.47157	26	1.01500	2.31805
27	0.96800	−12.77979	28	0.96086	−14.81917
29	0.96266	−15.96298	30	0.98503	−8.44339
31	0.96700	−15.80184	32	0.96300	−13.43800
33	0.96956	−16.54280	34	0.98432	−14.55629
35	0.98026	−15.04754	36	0.98000	−15.06703
37	0.99036	−13.84548	38	0.96206	−9.34235
39	0.96981	−13.88039	40	0.97000	−12.80683
41	0.96582	−13.09655	42	0.98500	−10.46738
43	0.97527	−15.79160	44	0.98134	−14.50294
45	0.98325	−12.93138	46	1.00500	−10.17481
47	1.01670	−7.82487	48	1.01989	−8.24179
49	1.02500	−6.99776	50	0.99917	−9.71351
51	0.96288	−13.23328	52	0.95224	−14.48713
53	0.94309	−15.90491	54	0.95500	−14.95242
55	0.95200	−15.32351	56	0.95400	−15.07383
57	0.96874	−13.25643	58	0.95629	−14.37548
59	0.98500	−10.24190	60	0.99273	−5.49976
61	0.99500	−4.42656	62	0.99800	−5.10670
63	0.96612	−5.73966	64	0.98165	−3.35888
65	1.00500	1.34171	66	1.05000	0.15089
67	1.01853	−3.20104	68	1.00262	2.56108
69	1.03500	0.00000	70	0.98400	−6.00923
71	0.98699	−5.76584	72	0.98000	−4.88148
73	0.99100	−5.64490	74	0.95800	−7.36624
75	0.96651	−5.84028	76	0.94300	−6.28828
77	1.00600	1.35487	78	1.00284	1.11098
79	1.00818	1.71766	80	1.04000	5.12033
81	0.99667	3.54875	82	0.97999	5.56006
83	0.97520	7.93645	84	0.97513	12.45971
85	0.98500	15.04248	86	0.98565	13.35651
87	1.01500	13.60774	88	0.98399	20.21280
89	1.00500	26.06887	90	0.98500	24.64343
91	0.98000	22.89843	92	0.98894	19.18680
93	0.97894	14.46112	94	0.98212	10.91659
95	0.97053	8.49862	96	0.98268	6.80268
97	1.00590	5.53222	98	1.02057	6.24620
99	1.01000	11.67053	100	1.01700	12.11071
101	0.98954	14.02675	102	0.98742	17.34131
103	1.00308	10.21286	104	0.97100	7.88146
105	0.96569	7.44666	106	0.96158	6.99241
107	0.95200	6.70098	108	0.96665	7.73429
109	0.96723	7.89558	110	0.97300	8.73614
111	0.98000	10.38122	112	0.97500	9.26708
113	0.99300	−13.99098	114	0.95962	−13.84419
115	0.95950	−13.85437	116	1.00500	2.97627
117	0.97226	−18.44475	118	0.94848	−6.61952

Generator Injections

Bus	Pg(MW)	Qg(MVAR)	Bus	Pg(MW)	Qg(MVAR)
1	0.00000	2.21020	4	9.00000	−18.34685
6	0.00000	19.62324	8	28.00000	68.23638
10	450.00000	−51.04215	12	85.00000	103.62316
15	0.00000	14.31401	18	−0.00000	30.96941
19	0.00000	−8.00000	24	13.00000	−18.03953
25	220.00000	51.97577	26	314.00000	10.26088
27	9.00000	5.78094	31	7.00000	37.00945
32	−0.00000	−9.49068	34	−0.00000	−8.00000
36	−0.00000	10.16795	40	46.00000	0.37370
42	59.00000	2.92222	46	19.00000	−0.10328
49	204.00000	113.10233	54	48.00000	15.78927
55	−0.00000	8.55296	56	−0.00000	9.06898
59	155.00000	91.31797	61	160.00000	−35.11668

62	−0.00000	7.48508	65	391.00000	104.52162
66	392.00000	−5.41834	69	123.84312	−48.95737
70	0.00000	8.86608	72	12.00000	−17.15057
73	6.00000	7.03703	74	−0.00000	0.78814
76	−0.00000	14.30907	77	0.00000	47.84113
80	477.00000	135.48539	85	0.00000	13.05747
87	4.00000	11.53179	89	607.00000	16.28241
90	85.00000	10.30322	91	10.00000	−16.26921
92	0.00000	9.00000	99	42.00000	−33.17079
100	252.00000	125.43563	103	40.00000	40.00000
104	−0.00000	5.31261	105	−0.00000	−8.00000
107	22.00000	−6.40885	110	−0.00000	9.60382
111	36.00000	−1.84382	112	43.00000	8.14639
113	6.00000	2.52160	116	184.00000	35.94270

List of Generators on VAR Limits

Bus	VAR Limit (MVAR)	Min/Max
19	−8.00000	Min
34	−8.00000	Min
92	9.00000	Max
103	40.00000	Max
105	−8.00000	Min

Line Flows

FB	TB	Pij (MW)	Qij (MVAR)	Pji (MW)	Qji (MW)
1	2	−14.458895	−11.860102	14.566400	9.859231
1	3	−46.741105	−12.929696	47.071997	13.017965
4	5	−106.533850	−27.670219	106.747829	28.430395
3	5	−82.609872	−10.694483	84.391244	15.923493
5	6	107.976110	1.123942	−106.594157	3.732273
6	7	44.194157	−6.109035	−44.101091	5.992138
8	9	−440.635012	−89.733625	445.254650	24.428906
9	10	−445.254650	−24.428906	450.000000	−51.042152
4	11	79.533850	−2.676632	−78.205804	5.331379
5	11	93.181676	0.778881	−91.425944	3.405355
11	12	47.285095	−43.658947	−47.031940	44.003765
2	12	−38.566400	−18.859231	38.926617	18.534623
3	12	−11.262125	−12.323482	11.384024	8.838527
7	12	21.301091	−7.992138	−21.256082	7.313733
11	13	38.346653	11.922214	−37.971023	−12.472407
12	14	16.968818	3.631176	−16.901169	−5.176311
13	15	−2.828977	−3.527593	2.835642	−2.325484
14	15	0.101169	4.176311	−0.074329	−8.876128
12	16	5.394245	5.835803	−5.377699	−7.853452
15	17	−115.295997	−20.591831	117.208942	22.637064
16	17	−24.622301	−2.146548	24.907121	−1.283201
17	18	90.937147	22.958758	−89.841096	−19.715989
18	19	17.841096	16.685394	−17.768400	−17.434400
19	20	−8.471793	6.525298	8.508334	−9.093991
15	19	9.862375	15.616049	−9.816947	−16.409636
20	21	−30.108334	6.093991	30.300309	−7.172824
21	22	−47.100309	−0.827176	47.608895	0.918384
22	23	−59.608895	−5.918384	60.917042	8.101281
23	24	−16.539282	15.274426	16.619022	−19.916459
23	25	−158.858781	−28.562681	162.899855	40.216655
25	27	150.741474	30.292631	−143.725477	−12.318736
27	28	38.735947	−0.909652	−38.429613	0.269684
28	29	18.029613	−7.269684	−17.936393	5.439122
8	30	76.338153	28.640789	−75.967262	−75.716871
26	30	220.358671	−11.429869	−216.495844	−37.816056
17	31	21.359408	9.794173	−21.074795	−12.697279
29	31	−10.863607	−9.439122	10.886916	8.737906
23	32	106.081021	2.186974	−102.482207	−0.383223
31	32	−34.412121	13.968828	34.862579	−14.817281
27	32	14.792101	1.103105	−14.737643	−2.718973
15	33	−5.327690	0.491403	5.340760	−3.452489
19	34	−17.942860	−5.681262	18.210500	0.572763
35	36	3.578056	1.573632	−3.577690	−1.829420
35	37	−43.178056	−10.573632	43.402789	10.309418
33	37	−32.940760	−5.547511	33.426260	3.693562
34	36	33.726862	4.776406	−33.622310	−5.002626
34	37	−135.606441	−26.006375	136.109540	26.894437
37	39	5.833407	16.115807	−5.722728	−18.344133
37	40	−5.419973	11.950724	5.556411	−15.599791
30	38	30.925049	18.998466	−30.804810	−57.601319
39	40	−26.677272	7.344133	26.829255	−8.304390
40	41	11.218683	4.433704	−11.195421	−5.500413
40	42	−21.604349	−3.155819	21.880213	−0.387497
41	42	−33.204579	−4.499587	33.692867	2.834144
43	44	−8.803710	−3.017580	8.853264	−2.590059
34	43	12.869079	0.221632	−12.796290	−3.982420
44	45	−28.053264	4.220366	28.242847	−5.619189
45	46	−36.292498	−5.827437	36.844838	4.418372
46	47	−32.634138	−0.410340	33.035345	−1.477823
46	48	−18.810700	−4.011061	19.022824	−0.160332
47	49	−25.740241	−6.296973	25.868192	5.044056
42	49	−20.486540	−11.262214	20.832881	4.137148

42	49	−20.486540	−11.262214	20.832881	4.137148
45	49	−55.550348	−0.885580	57.734717	2.346891
48	49	−43.022824	4.762961	43.346400	−5.165194
49	50	68.886564	11.289329	−67.642321	−9.704830
49	51	85.488314	18.615795	−81.914908	−11.924588
51	52	35.977435	4.727933	−35.687701	−5.168765
52	53	14.087701	0.168765	−13.997257	−3.448083
53	54	−13.602743	−7.551917	13.668727	5.065768
49	54	50.731675	11.394740	−48.781356	−10.915793
49	54	50.388115	9.011137	−48.151581	−8.685380
54	55	8.800748	1.054444	−8.785672	−2.827889
54	56	21.331177	3.545129	−21.317003	−4.162811
55	56	−27.404435	−3.865109	27.445608	3.652839
56	57	−31.382533	−4.033874	31.756945	2.851565
50	57	47.242321	5.704830	−46.156945	−5.851565
56	58	−10.912154	0.584324	10.958102	−2.662690
51	58	25.537473	−0.803345	−25.358102	−0.337310
54	59	−34.467714	−6.274896	35.129875	3.665527
56	59	−31.560880	−2.667636	32.463818	0.065188
56	59	−33.073037	−2.303861	34.038141	0.137024
55	59	−39.409892	−6.754037	40.231223	5.196689
59	60	−53.822811	6.998377	54.794739	−6.229445
59	61	−63.850326	8.875613	65.267700	−6.196607
60	61	−134.893968	10.272180	135.384647	−9.201222
60	62	−13.500772	−7.042736	13.528504	5.714787
61	62	28.292119	−14.438053	−28.209294	13.842837
63	64	−201.589921	−63.653014	202.391673	52.487930
38	65	−182.547213	−56.627906	185.797752	−9.030742
64	65	−271.336138	−59.063005	273.437718	45.157507
49	66	−143.895967	8.101356	147.458616	7.418070
49	66	−143.895967	8.101356	147.458616	7.418070
62	66	−46.586146	−14.361354	47.700222	13.335447
62	67	−31.133065	−11.711187	31.410917	9.819429
66	67	65.974895	18.317840	−65.010917	−16.819429
65	68	−131.627819	−4.501664	131.875040	−56.919280
47	69	−48.095104	7.774796	50.090661	−8.670441
49	69	−36.717804	6.088567	38.083938	−10.379345
69	70	89.800324	18.222385	−87.370302	−20.376127
24	70	1.400837	−3.092636	−1.400710	−6.838540
70	71	−12.878754	−5.485794	12.896195	4.703281
24	72	−5.019859	4.969568	5.059296	−9.555665
71	72	−6.904484	3.442519	6.940704	−7.594904
71	73	−5.991711	−8.145799	6.000000	7.037033
70	74	20.877930	11.579080	−20.625142	−13.921128
70	75	1.571836	9.987464	−1.509920	−13.207810
69	75	93.799082	24.578909	−90.104190	−25.881914
74	75	−60.974858	−1.277569	61.473227	1.965155
76	77	−87.694491	−9.774326	91.567320	19.185392
69	77	−13.894867	28.697385	14.289073	−38.221005
75	77	−60.079245	0.475580	62.406542	2.421251
77	78	38.855833	13.288090	−38.792534	−14.354538
78	79	−46.407466	−11.645462	46.531347	11.543905
77	80	−146.728624	−16.824572	150.380083	22.300988
77	80	−68.579508	−12.375656	69.982373	14.999143
79	80	−93.331347	−23.215470	94.744353	27.630463
68	81	−82.031615	−3.212151	82.173111	−75.897786
77	82	−65.010637	52.367636	67.195224	−54.175667
82	83	−94.685587	42.144406	95.956583	−41.613119
83	84	−45.522791	22.622463	47.258501	−21.410101
83	85	−74.433792	18.500857	77.122542	−12.589523
84	85	−60.458501	14.410101	61.690827	−12.979793
85	86	21.436838	−7.615758	−21.256851	5.568702
86	87	−3.943149	−15.568702	4.000000	11.531793
85	88	−81.546183	19.494612	83.006425	−14.722448
85	89	−107.504024	11.747932	110.399416	4.556759
88	89	−140.606425	4.722448	143.449241	7.926344
89	90	14.954106	4.067637	−14.816161	−8.794846
89	90	27.990485	8.432830	−27.761087	−17.967189
90	91	33.977247	−4.934746	−33.671042	3.876802
89	92	235.811970	−2.855634	−230.361489	25.211395
89	92	74.394782	−5.845520	−72.235793	10.415696
91	92	43.671042	−20.146008	−42.763480	19.961651
92	93	90.414684	−13.029858	−88.220386	18.131529
92	94	83.893198	−16.864406	−80.322865	24.648909
93	94	73.820386	−25.131529	−72.415663	27.938882
94	95	92.660383	−0.527509	−91.485401	3.332607
80	96	−9.661605	32.215105	10.092921	−35.066791
82	96	−37.309637	4.238697	37.552365	−8.683390
94	96	73.337599	−21.579250	−71.720798	24.582544
80	97	−0.585112	36.735179	0.830887	−38.139460
80	98	−14.443814	20.536646	14.597030	−22.877501
80	99	−51.589388	26.891074	53.080385	−25.863398
92	100	38.638531	−17.605209	−37.494306	18.065248
94	100	−49.259454	−46.481032	50.057526	43.044957
95	96	41.085401	−34.332607	−40.573531	34.564102
96	97	19.049042	−30.396466	−18.830887	29.139460
98	100	−55.397030	14.877501	56.681562	−14.026310
99	100	−11.080385	−7.307387	11.108845	5.217188
100	101	−20.708849	25.426553	21.020723	−27.307767
92	102	54.414350	−9.089268	−54.033148	9.392131
101	102	−47.420723	12.307767	48.033148	−12.392131
100	103	66.697232	4.924291	−65.999902	−8.104629
100	104	39.147030	12.798192	−38.372729	−14.643946
103	104	28.660120	10.347419	−28.208541	−12.778695
103	105	33.018082	10.855521	−32.349815	−12.780749
100	106	42.110961	11.985509	−40.938663	−13.620855
104	105	20.981270	7.735245	−20.927771	−8.456368

105	106	14.387974	2.962645	−14.354917	−4.165082
105	107	7.973359	2.755515	−7.923266	−6.922255
105	108	−6.283747	0.170014	6.295095	−1.860788
106	107	3.693579	1.785937	−3.676734	−6.048770
108	109	−8.695095	0.860788	8.703757	−1.547612
103	110	16.721701	10.901689	−16.545299	−14.584355
109	110	−18.303757	−1.452388	18.403388	−0.175617
110	111	−35.702945	0.956135	36.000000	−1.843825
110	112	−12.955144	−0.911966	13.000000	−4.853607
17	113	−6.074561	8.925912	6.085945	−9.647387
32	113	0.221145	−16.678471	−0.085945	12.168987
32	114	11.336127	2.107267	−11.316227	−3.521515
27	115	24.797430	4.906224	−24.683857	−6.224736
114	115	1.716227	0.521515	−1.716143	−0.775264
68	116	−183.879448	−51.031969	184.000000	35.942697
12	117	24.214318	5.465530	−24.000000	−8.000000
75	118	33.820129	25.648990	−33.535965	−25.804776
76	118	6.094491	−11.916602	−6.064035	10.804776

Transformer Flows

FB	TB	Pij (MW)	Qij (MVAR)	Pji (MW)	Qji (MVAR)
8	5	392.296859	129.329220	−392.296859	−86.426098
26	25	93.641329	21.690751	−93.641329	−18.533512
30	17	261.538057	94.534461	−261.538057	−66.032705
38	37	213.352023	114.229225	−213.352023	−93.484366
63	59	201.589921	63.653014	−201.589921	−46.620451
64	61	68.944465	6.575075	−68.944465	−5.280796
65	66	63.392349	72.896520	−63.392349	−69.907763
68	69	134.036023	111.163400	−134.036023	−101.406264
81	80	−82.173111	75.897786	82.173111	−71.823204

APPENDIX D

EPCL CODE FOR USER DEFINED CONTROLLED VOLTAGE SOURCE CONVERTER CONTROL MODEL

```
/*****************************************************************************/
/****** epcgen model for controlled voltage source representation of converter
                          along with associated control          ***************/
/*****************************************************************************/

/* Model comments and data description
This model depicts the converter as a controlled voltage source. The dc bus voltage has
also been represented.

Model created at Arizona State University (ASU)

This is the first version of this model and further development is ongoing.

Model Input Parameters

  rsrc    Coupling resistance
  xsrc    Coupling inductance
  Tr      Voltage transducer time constant (sec)
  Kp      Proportional Gain
  Ki      Integral Gain
  Kip     Active power integral gain
  Kiq     Reactive power integral gain
  Rq      Q-V droop coefficient
  TQ      Q time delay (sec)
  Rp      P-f droop coefficient
  Tg      Time constant (sec)
  T1      Lead time constant (sec)
  T2      Lag time constant (sec)
  TD      P time delay (sec)
  Ted     Ed time delay (sec)
  Teq     Eq time delay (sec)
  MWcap   Maximum MW cap for the governor part of the converter
  Pmax    Maximum Active power
  Qmax    Maximum Reactive Power
  Qmin    Minimum Reactive Power
  dV      Voltage variation for trip
  dt      Time for voltage variation
  Imax    Max Current
  Tfl     1.0 - indicates that governor is active
          0.0 - indicates that governor is not active

Sample Input dynamic data record:

epcgen Busno. "Bus Name" kV "id" : #9 mva=100.0 "convepc.p" 5.0 "rsrc" 0.0 "xsrc" 0.05
"Tr" 0.02...


***** End of comments */

define INIT 2
define SORC 3
define ALGE 4
define RATE 5
define OUTP 7
define NETW 8

@mx = dypar[0].cmi
@k = model[@mx].k
@bus=model[@mx].bus
@mode = dypar[0].mode
@kgen = genbc[@k].kgen

switch (@mode)

  case SORC:

        if (epcgen[@mx].er>0.)
      @delt=arctan(epcgen[@mx].ei/epcgen[@mx].er)
        elseif (epcgen[@mx].er<0. and epcgen[@mx].ei>=0.)
```

```
            @delt=arctan(epcgen[@mx].ei/epcgen[@mx].er)+(1.570796327*2)
          elseif (epcgen[@mx].er<0. and epcgen[@mx].ei<0.)
            @delt=arctan(epcgen[@mx].ei/epcgen[@mx].er)-(1.570796327*2)
          elseif (epcgen[@mx].er=0. and epcgen[@mx].ei>0.)
            @delt=1.570796327
          elseif (epcgen[@mx].er=0. and epcgen[@mx].ei<0.)
            @delt=-1.570796327
          endif

         /* Using Vdc to get the required internal converter ac voltage */
         @E = sqrt((epcgen[@mx].s6*epcgen[@mx].s6)+(epcgen[@mx].s7*epcgen[@mx].s7))
         @Vdc = epcgen[@mx].v10
         @VT = epcgen[@mx].v11
         @wst = 2*(22/7)*60*dypar[0].time
         @m = @E/@VT

         if (@m>1.0)
           @m=1.0
         endif
         if (@m<0.4)
           @m=0.4
         endif

         if (epcgen[@mx].s6>0.)
        @delt1=arctan(epcgen[@mx].s7/epcgen[@mx].s6)
          elseif (epcgen[@mx].s6<0. and epcgen[@mx].s7>=0.)
            @delt1=arctan(epcgen[@mx].s7/epcgen[@mx].s6)+(1.570796327*2)
          elseif (epcgen[@mx].s6<0. and epcgen[@mx].s7<0.)
            @delt1=arctan(epcgen[@mx].s7/epcgen[@mx].s6)-(1.570796327*2)
          elseif (epcgen[@mx].s6=0. and epcgen[@mx].s7>0.)
            @delt1=1.570796327
          elseif (epcgen[@mx].s6=0. and epcgen[@mx].s7<0.)
            @delt1=-1.570796327
          endif

         @Va = 0.5*@m*@Vdc*cos((@wst)+@delt1)
         @Vb = 0.5*@m*@Vdc*cos((@wst)+@delt1-2.094395102)
         @Vc = 0.5*@m*@Vdc*cos((@wst)+@delt1+2.094395102)

         @Ed = (2/3)*((@Va*cos(@wst))+(@Vb*cos(@wst-2.094395102))+(@Vc*cos(@wst+2.094395102)))
         @Eq = (-2/3)*((@Va*sin(@wst))+(@Vb*sin(@wst-2.094395102))+(@Vc*sin(@wst+2.094395102)))

         epcgen[@mx].v14=sqrt((@Ed*@Ed)+(@Eq*@Eq))

    epcgen[@mx].angle= @delt+1.570796327

         epcgen[@mx].ed=@Ed
         epcgen[@mx].eq=@Eq

break

case NETW:

break

case ALGE:

break

case RATE:

    @vmon = volt[@bus].vm

         @mvabase = gens[@kgen].mbase

        /* Setting of the limits */

         @x=epcgen[@mx].Imax
```

```
      @Qmax1=epcgen[@mx].Qmax
@Qmax2=sqrt(pow((@x*@mvabase),2)/1.19047)     /* 0.4 power factor */
      @deninv=2.0

if (@vmon>0.8)
 @qmax=@Qmax1-((@Qmax2-@Qmax1)*(@vmon-1.0)*4.0)     /*Qmax according to voltage*/
      else
       @qmax=@Qmax1-((@Qmax2-@Qmax1)*(0.8-1.0)*4.0)     /*Qmax according to voltage*/
      endif
@qmin=epcgen[@mx].Qmin
      @lim=pow((@x*@mvabase),2)-pow(@qmax,2)
      if (@lim<0.0)
        @qmax=0.9*@x*@mvabase
        @lim=pow((@x*@mvabase),2)-pow(@qmax,2)
      endif
@pmax=sqrt(@lim)     /* to preserve the MVA*/

      /* To preserve current */
      @I=sqrt(pow(epcgen[@mx].itr,2)+pow(epcgen[@mx].iti,2))
      if (dypar[0].time>2.0 and @I>@x)
        @qmax=0.85*@x*@mvabase*epcgen[@mx].s1
        @pmax=(sqrt((@x*@x)-pow((@qmax/@mvabase)/epcgen[@mx].s1,2)))*epcgen[@mx].s1*@mvabase
      endif

      /* Voltage Transducer */

      epcgen[@mx].ds1 = (@vmon-epcgen[@mx].s1)/epcgen[@mx].Tr

      @verr = genbc[@k].vref-epcgen[@mx].s1-(epcgen[@mx].Rq*gens[@kgen].qgen/@mvabase)

      /* PI Block */

      epcgen[@mx].ds0 = epcgen[@mx].Ki*(@verr-(100*epcgen[@mx].v3))
      @prop = epcgen[@mx].Kp*@verr

      @Qcmd = @prop+epcgen[@mx].s0

      epcgen[@mx].v3=@Qcmd
if ((@Qcmd*@mvabase)>@qmax)
 @Qcmd=@qmax/@mvabase
endif

if ((@Qcmd*@mvabase)<@qmin)
 @Qcmd=@qmin/@mvabase
endif
epcgen[@mx].v3=epcgen[@mx].v3-@Qcmd

      @Iqcmd = -@Qcmd/epcgen[@mx].s1-epcgen[@mx].s9

      /* Q time delay */

      epcgen[@mx].ds4 = (@Iqcmd-epcgen[@mx].s4)/epcgen[@mx].TQ

      /* Governor time constant */
      @perr = genbc[@k].pref-(netw[@bus].f/epcgen[@mx].Rp)
      epcgen[@mx].ds2 = (@perr-epcgen[@mx].s2)/epcgen[@mx].Tg

      /* Lead lag block */

      epcgen[@mx].ds3 = (epcgen[@mx].s2-epcgen[@mx].s3
                         -(epcgen[@mx].s2*epcgen[@mx].T1/epcgen[@mx].T2))/epcgen[@mx].T2

      @Pcmd = (epcgen[@mx].s3+(epcgen[@mx].s2*epcgen[@mx].T1/epcgen[@mx].T2))
                         *epcgen[@mx].MWcap/@mvabase

      if ((@Pcmd*@mvabase)>@pmax)
       @Pcmd=@pmax/@mvabase
```

```
endif

    if (epcgen[@mx].Tfl=0.0)
      @Pcmd=genbc[@k].pref*epcgen[@mx].MWcap/@mvabase
    endif

    @Ipcmd = (@Pcmd/epcgen[@mx].s1)+epcgen[@mx].s8

    /* P time delay */

    epcgen[@mx].ds5 = (@Ipcmd-epcgen[@mx].s5)/epcgen[@mx].TD

    /* Calculating the inner voltage */

     if (epcgen[@mx].er>0.)
   @delt=arctan(epcgen[@mx].ei/epcgen[@mx].er)
     elseif (epcgen[@mx].er<0. and epcgen[@mx].ei>=0.)
       @delt=arctan(epcgen[@mx].ei/epcgen[@mx].er)+(1.570796327*2)
     elseif (epcgen[@mx].er<0. and epcgen[@mx].ei<0.)
       @delt=arctan(epcgen[@mx].ei/epcgen[@mx].er)-(1.570796327*2)
     elseif (epcgen[@mx].er=0. and epcgen[@mx].ei>0.)
       @delt=1.570796327
     elseif (epcgen[@mx].er=0. and epcgen[@mx].ei<0.)
       @delt=-1.570796327
     endif


    @vq=(-epcgen[@mx].er*sin(@delt))+(epcgen[@mx].ei*cos(@delt))
    @vd=(epcgen[@mx].er*cos(@delt))+(epcgen[@mx].ei*sin(@delt))

     @iq=epcgen[@mx].s4
     @id=epcgen[@mx].s5

     @ed=epcgen[@mx].v12+(@id*epcgen[@mx].rsrc)-(@iq*epcgen[@mx].xsrc)
     @eq=epcgen[@mx].v13+(@iq*epcgen[@mx].rsrc)+(@id*epcgen[@mx].xsrc)

    epcgen[@mx].ds6 = (@ed-epcgen[@mx].s6)/epcgen[@mx].Ted
    epcgen[@mx].ds7 = (@eq-epcgen[@mx].s7)/epcgen[@mx].Teq

    epcgen[@mx].ds8 = epcgen[@mx].Kip*(@Pcmd-(gens[@kgen].pgen/@mvabase))
    epcgen[@mx].ds9 = epcgen[@mx].Kiq*(@Qcmd-(gens[@kgen].qgen/@mvabase))

    /*set variables for output file */
      epcgen[@mx].v0 = gens[@kgen].pgen
      epcgen[@mx].v1 = gens[@kgen].qgen
      epcgen[@mx].v2 = volt[@bus].vm


    /* remaining output variables */
    epcgen[@mx].v4=@Qcmd*@mvabase
    epcgen[@mx].v5=@Pcmd*@mvabase
    epcgen[@mx].v6=@Iqcmd
    epcgen[@mx].v7=@Ipcmd
    epcgen[@mx].v8=sqrt((epcgen[@mx].itr*epcgen[@mx].itr)+(epcgen[@mx].iti*epcgen[@mx].iti))
    epcgen[@mx].v9=epcgen[@mx].v14

    /* Setting the trip settings */
    /* Overcurrent trip*/

    if (epcgen[@mx].v8 > epcgen[@mx].Imax)
      gens[@kgen].st=0
      logterm("Tripping converter at bus ",busd[@bus].extnum," due to overcurrent<")
    endif

    /* Over voltage trip */
    if ((@vmon-genbc[@k].vref)>epcgen[@mx].dV)
  if(epcgen[@mx].v15=0.0)
```

```
            epcgen[@mx].v15=dypar[0].time
                logterm("Over voltage timer started at bus ",busd[@bus].extnum,"<")
          endif
          if ((dypar[0].time-epcgen[@mx].v15) > epcgen[@mx].dt)
             gens[@kgen].st=0
             logterm("Tripping converter at bus ",busd[@bus].extnum," due to overvoltage<")
          endif
        endif

    if ((@vmon-genbc[@k].vref)<epcgen[@mx].dV and epcgen[@mx].v15>0.0)
      epcgen[@mx].v15=0.0
      logterm("Over voltage timer reset at bus ",busd[@bus].extnum,"<")
    endif

break

case INIT:

  @mvabase = gens[@kgen].mbase
       @pgen = gens[@kgen].pgen/@mvabase
       @qgen = gens[@kgen].qgen/@mvabase


       epcgen[@mx].s1 = volt[@bus].vm
       genbc[@k].vref = epcgen[@mx].s1+(epcgen[@mx].Rq*@qgen)

       epcgen[@mx].s0 = @qgen
       @iqcmd = -@qgen/epcgen[@mx].s1
       epcgen[@mx].s4 = @iqcmd
       epcgen[@mx].v3=0.0                          /* for anti-windup limit*/

       genbc[@k].pref = @pgen*@mvabase/epcgen[@mx].MWcap
       epcgen[@mx].s2 = @pgen*@mvabase/epcgen[@mx].MWcap
       epcgen[@mx].s3 = epcgen[@mx].s2*(1-(epcgen[@mx].T1/epcgen[@mx].T2))
       @pcmd = @pgen
       @ipcmd = @pcmd/epcgen[@mx].s1
       epcgen[@mx].s5 = @ipcmd


       /* Calculating the inner voltage */

         if (epcgen[@mx].er>0.)
       @delt=arctan(epcgen[@mx].ei/epcgen[@mx].er)
         elseif (epcgen[@mx].er<0. and epcgen[@mx].ei>=0.)
           @delt=arctan(epcgen[@mx].ei/epcgen[@mx].er)+(1.570796327*2)
         elseif (epcgen[@mx].er<0. and epcgen[@mx].ei<0.)
           @delt=arctan(epcgen[@mx].ei/epcgen[@mx].er)-(1.570796327*2)
         elseif (epcgen[@mx].er=0. and epcgen[@mx].ei>0.)
           @delt=1.570796327
         elseif (epcgen[@mx].er=0. and epcgen[@mx].ei<0.)
           @delt=-1.570796327
         endif


        @vq=(-epcgen[@mx].er*sin(@delt))+(epcgen[@mx].ei*cos(@delt))
        @vd=(epcgen[@mx].er*cos(@delt))+(epcgen[@mx].ei*sin(@delt))

         @iq=epcgen[@mx].s4
         @id=epcgen[@mx].s5

        @ed=@vd+(@id*epcgen[@mx].rsrc)-(@iq*epcgen[@mx].xsrc)
        @eq=@vq+(@iq*epcgen[@mx].rsrc)+(@id*epcgen[@mx].xsrc)

        epcgen[@mx].v12=@vd
        epcgen[@mx].v13=@vq

        epcgen[@mx].s6 = @ed
```

```
 epcgen[@mx].s7 = @eq

 epcgen[@mx].s8 = 0.0
 epcgen[@mx].s9 = 0.0

 /* obtaining the value of dc link voltage */
 @E = sqrt((@ed*@ed)+(@eq*@eq))
 @VT = @E/0.6
 @Vdc = @E/(0.5*0.6)

epcgen[@mx].v4=@qgen
epcgen[@mx].v5=@pgen
epcgen[@mx].v6=@iqcmd

epcgen[@mx].v8=sqrt((epcgen[@mx].itr*epcgen[@mx].itr)+(epcgen[@mx].iti*epcgen[@mx].iti))
epcgen[@mx].v9=sqrt((@id*@id)+(@iq*@iq))
epcgen[@mx].v10=@Vdc
epcgen[@mx].v11=@VT
epcgen[@mx].v15=0.0



epcgen[@mx].ds0 = 0.0
epcgen[@mx].ds1 = 0.0
epcgen[@mx].ds2 = 0.0
epcgen[@mx].ds3 = 0.0
epcgen[@mx].ds4 = 0.0
epcgen[@mx].ds5 = 0.0
epcgen[@mx].ds6 = 0.0
epcgen[@mx].ds7 = 0.0
epcgen[@mx].ds8 = 0.0
epcgen[@mx].ds9 = 0.0


channel_head[0].type = "pg"
channel_head[0].cmin = 0.
channel_head[0].cmax = 150.0
channel_head[1].type = "qg"
channel_head[1].cmin = -50.0
channel_head[1].cmax = 50.0
channel_head[2].type = "vt"
channel_head[2].cmin = 0.
channel_head[2].cmax = 1.050
channel_head[3].type = "qwindup"
channel_head[3].cmin = 0.
channel_head[3].cmax = 1.050
channel_head[4].type = "qcmd"
channel_head[4].cmin = 0.
channel_head[4].cmax = 1.050
channel_head[5].type = "pcmd"
channel_head[5].cmin = 0.
channel_head[5].cmax = 1.050
channel_head[6].type = "iqcmd"
channel_head[6].cmin = 0.
channel_head[6].cmax = 1.050
channel_head[7].type = "ipcmd"
channel_head[7].cmin = 0.
channel_head[7].cmax = 1.050
channel_head[8].type = "Icurr"
channel_head[8].cmin = 0.
channel_head[8].cmax = 1.050
channel_head[9].type = "E"
channel_head[9].cmin = 0.
channel_head[9].cmax = 1.050
```

```
    break

    case OUTP:

    break

endcase
end
```